Spatiotemporal Assessment of Land Use & Climate Change and Unprecedented COVID-19 Impacts on the Environment in East and Southeast Asia: Case Studies from Malaysia and Taiwan

WONG YONG JIE

2022

Spatiotemporal Assessment of Land Use & Climate Change and Unprecedented COVID-19 Impacts on the Environment in East and Southeast Asia: Case Studies from Malaysia and Taiwan

東・東南アジアにおける土地利用・気候の変化および新型コロナによる環境影響の時空間的評価:マレーシアと台湾の事例

WONG YONG JIE

Department of Environmental Engineering
Graduate School of Engineering
Kyoto University

2022

Table of Content

Chapter 5 Spatiotemporal impact of COVID-19 on Taiwan air quality in the absence of lockdown

List of Figures

List of Tables

Executive Summary

1060-31-9049 Wong Yong Jie

In this research, spatiotemporal effects of land use, climate and COVID-19 impacts on environment in East (Taiwan) and Southeast Asia (Malaysia) are studied using four case studies (Chapter 3 to Chapter 6). The impacts of changing land use and occurrence of extreme climatic events have been alarming across the globe; however the local scale conditions remain unknown. Therefore, to address these questions, Chapters 3 and 4 focus on identifying the streamflow conditions under changing land use and changing climate, respectively. In addition, the occurrence of the COVID-19 pandemic has found to bring profound impacts on many aspects of life and the economy; notably, due to the new normal lifestyle, nature has been reclaiming itself. However, the air quality conditions in the absence of lockdown were not reported. Therefore, to understand the impacts of COVID-19, Chapters 5 and 6 performed the comparison in pollutants concentration between business-as-usual and simulated concentrations, using linear regression models and artificial intelligence (AI) models, respectively.

In Chapter 3, it could be observed that network optimization played an important role in improving the prediction accuracy of the land use type classification from satellite images. Compared to artificial neural network (ANN), support vector machine (SVM) has lesser sensitivity on the hyperparameter adjustment, but higher variation is observed across different training algorithms/membership functions. This is mainly due to SVM is a rule-based algorithm where the characteristics among parameters must be well understood before making the predictions. Therefore, in this research, ANN might be more suitable for predicting the land use type from the satellite images. For future land use simulation, the prediction accuracy for utilizing the present land use maps (1990 and 2000) to simulate 2016 land use maps could reach up to 97%, indicating the accuracy of the Land Change Modeller (LCM). The forestry in the region experienced drastic loss up to 300% in 2050 as compared to 1990, and the urban area expanded up to 200% over 60 years. The simulated land use is used to simulate the future streamflow. Extreme streamflow such as no flow rate or very high flow rate up to 100 m^3/s is more commonly encountered in the future. Through the simulation, it is important to have proper management for water resources to prevent prolonged drought or extreme rainfall induced flood events. Based on the findings, valuable information on designing future sustainable urban development strategies can be provided.

In Chapter 4, the present, near-, mid- and far future of extreme flooding events across different cities in Taiwan were simulated using high resolution Meteorological Research Institute of the Japan Meteorological Agency version 3.2 (hereinafter referred to as MRI-AGCM3.2s) dataset under Rainfall-Runoff-Inundation (RRI) model. Bias-correction procedure is found crucial when using MRI-AGCM 3.2s dataset in Taiwan as huge variation are observed between

uncorrected and gauge dataset. The precipitation and temperature trends are observed to vary dynamically in the future, with increment of temperature more than 3 °C and rainfall volume change spatiotemporally across different cities. For near-and-mid future simulation, the maximum river flood rate is expected to increase more than 20%. However, for the far future, the East and South regions are expected to face severe flooding issues; whereas prolonged draught and water stress issues are expected in the Central and Northern regions, providing insightful findings to the responsible authorities to have better water storage and management. The application of high resolution GCM and regional downscaled climate data would be able to capture the complexity of land surface and local topographic characteristics in the small river basin, such as tributaries across Taiwan. Studies on climate change impacts on hydrology changes such as floods and droughts using MRI-AGCM 3.2s could provide additional analysis to the responsible authorities for better water balance management. To reduce the possibility of severe damage caused by extreme flooding, adequate water resource management, flood adaptation and mitigation strategies, flood prevention infrastructure, and efficient real-time flood early warning and forecasting systems are required

In Chapter 5, long-term 2019 coronavirus disease (COVID-19) impacts on the atmospheric environment in Taiwan, incorporating public transportation use and meteorological impacts in the absence of lockdowns was studied. Substantial improvements were observed in the studied air pollutants, wherein both PM_{10} and $PM_{2.5}$ showed the highest annual mean concentration reduction in 2020 relative to 2018-2019, by 24% and 18%, respectively, followed by SO_2, NO_2, CO and O_3, with reductions of 15%, 9.6% and 7.4% and 1.3%, respectively, even in the absence of lockdown. The occurrence frequency of air pollutants that may cause adverse health effects decreased by more than 30% in 2020 compared to 2018-2019, particularly in O_3 and $PM_{2.5}$. This research makes an important contribution to the literature as it is the first to investigate the impact and patterns of different modes of public transportation (*i.e.*, including roadway, railway, air, and waterway) on air quality improvements in 2020. The change trends of CO and NO_2, the major pollutants emitted from the public transportation sector, were found to be in parallel with the shift in traffic volume patterns in 2020. Similar to other reported studies, the seasonal variation in air pollutants (Figs. 5.4-5.6) and their correlations with meteorological parameters (Fig. 5.9) were found to be significant in this study. However, in 2020, although a significant improvement in air quality was observed during the rainy season, the simulated meteorologically normalized BAU air pollutant concentrations were observed to be higher than those in 2018-2019 due to reduced precipitation (approximately 240 mm) and an approximately 5% reduction in the frequency of wind speeds of less than 1.5 m/s. This may imply a delayed COVID-19 effect on the improvement in the air quality of Taiwan compared to the immediate improvements observed in countries that imposed lockdown, a phenomenon that has yet to be reported elsewhere.

In Chapter 6, utilizing four different AI methods, namely generalized additive model (GAM), gradient boosting machine (GBM), generalized linear model (GLM) and random forest (RF) to quantify the spatiotemporal impacts of COVID-19 on NO_2 and O_3 concentrations across 62 cities in Taiwan under meteorological-normalized business-as-usual (BAU) conditions. The selection of modelling method and the optimization of hyperparameter is crucial for each studied monitoring station for simulating the BAU concentrations of air pollutants. For GLM, the optimal data distribution for both NO_2 and O_3 modelling is Gaussian data distribution, whereas for GAM, the optimal data distribution for NO_2 and O_3 simulation is Quasi and Poisson, respectively. Meanwhile, for RF and GBM, the optimized number of trees is highly site dependent. Due to the complicated and non-linear characteristics between the air pollutants with temporal and meteorological parameters, regression-based models (GAM and GLM) have the poorest performance. For Taiwan, it could be observed that tree-based models (RF and GBM) are more suitable for simulating the NO_2 and O_3 BAU concentrations. Throughout 2020, even in the absence of a lockdown, the daily mean meteorological-normalized NO_2 and O_3 across Taiwan were observed to reduce by 14.9% and 5.8%, respectively with significant spatiotemporal variation. Due to the frequent occurrence of downpour in recent decades, further studies on higher temporal resolution such as hourly are required to better understand the meteorological impacts to the air pollutants. However, measures like lockdown will be unlikely to be imposed indefinitely. Therefore, based on the findings in this study, it is expected to provide a new insight/approach for better air quality management.

The assessment of the surface water and ground air quality is often labor-intensive, costly and time consuming. Therefore, the number of monitoring stations are lacking, particularly in developing countries. To address the possible issue, Chapter 7 presented the effective integration of IoT with 3D printing, microcomputers, and low-cost sensors on water quality monitoring and its possibility to be widely used for environmental monitoring, paving a new path for the development of cost-effective and reliable systems for both water and air quality monitoring.

The application and integration of remote sensing techniques, geographical information system (GIS), AI, big data analysis/management and IoT system has been gaining popularity in addressing/evaluating environmental issues. The number of monitoring station for pollutants concentrations are limited in most developing countries, leading to the limited local scale pollution management. Concurrently, due to limited data availability, the hydrological or air quality modelling are facing huge simulation challenges due to low simulation accuracy. Therefore, this research has studied and proven the integration of these techniques to possibly evaluate/address the environmental issues in the region, overcoming the low simulation accuracy by optimizing the models and proposing new monitoring technique for enhancing the spatiotemporal monitoring frequency.

Acknowledgements

Reminiscing the five years journey in Japan for my master and Ph.D., allowing me to have a deep self-reflection and insights for every single thing occurred in Japan, particularly in the Research Center for Environmental Quality Management (RCEQM), Kyoto University. Completion of the Ph.D. dissertation was not possible without the support and help received along the journey and I would like to take this opportunity to express my sincere gratitude to all of them.

First and foremost, I am extremely grateful to my research supervisor, Yoshihisa SHIMIZU-sensei, one of the giants in the field of environmental engineering especially in water related research. Working under his supervision always open another window and his sharing about the Japanese Culture as well as the experience as researcher is indeed very useful as different perspectives should be taken into consideration when performing any studies. One of the phrases that I like the most will be "*Even with the best technology in the world, without understanding the culture and social aspects of the society, the environmental issues will be remained unsolved*." All the valuable comments and suggestions provided by him have been very helpful not only in research, as well as in personal growth.

Also, I am extremely grateful to my PhD examination committee members, Minoru YONEDA-sensei and Tomonari MATSUDA-sensei for providing constructive and critical feedback on the thesis, as well as the aspects that I have overlooked in the study. Their advice has helped me to looked into my current research more deeply, and allowing me to further develop/plan for my route in research. From them, I have learned that the importance of mechanism in environmental processes are critical, and being able to clearly to present the reactions are especially crucial an engineering graduate. I will be keeping that in my mind!

Throughout my research journey in Japan, it cannot be done without the help from everyone in RCEQM. I would like to take this opportunity to express my gratitude to Hiroaki TANAKA-sensei, Fumitake NISHIMURA-sensei, Norihide NAKADA-sensei and Masaru IHARA-sensei. Thanks to their kind suggestions, technical knowledge sharing, and support provided along my academic journey in center. Besides that, there are two very important people in center that I am always indebted to, who are Yoshimi NISHIO-san and Kazumi HATTORI-san. They are just taking care of us like their siblings and children. Most of the application or documents required by the university are coordinated and well prepared by them, which have greatly reduced our burden. They have been great listeners and supporters whenever we shared our challenges with them and getting support to continue the journey. I am really thankful for all the great supports from them.

My persistence in this journey also credit to my friends in the center, who have been there supporting and standing side-by-side along the journey. The special culture, preparing the dinner and having it together with graduating students are indeed one of the best experiences that I have ever had in the center. As someone who has been through the stressful moments towards the end of graduation, the companion from friends, and the little chit chatting during the dinner time have greatly ease the condition and allowing us to keep fighting. All these little moments have definitely colored my center life. So special credit to Fern-san, Daigo-san, Shin-san, Higuchi-san, Ga-san,

Khagen-san, Tan-san, Phoebe-san, Miao-san, Zhao-san, Zhang-san, Mu-san, Yang-san, Han-san, Chen-san, Ngoc-san, Masuda-kun, Nishida-kun, Kato-kun, Araki-kun, Yoshino-kun and Aiko-kun, Tango-kun, Wada-kun, Nishijima-kun, Yoshida-kun, Lee-kun, Li-kun, Yu-kun, Huang-kun, Fan-kun, Nakakawa-kun and Fang-kun for enriching my center life!

Special credit also given to Nakayama and Kamiya, who are still meeting with each other whenever possible till now. Honestly, they are someone who I really looked up to, due to their persistence in work. Nakayama has initiated the whole 3D printed IoT-based monitoring system from zero, and then continued by Kamiya and me. I still remember vividly that Nakayama and I were still printing the system parts in center hours before our departure to Malaysia and the only time we were able to take rest was during the flight. Upon our arrival, we are starting our work from 6am, and reaching our hotel at 8/9pm every day. More interestingly, after dinner, that's the time we are enhancing/improving the system and then only can go to bed after 12am. The 2 weeks were exhausting, but one of my best memories as a researcher.

Also, along my PhD journey, I also would like to express my gratitude to Homma-san, who has been a great supporter, senpai and my Japanese sensei too. He has been willingly spending time to teach and share the required knowledge on experiment and for documentation for center and also for my dissertation. Homma-san also helped me to spend up to 7-8 hours to check sentence for sentence, slide by slide for my first Japanese presentation up to 30 mins for our seminar. And he will say this is for enhancing your achievement for better job application. Truly appreciate for the time on these!

I would like to acknowledge and thank the Japan Ministry of Education, Culture, Sport, Science and Technology (Monbukagakusho:MEXT) for providing me the scholarship to study at Kyoto University, Japan. The extraordinary experience is definitely an eye opening experience for me and bring back some ideas on how to contribute the nation.

Last but not least, my beloved family members who have been providing me endless support, encouragement as well as the prayers has made me to strive towards this important achievement. Without all your understanding, it would definitely a more challenging path for me. Thank you to sensei, this defense is performed in both physical and online platforms, allowing them to at least to understand or have a feel what I am working in Japan. Although they can't understand anything, but at least they feel they participated it.

2022, indeed a very special year, I have achieved what I have been wishing since years ago but at the same time, I have lost my backbone in my life in a sudden. Being a traditional parent, you have your own ways of loving us. As I am growing up, I know how much things you are keeping to yourself and giving the best to us. Your strength, attitude and everything in life, made me feel that you will be always here for us. Similar to all dads in the world, you seem to be capable in everything. So, you are the one who I least worry. Never thought of within a few hours, things would have changed drastically. And let me understand that, never takes things for granted, and expect the unexpected. I believe, you are always looking us up there, protecting us as always. Thanks for everything and as you can see, I am achieving another milestone.

In loving memory of my beloved dad

Chapter 1 Introduction

1.1 Hydrometeorological Natural Disasters

"We cannot stop natural disasters; but we can arm ourselves with knowledge: many lives wouldn't have to be lost if there was enough disaster preparedness.

***-Petra Nemcova** (2011)"*

Globally, the occurrence of disasters caused by weather-, climate- and water-related hazards (herein known as hydrometeorological disasters) are rising. In recent, the hydrometeorological hazards are usually associated with the extreme meteorological and climate events, such as flash floods, prolonged droughts, hurricanes, tornadoes, or landslides. They account for a dominant fraction of natural hazards and occur in all regions of the world, although the frequency and intensity of certain hazards and society's vulnerability to them differ among regions. Severe storms, strong winds, floods, and droughts develop at different spatial and temporal scales, but all can become disasters that cause significant infrastructure damage and claim hundreds/thousands of lives annually worldwide. According to World Meteorological Organization, on average, over the past 50 years from 1970 to 2019 – has been causing significant loss of life and set back economic and social development by years, if not decades, with daily casualty of 115 people and US$ 202 million in losses (WMO, 2021). The number of disasters has increased by a factor of five over the 50-year period, driven by climate change and more extreme weather events. The WMO originated from the International Meteorological Organization, which was founded in 1873, to facilitate the exchange of weather information across different countries. Till present, the WMO's mandate is in the areas of meteorology (weather and climate), operational hydrology and related geophysical sciences, playing a unique and powerful role in contributing to the safety and welfare of humanity, with 193 countries as joining members. Established in 1950, WMO became a specialized agency of the United Nations in 1951, it has furthered the application of meteorology in many areas.

In addition, WMO has contributed to the implementation of early warning systems to protect people and livelihoods since its establishment. It has now refocused its assistance to its members to strengthen their Impact-based Multi-hazard Early Warning Systems (through a number of initiatives such as the Severe Weather Forecasting Programme, the Flash Flood Guidance System, the Coastal Inundation Forecasting Initiative, the Climate Services Information System, the Global Multi-hazard Alert System and the High-Impact Weather Project). These systems seek to strengthen forecasting and warning for the impacts of hydrometeorological hazards and, in so doing, will significantly increase WMO Members' capacities to identify and reduce the risks associated with such hazards. The main goal is to provide the national agencies responsible for loss and damage accounting with an authoritative, scientifically reviewed dataset of hazardous events to aid in loss and damage accounting and to enhance risk assessment. The initiative is being implemented through the established WMO global observing, monitoring, and forecasting network at the national level as well as the regional and global levels

Therefore, to quantify the risk across the globe, WMO is working closely with CRED-EM DAT, which contains data on disasters associated with several types of natural hazards – geophysical, meteorological, climatological, hydrological, biological, and extra-terrestrial – and technological disasters dating back to the year 1900. According to CRED-EM DAT, from 1970 to 2019 there were 22,326 disasters, with reported deaths of 4,607,671 and US$ 4.92 trillion in economic losses. Based on the reports, oftentimes, multiple hazards can occur simultaneously or trigger cascading impacts from one extreme weather event. For example, in addition to causing injuries, deaths, and material damage, a tropical storm can also result in flooding and mudslides, which can disrupt water purification and sewage disposal systems, cause overflow of toxic wastes, and increase propagation of mosquito-borne diseases. Regardless of the economic status of the country (developed, developing or underdeveloped), they are encountering the burden of increasing frequency and severity of the disasters. Additionally, the escalating impact of disasters also associated to the growing vulnerability of human societies, especially those surviving on the margins of development. From 1970 to 2019, hydrometeorological hazards accounted for 50% of all disasters, 45% of

all reported deaths and 74% of all reported economic losses. Unfortunately, more than 91% of these deaths occurred in developing countries (using the United Nations Country Classification), mainly due to the unpreparedness/emergency mitigations to tackle the emerging climate crisis.

1.2 Atmospheric Natural Disasters

Apart from the hydrometeorological disasters, atmospheric pollution is also one of the silent killers that has been causing more than 7 million premature deaths annually, being recognized as the largest environmental health risk globally. It accounts for 1 in 8 deaths worldwide, particularly in developing countries (WHO, 2021). The risks from air pollution are now far greater than previously thought or understood, particularly for heart disease and stroke. Compared to 2012, the number of deaths has been increased double due to the uncontrolled urbanization and deforestation, particularly in Asia. As shown in Fig. 1.1, it could be observed that significant number of deaths is observed in Asia. Outdoor air pollution exposure has been one of the undeterred contributors to the wide range of adverse health problems, with millions of premature annual deaths worldwide. In most of the countries, the rapid economic development and uncontrolled urbanization have exacerbated the air pollutants emission, particularly from industry, power generation and transportation sectors.

According to Air Quality and Climate Bulletin by World Meteorological Organization (WMO, 2021), the global mortality due to air pollution was increased by 2-fold in 2019 (4.5 million deaths) as compared to 1990, with approximately 99% of the global population living with air pollutants level exceeded World Health Organization guidelines (WHO, 2021). Despite numerous blueprints/actions were proposed and implemented across different nations (Global Clean Air Initiative, Climate and Clean Air Coalition, Clean Air Fund *etc.*), the cross-cutting challenges including the lack of financial resources, government transparency, institutional and expert capacity, have resulted outdoor air pollution remains an unresolved problem (UNEP, 2021).

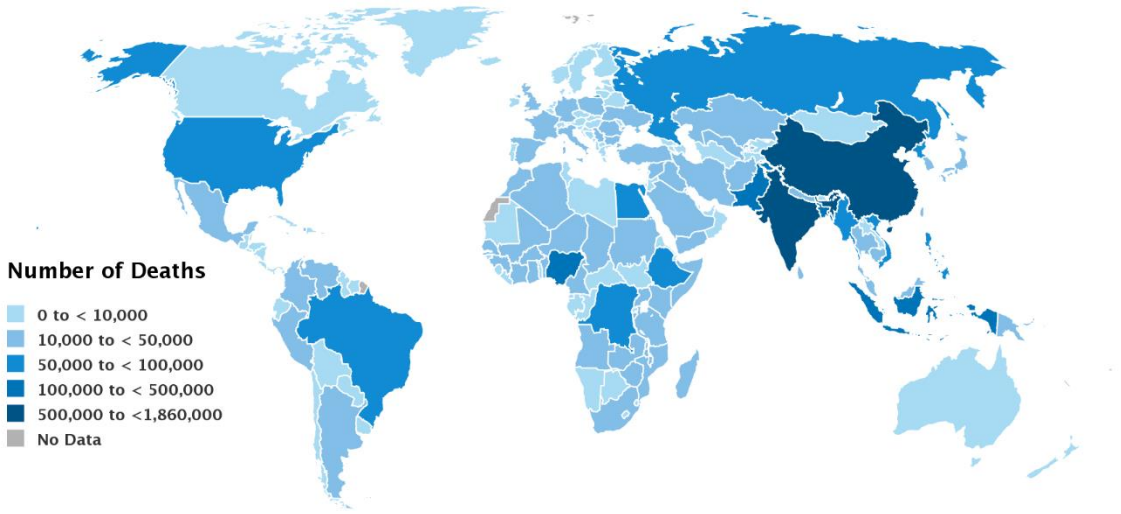

Fig. 1.1: Numbers of deaths attributable to total air pollution in 2019 (Ourworlddata, 2020)

In particular, three major threatening air pollutants are (i) ozone (O_3), (ii) particulate matter (PM) and (iii) nitrogen dioxide (NO_2). Although tremendous efforts to combat air pollution have been made across the globe, such as formulating numerous frameworks/laws/policies at both the national (Li *et al*., 2017; Amann *et al*., 2017) and international levels (Shapiro and Yarime, 2021). Nevertheless, large gaps have been observed in implementation, financing and enforcement capacity (United Nations Environment Programme, 2021), causing air pollution to remain a major health threat worldwide.

1.3 Drivers for increased natural disasters

For both hydrometeorological and atmospheric disasters, the increasing occurrence frequency are observed, and this may be generally due to two main drivers, which are (i)land use and (ii) climate change. According to the simulation reported by Karina *et al.* (2021), the global land use change is four times faster than simulated, marking the rapid and uncontrolled urbanization activities across the globe. Among the land use type that is usually converted is forest. Based on Fig. 1.2, the annual average deforestation between 2015-2020 has increased by almost 80% as compared to 1990-1995 (Ourworldindata, 2020). Intensive deforestation (up to 1 million ha per year) was observed particularly in developing countries in Asia, which has significantly disturbed the hydrologic storage or retention. These

disturbances have impaired resilience of water resources to other non-abrupt changes such as climate shifts (Jones *et al*., 2009). Moreover, it also significantly disturbed the water balance in a watershed by inducing significant decrease in the infiltration and evapotranspiration (by 76% and 12%, respectively). At the same time, total runoff, surface runoff, interflow and base flow increased by 20.4, 38.8, 9.0 and 25.5%, respectively. Daily discharge increased by 20%. The deforestation significantly increased peak discharge induced by a simulated extreme precipitation event with the recurrence interval of 100 years. In the deforested watershed, the peak discharge was higher by 58% as compared to 1990s. Therefore, it is necessary to understand the conditions of water balance in changing land use.

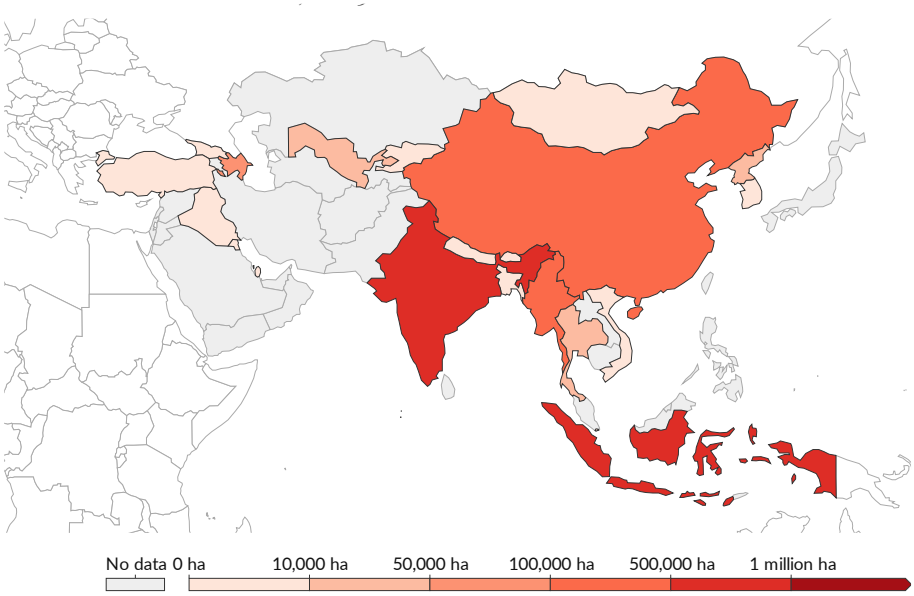

Fig. 1.2: Global annual average deforestation in hectare (Ourworldindata, 2020)

On the other hand, reported and proven in many studies, the climate change impacts are significant, particularly in Asia region. Asia has been known as the most vulnerable region for the climate change impacts, where the highest number of extreme climatic events are reported in this region. According to United Nation for Disaster Risk Reduction (UNDRR), between 2000 and 2019, there were 3,068 disaster events in Asia, which has been constituting 60% of global disasters. The high frequency and impact of disasters in Asia are largely due to the size of the continent and landscapes that represent a high risk of natural

hazards, such as river basins, flood plains, and seismic fault lines. Additionally, there are high population densities in many disaster-prone areas of the continent. In terms of affected countries globally, China (577 events), followed by India (321 events), Philippines (304 events), and Indonesia (278 events) reported the highest disasters in these countries. These countries all have large and heterogenous landmasses and relatively high population densities in at-risk areas as shown in Fig. 1.3.

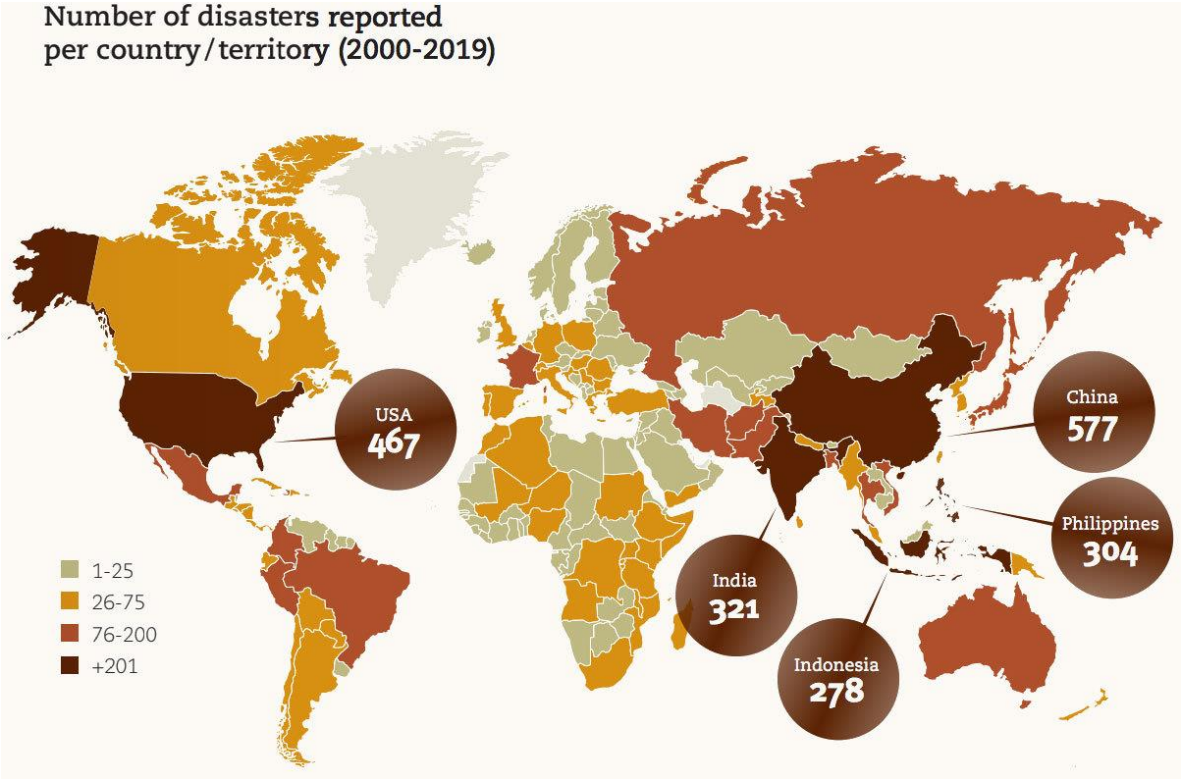

Fig. 1.3: Number of extreme weather events (2000-2019) (DRR, 2020)

Under changing climate, seasonal meteorological impacts on air pollutants have been studied extensively (Yousefian *et al*., 2020; Liu *et al*., 2020); however, due to their complex, coupled, and adaptive interactions and dynamic characteristics, the reported findings may vary according to geographical region and intensity of meteorological parameters (Tfwala *et al.*, 2017). Although numerous flood risk management frameworks have been proposed and developed for minimizing the potential losses and ensuring public safety, for instance, identifying flood risk zone through flood inundation maps utilizing historical precipitation

data (Chen *et al.* 2011; Doong *et al.*, 2016); however, due to the complex and heterogeneous climate variability, the distribution and intensity of precipitation varied spatiotemporally, which has been supported by both historical observations and model simulations (Rajah *et al.*, 2014). Therefore, it is fundamental to develop robust and reliable future climate simulations to identify the future flow regime and allow decision-makers to formulate corresponding prevention policies for the emerging risk.

1.4 Unprecedented COVID-19

Since the end of 2019, COVID-19 has tremendously disrupted the normal rhythm of livelihood and has led to dramatic loss of human life worldwide, with infections and deaths exceeding 242 million and 4.9 million, respectively, as of October 2021 (Worldometer, 2021). The COVID-19 is caused by the novel severe acute respiratory syndrome coronavirus 2 that can be transmitted through the air, particularly in crowded areas or poorly ventilated indoor areas (Dinoi *et al.*, 2022) and can survive on a variety of surfaces for hours (van Doremalen *et al.*, 2020). Due to its high infectivity and transmissibility, it was classified as a global pandemic by the World Health Organization (WHO) on March 11, 2020 (WHO, 2020). Therefore, most governments across the globe have imposed restrictive/preventive measures, such as lockdowns, travel restrictions, shelter-at-home policies, social distancing, and mandatory mask wearing in public places, to contain or slow down the spread of COVID-19. Concurrently, these measures also reduced emissions from major anthropogenic and economic activities due to the disruption of anthropogenic emissions. Consequently, a remarkable change in air pollutant concentrations was observed throughout the world, particularly in countries that imposed lockdown, creating a silver lining in the dark cloud of COVID-19 (Jephcote *et al.*, 2021; Nakada & Urban, 2020; Kanniah *et al.*, 2020).

1.5 Research Questions

Built upon the findings obtained above, this research has identified three major gaps explored within the literature for hydrometeorological, atmospheric and sudden social change due to COVID-19 to the environment, which are

(i) Conditions of the water balance in changing land use?

(ii) Extreme floods events in changing climate?

(iii) Atmospheric pollution for regions without lockdown?

1.6 Research Objectives

Therefore, in light of these, the research aims to evaluate and propose adaptation/mitigation strategies to the spatiotemporal effects of land use, climate and COVID-19 impacts on environment in East and Southeast Asia. Four specific research objectives are proposed in this dissertation, including:

1) To assess the impact of decadal land use change on the water balance using SWAT (Chapter 3);

2) To evaluate the climate change impacts on extreme floods using high resolution MRI-AGCM (Chapter 4);

3) To investigate the spatiotemporal impact of COVID-19 on air quality in the absence of a lockdown (Chapter 5); and

4) To perform change analysis of meteorological-normalized air pollutants during COVID-19 pandemic in the absence of a lockdown (Chapter 6).

1.7 Methodology Framework

To achieve the following objectives, a detailed methodology framework, as illustrated in Fig. 1.4 was adopted. The brief introduction of hydrometeorological, atmospheric, and COVID-19 disasters are provided in Chapter 1. In addition, research gaps and objectives are provided in this chapter, too. In the following chapter, the modelling techniques, and its driving parameters land use land cover and hydrological are described. Chapter 2 also

investigates different normalization techniques for eliminating the meteorological biases for spatiotemporal change analysis of COVID-19.

In Chapter 3, the effects of land use change on the water balance components are studied. Two modelling techniques, namely support vector machine (SVM) and artificial neural network (ANN) models are utilized. Systematic hyperparameter optimization is performed in both modelling techniques for LULC detection from satellite images. The future land use map simulated and validated, and used to project the future streamflow under changing land use.

In Chapter 4, the impacts of climate change on extreme floods are investigated utilizing high resolution satellite images, known as MRI-AGCM 3.2s. Prior to utilizing the MRI-AGCM 3.2s dataset, cumulative distribution function is used to correct the bias in the dataset. The future temperature and precipitation change are simulated and the future average annual peak discharge changes for near future (2020-2040), future (2050-2070) and far future (2079-2099) are simulated.

Chapter 5 investigated the spatiotemporal impact of COVID-19 on air quality in the absence of lockdown. A novel research framework is proposed to evaluate the long-term monthly spatiotemporal impact of COVID-19 on Taiwan air quality through different statistical analyses, including geostatistical analysis, change detection analysis and identification of nonattainment pollutant occurrence between the average mean air pollutant concentrations from 2018-2019 and 2020, considering both meteorological and public transportation impacts. The underlying reasons during the anomalous months was identify through backward trajectory analysis using hybrid single-particle Lagrangian integrated trajectory (HYSPLIT) model.

In Chapter 6, a novel research framework was proposed to investigate the observed and meteorological-normalized concentrations of nitrogen dioxide (NO_2) and ozone (O_3) across 62 cities in Taiwan. Four commonly adopted meteorological-normalization techniques, namely generalized additive model (GAM), generalized linear model (GLM), gradient boosting machine (GBM) and random forest (RF) were developed, optimized, and compared, utilizing nine meteorological and temporal variables. In search of robust and best

models, the data distribution type in GAM and GLM, and tree numbers in GBM and RF are optimized using systematic trial-and-error and grid-search approach, respectively. The best performing optimized model was selected to identify the changes of NO_2 and O_3 during COVID-19 using geographical information system (GIS).

The comparison, mitigation and adaptation strategies for global environmental change are discussed in Chapter 7. The environmental challenges in Asia are identified and the application of utilizing 3D printed monitoring system associated with the industrial revolution 4.0 is discussed in this chapter. Lastly, chapter 8 summarized significant findings of the research and future research studies and recommendations are proposed.

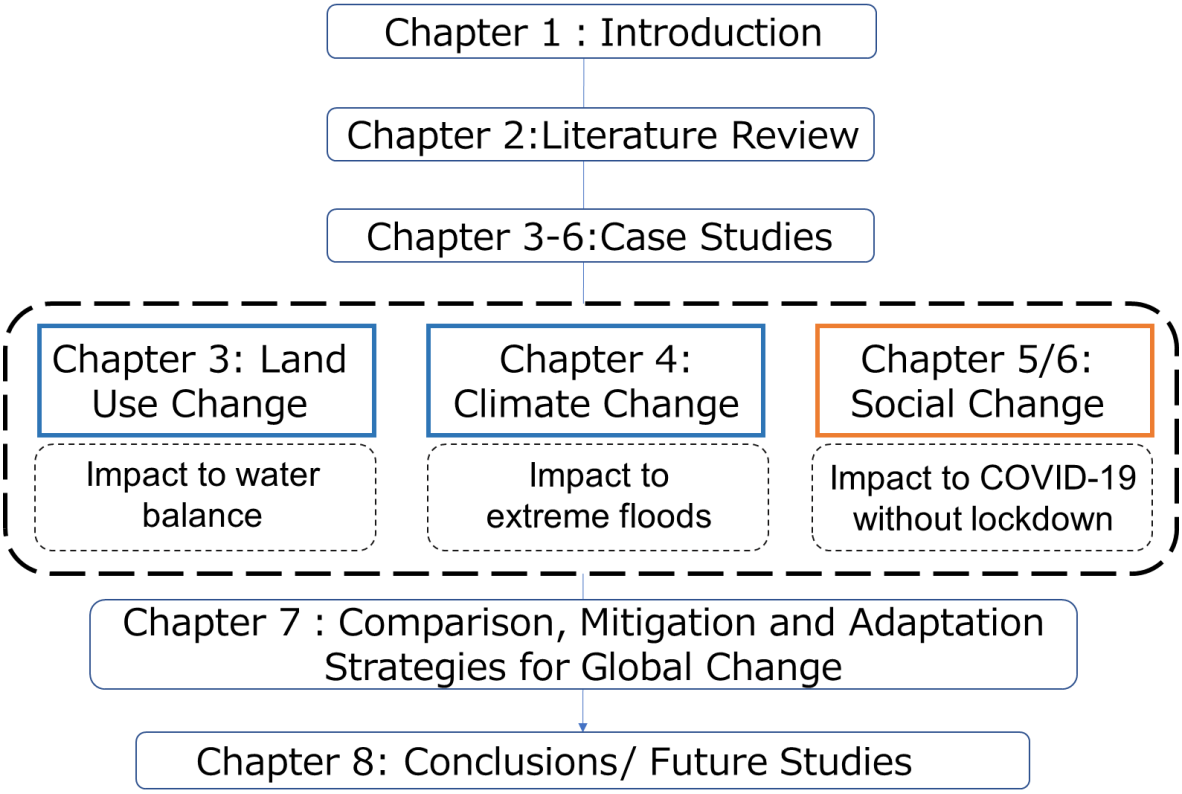

Fig.1.4: Research framework methodology

List of References

Abdullah, S., Mansor, A. A., Napi, N. N. L. M., Mansor, W. N. W., Ahmed, A. N., Ismail, M., & Ramly, Z. T. A. (2020). Air quality status during 2020 Malaysia Movement Control Order (MCO) due to 2019 novel coronavirus (2019-nCoV) pandemic. *Science of The Total Environment, 729*, 139022. doi:10.1016/j.scitotenv.2020.139022

Addas, A., & Maghrabi, A. (2021). The Impact of COVID-19 Lockdowns on Air Quality—A Global Review. *13*(18), 10212.

Anugerah, A. R., Muttaqin, P. S., & Purnama, D. A. (2021). Effect of large-scale social restriction (PSBB) during COVID-19 on outdoor air quality: Evidence from five cities in DKI Jakarta Province, Indonesia. *Environmental Research, 197*, 111164. doi:10.1016/j.envres.2021.111164

Archer, C. L., Cervone, G., Golbazi, M., Al Fahel, N., & Hultquist, C. (2020). Changes in air quality and human mobility in the USA during the COVID-19 pandemic. *Bulletin of Atmospheric Science and Technology*, *1*(3), 491-514. doi:10.1007/s42865-020-00019-0

Ash'aari, Z. H., Aris, A. Z., Ezani, E., Ahmad Kamal, N. I., Jaafar, N., Jahaya, J. N., . . . Umar Saifuddin, M. F. (2020). Spatiotemporal Variations and Contributing Factors of Air Pollutant Concentrations in Malaysia during Movement Control Order due to Pandemic COVID-19. *Aerosol and Air Quality Research, 20*(10), 2047-2061. doi:10.4209/aaqr.2020.06.0334

Baysan, C., Palanbek Yavaş, S., & Çöl, M. (2021). Change in Air Pollution and Human Mobility Trends during COVID-19 Lockdown Measures in Turkey. *The Anatolian Journal of Family Medicine, 4*(2), 170-177. doi:10.5505/anatoljfm.2021.25338

Chen, S.-C., Liao, C.-M., Chio, C.-P., Chou, H.-H., You, S.-H., & Cheng, Y.-H. (2010). Lagged temperature effect with mosquito transmission potential explains dengue variability in southern Taiwan: Insights from a statistical analysis. *Science of The Total Environment, 408*(19), 4069-4075. doi:10.1016/j.scitotenv.2010.05.021

Chen, Y.-R., Yeh, C.-H., & Yu, B. (2011). Integrated application of the analytic hierarchy process and the geographic information system for flood risk assessment and flood plain management in Taiwan. *Natural Hazards, 59*(3), 1261-1276. doi:10.1007/s11069-011-9831-7

Chiang, Y.-C. (2018). Exploring community risk perceptions of climate change - A case study of a flood-prone urban area of Taiwan. *Cities, 74*, 42-51. doi:10.1016/j.cities.2017.11.001

Chjeng-Lun, S., Chun-Ming, W., Wen-Chi, L., Yun-Chung, T., & Shin-Ping, L. (2009). The composite hazard resulted from Typhoon Morakot in Taiwan. *砂防学会誌, 62*(4), 61-65. doi:10.11475/sabo.62.4_61

Dang, H.-A. H., & Trinh, T.-A. (2021). Does the COVID-19 lockdown improve global air quality? New cross-national evidence on its unintended consequences. *Journal of Environmental Economics and Management, 105*, 102401. doi:10.1016/j.jeem.2020.102401

Department of Statistic (2016). Current Population Estimates, Malaysia, 2014-2016 [Press release]. Retrieved from https://www.dosm.gov.my/v1/index.php?r=column/pdfPrev&id=OWlxdEVoYlJCS0hUZzJyRUcvZEYxZz09

Ding, X., Zheng, L., Zheng, X., & Kao, S.-J. (2020). Holocene East Asian Summer Monsoon Rainfall Variability in Taiwan. *Frontiers in Earth Science, 8*(234). doi:10.3389/feart.2020.00234

Doong, D.-J., Lo, W., Vojinovic, Z., Lee, W.-L., & Lee, S.-P. (2016). Development of a New Generation of Flood Inundation Maps—A Case Study of the Coastal City of Tainan, Taiwan. *8*(11), 521.

Ge, X., Li, T., Zhang, S., & Peng, M. (2010). What causes the extremely heavy rainfall in Taiwan during Typhoon Morakot (2009)? *Atmospheric Science Letters, 11*(1), 46-50. doi:10.1002/asl.255

Gualtieri, G., Brilli, L., Carotenuto, F., Vagnoli, C., Zaldei, A., & Gioli, B. (2020). Quantifying road traffic impact on air quality in urban areas: A Covid19-induced lockdown analysis in Italy. *Environmental Pollution, 267*, 115682. doi:10.1016/j.envpol.2020.115682

Henny, L., Thorncroft, C. D., Hsu, H.-H., & Bosart, L. F. (2021). Extreme Rainfall in Taiwan: Seasonal Statistics and Trends. *Journal of Climate, 34*(12), 4711-4731. doi:10.1175/JCLI-D-20-0999.1

Hsu, H. H., & Chen, C. T. (2002). Observed and projected climate change in Taiwan. *Meteorology and Atmospheric Physics, 79*(1), 87-104. doi:10.1007/s703-002-8230-x

Hsu, T.-W., Shih, D.-S., Li, C.-Y., Lan, Y.-J., & Lin, Y.-C. (2017). A Study on Coastal Flooding and Risk Assessment under Climate Change in the Mid-Western Coast of Taiwan. *Water, 9*(6), 390.

Lin, M.-Y., Sun, W.-Y., Chiou, M.-D., Chen, C.-Y., Cheng, H.-Y., & Chen, C.-H. (2018). Development and evaluation of a storm surge warning system in Taiwan. *Ocean Dynamics, 68*(8), 1025-1049. doi:10.1007/s10236-018-1179-z

Lin, Y.-F., Wu, C.-C., Yen, T.-H., Huang, Y.-H., & Lien, G.-Y. (2020). Typhoon Fanapi (2010) and Its Interaction with Taiwan Terrain – Evaluation of the Uncertainty in

Track, Intensity and Rainfall Simulations. *気象集誌. 第 2 輯, advpub*. doi:10.2151/jmsj.2020-006

Nakada, L. Y. K., & Urban, R. C. (2020). COVID-19 pandemic: Impacts on the air quality during the partial lockdown in São Paulo state, Brazil. *Science of The Total Environment, 730*, 139087. doi:10.1016/j.scitotenv.2020.139087

Rajah, K., O'Leary, T., Turner, A., Petrakis, G., Leonard, M., & Westra, S. (2014). Changes to the temporal distribution of daily precipitation. *41*(24), 8887-8894. doi:10.1002/2014GL062156

Rodríguez-Urrego, D., & Rodríguez-Urrego, L. (2020). Air quality during the COVID-19: PM2.5 analysis in the 50 most polluted capital cities in the world. *Environmental Pollution, 266*, 115042. doi:10.1016/j.envpol.2020.115042

Rudke, A. P., Martins, J. A., de Almeida, D. S., Martins, L. D., Beal, A., Hallak, R., . . . de, A. A. T. T. (2021). How mobility restrictions policy and atmospheric conditions impacted air quality in the State of São Paulo during the COVID-19 outbreak. *Environ Res, 198*, 111255. doi:10.1016/j.envres.2021.111255

Tian, X., An, C., Chen, Z., & Tian, Z. (2021). Assessing the impact of COVID-19 pandemic on urban transportation and air quality in Canada. *Science of The Total Environment, 765*, 144270. doi:10.1016/j.scitotenv.2020.144270

Tobías, A., Carnerero, C., Reche, C., Massagué, J., Via, M., Minguillón, M. C., . . . Querol, X. (2020). Changes in air quality during the lockdown in Barcelona (Spain) one month into the SARS-CoV-2 epidemic. *Science of The Total Environment, 726*, 138540. doi:10.1016/j.scitotenv.2020.138540

Tu, J.-Y., & Chou, C. (2013). Changes in precipitation frequency and intensity in the vicinity of Taiwan: typhoon versus non-typhoon events. *Environmental Research Letters, 8*(1), 014023. doi:10.1088/1748-9326/8/1/014023

United Nations Environment Programme (2021). The First Global Assessment of Air Pollution Legislation. Air Pollution Series: Regulating Air Quality.

Wetchayont, P. (2021). Investigation on the Impacts of COVID-19 Lockdown and Influencing Factors on Air Quality in Greater Bangkok, Thailand. *Advances in Meteorology, 2021*, 6697707. doi:10.1155/2021/6697707

WHO (2020). Timeline of WHO's Response to COVID-19. https://www.who.int/news-room/detail/29-06-2020-covidtimeline. Accessed 25 June 2021.

WHO (2021). Air pollution. https://www.who.int/health-topics/air-pollution#tab=tab_1. Accessed 6 June 2021.

Worldometer (2021). COVID-19 Coronavirus Pandemic. https://www.worldometers.info/coronavirus/. Accessed 15 Oct 2021.

Yeh, H.-F., & Huang, C.-C. (2019). Evaluation of basin storage–discharge sensitivity in Taiwan using low-flow recession analysis. *Hydrological Processes, 33*(10), 1434-1447. doi:10.1002/hyp.13411

Yousefian, F., Faridi, S., Azimi, F., Aghaei, M., Shamsipour, M., Yaghmaeian, K., et al., (2020). Temporal variations of ambient air pollutants and meteorological influences on their concentrations in Tehran during 2012–2017. Scientific Reports, 10(1), 292, doi:10.1038/s41598-019-56578-6.

Zangari, S., Hill, D. T., Charette, A. T., & Mirowsky, J. E. (2020). Air quality changes in New York City during the COVID-19 pandemic. Science of The Total Environment, 742, 140496, doi.org/10.1016/j.scitotenv.2020.140496.

Zhai, Z., Fu, X., Yi, M., Sheng, M., & Guang, F. (2022). Haze management: is urban public transportation priority effective? *Environmental Science and Pollution Research*, doi:10.1007/s11356-021-17871-y.

Zhu, Y., Xie, J., Huang, F., & Cao, L. (2020). The mediating effect of air quality on the association between human mobility and COVID-19 infection in China. *Environmental Research, 189*, 109911. doi:10.1016/j.envres.2020.109911

Chapter 2 Literature Review

In this chapter, a review of literature on future land use change, climate change and impacts of COVID-19 across the globe are studied. The selection of modelling/ optimization techniques is chosen based on the knowledge gap identified in during the literature review process.

2.1 Hydrometeorological-disasters-induced Economic and Mortality Losses

In this section, a detailed literature review on hydrometeorological-induced economic and mortality losses across the globe and particularly, in Asia are discussed. The findings of the section are to highlight and identify the most disastrous and common natural disasters in the study area.

2.1.1 Global

Of the top 10 disasters, the hazards that led to the largest human losses during the period have been droughts (650,000 deaths), storms (577,232 deaths), floods (58,700 deaths) and extreme temperature (55,736 deaths) (Table 1(a)). Regarding to economic losses, the top 10 events include storms (US$ 521 billion) and floods (US$ 115 billion) (Table 1(b)). All the storm events positioned in top 10 categories in terms of both deaths and economic losses were tropical cyclones. Three of the top 10 disasters in terms of economic losses occurred in 2017: Hurricanes Harvey (US$ 96.9 billion), Maria (US$ 69.4 billion) and Irma (US$ 58.2 billion). These three hurricanes alone accounted for 35% of the total economic losses of the top 10 disasters around the world from 1970 to 2019. Floods were most common of the hydrometeorological disaster types recorded, but it could be observed that storms had the highest human and economic loss.

Based on Fig. 2.1(a), the number of disasters has increased by five-fold over the 50 years period: whereas 711 disasters were recorded for 1970–1979, 3,536 were recorded in 2000–2009. In term of number of scarified during the disaster, it could be observed that deaths decreased almost threefold by hydrometeorological disasters from 1970 to 2019. Death rates have fallen decade by decade – from over 50 thousand deaths in the 1970s to less

than 20 thousand in the 2010s. The 1970s and 1980s reported an average of 170 related deaths per day. In the 1990s, that average fell by one third to 90 related deaths per day, then continued to fall in the 2010s to 40 related deaths per day as shown in Fig. 2.1(b). However, in term of economic loss, it has increased sevenfold from the 1970s to the 2010s as shown in Fig. 2.1(c).

Table 1: Top 10 global disasters ranked according to reported (a) deaths and (b) economic losses (1970–2019)

(a)	Disaster Type	Year	Country	Deaths
1	Drought	1983	Ethiopia	300,000
2	Storm (Bhola)	1970	Bangladesh	300,000
3	Drought	1983	Sudan	150,000
4	Storm (Gorky)	1991	Bangladesh	138,866
5	Storm (Nargis)	2008	Myanmar	138,866
6	Drought	1973	Ethiopia	100,000
7	Drought	1981	Mozambique	100,000
8	Extreme Temperature	2010	Russian Federation	55,736
9	Flood	1999	Bolivarian Republic of Venezuela	30,000
10	Flood	1974	Bangladesh	28,700
(b)	**Disaster Type**	**Year**	**Country**	**Economic Losses (USD billion)**
1	Storm (Katrina)	2005	United States	163.61
2	Storm (Harvey)	2017	United States	96.94
3	Storm (Maria)	2017	United States	69.39
4	Storm (Irma)	2017	United States	58.16
5	Storm (Sandy)	2012	United States	54.47
6	Storm (Andrew)	1992	United States	48.27
7	Flood	1998	China	47.02
8	Flood	2011	Thailand	45.46
9	Storm (Ike)	2008	United States	35.63
10	Flood	1995	Democratic People's Public of Korea	25.17

The reported losses from 2010–2019 (US$ 383 million per day on average over the decade) were seven times the amount reported from 1970–1979 (US$49 million per day). Storms were the most prevalent cause of damage, resulting in the largest economic losses around the globe. It is the sole hazard for which the attributed portion is continually increasing. Worldwide, it could be observed that 44% of disasters have been associated with floods (riverine floods 24%, general floods 14%) and 17% have been associated with tropical cyclones. Tropical cyclones and droughts were the most common encounter hazards with respect to human losses, accounting for 38% and 34% of disaster related deaths from 1970 to 2019, respectively. When it comes to economic losses, it could be observed that 38% were associated with tropical cyclones, while different types of floods account for 31%, riverine floods (20%), general floods (8%) and flash floods (3%), marking its significant importance in mitigating/preparing for these disasters.

Of all of human life and financial loss due to hydrometeorological disasters, it could be observed that 91% occurred in developing economies according to the United Nations country classification. The proportion remains similar for the World Bank country classification, according to which 82% of deaths occurred in low and lower-middle income countries. Based on these two economic classification methodologies, both reveal that the majority of reported deaths from meteorological disasters occurred in developing countries, while countries with developed economies incurred the majority of economic losses. According to the United Nations country classification, 91% of recorded deaths occurred in developing economies while 59% of economic losses were recorded in developed economies. On the other hand, based on the World Bank country classification, 82% of deaths have occurred in low and lower-middle-income countries and most (88%) of the economic losses have occurred in upper-middle- and high-income countries. Among different continents, Asia, accounts for almost 30% of global disasters and 50% of deaths, driving the importance to quantify its impacts in Asia.

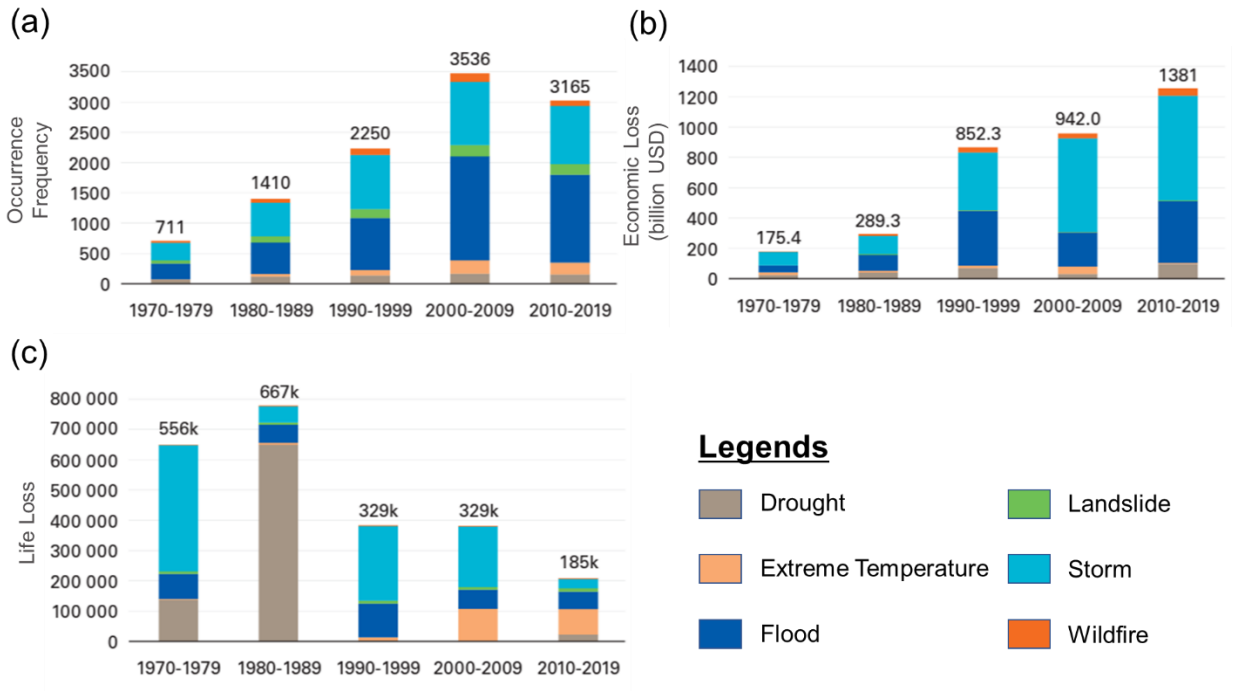

Fig. 2.1: Distribution of (a) number of disasters, (b) number of deaths and (c) economic losses by hazard type by decade globally (WMO,2021)

2.1.2 Asia

According to EM-DAT records from 1970 to 2019, in Asia, 3,454 disasters were recorded from 1970–2019, with 975,622 lives lost and US$ 1.2 trillion in reported economic damages, accounting for nearly a third (31%) of hydrometeorological disasters reported globally, accounting for nearly half of deaths (47%) and a third (31%) of associated economic losses. Most of these disasters were associated with floods (45%) and storms (36%). Storms had the highest impacts on life, causing 72% of the lives lost, while floods led to the greatest economic losses (57%). The top 10 recorded disasters in Asia account for 70% (680,837 deaths) of the total lives lost and 22% (US$ 266.62 billion) of economic losses for the region. In Asia, in terms of loss of life, tropical cyclones were the most prevalent hazard, similar to the observed global trend. Three tropical cyclones, including two in Bangladesh in 1970 and 1991 (total of 438,866 deaths) and one in Myanmar in 2008 (138,366 deaths) distort the overall disaster statistics whereby 0.1% of events account for 60% of deaths reported for the region (Table 2 (a)). Bangladesh, due to the significant loss of life caused by the two tropical

cyclones, accounted for more than half of deaths (53%) reported in Asia in the last 50 years. On the other hand, the most prevalent hazard in terms of economic losses were floods. Six costliest disasters in the region occurred in China (Table 2 (b)), which accounted for 60% of the top 10 events in Asia.

There was an increase in the number of recorded hydrometeorological disasters between 1950-2019, where the number of reported disasters were found more frequently by decade, from one disaster on average of every fifteen day to one every three days over the 50 years. Over the last decades, the average number of disasters recorded is 104 disasters per year. This increase may be a result of reporting bias whereby disasters have been recorded more frequently since the year 2000 than during previous decades due to advances in technology and the international focus on disaster risk reduction. The number of reported deaths has fluctuated over the period, with increases and decreases by decade, while economic losses have continuously and substantially increased. Five of the 10 deadliest recorded events occurred in the 1970s and nine prior to the year 2000 whereas four out of the 10 costliest events occurred in the recent decade 2010–2019 as shown in Table 2. This has shown that the occurrence of disastrous hydrometeorological events have been increasing in both frequency and severity in the past two decades compared to previous years.

In Fig. 2.2, the distribution in terms of total number, resulting deaths and economic losses as a function of hazard type are shown. The two most prevalent hazards in terms of number of recorded disasters: floods (37%) and tropical cyclones (21%). Tropical cyclones accounted for the most deaths (70%), while floods caused 21% of deaths. In terms of economic losses, flood (53%) and tropical cyclones (30%) were the most prelavent hazards in Asia. These two hazard types combined contributed to 58% of disasters, 91% of deaths and 83% of economic losses for the region. Moreover, according to the report, it could be observed that nine out of ten recorded disasters occurred in developing countries in Asia, constituting 89% of deaths and 25% of economic loss.

Among developing countries, considering the hydrometeorological impacts, the number of disasters occurred in Malaysia and Taiwan are relatively high, with 65 and 79 recorded disasters for the past 50 years, and an increasing trend is observed. Therefore, this research selected to further investigate the hydrometeorological occurrence in these two regions.

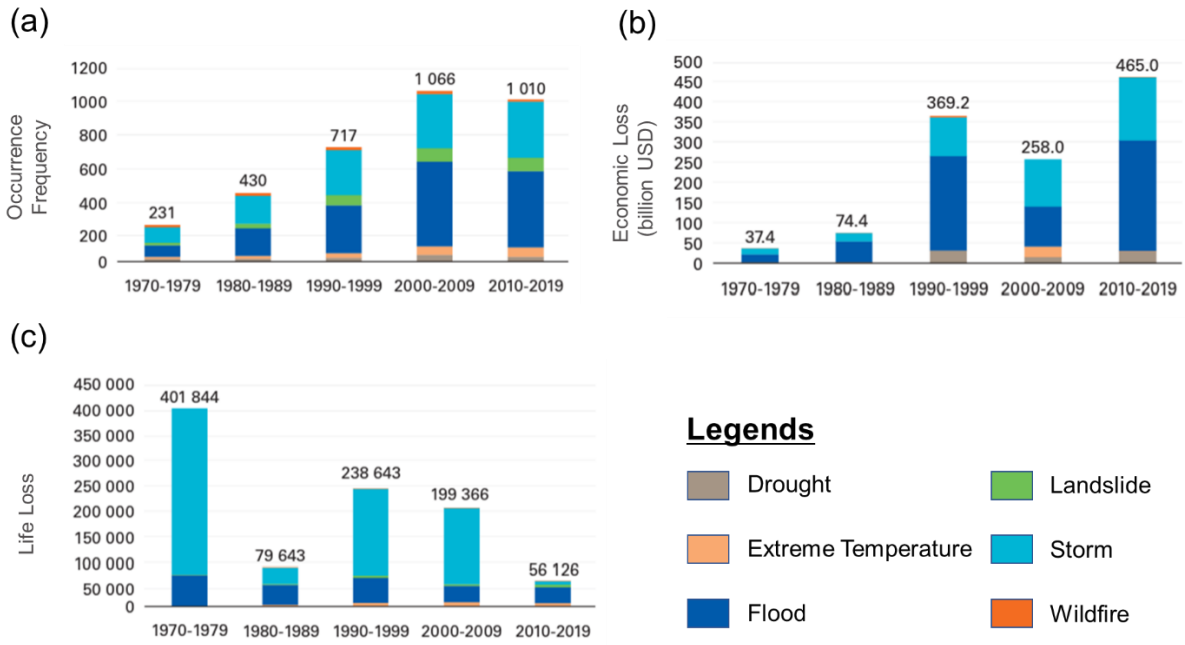

Fig. 2.2: Distribution of (a) number of disasters, (b) number of deaths and (c) economic losses by hazard type by decade in Asia (WMO,2021)

Table 2: Top 10 disasters ranked according to reported (a) deaths and (b) economic losses (1970–2019) in Asia

(a)	Disaster Type	Year	Country	Deaths
1	Storm (Bhola)	1970	Bangladesh	300,000
2	Storm (Gorky)	1991	Bangladesh	138,866
3	Storm (Nargis)	2008	Myanmar	138,866
4	Flood	1974	Bangladesh	28,700
5	Flood	1975	China	20,000
6	Storm (Cyclone)	1985	Bangladesh	15,000
7	Storm (Cyclone)	1977	India	14,204
8	Storm (Cyclone)	1999	India	9,843
9	Storm (Cyclone)	1971	India	9,658
10	Flood	1980	China	6,200
(b)	**Disaster Type**	**Year**	**Country**	**Economic Losses (USD billion)**
1	Flood	2011	Thailand	45.46
2	Storm (Ike)	2008	United States	35.63
3	Flood	1995	Democratic People's Public of Korea	25.17
4	Extreme Temperature	2008	China	25.06
5	Drought	1994	China	23.72
6	Flood	2016	China	22.92
7	Flood	2010	China	21.10
8	Flood	1996	China	20.52
9	Storm (Mireille)	1991	Japan	18.76
10	Flood	2014	China	16.90

2.1.2.1 Malaysia

Malaysia is a federal constitutional monarchy in Southeast Asia. It is located between 2° North and 7° North of Equator in Southeast Asia. The total land area is about 329,847 km^2 separated by the South China Sea in two regions, Peninsular and Malaysian Borneo. Land borders are shared with Thailand, Indonesia and Brunei, and maritime borders exist with Singapore, Vietnam, and the Philippines, as shown in Fig. 2.3. Almost 45% of Peninsular Malaysia is covered by tropical rainforest and swamp. Sabah is split in two by the Crocker Mountains, rising to over 4,100 m at Mt. Kinabalu, the highest point in Malaysia. The rainforests cover the greater part of Sarawak and many of the rivers are navigable as one the

famous longest river in Malaysia is Rajang River. By year 2017, the total population in Malaysia is about 32.0 million with 28.7 million are citizens and 3.3 million are noncitizens. The Capital City is Kuala Lumpur, while Putrajaya as Federal Government. Malaysia's climate is a tropical climate with uniform temperature (maximum = 33°C, minimum = 23°C) in high humidity, situated in equatorial doldrums area. It is divided into two seasons, which are Southwest Monsoon (May– September), Northeast Monsoon (November–March), and two shorter periods of Inter-monsoon seasons (April and October).

Malaysia is geographically located just outside the "Pacific Rim of Fire" and is generally free from severe natural disasters such as earthquake, volcanic eruption and typhoon. Although Malaysia is spared from the threats of severe natural disasters and calamities, Malaysia is nonetheless not spared from other disasters such as flood, man-made disaster, landslide and severe haze. In the past few years, Malaysia has experienced several extreme weather and climatic events, ranging from freak thunderstorms to monsoonal floods and strong earthquake which have caused havoc in the country. Monsoonal flood is one of the major disasters in Malaysia, where they are an annual occurrence which varies in terms of severity, spatial and temporal of occurrences. Flood is the most significant natural hazard in Malaysia. Annually, an estimated 29,799 km^2 are flooded, affecting 4.9 million people, and causing physical damages amounting up to USD 350 million. Rapid development, unplanned urbanization, climate change and environmental degradation have caused worse and more frequent occurrence of flash floods especially in urban areas. The state of Selangor, situated in the centre and on the west coast of Peninsular Malaysia, is the most developed state in Malaysia with approximately 6.4 million citizens or 19.9% of the total national population (Department of Statistic, 2016). In 2021, a disastrous flood has hit the peninsular Malaysia, causing tremendous human lives and financial losses in the region

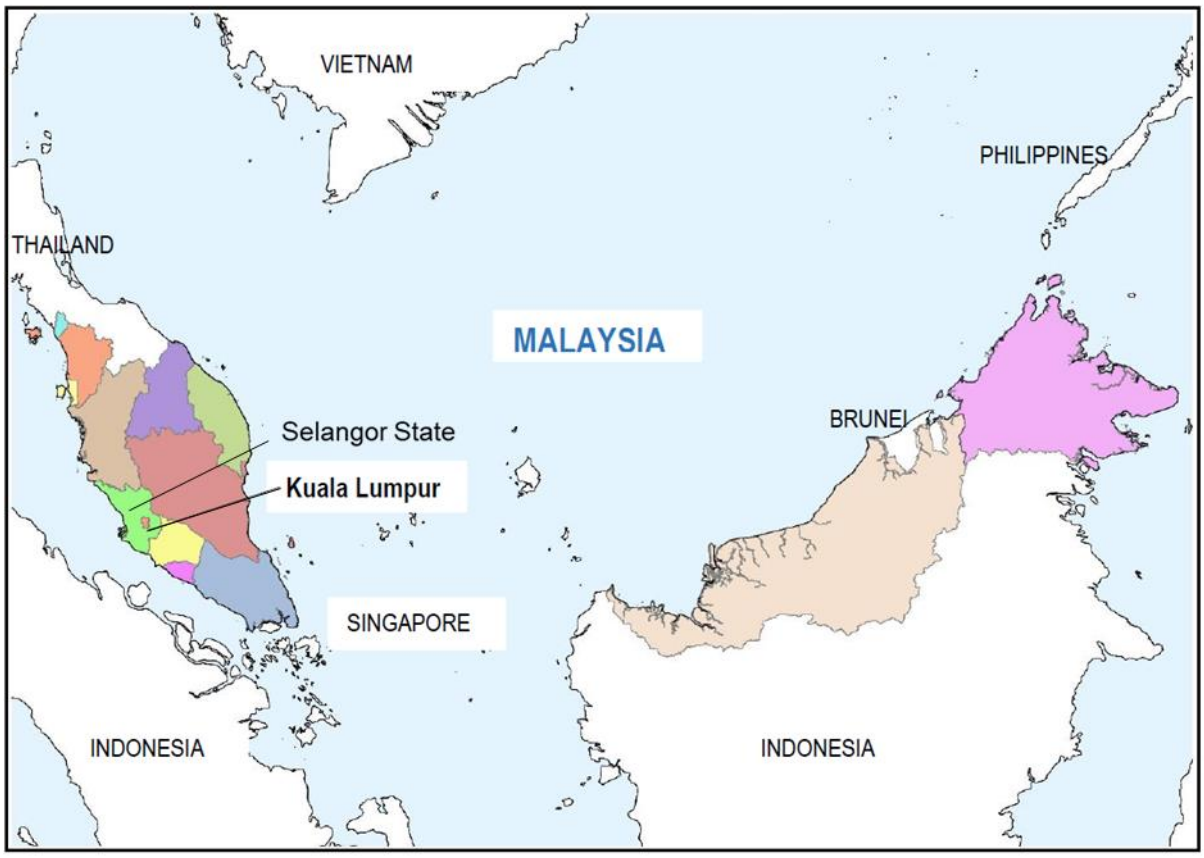

Fig. 2.3: Geographical location of Malaysia

On 16 December 2021, a tropical depression made landfall on the eastern coast of Peninsular Malaysia, bringing torrential downpours throughout the peninsula for three days. The resulting floods affected eight states across the Peninsula Malaysia and caused at least 54 dead and 2 missing. During its furthest extent, it caused the concurrent displacement of more than 71,000 residents and have affected over 125,000 people. Declared by government officials as a "once in a century" disaster, it is the worst flood in the country in terms of displaced residents since the 2014–2015 Malaysia floods, as shown in Fig. 2.4. Record-high precipitations up to 316 mm of rain in 24 hours were measured at weather stations at Selangor and Kuala Lumpur. Widespread damages were reported at the states of Selangor, especially the district of Hulu Langat and the city of Shah Alam.

Fig. 2.4: Flood conditions recorded by residents in Shah Alam, Selangor on Dec 20, 2021 (Starnews,2021)

2.1.2.2 Taiwan

Taiwan is a densely populated island, with 23.8 million people spread across a total land area of approximately 36,000km^2 in Eastern Asia, on the west edge of the Pacific Ocean. As Taiwan is situated at the transition between tropical and temperate latitudes (21.5 – 25.2 °N and 120.0 – 122.0 °E), its climate is strongly influenced by the East Asian Monsoons (southwesterly monsoon during the wet-warm season (May–August) and northeasterly monsoon during the dry-cold season (September–April) (Henny *et al.*, 2021). The mean annual temperature for the subtropical region is about 23.4 ºC (highest: 35.8 ºC and lowest: 7.4 ºC) whereas for the tropical region is about 25.4 ºC (highest: 35.0 ºC and lowest: 9.3 ºC) (Chen *et al.*, 2010). Approximately 90% of the total precipitation (~2,000mm) are contributed during the wet-warm season (Ding *et al.*, 2020) associated with the episodic

typhoon impact (mid-July to August). The magnitude and scale of a typhoon hitting Taiwan have increased over the past decades (Hsu *et al*., 2017a), bringing extremely heavy rain and strong wind, and might eventually cause disastrous flooding, particularly in the coastal area. The complicated and steep topography is also one of the key drivers that have substantially increased the total rainfall accumulation and affected its distribution over Taiwan, especially due to the north-south oriented Central Mountain Range (CMR) (Fig. 2.5). Lin *et al.*, (2020) demonstrated the distribution of rainfall in Taiwan is strongly modulated by the topography of CMR due to orographic forcing over mountains, in which the southwest region receives a large amount of rain. Therefore, the inundation susceptibility varied across the region.

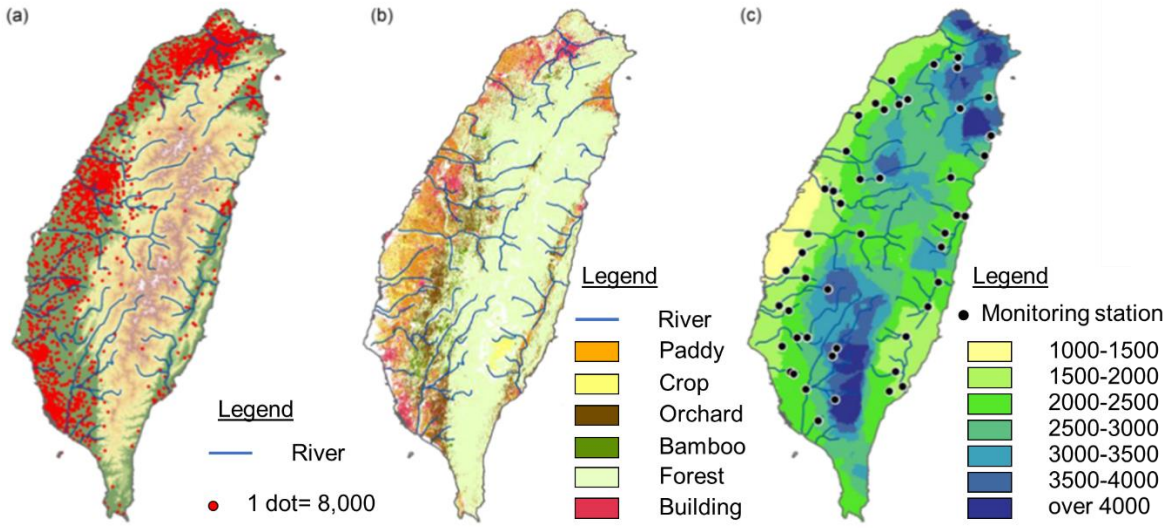

Fig. 2.5: Maps of Taiwan to show the population density (a), land cover (b), and mean annual rainfall (c).

Based on the findings performed by Henny *et al.* (2021), the change trends of extreme precipitation for typhoon and annual seasons have increased drastically, but relatively less significant increasing trend. The number of extreme precipitation events during the typhoon seasons increased by almost three folds during the 2010s compared to 1960s, indicating the impact of climate change receiving in this region as shown in Fig. 2.6. Over the past decade, the mean air temperature in Taiwan was observed to have increased twice (0.14 °C per

decade) as much as the global mean warming rate per decade (°C per decade) (Hsu & Chen, 2002). This may have exacerbated the trend of heavy precipitation phenomenon (Tu & Chou,2013), resulting in a significant impact on the hydrological system and inducing the occurrence of extreme floods in Taiwan (Chiang *et al.*, 2018). The frequency of increased intensity of precipitation (>3,500 mm within 48h) (Lin *et al.*, 2018) has been gradually escalating (Yeh & Huang 2019). In 2009, the flood induced by Typhoon Morakot with accumulated rainfall of 2,777 mm, one of the most catastrophic flooding, has caused nearly 700 deaths and direct loss of up to 4.7 billion USD (Chjeng *et al.*, 2009; Ge *et al.*, 2010).

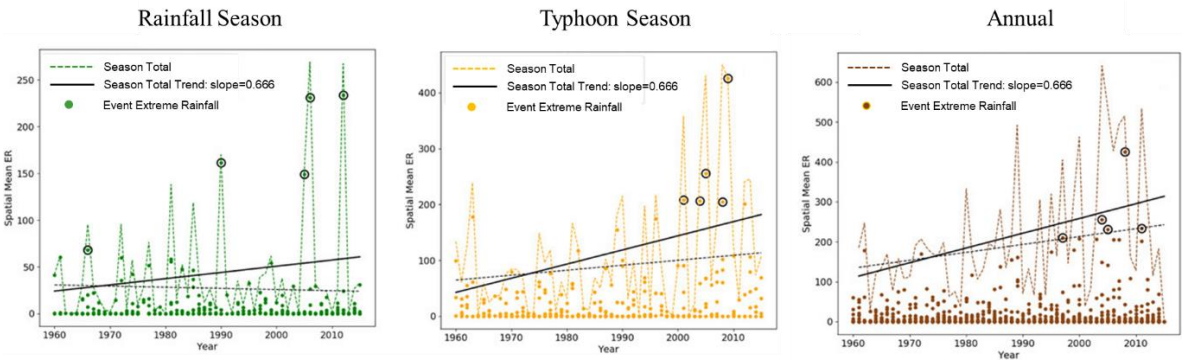

Fig. 2.6: Time series of seasonal extreme precipitation events during rainfall, typhoon and annual phenomenon. Filled circles indicate total extreme rainfall occurring on consecutive days. The top five events are marked with rings. Dashed colored lines show season total ER by year. Linear regression trend lines for seasonal or annual ER are shown as dashed (without the top five events) and solid (with the top five events) black lines (Shetha *et al.*,2018).

Although numerous flood risk management frameworks have been proposed and developed for minimizing the potential losses and ensuring public safety, for instance, identifying flood risk zone through flood inundation maps utilizing historical precipitation data (Chen *et al.*, 2011; Doong *et al.*, 2016). However, due to the complex and heterogeneous climate variability, the distribution and intensity of precipitation varied spatiotemporally, which has been supported by both historical observations and model simulations (Rajah *et al.*, 2014). Therefore, it is fundamental to develop robust and reliable future climate

simulations to identify the future flow regime and allow decision-makers to formulate corresponding prevention policies for the emerging risk.

2.2 Land Use Land Cover (LULC)

2.2.1 Classification of LULC

Land use land cover (LULC) classification is the process of appointing land cover classes to pixels and categorizing them into waterbodies, urban area, agriculture, forest and bare land etc. The general goal of picture grouping is to naturally arrange all pixels in a picture according to the land cover classes. That is, diverse component types show a distinctive blend of dependent on their intrinsic otherworldly reflectance. The LULC maps play a significant and prime role in planning, management, and monitoring programs at local, regional, and national levels, which is necessary to monitor the ongoing process of LULC patterns over some time.

Remote sensing is one of the distant detecting techniques in obtaining the physical properties of a region by capturing the reflectance on the land surface. In general, creating LULC classifications builds upon two imaging methods: optical and microwave remote sensing. Both sensing approaches imply distinct advantages and disadvantages. While optical sensors rely on reflectance and cloud free conditions, microwave sensors only capture the backscatter in a given wavelength. Examples of optical LULC analysis on a global scale are reported in Chen *et al.* (2019); on the other hand, for a regional scale, it is reported in Lo & Fung (2020) and Immitzer *et al.* (2017). Microwave imaging using synthetic aperture radar images for LULC emerged in the 1980s, and examples are described in Dobson *et al.* In light of these, the application of remote sensing has a marked importance in identifying the LULC change trends and intensive researches have performed to increase the accuracy of the classified image.

In general, the type of classification in remote sensing analysis can be divided into two groups: (i) pixel-based classification, and (ii) object-based classification. For pixel-based classification, the classification is done at every pixel, by only utilizing the spectral data which are accessible for that singular pixel. Therefore, the pixels inside the region are overlooked. In this sense, every pixel would speak to a training model for a classification

algorithm, and this preparation model would be as an n-dimensional vector, where n was the number of spectral groups in the picture information. On the other hand, the object-based classification is done on a restricted gathering of pixels, considering the spatial properties of every pixel as they identify with one another. In this regard, a preparation model for the classification algorithm would comprise a gathering of pixels, and the classification algorithm would likewise yield a class forecast for pixels on a gathering premise for an unrefined model.

2.2.2 Drivers Factors of LULC Change

In general, land use change in developed regions is mainly a result of changes in production systems (*e.g.*, crops, fertilizer, livestock numbers). Whilst these changes can lead to higher productivity and subsequent abandonment of agricultural land (van Vliet *et al.*, 2015), they do not generally cause major shifts in land cover such as from forest to agriculture. On the other hand, for developing regions, the land use change is mainly due to the urbanization. These processes are generally fast, and policy driven. These shifts in production systems follow thousands of years of land-use change, with the dramatic change from natural to more human dominated systems occurring hundreds or thousands of years ago. In the tropics, however, demand for new agricultural land from a rapidly expanding human population continues to be the main driving force for land-cover changes, and land-use and land-cover changes in those regions are often proceeding rapidly. Generally, it could be described in two driving factors: (i) Proximate and (ii) Biophysical.

2.2.2.1 Proximate Drivers

Proximate causes or land management actions are local or direct human modifications that cause changes in the landscape. Proximate causes are human activities or immediate actions at the local level, such as agricultural expansion, which directly impacts forest cover (Geist & Lambin, 2002). Underlying proximate causes are, for instance, social processes such as agricultural policies or population dynamics. In addition, characteristics of societies, such as cultural background (Rockwell, 1994), wealth and lifestyle, can be considered underlying causes as they have an impact on the demand for land-intensive commodities (Delgado *et al.*,

2003), which leads to agricultural expansion. Land management is also a proximate cause that is determined by the societal setting (Heistermann *et al.,* 2006) and impacts land use at different spatial scales. Examples of land management include farming practices such as fertilizer use that can increase crop yields or practices such as slash and burn and selective logging to manage tree density in forests. Political decisions, such as policy interventions in developed countries and development projects in developing countries, can also underpin land-use change at local to regional scales (Batistella, 2001). Governance, law enforcement, land tenure and access to markets are also very important factors driving land-use change (Geist & Lambin, 2002).

2.2.2.2 Biophysical

Biophysical drivers in most cases do not 'drive' land-use change directly (Verburg *et al.,* 2004), but rather cause land-cover changes: for example, through climate change and influencing land-use allocation decisions. Key biophysical drivers for land-use change are climate (Ogallo *et al.,* 2000), freshwater availability (Rosegrant *et al.,* 2002) and soil conditions as all of these could affect land suitability. Climate change drives land-use change, as changes in temperature and precipitation result in changes in land and water regimes, which can drive a shift in vegetation and agricultural cultivation. Therefore, aiming to simulate the real-life conditions, in this research, both of these factors are considered.

2.3 Climate Change

Since early of 21st century, the Earth has experienced a mean increase in temperature of 0.6°C, reaching up to 4°C in the most northern latitudes, which has already caused significant changes in species' distribution patterns, the structure and functioning of ecosystems and the timing of biological processes (Root *et al.,* 2003; Parmesan, 2006). The Intergovernmental Panel on Climate Change (IPCC, 2007) defines climate change as "any change in climate over time, whether due to natural variability or as a result of human activity". In 2014, IPCC has redefined the definition of climate change to "a change of climate which is attributed directly or indirectly to human activity that alters the composition of the global atmosphere and which is in addition to natural climate variability observed over

comparable time periods". Both definitions acknowledged the major cause of climate change is due to human activities that have altered the atmospheric composition. In the sixth IPCC Report (2021), a summary of the key findings concerning projections of climate change impacts on freshwater resources and their management, adaptation and vulnerabilities was provided. Changes in the pattern of water flows and groundwater recharge over space and time are determined by changes in temperature, evaporation and, crucially, precipitation etc.

2.3.1 Definition of Extreme Events

"Extreme event", a term today most commonly used in relation to extreme weather phenomena and experiencing an upsurge in its usage due to their increased frequency caused by climate change, is applied in a variety of scientific disciplines. Based on the IPCC sixth assessment report, a five-fold increase in warming rate for the coming decades, including the increase of extreme climatic events (Schär *et al.,* 2004; Diffenbaugh and Ashfaq, 2010) and alteration of global precipitation patterns are expected. Extreme weather or climate events includes unexpected, unusual, severe, or unseasonal weather; weather at the extremes of the historical distribution—the range that has been seen in the past. Often, extreme events are based on a location's recorded weather history and defined as lying in the most unusual 10% and in recent, up to the most unusual 5%.

Four aspects are studied the change in extreme weather and climate events, including

- **Frequency:** Are events occurring more often than they did in the past?
- **Intensity:** Are events getting more severe, with the potential for more damaging effects?
- **Duration:** Are events lasting longer than "the norm"?
- **Timing:** Are events occurring earlier or later in the season or the year than they used to?

Floods are one of the most devastating disasters, especially in Asia (Whitehead *et al.*, 2012). Poor people in society are the most vulnerable, as they live in the most threatened

locations and struggle to cope with the impacts due to income, political, and social constraints (Bowyer *et al.,* 2014). This can be compounded by the observation that developing countries are particularly threatened by flooding because of their limited capacity to prevent and absorb disaster impacts (Bowyer *et al.,* 2014). Moreover, the future threat from flooding is likely to increase due to the effects of climate change, changing flood patterns and rapid land use/land cover change placing more people in harm's way (Bubeck, 2018).

There have been changes in some types of global extreme weather events over the last several decades, including more intense and frequent heat waves, less frequent and intense cold waves, and regional changes in floods, droughts, and wildfires, as shown in Fig. 2.7. This rise in extreme weather events fits a pattern you can expect with a warming planet. It is projected that climate change will make some of these extreme weather events more likely to occur and/or more likely to be severe.

2.3.2 Drivers of Climate Change

The temperature of the Earth system is determined by the amounts of incoming (short wavelength) and outgoing (both short-and long-wavelength) radiation. In general, the Earth's equilibrium temperature in modem era can be affected several factors: incoming sunlight, absorbed and reflected sunlight, emitted infrared radiation, and infrared radiation absorbed and re-emitted in the atmosphere, primarily by GHGs. The changes in these factors affect Earth's radiative balance and therefore its climate, including but not limited to the average near-surface air temperature. The driving factors of causing climate change can be grouped into natural forcing and anthropogenic activities. A brief explanation is provided below for each driving factor:

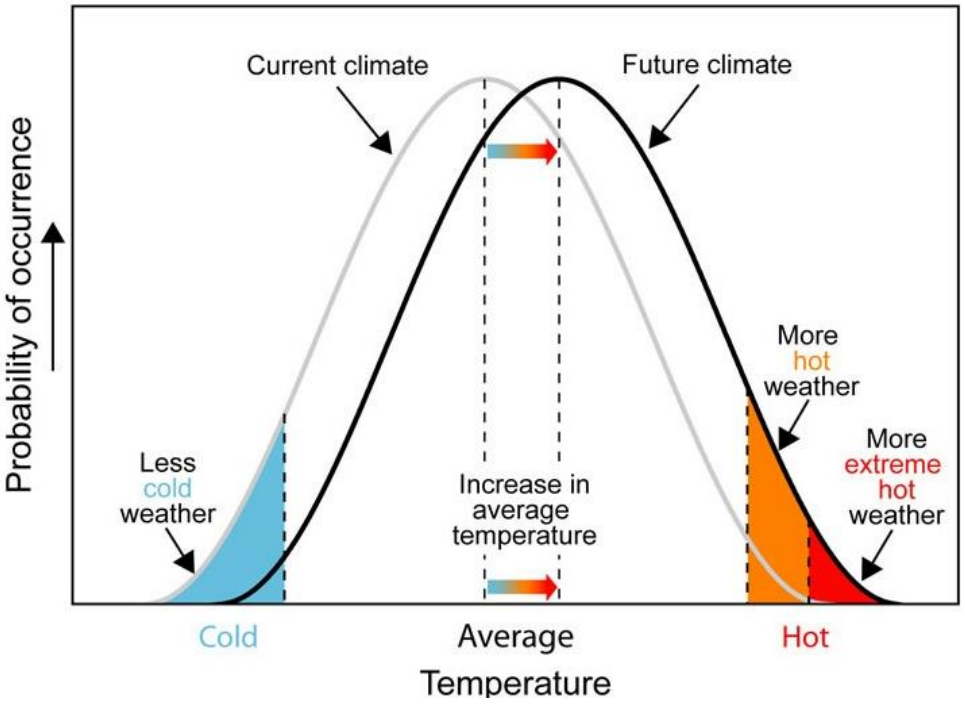

Fig. 2.7: Future climate projection and the shift of extreme temperature events (DRR, 2021)

2.3.2.1 Natural Drivers

The changes in solar irradiance directly impact the climate system because the irradiance is Earth's primary energy source (Lean, 1997). In the industrial era, the largest variations in total solar irradiance follow an 11-year cycle (Frölich and Lean, 2004; Gray *et al.*, 2010). Although these variations amount to only 0.1% of the total solar output of about 1,360 W/m^2 (Kopp and Lean, 2011), relative variations in irradiance at specific wavelengths can be much larger, more than tens of percentage. Spectral variations in solar irradiance are highest at near-ultraviolet (UV) and shorter wavelengths (Floyd *et al.*, 2003), which are also the most important wavelengths for driving changes in ozone (Ermolli *et al.*, 2013; Bolduc *et al.*, 2015). By affecting ozone concentrations, variations in total and spectral solar irradiance induce discernible changes in atmospheric heating and changes in circulation (Gray *et al.*, 2010; Lockwood, 2012; Seppälä *et al.*, 2014). The relationships between changes in irradiance and changes in atmospheric composition, heating, and dynamics are such that

changes in total solar irradiance are not directly correlated with the resulting radiative flux changes (Ermolli *et al.,* 2013; Xu and Powell, 2013; Gao *et al.,* 2015).

Another nature induced climate change forcing is due to the volcanic eruptions, with the effects of emissions confined to the troposphere which may be lasting for weeks to months. The gases and solids released by volcanic eruptions can include CO_2, water vapor, SO_2, H_2S, H_2, and CO. Generally, volcanic eruptions cool the climate. The explosive volcanic eruptions could inject substantial amount of SO_2 and ash into the stratosphere and leading to significant short-term climate effects which condenses, forming new particles or adding mass to preexisting particles, thereby substantially enhancing the attenuation of sunlight transmitted through the stratosphere.

2.3.2.1 Anthropogenic

On the other hand, under the uncontrolled urbanization and development, the anthropogenic activities are increasingly influencing the climate and the earth's temperature by burning fossil fuels, cutting down forests and farming livestock. Among anthropogenic activities, the main driver of climate change is the greenhouse effect, which trap the heat in the atmosphere, as do the glass panes of a greenhouse keep heat from escaping. Greenhouse gases, however, reflect much of the thermal energy back to the Earth’s surface. The more greenhouse gases there are in the atmosphere, the more thermal energy is reflected back to the Earth’s surface. Greenhouse gases absorb and emit radiation and are an important factor in the greenhouse effect: the warming of Earth due to carbon dioxide and other greenhouse gases in the atmosphere.

2.3.3 Type of Hydrological Modelling

2.3.3.1 Soil and Water Assessment Tool (SWAT)

The Soil and Water Assessment Tool (SWAT), a physically based and continuous-time model, was developed to assist water resource managers in assessing water supplies and nonpoint source pollution in watersheds and large river basins (Arnold *et al*., 1998). The SWAT employs some empirical/conceptual methods (*e.g.*, Penman-Monteith method for potential evapotranspiration calculation, and Soil Conservation Service (SCS) curve number

method for surface runoff simulation), which were formulated in the USA. These methods lead to one of the merits of SWAT: *i.e.*, minimal input data are required for modeling (Neitsch *et al.*, 2011). As reported in Tan *et al.* (2021), up to 2021, there are up to 4,300 related publications utilized SWAT for different purposes, marking it as one of the most popular model in the management of water, soil and waste applications, particularly in Southeast Asia.

In general, SWAT requires a Digital Elevation Model (DEM), a land use map, a soil map and daily-scale climate data for the simulation of a basin system. There is a critical team need for the best datasets, especially climate information, to ensure that the model performance replicates observed streamflow as accurately as possible (Abbaspour *et al*., 2018). Therefore, an assessment of available climate data sources is required before the development and application of a specific SWAT watershed model. As mentioned earlier, climate data such as daily precipitation, minimum and maximum temperatures, are normally collected from local meteorological and/or hydrology agencies. However, local climate datasets are sometimes expensive and not easily accessible for model users. Hence, this review can provide insights as to which open-source climate data are most available and reliable for SWAT model applications.

For Malaysia, there are more than 400 research utilized SWAT modelling in the last decade, and the number of publications is increasing over time. Based on these findings, it could be observed that the application of SWAT model is established and suitable for modelling the conditions in Malaysia. Therefore, in this research, SWAT modelling is adopted for modelling the runoff scenarios in Malaysia under changing land use.

2.3.3.2 Rainfall-Runoff-Inundation (RRI)

On the other hand, another physically based hydrological model, known as Rainfall-Runoff-Inundation (RRI) developed in 2017 by Sayama *et al.* (2017) has gained significant attention to use for investigating the climate change impacts on hydrological processes of river basins. The RRI model, an integrated two-dimensional grid cell-based hydrodynamic model for rainfall-runoff and inundation simulations from areas encompassing downstream flood plains and upstream mountain zones is selected in this research. The RRI has been

widely adopted and applied in different nations (*e.g.,* Thailand (Sayama *et al.,* 2017), Myanmar (Bhagabati & Kawasaki, 2017), Pakistan (Siddiqui *et al.,* 2018), Japan (Shakti *et.al.*, 2020) *etc.*) for various hydrological applications. The flow on the floodplain slope grid cell and channel flow are calculated independently, through 2D and 1D diffusive wave models, respectively.

The complicated flow interactions between river channel and slope are computed through different overflowing formulae (refer to Sayama *et.al* (2012) for detailed explanation). On top of these, to better represent the RRI processes, lateral subsurface (particularly important for the mountainous region), vertical infiltration, and surface flows are also considered in the model, thereby increasing the reliability and accuracy of the simulation in Taiwan. Therefore, in this research, RRI is adopted to simulate the Taiwan extreme rainfall precipitation under changing climate.

2.4 Spatiotemporal analysis of COVID-19 on Atmosphere

Since the end of 2019, COVID-19 has tremendously disrupted the normal rhythm of livelihood and has led to dramatic loss of human life worldwide, with infections and deaths exceeding 481 million and 6.1 million, respectively, as of 27 March 2022 (Worldometer, 2022). Due to its high infectivity and transmissibility, it was classified as a global pandemic by the World Health Organization (WHO) on March 11, 2020 (WHO, 2020). Therefore, most governments across the globe have imposed restrictive/preventive measures, such as lockdowns, travel restrictions, shelter-at-home policies, social distancing, and mandatory mask wearing in public places, to contain or slow down the spread of COVID-19. These timely and strict measures have effectively slowed virus transmission among people.

In particular, three major threatening air pollutants are (i) ozone (O_3), (ii) particulate matter (PM) and (iii) nitrogen dioxide (NO_2). For O_3, it is a secondary air pollutant that is formed when NO_2 and volatile organic compounds (VOC) under photochemical reactions, which is particularly profound during summer. O_3 are generally found in two places, which are near the ground (major part of smog) and in the stratosphere. The former is harmful to the human health, creating a number of health problems; whereas the latter one is the

protective layer of ozone, helping to screen out harmful ultraviolet rays. O_3 can lead to more frequent asthma attacks in people who have asthma and can cause sore throats, coughs, and breathing difficulty, and it may even lead to premature death.

For PM is major health issues that coming from a variety of sources of primary particles include fires, smokestacks, construction sites, and unpaved roads; sources of secondary particles include reactions between gaseous chemicals emitted by power plants and automobiles. All these contributes to formation of haze as well as acid rain, which changes the pH balance of waterways and damages foliage, buildings, and monuments. Data revealed significant associations of PM_{10} concentration to increase in daily all-cause mortality, daily cardiovascular mortality, and daily respiratory mortality (Tanaka *et al.*, 2020). $PM_{2.5}$ concentration similarly exhibited significant associations to daily mortality for all causes, cardiovascular, and respiratory (Tan *et al.*, 2020).

NO_2 is major air pollutant that is mainly released from transportation sector and is formed in two ways-when nitrogen in the fuel is burned, or when nitrogen in the air reacts with oxygen at very high temperatures. High levels of NO_2 exposure can give people coughs and can make them feel short of breath. People who are exposed to NO_2 for a long time have a higher chance of getting respiratory infections.

2.4.1 Attributed premature death

The World Health Organization (WHO) highlights air pollution as the number one reason for environment-related deaths in the world. It's estimated to be the cause of seven million premature deaths every year – 4.3 million from outdoor air pollution, and 2.6 million from indoor pollution. With historical links to development and economic growth, we expect the number of deaths from outdoor pollution to grow (largely in Asia and Africa) as shown in Fig. 2.8.

Among air pollutants, 307,000 premature deaths were attributed to chronic exposure to fine particulate matter; 40,400 premature deaths were attributed to chronic nitrogen dioxide exposure; 16,800 premature deaths were attributed to acute ozone exposure. $PM_{2.5}$ is the most consistent and robust predictor of health effects from studies of long-term exposure

to air pollution, whereas O_3 has been associated with increased respiratory mortality (Health Effects Institute, 2018).

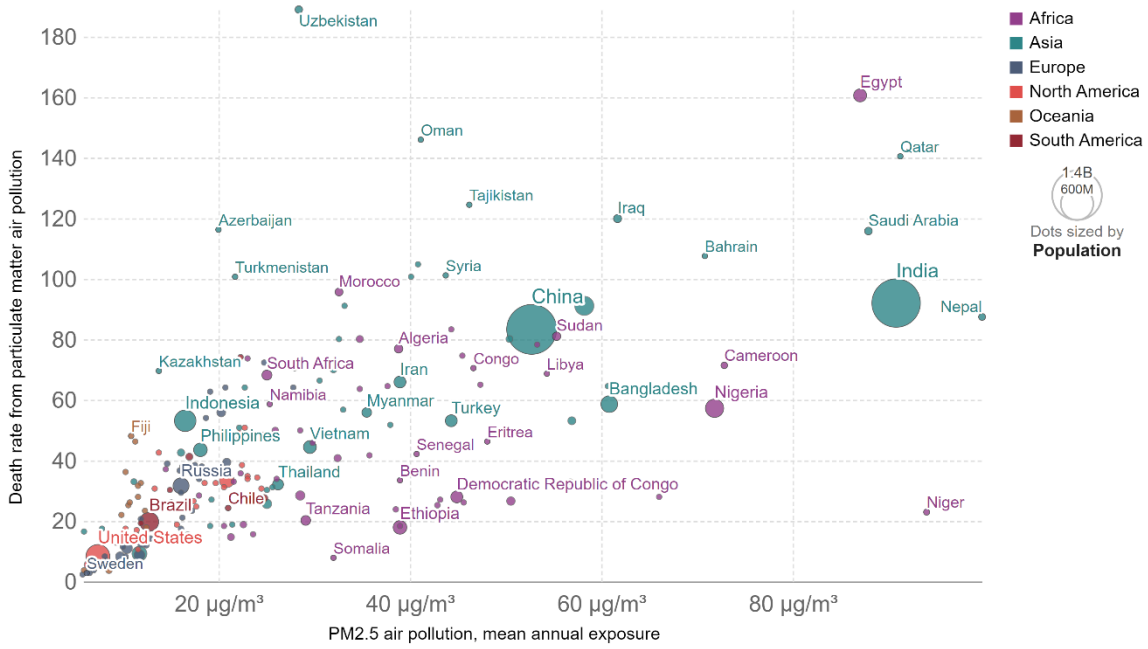

Fig. 2.8: Death rate from particulate matter air pollution *vs* $PM_{2.5}$ concentration exposure per 100,000 people (Ashiawa *et al.*, 2021).

In general, there are four main air pollution pathways, which are:

- ***Mobile Sources*** – cars, buses, planes, trucks, and trains
- ***Stationary Sources*** – power plants, oil refineries, industrial facilities, and factories
- ***Area sources*** – agricultural areas, cities, and wood burning fireplaces
- ***Natural sources*** – wind-blown dust, wildfires, and volcanoes

Exposure to air pollution is a risk factor that causes health impacts. The risk assessment of air pollution follows the air pollution pathway, from sources through emissions, concentrations, exposures, doses, to health impacts. Sources are generally the quantity and quality of fuel used. Emissions are air pollutants released from the source and are characterized by the environment, transported, and transformed. Concentrations are the

amount of an air pollutant in space and time. Exposures are concentrations of air pollutants that are breathed in and depend on pathways, durations, intensities, and frequencies of contact with the pollutant. Doses are how much of the exposure is deposited in the body. Health impacts accrue from doses, can be acute (short-term) or chronic (long-term), and are non-specific in that they have many risk factors. Monitoring and intervention can occur at any stage along this pathway. Health impacts are the primary risk indicators, although control measures at this stage are often too late and complicated due to their non-specific nature. Doses are also too late in the air pollution pathway and are poorly understood for many pollutants.

However, the emergence of COVID-19 has caused a significant reduction in air pollutant concentration worldwide, wherein the average concentrations of ground-level nitrogen dioxide (NO_2) and particulate matter with average aerodynamic diameters less than 10 μm and 2.5 μm (PM_{10} and $PM_{2.5}$) declined by approximately 30% and 20%, respectively, compared to 2019 (Yang *et al.,* 2021). Since then, there has been growing attention to utilizing both high-resolution satellite images and/or ground-based monitoring data to quantify the impact of COVID-19 on the local atmospheric environment, particularly to compare the differences before and after lockdown implementation: for instance, in India (Mahato *et al.,* 2020), China (Shen *et al.,* 2021), Singapore (Li and Tartarini 2020), Malaysia (Abdullah *et al.,* 2020), Iran (Broomandi *et al.,* 2020), Bangladesh (Rahman *et al.,* 2020), Brazil (Nakada & Urban, 2020), and Turkey (Ghasempour *et al.,* 2021).

2.4.2 Economic Losses

The COVID-19 cause a short-term fiscal impact and a long-term economic impact over the globe. There are efforts to curb the pandemic include imposing quarantine, preparing health facilities, isolating infectious cases, and tracing contacts involving public health resources, human resources and implementation costs. It also involves health system expenditures to provide health facilities to infectious cases and the arrangement of consumables such as antibiotics, medical supplies, and personal protective equipment.

The COVID-19 pandemics resulted in declined tax revenues and increased expenditure, which causes fiscal stress, especially in lower-middle-income countries (LMICs) where fiscal constraints are higher, and tax systems still need improvement. This economic impact severity was observed during the Ebola virus in Liberia caused by the rise in public health expenditure, economic downfall, and revenue decline due to the government's inability to raise revenue because of quarantine and curfews. Economic shocks are common during pandemics due to shortage of labor because of illness, rise in mortality, and a fear-induced behavior. Other than labor shortages, disruption of transportation, closed down of workplaces, restricted trade and travel, and closed land border are reasons for the pandemic's economic slowdown.

Based on Fig. 2.9, it could be observed that among the major economies, those who have timely imposed containment measures and successfully curbed the outbreak of COVID-19 have significantly less economic loss and deaths than those who have waited and hesitated. Although imposing stringent containment measures at an early stage would lead to an temporary contraction on economic growth, countries who have acted early enjoy a faster economic recovery in the long-term by effectively mitigating and containing the outbreak. Fig. 2.9 illustrates the loss of economic activity in different regions over the cause of the pandemic. It can be seen that regions like East Asia performed significantly better on epidemic control compared to Europe and North America and suffered less economic loss than the latter ones. To successfully contain the outbreak, social distancing measures to break the chain of transmission is required. However, the differences in the rapidity with which countries imposed such policies and the strictness of the policies reflect divergent assessments of both the public health risk of COVID-19 and the social and economic impacts of the different policies.

Based on the findings obtained from Guan *et al.* (2021), even for countries that are not directly affected by COVID-19 can experience large losses (*e.g.*, >20% of their GDP)—with such cascading impacts often occurring in low- and middle-income countries. Open and highly specialized economies suffer particularly large losses (*e.g.*, energy exporting Central

Asian countries or tourism-focused Caribbean countries). Supply bottlenecks and declines in consumer demand led to especially large losses in globalized sectors such as electronics (production decreases of 13-53%) and automobiles (2-49%). Many studies have identified that shorter lockdowns are likely to minimize overall economic damages, that a "go-slow" approach to lifting restrictions may reduce overall damages if it avoids further lockdowns, and that global supply chains will magnify economic losses in some countries and industry sectors regardless of direct effects of the coronavirus.

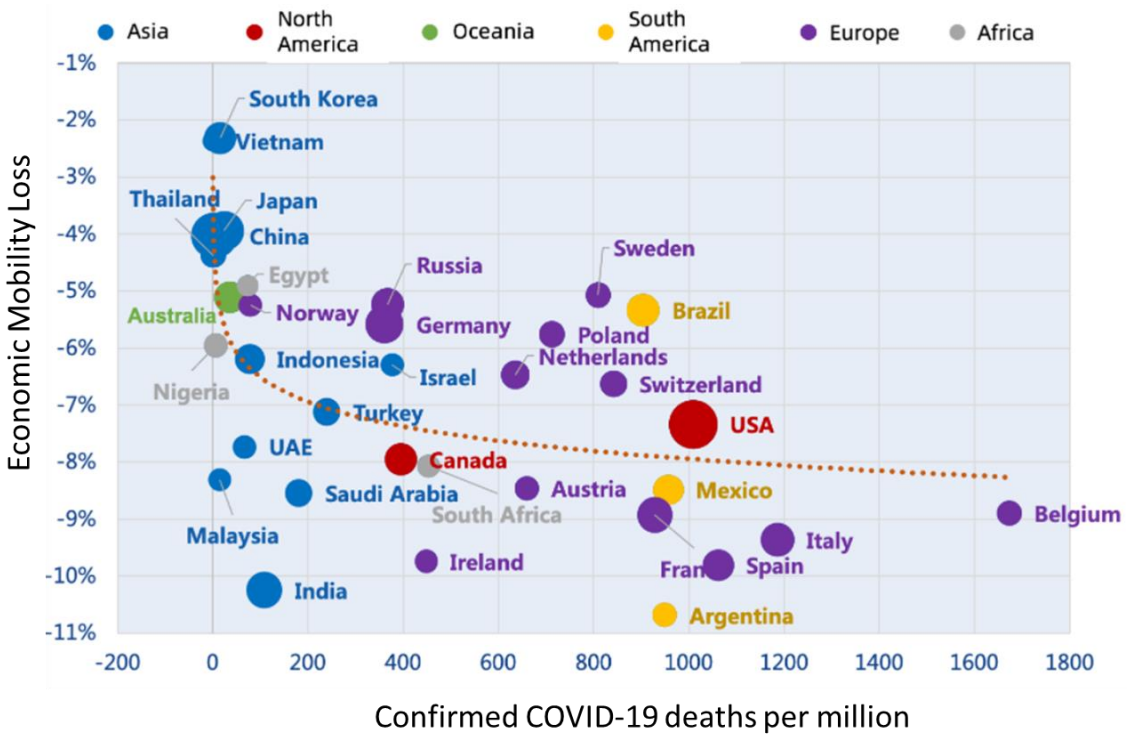

Fig. 2.9: Economic losses across different countries *vs* confirmed COVID-19 deaths per million (Guan *et al.*, 2021*)*

2.4.3 A blessing in disguise to the nature?

Nevertheless, despite the disastrous loss brought by the pandemic, these timely and strict measures associated with the local governments' policies have effectively slowed virus transmission among people. Concurrently, these measures also reduced emissions from major anthropogenic and economic activities due to the disruption of anthropogenic emissions. Consequently, a remarkable change in air pollutant concentrations was observed

throughout the world, particularly in countries that imposed lockdown, creating a silver lining in the dark cloud of COVID-19 (Jephcote *et al.,* 2021; Nakada and Urban, 2020; Kanniah *et al.,* 2020). A significant reduction in air pollutant concentration is observed worldwide, wherein the average concentrations of ground NO_2, PM_{10} and $PM_{2.5}$ declined by approximately 30% and 20%, respectively, compared to 2019 (Yang *et al.,* 2021).

Since then, there has been growing attention to utilizing both high-resolution satellite images and/or ground-based monitoring data to quantify the impact of COVID-19 on the local atmospheric environment, particularly to compare the differences before and after lockdown implementation, for instance, in India (Mahato *et al.,* 2020), China (Shen *et al.*, 2021), Singapore (Li and Tartarini, 2020), Malaysia (Abdullah *et al.,* 2020), Iran (Broomandi *et al.,* 2020), Bangladesh (Rahman *et al.,* 2020), Brazil (Nakada and Urban 2020), and Turkey (Ghasempour *et al.,* 2021). Throughout 2020, significant improvement of air pollution was observed worldwide, with approximately 30% reduction observed in major air pollutants (*e.g.,* carbon monoxide (CO), sulfur dioxide (SO_2), nitrogen monoxide (NO), nitrogen dioxide (NO_2), ozone (O_3), and particulate matters with average aerodynamic diameter < 10 and 2.5 µm (PM_{10} and $PM_{2.5}$)) (Addas and Maghrabi, 2021), as summarized in Fig. 2.10. Numerous studies investigated the impact of lockdown and performed changed analysis of air pollutant concentrations between pre-lockdown with lockdown period (Rodríguez-Urrego & Rodríguez-Urrego, 2020, Tobías *et al*., 2020) or in relative to the selected base-year (Abdullah *et al.,* 2020, Nakada & Urban, 2020). Based on findings observed utilizing the high resolution Sentinel-5P/TROPOMI satellite and Google Community Mobility Reports over 164 countries, Similar findings utilizing station-based data were also reported in China (Zhu *et al.,* 2020), Malaysia (Ash'aari *et al.,* 2020), Brazil (Rudke *et al.,* 2021), United States of America (Archer *et al.,* 2020), Italy (Gualtieri *et al*., 2020) and many other regions worldwide *(Anugerah et al.,* 2021; *Baysan et al.,* 2021; Tian *et al.,* 2021; Wetchayont, 2021). Nevertheless, limited studies have focused on the air quality changes in regions that did not impose lockdowns.

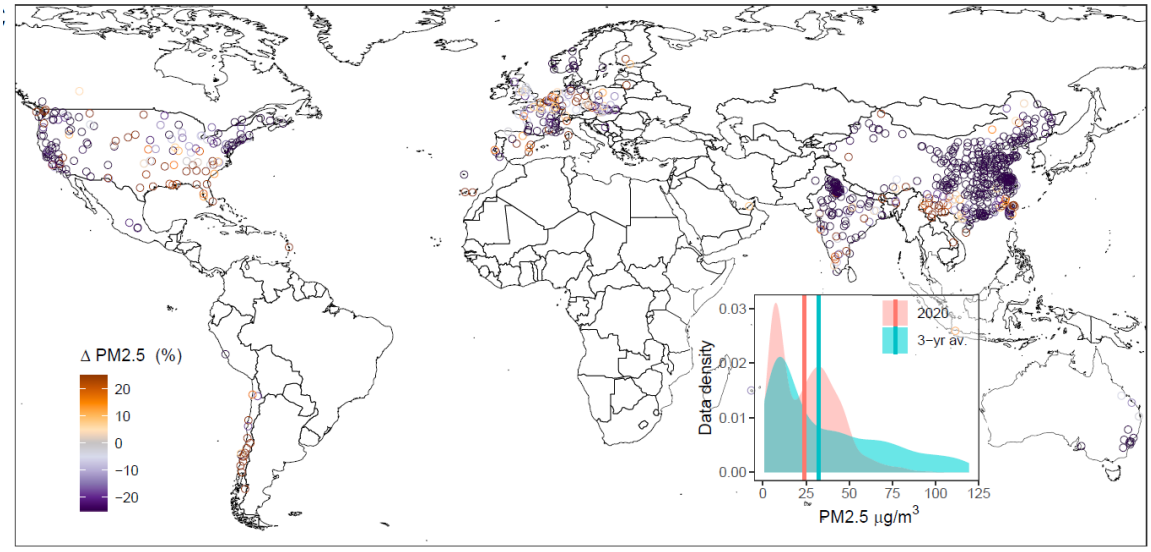

Fig 2.10: Global 2020 $PM_{2.5}$ concentrations change for lockdown regions (Yang *et al.*, 2021)

2.4.4 Influencing Factors

To quantify the impact of COVID-19 to the atmospheric environment, growing attention has been given to investigating the influencing factors of air quality changes during the COVID-19 period, for which the impacts of meteorology and public transportation are most reported. Therefore, in this research, both of these factors are included for discussion. To date, only a few studies have focused on the air quality changes in cities that did not impose lockdowns, such as Taiwan. As compared to regions imposed lockdown, contradicted finding was reported in Taiwan (Chang *et.al.*, 2021), in which there was insignificant changes or even higher concentrations of air pollutants were observed in spite of the reduced mobility. Therefore, to understand the effects of meteorology and transportation volume to the regions without lockdown during COVID-19, detailed analysis is performed as described in Chapters 5 and 6.

2.4.4.1 Transportation

Most of the reported studies have considered only the impact of public roadway transportation reduction during the lockdown period (Gao *et al.*, 2021; Tian *et al.*, 2021), but according to the annual transportation report of Taiwan, the use of public urban transportation, including different transportation modes (*e.g.*, railway, air and waterway), in 2020 declined

and dropped to almost the lowest level of the past decade (Ministry of Transportation and Communication, 2021). Significant concentrations of air pollutants have been reported in railways (Moreno *et al.,* 2015), air (Psanis *et al.,* 2017) and waterways (Solomon *et al.,* 2021), as different transportation modes have different features and may constitute divergent air pollutants to the environment. Therefore, to provide a comprehensive evaluation of the impact of public urban transportation on air quality during the study period, four transportation modes were included in this research.

2.4.4.2 Meteorological

Since meteorological parameters also play a significant role in affecting the dynamics of pollutants (such as dispersion rate, transportation, and transformation) (Singh & Tyagi, 2021), various methods have been introduced: *e.g.,* the application of black-box models to eliminate the associated effects caused by meteorological variability (Grange *et al.,* 2018; Solberg *et al.,* 2021). For instance, Petetin *et al.* (2020) and Talbot *et al.* (2021) performed a random forest machine learning algorithm to estimate the business-as-usual (BAU) pollutant concentration based on the emission scenario and meteorological parameters in the absence of COVID-19 in Spain and New Zealand, respectively. Although it is undeniable that black-box models usually have high prediction accuracy, white-box models are still preferred compared to black-box models due to their transparency. Additionally, the relative importance of the predictor variables, which are necessary for decision making in air quality management, can be recognized (Fung *et al.,* 2021). Compared to black-box models, white-box models require fewer datasets for model construction and are commonly adopted for practical application due to their simplicity and robustness (Wong *et al.,* 2021; Loyola-González, 2019).

Therefore, in this research, the white-box model, known as stepwise regression model (SRM) was constructed for each pollutant in Chapter 5 whereas four different artificial intelligence models, namely generalized additive model (GAM), gradient boosting machine (GBM), generalized linear model (GLM) and random forest (RF) were constructed and evaluated in Chapter 6 for comparison.

List of References

Abdullah, S., Mansor, A. A., Napi, N. N. L. M., Mansor, W. N. W., Ahmed, A. N., Ismail, M., et al., (2020). Air quality status during 2020 Malaysia Movement Control Order (MCO) due to 2019 novel coronavirus (2019-nCoV) pandemic. Science of The Total Environment, 729, 139022, doi.org/10.1016/j.scitotenv.2020.139022.

Amann, M., Purohit, P., Bhanarkar, A. D., Bertok, I., Borken-Kleefeld, J., Cofala, J., et al., (2017). Managing future air quality in megacities: A case study for Delhi. Atmospheric Environment, 161, 99-111, doi.org/10.1016/j.atmosenv.2017.04.041.

Arnold, M., Dilley, M., Deichmann, U., Chen, R. S., & Lerner-Lam, A. L. J. W. B., Washington, DC (2005). Natural disaster hotspots: a global risk analysis.

Abdullah, S., Mansor, A. A., Napi, N. N. L. M., Mansor, W. N. W., Ahmed, A. N., Ismail, M., et al., (2020). Air quality status during 2020 Malaysia Movement Control Order (MCO) due to 2019 novel coronavirus (2019-nCoV) pandemic. Science of The Total Environment, 729, 139022, doi.org/10.1016/j.scitotenv.2020.139022.

Amann, M., Purohit, P., Bhanarkar, A. D., Bertok, I., Borken-Kleefeld, J., Cofala, J., et al., (2017). Managing future air quality in megacities: A case study for Delhi. Atmospheric Environment, 161, 99-111, doi.org/10.1016/j.atmosenv.2017.04.041.

Bai, H., Gao, W., Zhang, Y., & Wang, L. (2022). Assessment of health benefit of PM2.5 reduction during COVID-19 lockdown in China and separating contributions from anthropogenic emissions and meteorology. *Journal of Environmental Sciences, 115,* 422-431, doi:10.1016/j.jes.2021.01.022.

Benis, K. Zoroufchi, Fatehifar, E., Ahmadi, J., & Rouhi, A. (2015). Optimal design of air quality monitoring network and its application in an oil refinery plant: an approach to keep health status of workers. Health Promot Perspect, 5(4), 269-279, doi:10.15171/hpp.2015.032.

Broomandi, P., Karaca, F., Nikfal, A., Jahanbakhshi, A., Tamjidi, M., & Kim, J. R. (2020). Impact of COVID-19 event on the air quality in Iran. Aerosol and Air Quality Research, 20(8), 1793-1804, doi:10.4209/aaqr.2020.05.0205.

Chang, H.-S., Su, Q., & Katayama, T. (2021). Research on establishment of the region flood protection standard - a case of watershed of Dajiaxi, Taiwan. *Urban Water Journal, 18*(3), 173-182, doi:10.1080/1573062X.2020.1864831.

Chen, H., Liang, Q., Liu, Y., & Xie, S. (2018). Hydraulic correction method (HCM) to enhance the efficiency of SRTM DEM in flood modeling. *Journal of Hydrology, 559,* 56-70, doi:10.1016/j.jhydrol.2018.01.056.

Chen, S.-C., Liao, C.-M., Chio, C.-P., Chou, H.-H., You, S.-H., & Cheng, Y.-H. (2010). Lagged temperature effect with mosquito transmission potential explains dengue

variability in southern Taiwan: Insights from a statistical analysis. *Science of The Total Environment, 408*(19), 4069-4075, doi:10.1016/j.scitotenv.2010.05.021.

Chen, Y.-R., Yeh, C.-H., & Yu, B. (2011). Integrated application of the analytic hierarchy process and the geographic information system for flood risk assessment and flood plain management in Taiwan. *Natural Hazards, 59*(3), 1261-1276, doi:10.1007/s11069-011-9831-7.

Chiang, Y.-C. (2018). Exploring community risk perceptions of climate change - A case study of a flood-prone urban area of Taiwan. *Cities, 74*, 42-51, doi:10.1016/j.cities.2017.11.001.

Chjeng-Lun, S., Chun-Ming, W., Wen-Chi, L., Yun-Chung, T., & Shin-Ping, L. (2009). The composite hazard resulted from Typhoon Morakot in Taiwan. *砂防学会誌, 62*(4), 61-65, doi:10.11475/sabo.62.4_61.

Ding, X., Zheng, L., Zheng, X., & Kao, S.-J. (2020). Holocene East Asian Summer Monsoon Rainfall Variability in Taiwan. [Original Research]. *Frontiers in Earth Science, 8*(234), doi:10.3389/feart.2020.00234.

Doong, D.-J., Lo, W., Vojinovic, Z., Lee, W.-L., & Lee, S.-P. (2016). Development of a New Generation of Flood Inundation Maps—A Case Study of the Coastal City of Tainan, Taiwan. *8*(11), 521.

Duan, Q., & Phillips, T. J. (2010). Bayesian estimation of local signal and noise in multimodel simulations of climate change. *115*(D18), doi:10.1029/2009JD013654.

Ge, X., Li, T., Zhang, S., & Peng, M. (2010). What causes the extremely heavy rainfall in Taiwan during Typhoon Morakot (2009)? [10.1002/asl.255]. *Atmospheric Science Letters, 11*(1), 46-50, doi:10.1002/asl.255.

Giorgi, F. (2019). Thirty Years of Regional Climate Modeling: Where Are We and Where Are We Going next? , *124*(11), 5696-5723, doi:10.1029/2018JD030094.

Guo, Y., Fang, G., Wen, X., Lei, X., Yuan, Y., & Fu, X. (2018). Hydrological responses and adaptive potential of cascaded reservoirs under climate change in Yuan River Basin. *Hydrology Research, 50*(1), 358-378, doi:10.2166/nh.2018.165 %J Hydrology Research.

Hashim, J. H., & Hashim, Z. (2016). Climate Change, Extreme Weather Events, and Human Health Implications in the Asia Pacific Region. *Asia Pac J Public Health, 28*(2 Suppl), 8s-14s, doi:10.1177/1010539515599030.

Henny, L., Thorncroft, C. D., Hsu, H.-H., & Bosart, L. F. (2021). Extreme Rainfall in Taiwan: Seasonal Statistics and Trends. *Journal of Climate, 34*(12), 4711-4731, doi:10.1175/JCLI-D-20-0999.1.

Hirabayashi, Y., Tanoue, M., Sasaki, O., Zhou, X., & Yamazaki, D. (2021). Global exposure to flooding from the new CMIP6 climate model projections. *Scientific Reports, 11*(1), 3740, doi:10.1038/s41598-021-83279-w.

Hirt, C. (2018). Artefact detection in global digital elevation models (DEMs): The Maximum Slope Approach and its application for complete screening of the SRTM v4.1 and MERIT DEMs. *Remote Sensing of Environment, 207*, 27-41, doi:10.1016/j.rse.2017.12.037.

Hsiao, S.-C., Chiang, W.-S., Jang, J.-H., Wu, H.-L., Lu, W.-S., Chen, W.-B., et al. (2021). Flood risk influenced by the compound effect of storm surge and rainfall under climate change for low-lying coastal areas. *Science of The Total Environment, 764*, 144439, doi:10.1016/j.scitotenv.2020.144439.

Hsu, H. H., & Chen, C. T. (2002). Observed and projected climate change in Taiwan. *Meteorology and Atmospheric Physics, 79*(1), 87-104, doi:10.1007/s703-002-8230-x.

Hsu, T.-W., Shih, D.-S., Li, C.-Y., Lan, Y.-J., & Lin, Y.-C. (2017a). A Study on Coastal Flooding and Risk Assessment under Climate Change in the Mid-Western Coast of Taiwan. *Water, 9*(6), 390.

Hsu, T.-W., Shih, D.-S., Li, C.-Y., Lan, Y.-J., & Lin, Y.-C. (2017b). A Study on Coastal Flooding and Risk Assessment under Climate Change in the Mid-Western Coast of Taiwan. *9*(6), 390.

Ito, R., Nakaegawa, T., & Takayabu, I. (2020). Comparison of regional characteristics of land precipitation climatology projected by an MRI-AGCM multi-cumulus scheme and multi-SST ensemble with CMIP5 multi-model ensemble projections. *Progress in Earth and Planetary Science, 7*(1), 77, doi:10.1186/s40645-020-00394-4.

Lin, C.-Y., Chien, Y.-Y., Su, C.-J., Kueh, M.-T., & Lung, S.-C. (2017). Climate variability of heat wave and projection of warming scenario in Taiwan. *Climatic Change, 145*(3), 305-320, doi:10.1007/s10584-017-2091-0.

Lin, I. I., & Chan, J. C. L. (2015). Recent decrease in typhoon destructive potential and global warming implications. *Nature Communications, 6*(1), 7182, doi:10.1038/ncomms8182.

Lin, M.-Y., Sun, W.-Y., Chiou, M.-D., Chen, C.-Y., Cheng, H.-Y., & Chen, C.-H. (2018). Development and evaluation of a storm surge warning system in Taiwan. *Ocean Dynamics, 68*(8), 1025-1049, doi:10.1007/s10236-018-1179-z.

Lin, Y.-F., Wu, C.-C., Yen, T.-H., Huang, Y.-H., & Lien, G.-Y. (2020). Typhoon Fanapi (2010) and Its Interaction with Taiwan Terrain – Evaluation of the Uncertainty in Track, Intensity and Rainfall Simulations. *気象集誌. 第2輯, advpub*, doi:10.2151/jmsj.2020-006.

McClean, F., Dawson, R., & Kilsby, C. (2020). Implications of Using Global Digital Elevation Models for Flood Risk Analysis in Cities. *Water Resources Research, 56*(10), e2020WR028241, doi:10.1029/2020WR028241.

Mizuta, R., Yoshimura, H., Murakami, H., Matsueda, M., Endo, H., Ose, T., et al. (2012). Climate Simulations Using MRI-AGCM3.2 with 20-km Grid. *Journal of the Meteorological Society of Japan. Ser. II, 90A*, 233-258, doi:10.2151/jmsj.2012-A12.

Rahman, M. M., Ferdousi, N., Abdullah, S. M. A., Kusunoki, S., & Islam, A. (2019). Recent Climate Simulation over SAARC Region Including Bangladesh Using High Resolution AGCM. *Asia-Pacific Journal of Atmospheric Sciences, 55*(2), 115-134, doi:10.1007/s13143-018-0077-0.

Rajah, K., O'Leary, T., Turner, A., Petrakis, G., Leonard, M., & Westra, S. (2014). Changes to the temporal distribution of daily precipitation. *41*(24), 8887-8894, doi:10.1002/2014GL062156.

S. Bhagabati, S., & Kawasaki, A. (2017). Consideration of the rainfall-runoff-inundation (RRI) model for flood mapping in a deltaic area of Myanmar. *Hydrological Research Letters, 11*(3), 155-160, doi:10.3178/hrl.11.155.

Sayama, T., Ozawa, G., Kawakami, T., Nabesaka, S., & Fukami, K. (2012). Rainfall–runoff–inundation analysis of the 2010 Pakistan flood in the Kabul River basin. *Hydrological Sciences Journal, 57*(2), 298-312, doi:10.1080/02626667.2011.644245.

Sayama, T., Tatebe, Y., & Tanaka, S. (2017). An emergency response-type rainfall-runoff-inundation simulation for 2011 Thailand floods. *Journal of Flood Risk Management, 10*(1), 65-78, doi:10.1111/jfr3.12147.

Schendel, U. (1967). Vegetationswasserverbrauch und-wasserbedarf. *Habilitation, Kiel, 137*, 1-11.

Shakti, P. C., Kamimera, H., & Misumi, R. (2020). Inundation Analysis of the Oda River Basin in Japan during the Flood Event of 6–7 July 2018 Utilizing Local and Global Hydrographic Data. *Water, 12*(4), 1005.

Siddiqui, M. J., Haider, S., Gabriel, H. F., & Shahzad, A. (2018). Rainfall–runoff, flood inundation and sensitivity analysis of the 2014 Pakistan flood in the Jhelum and Chenab river basin. *Hydrological Sciences Journal, 63*(13-14), 1976-1997, doi:10.1080/02626667.2018.1546049.

Su, Y.-F., Wu, C.-H., & Lee, T.-F. (2017). Public Health Emergency Response in Taiwan. *Health security, 15*(2), 137-143, doi:10.1089/hs.2016.0108.

Sun, Q., Miao, C., & Duan, Q. (2016). Extreme climate events and agricultural climate indices in China: CMIP5 model evaluation and projections. *36*(1), 43-61, doi:10.1002/joc.4328.

Tu, J.-Y., & Chou, C. (2013). Changes in precipitation frequency and intensity in the vicinity of Taiwan: typhoon versus non-typhoon events. *Environmental Research Letters, 8*(1), 014023, doi:10.1088/1748-9326/8/1/014023.

United Nations Office for Disaster Risk Reduction (2020). Human cost of disasters: an overview of the last 20 years.

Usman, M., Ndehedehe, C. E., Farah, H., & Manzanas, R. (2021). Impacts of climate change on the streamflow of a large river basin in the Australian tropics using optimally selected climate model outputs. *Journal of Cleaner Production, 315*, 128091, doi:10.1016/j.jclepro.2021.128091.

World Meteorological Organization (2021). WMO Atlas of Mortality and Economic Losses from Weather, Climate and Water Extremes (1970–2019).

Yamazaki, D., Ikeshima, D., Tawatari, R., Yamaguchi, T., O'Loughlin, F., Neal, J. C., et al. (2017). A high-accuracy map of global terrain elevations. *Geophysical Research Letters, 44*(11), 5844-5853, doi:10.1002/2017GL072874.

Yano, J. I., Cheedela, S. K., & Roff, G. L. (2012). A compressed super-parameterization: test of NAM-SCA under single-column GCM configurations. *Atmos. Chem. Phys. Discuss., 2012*, 28237-28303, doi:10.5194/acpd-12-28237-2012.

Yeh, H.-F., & Huang, C.-C. (2019). Evaluation of basin storage–discharge sensitivity in Taiwan using low-flow recession analysis. [10.1002/hyp.13411]. *Hydrological Processes, 33*(10), 1434-1447, doi:10.1002/hyp.13411.

Yoshida, K., Sugi, M., Mizuta, R., Murakami, H., & Ishii, M. (2017). Future Changes in Tropical Cyclone Activity in High-Resolution Large-Ensemble Simulations. *Geophysical Research Letters, 44*(19), 9910-9917, doi:10.1002/2017GL075058.

Zhuan, M., Chen, J., Xu, C.-Y., Zhao, C., Xiong, L., & Liu, P. (2019). A method for investigating the relative importance of three components in overall uncertainty of climate projections. *International Journal of Climatology, 39*(4), 1853-1871, doi:10.1002/joc.5920.

Chapter 3

Scenario-based Impacts of Decadal Land Use Change on the Water Balance Components using SWAT in Selangor River Basin

In this chapter, the effects of land use (LU) change on water balance in Selangor river basin, Malaysia was studied. Two artificial intelligence methods, namely support vector machine (SVM) and artificial neural network (ANN) were developed and its prediction performance for LU identification using satellite images were compared. To simulate future land use scenarios, Land Change Modeller in Terrset was used, utilizing the LU maps simulated from the satellite images. The future streamflow was simulated using Soil and Water Assessment Tool (SWAT) from ArcGIS software. Extreme streamflow such as no flow rate or very high flow rate up to 100 m^3/s is more commonly encountered in the future. Through the simulation, it provides an insight for the responsible authority in planning proper management for water resources for preventing prolonged drought or extreme rainfall induced flood events.

3.1 Introduction

Since 21st century, the decrease in flow discharge and the increase in contaminant concentration in streamflow are common global phenomena, especially for the water-limited regions of developing countries. Till present, researchers focus on the effect of land-use change in catchment hydrology. Many researchers have found that a strong relationship between land use and water quantity (Bultot *et al.,* 1990; Krause, 2002; Li *et al.,* 2007; Ranjan *et al.,* 2006), as well as water quality (Ahearn *et al.,* 2005; Baker, 2003; Heathwaite *et al.,* 2005; Tong & Chen, 2002). Land use is tightly linked to evapotranspiration, initiation of surface runoff, washout of nutrients from soil, and other hydrological processes. Land-use changes pertain to variations in surface roughness, soil aggregate structure, stomatal conductance, and soil organic content and nutrients, including nutrient input from manure and fertilizer (Hormann *et al.,* 2005). In general, these changes affect water and nutrient cycles in watersheds. For example, converting grazing lands or farmlands into woodlands

decreases water and nutrient discharge (Dagnachew *et al.,* 2003; Guo *et al.,* 2008). Given the complex effect of these factors on hydrological responses, especially on hydro-chemical responses, the direct effects of land use and climatic variability on streamflow or non-point source pollution are difficult to separately identify (Juckem *et al.,* 2008; Kent, 1999; Lettenmaier *et al.,* 1994)

The methods for detecting the effect of land-use changes on streamflow include historical data analysis and numerical modeling. In general, numerical models are commonly used for hydrological simulation, these are simple and effective tools even under changing conditions (Andersen *et al.,* 2006; Ewen and Parkin, 1996; Manus *et al.,* 2009). Using lumped or distributed hydrological models, most past research has focused on the influences of land-use changes on river discharge and water balance (Chen *et al.,* 2005; Dagnachew *et al.,* 2003; Samaniego & Andras, 2006; Wang *et al.,* 2006). Additionally, impacts of these factors on watershed hydrology is different across watersheds. Therefore, sites must be evaluated on a local scale (Khoi & Thom, 2015). Due to limited available data, it is essential to use both comprehensive and physical tools to extract as much information about hydrologic responses as possible (Li *et al.,* 2009). Hydrological models are considered an appealing approach to carry out impact assessment studies, as they provide a conceptualized framework to be used in scenario studies on the relationship between hydrological components, land use change and climate variability (Jothityangkoon *et al.,* 2001). Model parameters can have physical meaning as related to measurable landscape properties and meteorological conditions (Legesse *et al.,* 2003), and explicitly represent spatial variability (Lu *et al.,* 2015). Initial model parameters describing vegetation, land use and soil types are called physically based parameter values; they can be adjusted to improve streamflow simulation through subsequent model calibration processes (Beven, 2006).

Recently, water resource managers and modelers have counted on hydrological models to identify alternative strategies for water resource allocation and to obtain more information about watershed systems, hydrological processes, and their responses to both anthropogenic and natural factors. To simulate future land use scenarios, Land Change

Modeller in Terrset is used and the land use maps are simulated from the satellite images. In this research, artificial intelligence aided techniques, for instance artificial neural network and support vector machines were used. To obtain highly classified land use maps, trial-and-error approach was adopted to optimize the models.

Due to the limited dataset and land soil type suitability of Malaysia, Soil and Water Assessment Tool (SWAT) was adopted in this research. Future land use maps in 2030 and 2050 were used to simulate future streamflow scenarios under business-as-usual scenario, adopting the changing trends from 1990 to 2016. The findings of this study are expected to provide compendious information, including practical implications, to relevant authorities for policy planning and implementation for better water resources and risk management according to regions.

3.2 Data Collection and Methodology

3.2.1 Study Area and Data Collection

The Selangor river basin, located between latitudes 3°12’09”N - 3°44’08”N and longitudes 101°10”24E - 101°48’0”E, is found in Selangor - one of the most developed and progressive states that contributes 23.7% of Malaysia’s 2018 gross domestic product (Department of Statistics, 2019). It is one of the largest river basin in Malaysia (2200 km^2) with a total stream length of 110 km (Camara *et al.*, 2020). As illustrated in Fig. 3.1, the river basin flows from the foothill of Fraser’s Hill (upstream) to the southwest direction until the river mouth of Kuala Selangor (downstream); traversing through three districts in the Selangor state: Hulu Selangor, Gombak, and Kuala Selangor (Othman *et al.*, 2018; Cheah *et al.*, 2019). The Selangor river basin is the primary water resource (over 60%) for over 4 million people residing in the Selangor State and Kuala Lumpur, the capital of Malaysia (Santhi & Mustafa, 2013).

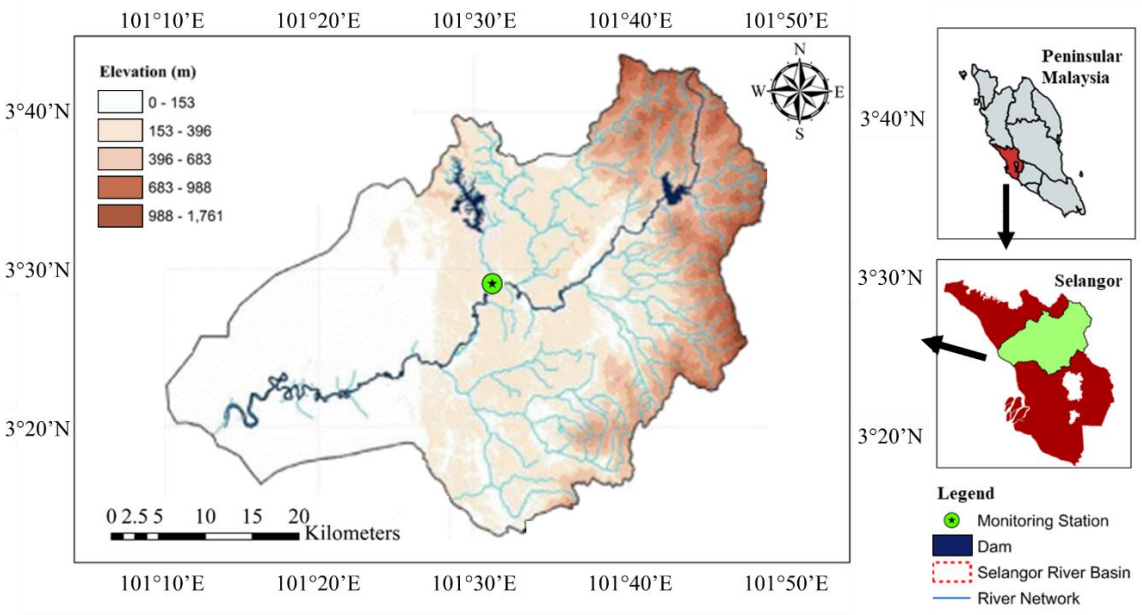

Fig. 3.1: Topography and geographical location of Selangor river basin with flow discharge monitoring station

The Selangor river basin is located in the tropical region, characterised with hot and humid climate year-round with plentiful of annual rainfall due to two monsoons; Northeast Monsoon (December to March) and Southwest Monsoon (June to August). These periods are known as wet season, while the remaining months are dry season. The mean annual rainfall and temperature in this river basin are 2,200 mm and 27 °C, respectively (Palizdan *et al.*, 2014). Surface runoff due to prolonged and heavy rainfall with river flow can exceed 122 m^3/s during the monsoon seasons, which may severely affect the people and also the surrounding facilities (Seyam & Othman, 2015; Al-Badaii & Shuhaimi-Othman, 2014). Although Selangor river basin is one of the major water supply river basin, the number of discharge monitoring station with data over 30 years is very limited, with only one in the central of the basin.

3.2.2 Model Development

To investigate streamflow trend analysis under changing land use, a research framework is proposed, consisting of two major sections: land use land cover modelling and hydrological modelling, as shown in Fig. 3.2. Under land use land cover modelling, two artificial intelligence models namely support vector machine (SVM) and artificial neural network (ANN) is optimized and developed for present land use change detection, for 1990, 2000 and 2016 using satellite image from United States Geological Survey (USGS). The classified satellite image is used as input for future land use simulation for year 2030 and 2050. The simulated land use maps are used to investigate the future streamflow using SWAT modelling.

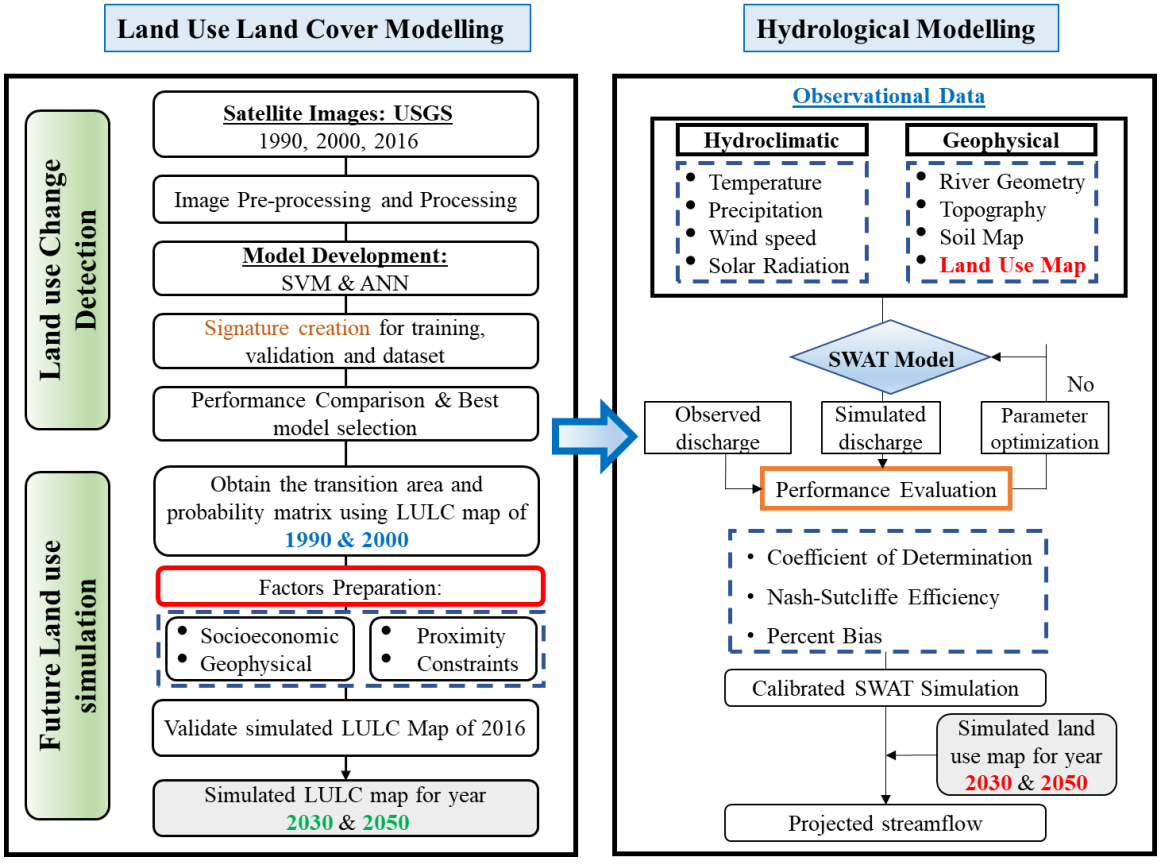

Fig. 3.2: Overall schematic diagram for streamflow simulation under changing land use.

3.2.2.1 Current Land Use Change Detection

In general, remote sensing analysis can be divided into three sections, which are (i) image segmentation, (ii) classification and (iii) accuracy assessment as shown in Fig. 3.3. In this section, the accuracy assessment of the satellite image classified using machine learning methods will be focused and discussed. Accuracy assessment is the step to identify the exactness level of the classification that has been done. The level of accuracy is calculated by the Kappa Coefficient whereas if the result approached to number one its mean that the classification done is more accurate. Kappa coefficient is a measure of overall agreement of a matrix. In contrast to the overall accuracy, the Kappa coefficient takes also non-diagonal elements into account.

After subset the data via ROI, classification of Selangor river basin satellite imagery nis performed according to its spatial representation. The basic step for classification is by creating the ROI for each image according to the type of land cover/use that exists in the satellite imagery. In this study, five different land cover/use classes have been chosen for creating ROI's polygon in Selangor river basin area *viz.* forest, urban, water bodies, agriculture and cleared land.

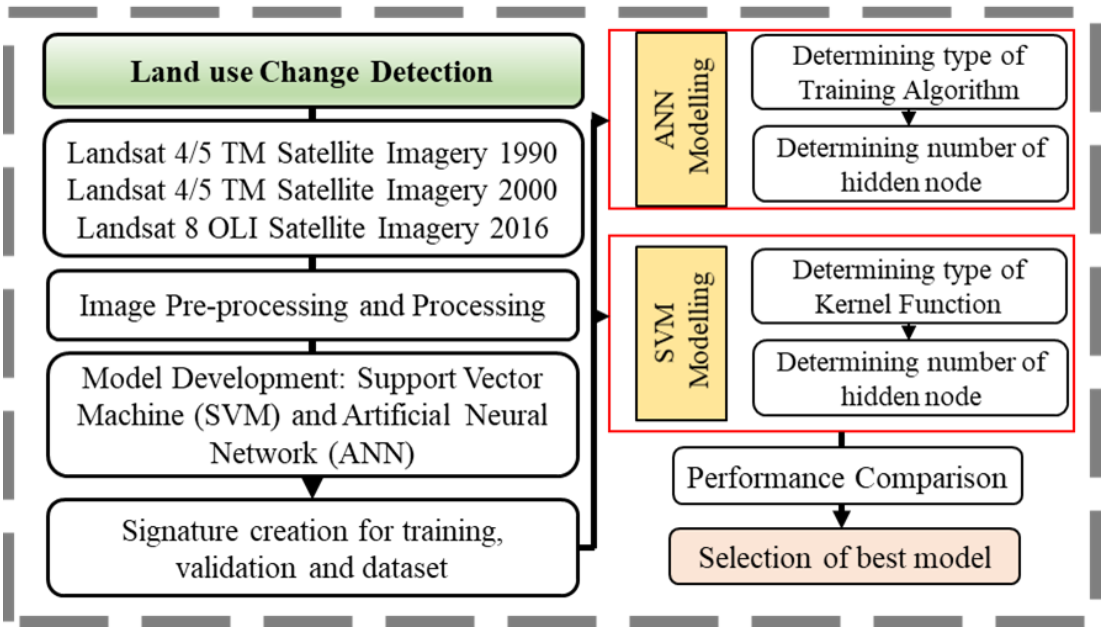

Fig. 3.3: Detailed schematic diagram for LULC classification

3.2.2.1.1 ANN Model

The ANN model has been widely applied to solve non-linear and complex problems due to its capability of learning, memorising, and generalising from experience. It is comprised of three main layers; (i) Input Layer to receive input variable(s) of the models, (ii) Output Layer to perform computations on the input variables, and (iii) Hidden Layer to generate output variable(s), in order to mimic the information processing system as the human brain. Amongst the different network architectures found in the ANN family, feedforward backpropagation network (FFBN), the most prevalent network architecture for classification and management of water resources, was selected (Oyebode & Stretch, 2019). In FFBN, the flow of information is unidirectional, which advances from the input layer to the output layer through artificial neurons (elementary unit in ANN), without forming any cycle or loop, as portrayed in Fig. 3.4(a) (Urso *et al.*, 2019).

The weighted input data and bias were propagated forwardly under tangent sigmoid activation function *(tansig)* to the hidden layer, while outputs were generated at the output layer through linear activation function (*purelin*) (Ullah and Bhuiyan 2018). Backpropagation was performed to adjust the weight value of the network and to seek the optimum solution. The mathematical expression of FFBN is displayed in Eq. (3.1).

$$Y(x) = \sum_{j=1}^{J} W_{jk}\, f\left(p_i + \sum_{i=1}^{n} W_{ij} x_i\right) + q_j \qquad (3.1)$$

In Eq. (3.1), $Y(x)$ is output; W_{ij} and W_{jk} denote the weight from input layer to hidden layer and from hidden layer to output layer, respectively; x_i represents input data; p_i and q_j are bias from input layer to hidden layer and from hidden layer to output layer, respectively; and f is activation function (*tansig*).

In this study, 11 training algorithms that belong to six classes are compared and evaluated in this study (Bisht *et al.*, 2017; Kadam *et al.*, 2019). The brief explanation of each training algorithm is summarised in Table 3.1.

Table 3.1: Brief description for training algorithms used in this study.

Training Algorithm	Training Function	Description
(i) Levenberg-Marquardt		
Levenberg-Marquardt backpropagation	trainlm	Weight and bias values are updated by using Levenberg-Marquardt optimization method.
(ii) Gradient descent with variable learning rate		
Gradient descent with momentum backpropagation	traingdm	Weight and bias values are updated by using gradient descent with momentum method
Gradient descent with adaptive learning rate backpropagation	traingda	Weight and bias values are updated by using gradient descent with adaptive learning rate method
Gradient descent with momentum and adaptive learning rate backpropagation	traingdx	Weight and bias values are updated by using gradient descent with momentum and adaptive learning rate backpropagation
(iii) Resilient backpropagation		
Resilient backpropagation	trainrp	Weight and bias values are updated by using resilient backpropagation method
(iv) Conjugated gradient descent		
Conjugate gradient backpropagation with Powell-Beale restarts	traincgb	Weight and bias values are updated by using conjugate gradient backpropagation with Powell-Beale restarts method.
Conjugate gradient backpropagation with Polak-Ribiére updates	traincgp	Weight and bias values are updated by using conjugate gradient backpropagation with Polak-Ribiére updates method.
Scaled conjugate gradient backpropagation	trainscg	Weight and bias values are updated by using scaled conjugate gradient method.

3.2.2.1.2 SVM Model

The SVM model developed by Vapnik (1995) is a widely used supervised method for regression and classification. The SVM is used for binary classification (true or false Boolean operation) (Oh & Kim, 2020) and it has been extended for multi-class classification by fusing Error-Correcting Output Codes (ECOC) method that decomposes multi-class classification into many binary classification tasks (Al-shargie *et al.*, 2018). The ECOC involves two stages: (i) Encoding to construct coding matrix ($2^{n-1}-1$, n=number of class) and assigning each class a unique codeword, and (ii) Decoding to assign the data points to the class with the closest codeword (Liu *et al.*, 2018; Samat *et al.*, 2019).

The SVM model is a kernel-based learning algorithm, wherein classification is performed by setting the input data into a high-dimensional feature space *via* non-linear mapping. Input and support vectors (data points closest to the hyperplane) are optimised by kernel function to identify the maximal separating hyperplanes (see Fig. 3.4(b)). The solution function of SVM model is expressed in Eq. (3.2).

$$Y(x) = \sum_{i=1}^{I}(-\alpha_i + \alpha_i^*)K(x,y) + b_{SVM} \quad (3.2)$$

In Eq. (3.2), $Y(x)$ is output; $-\alpha_i and\ \alpha_i^*$ are Lagrangian multipliers (Kisi and Parmar 2016) (to identify the extrema of a function subject to equality constraints); $K(x,y)$ is kernel function; and b_{SVM} is bias.

For SVM modelling, eight different MFs under five categories namely are compared and evaluated. The brief description for each MF is summarised in Table 3.2 (Modaresi and Araghinejad 2014; Ji *et al.*, 2017). The function is defined in Eq. (3.3).

$$K(x,y) = \exp(-\sigma\|x-y\|^2)\ for\ \sigma > 0 \quad (3.3)$$

In Eq. (3.3), σ denotes the kernel parameter that adjusts the smoothness of hyperplane in the feature space.

Table 3.2: Brief description for MFs used in this study

Membership Function	Function	Description
(i) Piecewise Linear Functions		
Trapezoid-shaped MF	trapmf	Function of vector, x is mapped onto a trapezoid curve.
Triangular-shaped MF	trimf	Function of vector, x is mapped onto a triangular curve.
(ii) Gaussian Distribution Functions		
Gaussian MF	gaussmf	Function of vector, x is mapped onto gaussian distribution curve.
Gaussian Combination MF	gauss2mf	Function of vector, x is mapped onto combination of two gaussian distribution curves.
(iii) Bell-shaped Function		
Bell-shaped MF	gbellmf	Function of vector, x is mapped onto a bell-shaped curve.
(iv) Sigmoidal Function		
Difference Sigmoidal MF	dsigmf	Function of vector, x is mapped onto a difference of two sigmoidal curves.
Product Sigmoidal MF	psigmf	Function of vector, x is mapped onto a product of two sigmoidal curves.
(v) Polynomial Based Function		
Polynomial-Pi MF	pimf	Function of vector, x is mapped onto a π-shaped curve.

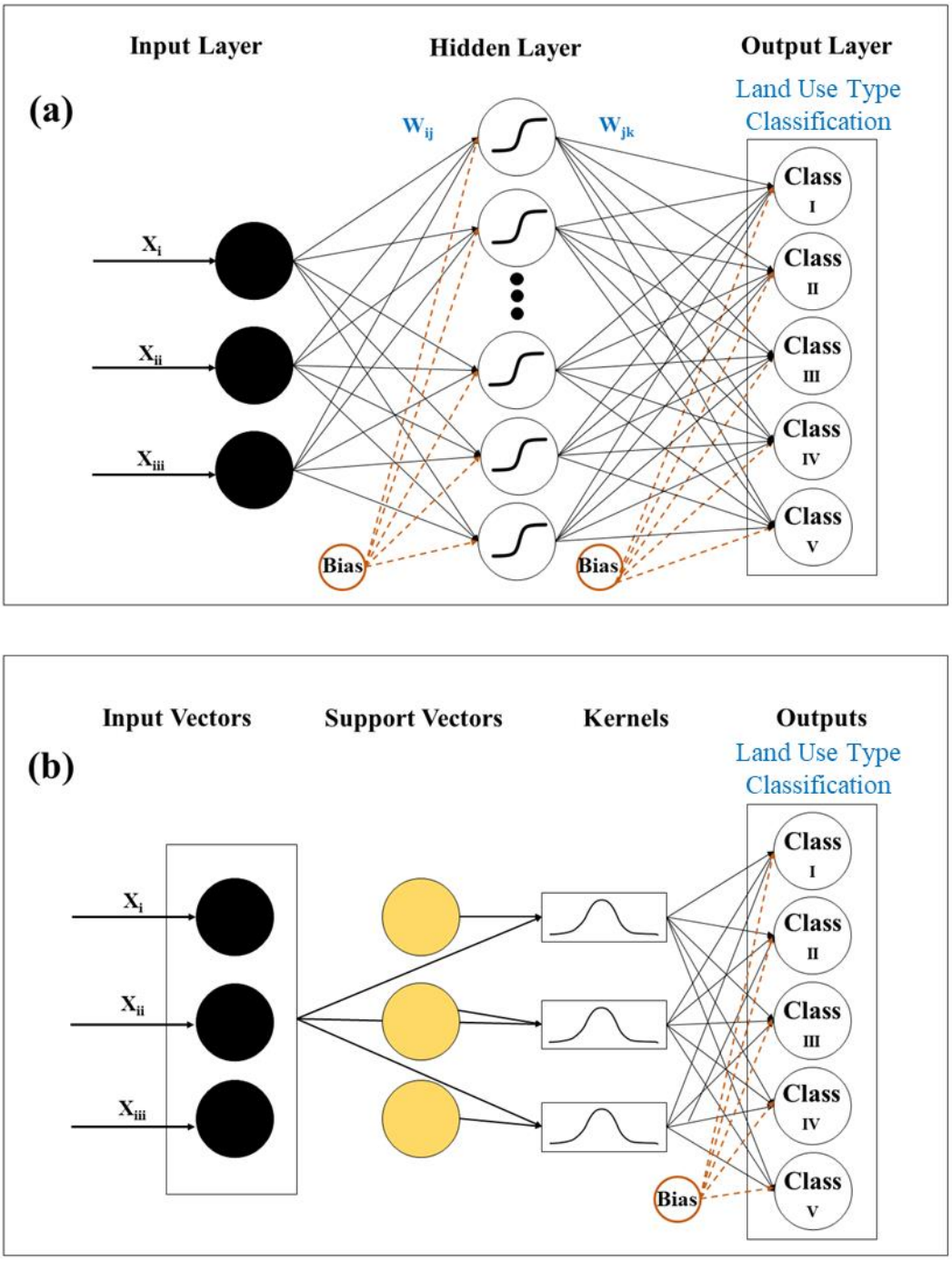

Fig. 3.4: Schematic diagram for (a) feed-forward neural network (b) support vector machine

3.2.2.1.3 Model performance

The classification performance was assessed statistically using different widely adopted criteria; (i) Accuracy, (ii) Sensitivity and (iii) Precision, as expressed mathematically in the following:

$$Accuracy_{Overall} = \frac{\sum_{Class=1}^{n}(True\ Positive)}{Total\ number\ of\ Testing\ data} \times 100\% \quad (3.4)$$

$$Sensitivity_{\ Class} = \frac{True\ Positive_{\ Class}}{(True\ Positive + False\ Negative)_{Class}} \times 100\% \quad (3.5)$$

$$Precision_{\ Class} = \frac{True\ Positive_{\ Class}}{(True\ Positive + False\ Positive)_{Class}} \times 100\% \quad (3.6)$$

Accuracy denotes the capability of the model to correctly identify and reject the land use class based on the RGB pixel combination. Meanwhile, *Sensitivity* of each class refers to the ratio of correctly identified land use classification within the same class, and *Precision* of each class is the ratio of correctly identified land use classification among the different classes. In order to better visualise the classification performance, a confusion matrix that can exemplify each land use class with a dimension of 5 x 5 was developed. Each column of the matrix represents the actual classifications, while the row of the matrix reflects the system prediction for each land use class.

3.2.2.2 Future Land Use Simulation

For simulating future land use, a detailed methodology framework is provided in Fig. 3.5. The classified satellite images using SVM and ANN models are used in this step. Factors summarized in Chapter 2, including both biophysical and proximate drivers are included in this study. Land Change Modeller (LCM) in TerrSet2019 software developed by Clack Labs (Clark Labs 2020) is used for the modelling. The LCM is based on historical land cover data, transition potential maps, and Markov matrices, to simulate future LC change. The LCM consists of 3 main steps, change analysis, transition potential modelling, and change prediction. The base maps used for capturing the change trend used are the classified satellite images of 1990 and 2000, to simulate the land use in 2016. The classified satellite image

2016 was used to verify the simulation results. Future land use maps of 2030 and 2050 are simulated once the accuracy of the developed land use maps are verified.

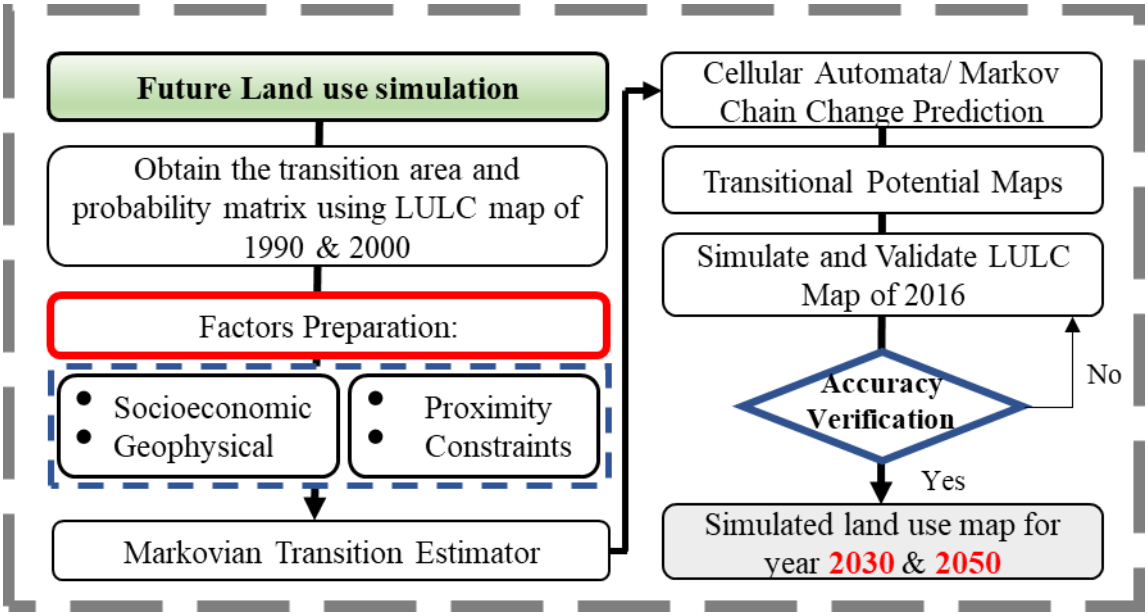

Fig. 3.5: Detailed schematic diagram for future land use simulation

3.2.2.2.1 Identification proximate drivers

In this step, the potential of land to transition is identified, and transition potential maps for each transition are created. The transition potential maps that have the same underlying driver variables are grouped within an empirically evaluated transition sub-model. These driver variables are used to model the historical change process. The driver variables used in this study are: distance to rivers, distance to roads, distance to urban area, DEM, and slope (Fig. 3.6). The driver variables were selected based on the literature review (Camara *et al.*, 2020; Rafaai *et al.*, 2020). This study applied the CA - Markov model for simulating and predicting land use change in Selangor River basin. The CA model is expressed by Eq. 3.7 (Liping *et al.*, 2018):

$$S_{t+1} = f(S_t, N) \quad (3.7)$$

In Eq. 3.7, S_t is the set of states of finite cells; While S_{t+1} are different moments; the neighborhood of cells is N ; and the transformation rule of local space is f .

3.2.2.2.1 Markov Transition Estimator

Markov model is a discrete random process both in time and in state (Al-sharif and Pradhan, 2014). The simulation process of the model mainly generates a land use area transfer matrix and a probability transfer matrix to predict the trends of land use change. The transition potential maps are created using the Decision Forest algorithm, which is an implementation of the Random Forest method. The CA Markov model successfully integrates the benefits of the Markov and CA models. Implemented into the IDRISI software model, the prediction steps with the CA-Markov model involve 1) the construction of the suitability atlas; 2) the generation of the transfer matrix and the state of transition probability matrix using the Markov model; 3) the prediction of future land use using the CA model. The business-as-usual scenario adopting the trends obtaiend from previous years are used to simulate for year 2030 and 2050.

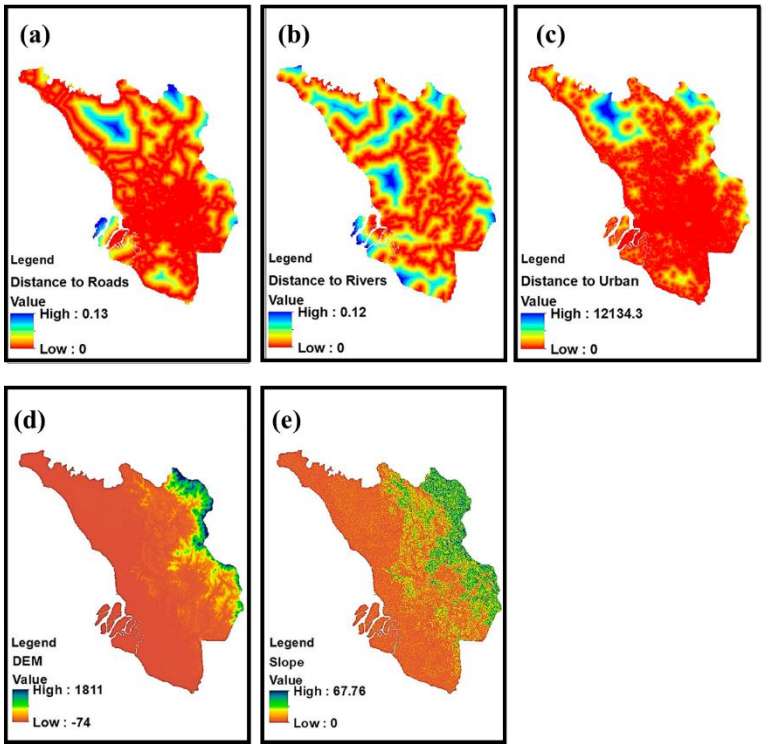

Fig. 3.6: Raster maps of (a) distance to roads, (b) distance to rivers, (c) distance to urban area, (d) DEM and (e) slope used as driver variables for the transition potential modelling.

3.2.2.3 Future Streamflow Simulation

For simulating future streamflow, SWAT model was selected as discussed in Chapter 2. The watershed was delineated to identify the drainage area of river network, utilizing digital elevation models (DEM) and geographic information system (GIS) software. To evaluate the performance of model simulation, three performance indicators were applied, namely coefficient of determination (r), Nash-Sutcliffe efficiency (NSE) and percent bias (PB), expressed mathematically below:

$$r = \frac{\sum_{t=1}^{n}(Q_s^t - \overline{Q_s})(Q_o^t - \overline{Q_o})}{\sqrt{(\sum_{t=1}^{n}(Q_o^t - \overline{Q_o})^2)(\sum_{t=1}^{n}(Q_s^t - \overline{Q_s})^2)}} \quad (3.8)$$

$$NSE = 1 - \frac{\sum_{t=1}^{n}(Q_s^t - \overline{Q_s})}{(\sum_{t=1}^{n}(Q_o^t - \overline{Q_o})^2)} \quad (3.9)$$

$$PB = 1 - \frac{\sum_{t=1}^{n}(Q_s^t - \overline{Q_s})}{\sum_{t=1}^{n} Q_s^t} \times 100\% \quad (3.10)$$

where Q_s^t and Q_o^t are simulated and observed discharge at time step t respectively; $\overline{Q_s}$ and $\overline{Q_o}$ are the mean simulated and observed discharge; β and α are the measures of bias and variability.

3.3 Results and Discussion

3.3.1 Assessment of Classified Image using ANN and SVM

In this section, the results obtained for classified satellite images using ANN and SVM are evaluated and compared. To obtain optimized network structure, systematic trial-and-error approach are adopted. The accuracy of the classified LULC maps was assessed by comparing the land use classes with the satellite image (reference) ground truth data. The pixel-by-pixel accuracy assessment approach was undertaken based on which 150 random points were generated on the LULC maps of 1990, 2000, and 2016. The selected points were cross-referenced with the satellite images, as well as spatial maps of the study area. The selected points represent the various land use classes used for image classification. A confusion matrix was generated using the cross-referenced data to identify the degree of misclassified pixels by the image classification. Multiple land use classification trails were

conducted to achieve the optimum accuracy, based on Anderson's classification scheme. An overall accuracy minimum of 85% is considered satisfactory of land use classification (Kingter *et al.,* 2021).

3.3.1.1 Hyperparameter Optimization ANN

To determine the optimum ANN model for satellite image classification in this study, a structured trial-and-error method is applied on selecting the training algorithm and number of hidden neurons. Wong *et al.,* (2019) and Lima *et al.*, (2017) reported that the excessive or inadequate number of hidden neurons will lead to overfitting or underfitting in the network, respectively, causing poor generalization and prediction. Therefore, to determine optimized training algorithm and hidden neuron number, the effect of hidden neuron is studied, ranging from 1-20.

Fig. 3.7 presents the box plots of distribution and variation of ANN classification performance under hidden neuron numbers. The effect of hidden neuron number is significantly affecting the performance of the ANN model in which the prediction accuracy varied from 58.7% to 86.4%. The optimum hidden neuron for training, validation and testing dataset in different training algorithms is summarized in Table 3.3. The best input combination for ANN model is under 17 hidden neurons of Levenberg-Marquardt backpropagation training algorithm, with accuracy of 92.4% 90.5% and 88.7%, for training, validation and testing dataset, respectively. Referring to Fig. 3.8, the vertical and horizontal grey columns represent sensitivity and precision for each classification, respectively and the accuracy can be found at the bottom right corner of the confusion matrix. It can be observed that the application of ANN could substantially predict the different type of land uses, including urban, water bodies and cleared land; however, as the pixel between agricultural and forest have high similarity, leading to the lower sensitivity for agricultural and forest prediction in testing dataset (70.0%). Areas with a greater concentration of mixed pixels belonging to different land use classes had a higher tendency of misclassification during the image classification process.

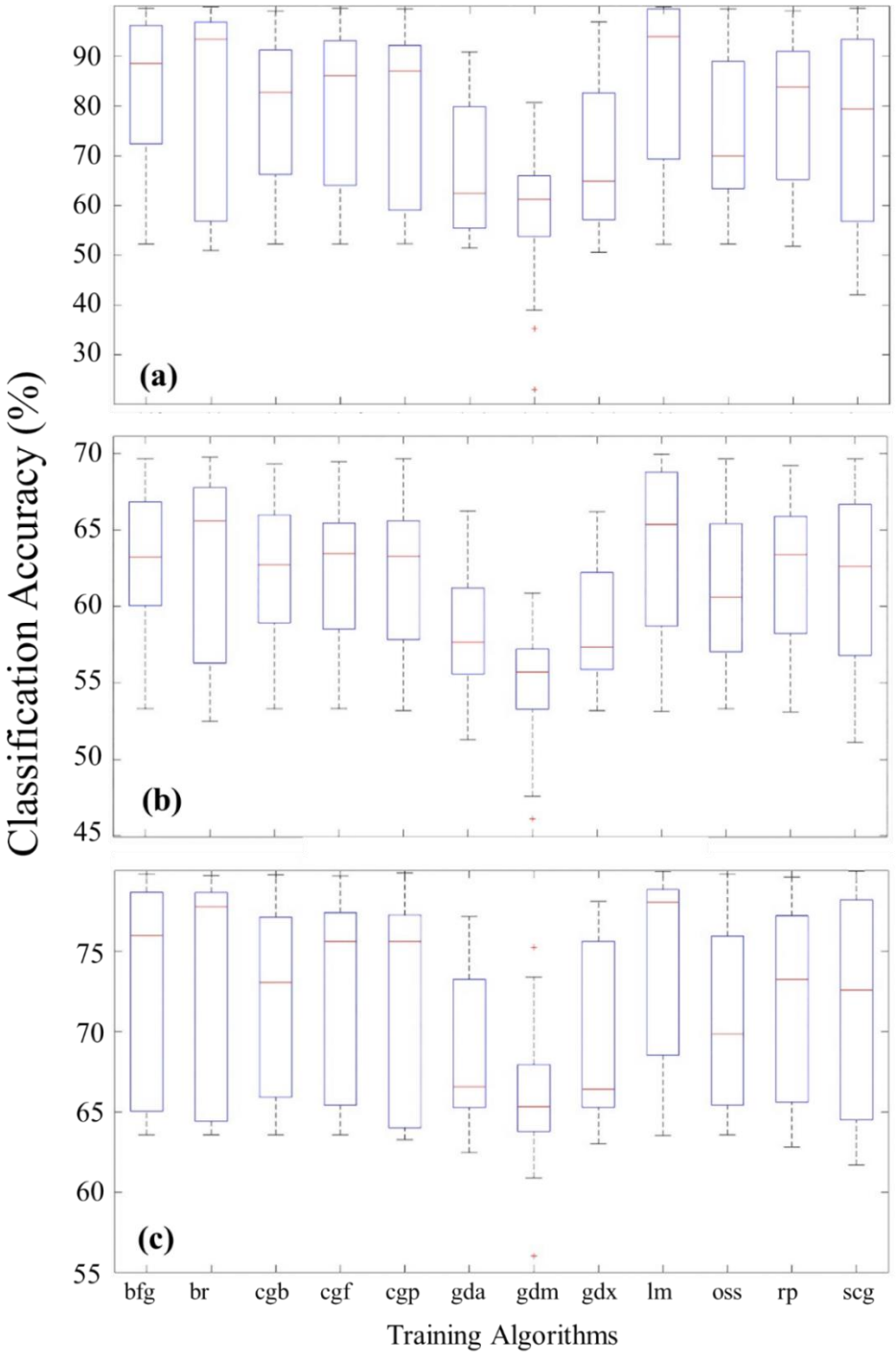

Fig. 3.7: Box plot of overall prediction accuracy of ANN models for different training algorithms in (a) Training Dataset, (b) Validation Dataset and (iii) Testing Dataset for land use classification

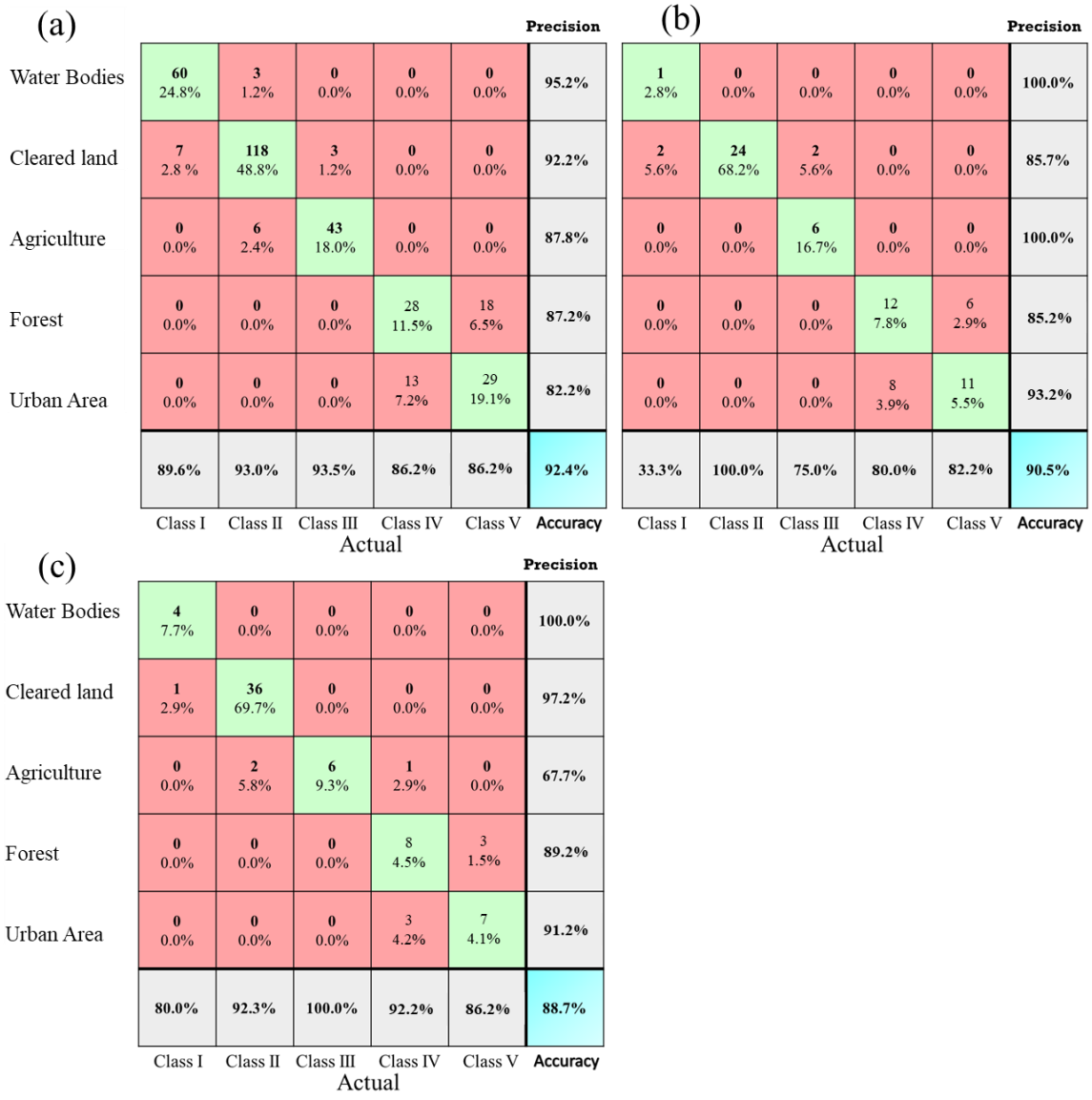

Fig. 3.8: Confusion matrix of optimized ANN model for (a) Training Dataset, (b) Validation Dataset and (c) Testing Dataset on land use classification

Table 3.3: Summary of ANN model performance with its optimized hidden neuron number for different training algorithms for land use classification

Training Algorithm	Optimum hidden neuron	Accuracy		
		Training	Validation	Testing
trainlm	11	85.91	84.13	84.96
traingdm	13	86.79	80.95	76.69
traingda	14	88.68	92.06	87.21
traingdx	6	84.91	77.78	76.69
trainrp	7	86.79	85.71	87.22
traincgb	12	90.57	80.95	87.22
traincgp	19	86.93	82.54	84.96
trainscg	10	92.45	77.78	83.46

3.2.1.2 Hyperparameter Optimization SVM

Numerous studies have reported that kernel parameter can implicitly affect the generalisation ability in the feature space, which can cause overfitting or underfitting phenomenon (Abobakr Yahya *et al.*, 2019; Roushangar & Shahnazi 2020; Choubin *et al.*, 2018), similar to the ANN model. Thus, the structured trial-and-error approach was used to determine the optimum σ value that ranged at 0.1-10.0. For σ value ranges at 0.1-1.0 and 1.0-10.0, the increment had been 0.1 and 1.0, respectively.

The box plots of distribution and variation of SVM classification performance under varying membership functions and kernel parameters are presented in Fig. 3.9. In comparison to the ANN models, the variation in SVM models was smaller for both seasons, which signified insignificant effect of the σ value, as displayed in the ANN model. The average prediction accuracy in the testing dataset for all input combinations was 75.2 ± 6.6%. The

optimum σ values for training, validation, and testing datasets in 8 different membership functions are summarised in Table 3.4.

According to Table 3.4, the most suitable membership function for SVM model is trimf under σ value of 0.2 with accuracy scores of 86.7%, 82.1%, and 82.2% for training, testing, and validation datasets, respectively. Fig. 3.10 illustrates the confusion matrix of the optimised SVM model for. Similarly, the optimised SVM model for dry season displayed the capability to make high precision for urban, cleared land and water bodies, but the SVM model also insufficiently capture the complex relationship between agricultural and forest classification. This outcome is attributed to the main feature of SVM, which placed the optimal hyperplane among varied classes. The optimal hyperplane in SVM was biased and this led to low precision and sensitivity in prediction (Gupta & Richhariya, 2018; Richhariya & Tanveer, 2020).

Table 3.4: Summary of SVM model performance with its optimized kernel parameter for different membership functions for land use classification

Parameters	Optimum σ value	Accuracy		
		Training	Validation	Testing
TrapMF	0.2	84.96	83.37	80.21
TriMF	0.3	76.69	76.92	71.73
GaussMF	0.3	87.22	90.02	82.25
Gauss2MF	0.3	76.69	74.70	74.23
GbellMF	0.1	87.22	83.07	83.25
DsigMF	0.1	87.22	77.32	78.33
PsigMF	0.1	84.96	79.19	83.32
PiMF	0.3	83.46	74.53	76.65

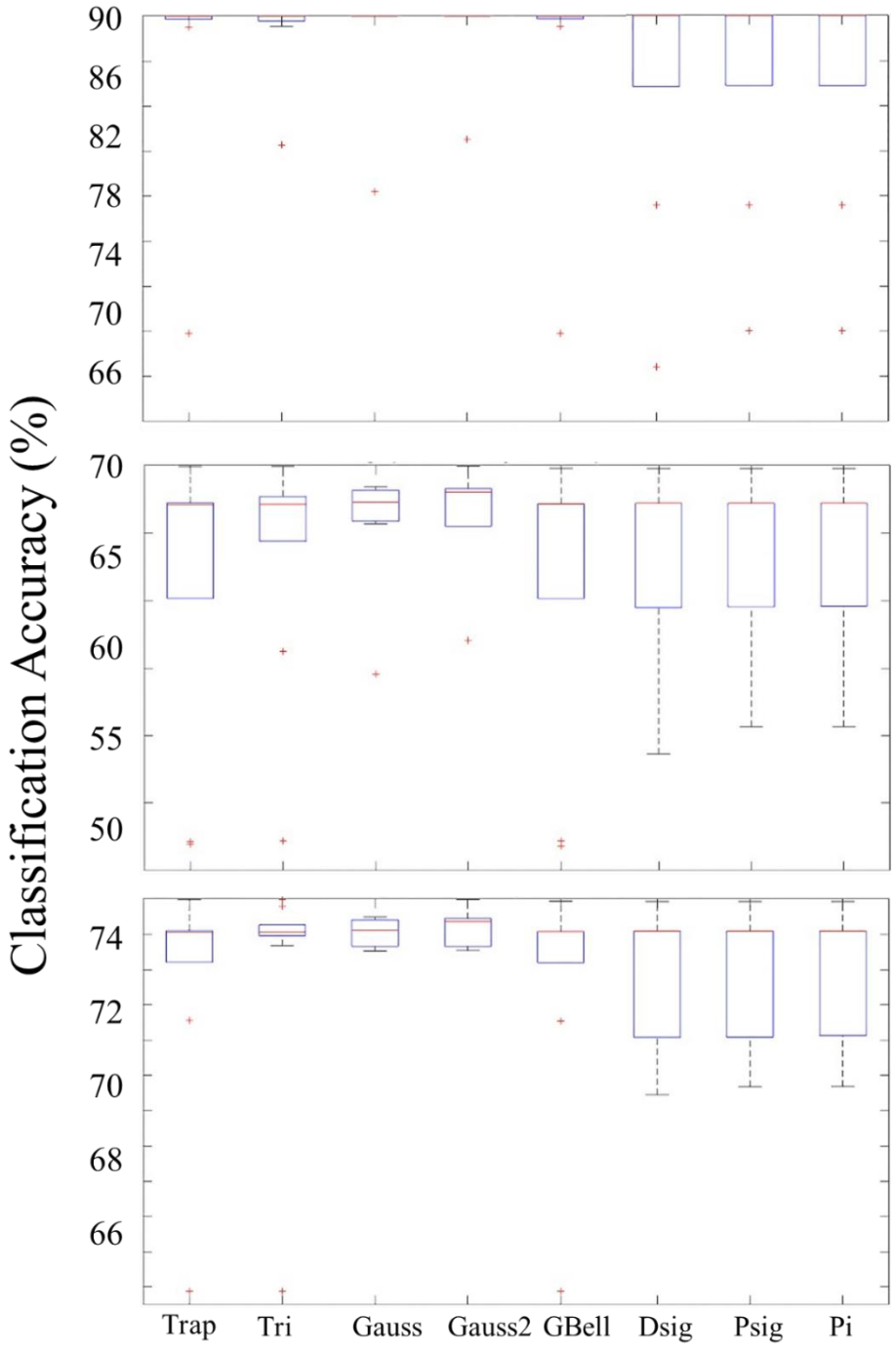

Fig. 3.9: Box plot of overall prediction accuracy of SVM models for different membership functions in (a) Training Dataset, (b) Validation Dataset and (iii) Testing Dataset for land use classification

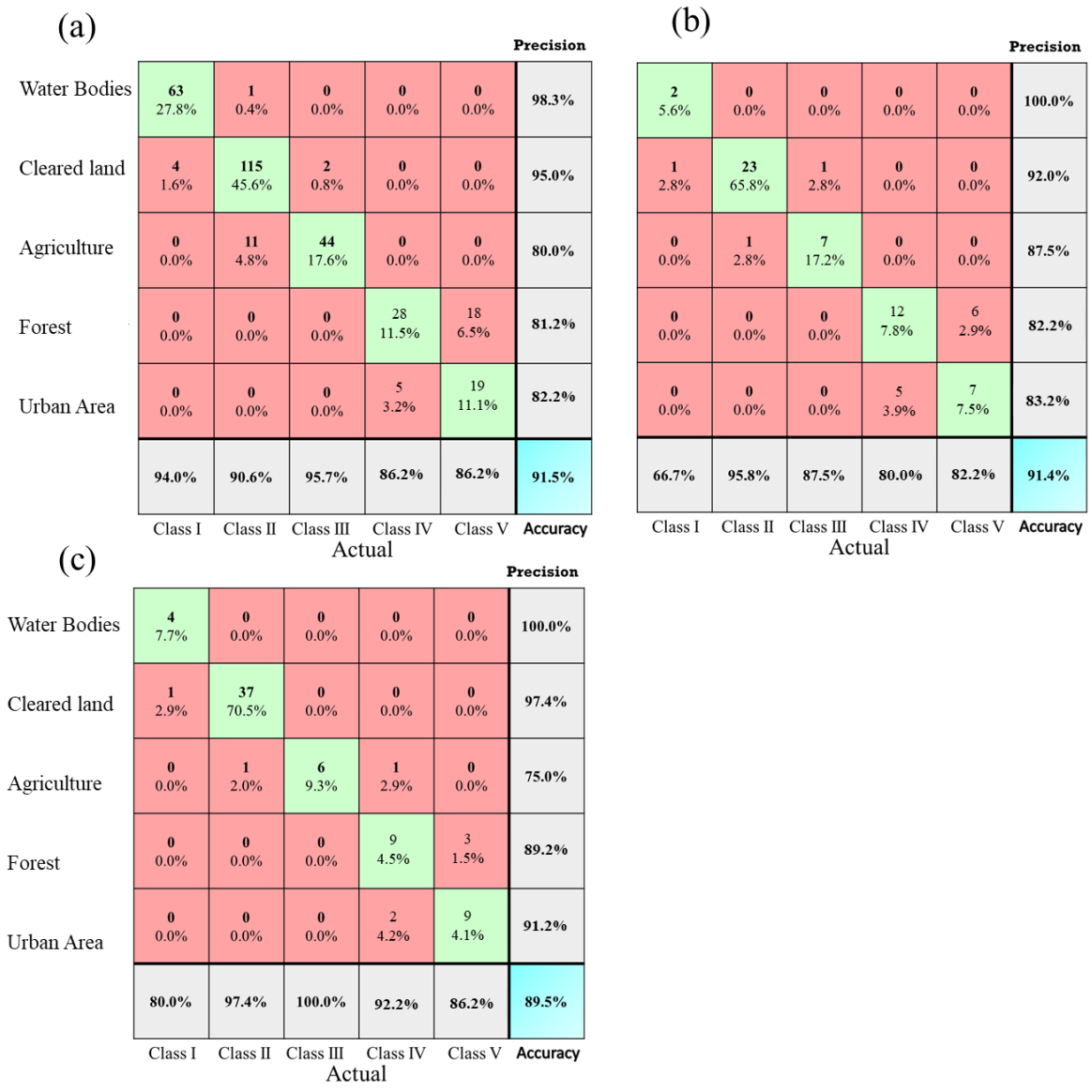

Fig. 3.10: Confusion matrix of optimized SVM model for (a) Training Dataset, (b) Validation Dataset and (c) Testing Dataset on land use classification

3.3.1.3 Comparison between ANN and SVM

Structurally, both SVM and ANN models appeared similar, as they applied linear learning models for classification. Both ANN and SVM models are data-driven models, indicating large volume of dataset is necessary for training and tuning the model. The models, nonetheless, differed in how the non-linear data were classified (Ren, 2012; Moraes *et al.*,

2013). In this study, the ANN model was trained with Levenberg-Marquardt training algorithm - a blend of gradient descent and Gauss-Newton method – to identify the local optimum of the solution (Lourakis, 2005; Cömert & Kocamaz, 2017). When the difference between actual solution and solution given by the model was small, it turned into the Gauss-Newton method; otherwise, Levenberg-Marquardt training algorithm behaved in the steepest descent method; slow but guaranteed to converge. Both weights and biases were adjusted by using the following expressions (Mustafa *et al.*, 2012):

$$w_{t+1} = w_t - \Delta w_t \tag{3.11}$$

$$\Delta w_t = [J^T(w_t)J(w_t) + \mu I]^{-1} J^T(w_t)e(w_t) \tag{3.12}$$

where w_t is the current weight vector; w_{t+1}denotes the updated weight vector; μ indicates the scalar regulation parameter dynamically adjusted during learning; I represents identity matrix; J refers to Jacobian matrix; and $e(w_t)$ signifies the matrix of error function evaluated at previous iteration.

One of the main issues of ANN model is that it suffers from multiple local minima, especially in a complex non-linear function that lowers the accuracy in prediction (Salkuti, 2018). In comparison to the ANN model, the SVM model can identify the global optimum of the solution, which is unique and appeared to be the smallest local optimum of the solution (Olson & Delen, 2008). The results obtained from optimised SVM models revealed that the sensitivity and precision for urban area, water bodies, cleared land were slightly higher than those recorded for optimised ANN models. As for Class agricultural and forest predictions, SVM displayed poorer prediction precision due to imbalanced dataset that further led to insufficient support vectors for placing an optimal hyperplane. The learning capacities in ANN models can extract the characteristics from the available data to generalise the testing data (Sari *et al.*, 2017); thus making the ANN model suitable for this application.

3.3.2 Land Use Change Analysis

In this section, the current land use change (1990-2016) and future land use change (2030 and 2050) will be discussed.

3.3.2.1 Current Land Use Change

The classified LULC maps of the study area for 1990 to 2016 were classified into five different land use classes, namely (i) water bodies, (ii) urban, (iii) cleared land, (iv) forest, (v) and agriculture. LULC changes were observed over the period of more than 3 decades, ranging from 1990 to 2000, and then to 2016. Agricultural, forest, and urban areas were found to be the major land use types that cover Selangor, Malaysia, as shown in Fig. 3.11. The distribution of total area covered by the different LULC classes and their percentage of cover in the years 1990, 2000, and 2016 is shown in Table 3.5. Agricultural areas experienced a rapid growth from 1990 to 2000, where it increased from 2921.91 km^2 to 3416.77 km^2 (35.8% to 41.9%). Between the years 2000 and 2016, agricultural areas experienced a slight growth with increment from 3416.77 km^2 in 2000 to 3512.24 km^2 in 2016. On the other hand, forest covers experienced a significant drop in percentage cover from 46.65% to 36.59% (3805.57 km^2 to 2985.31 km^2) between the years of 1990 and 2000. A steady decrease in forest covers continued in the years 2016 as the area covered was 2734.60 km^2 (33.52%). In contrast, developed areas experienced an exponential growth over the observed period. The developed area grew from 707.32 km^2 (8.67%) in 1990 to 1003.50 km^2 (12.30%) in 2000. Between the years 2000 and 2016, developed areas had a major expansion as the total area cover in the year 2016 increased to 1878.31 km^2 (23.02%).

The main factors related to the increasing development land use at the expense of deteriorating the forest and agricultural covers can be attributed to urban expansion and growth in commercial agricultural (Shawn *et al.*, 2020). The rapid urbanization has radically altered the natural environment and landscape patterns around the world, particularly in the 21st century (Tan *et al.*, 2020). The most important driving factors for urbanization are physical and social aspects, such as topography, population, and industrial growth (Aziz *et al.*, 2021). Consequently, urban expansion is influenced more by economic growth than by population increase.

It was noted from 1991–2001 that forest cover decreased dramatically in covered area, which was attributed to agricultural lands taking over forest lands. Due to this conversion, agricultural lands saw great expansion, accompanied by significant changes in barren lands. Minimal changes were observed in the land use classes of water bodies and cleared land. Water had marginal area changes, where an increasing trend was noted as the total area cover inflated from 99.14 km^2 in 1991 to 142.49 km^2 in 2016. These expansions raise concerns regarding the effects of urbanization and disruption of land use patterns, which have effects on climate change, food security, and natural resources. The results obtained from the LULC classification indicate that the changes in the land use patterns are supported by the polices of the state (Shawn *et al.*, 2020).

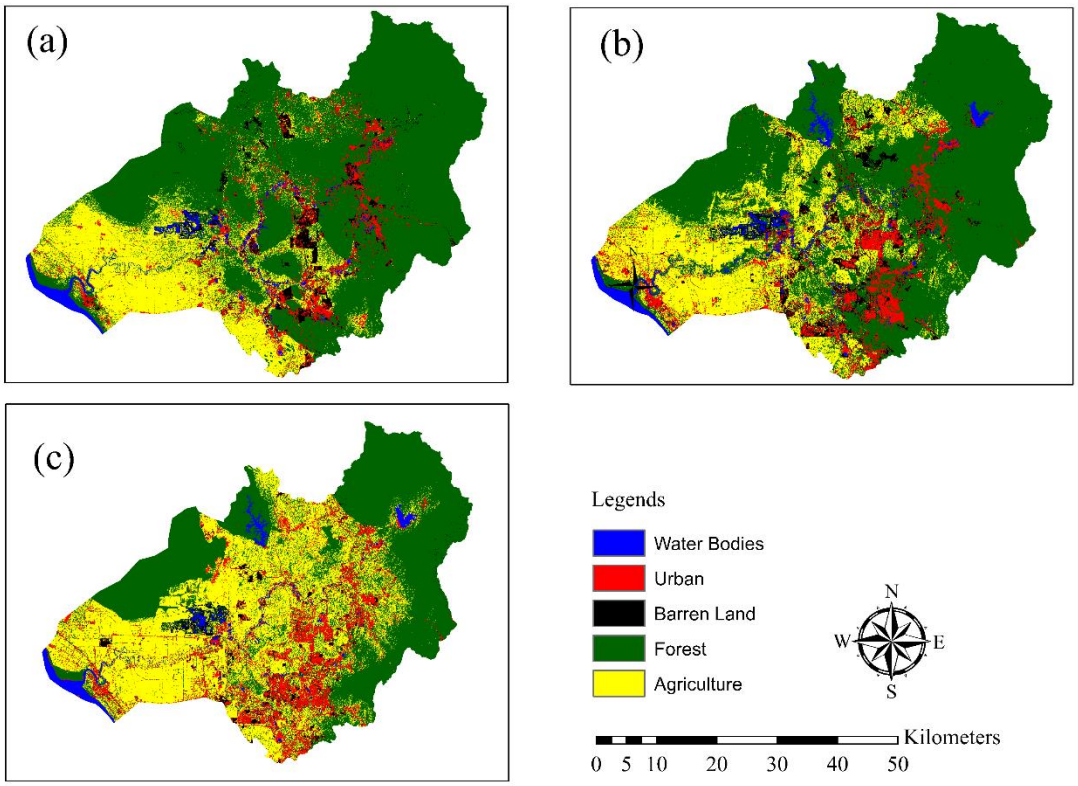

Fig. 3.11: Land use classification using optimized ANN model for (a) 1990, (b) 2000 and (c) 2016.

Table 3.5: Total land use area (km²) and percentage (%) in Selangor river basin for the year of 1990, 2000, and 2016

LULC Areas	Year-1990		Year- 2000		Year- 2016	
	Area (km^2)	Area (%)	Area (km^2)	Area (%)	Area (km^2)	Area (%)
Water Bodies	48.41	1.22	97.74	1.20	56.53	1.66
Cleared land	126.49	8.67	176.45	12.30	235.00	23.02
Agriculture	80.47	4.19	486.02	113.74	362.63	6.02
Forest	1,491.57	46.65	1,333.71	36.59	1,022.34	33.52
Urban Area	456.56	39.28	513.69	43.95	827.04	35.78
Total	**2,200**	100	**2,200**	100	**2,200**	100

3.3.2.1 Future Land Use Change

The transitional changes undergone by the different land use classes between the years 1990 and 2000 are expressed and calculated. These changes represent the distribution and conversion of individual land use class, as well as their nature of conversion. The major transitions are agriculture to developed, forest to agriculture, and barren to developed and agricultural lands. These trends of land conversion and transition forms the basis of transition potential modelling for CA-Markov model for simulating and predicting land use change in Selangor River basin simulation. A changes map was created using the transition matrix. The changes map of 2001–2011 and spatial parameters (slope, aspect, and distance form roads) were considered as input parameters for training the model.

The transition potential model of CA-Markov model was validated by comparing the classified land use map of 2016 with the simulated 2016 map. The comparison of the maps was evaluated based on the kappa coefficient value and percentage of correctness. The magnitude of correlation between the classified map and simulated map of 2021 is represented in the Table 3.6. The table illustrates the degree of agreement between the

different land use classes from the two maps. The classified and simulated land use classes are in relatively good agreement among each other, indicating that the land use pattern was simulated correctly, whereas deviance from the classified line denotes an inaccurate simulation of the land use pattern. The percentage of correctness for the simulation was 97.99%, with the overall kappa coefficient of 0.9585. Based in the validated model, the CA-Markov simulation was executed to obtain the predicted land use maps of the years 2030 and 2050.

Table 3.6: Accuracy Assessment for classified and simulated 2016 dataset

Overall Accuracy	93.9%
Kappa Coefficient	0.9585

Ground Truth (%)

Class	Urban-area	Forest	Cleared land	Water body	Agriculture	Total
Unclassified	0.00	0.00	0.00	0.00	0.00	0.00
Urban area	93.85	0.39	9.10	3.27	1.27	10.24
Forest	0.40	88.72	0.00	1.91	3.91	63.15
Cleared land	4.27	0.00	90.67	0.41	0.41	4.21
Water body	1.49	0.89	0.23	94.41	94.41	7.50
Agriculture	2.44	0.29	0.82	1.41	1.21	19.20
Total	100.00	100.00	100.00	100.00	100.00	100.00

The CA-Markov simulation was performed to obtain the predicted LULC maps for 2030 and 2050. Fig. 3.12 shows the predicted changes in different LULC classes from the years 2030 and 2050 in Selangor river basin. The observed outcomes elucidated the steady changes within the study period. A continued growth was noted in the developed land use pattern, where the area increased from 1,174.31 km^2 (35.23%) in 2030 to 1,492.40 km^2 (40.36%) in the 2050. Due to the increasing rate of area covered by developed land,

diminishing trends for forest and agricultural lands were observed in the simulated maps. Forest cover experiences a decline from 2536.46 km^2 (31.09%) in 2031 to 2,247.83 km^2 (30.01%) in 2050. Similarly, agricultural cover also maintains its decreasing trend between the years 2030 and 2050 as the total percentage cover regresses from 27.51% to 23.78%, respectively. Water, barren, and wetlands experience insignificant changes in their total area covered over the study period. Water cover reduced slightly as the areas decreased from 85.14 km^2 in 2030 to 81.80 km^2 in 2050. Similarly, barren lands reduced from 284.25 km^2 in 2030 to 266.75 km^2 in 2050.

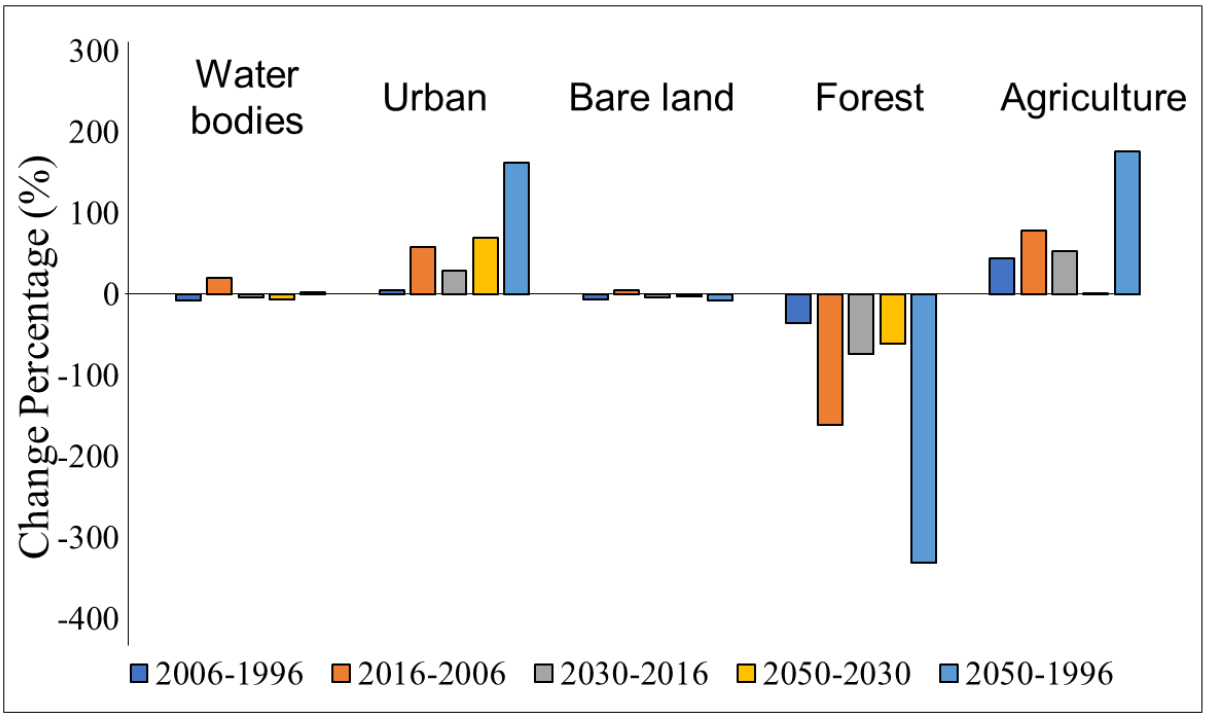

Fig. 3.12: Land use change percentage difference from 1990 to 2050 across five different land use categories

3.3.3 Future Streamflow Simulation

In this study, the observed streamflow in Selangor gauging station during period 2000–2018 was obtained from the Department of Irrigation, Malaysia. 2000 to 2010 was set as the warm-up period, while the period from 2011 to 2018 was chosen to be the calibration period. In validation period, CMADS (The China Assimilation Driving Datasets for the SWAT) also was applied to simulate the processes of streamflow. The comparison between the simulated streamflow and observations of gauging stations is shown in Fig. 3.13, which describes that the variations of simulated streamflow processes with the CMADS are closer to the actual streamflow processes, thereby validating the better applicability of CMADS for SWAT model for this region. The observed differences are partly due to the limited forcing meteorological data for the studied region. Certainly, the effectiveness of model simulation, regarding to the model structure and parameterizations, also affects the simulation accuracy. The fitness of SWAT model in study area can be quantified, as the value of R was within the range of 0.71 to 0.84, and NSE was above 0.7 at each gauging station, especially for the simulated results with the CMADS in the gauging station.

The land use changes for the historical period are examined in terms of both land use area and its structure based on the land use data in 1990, 2000, and 2016. AGRL stands for agricultural land; FRST for forest land; CLR for cleared land; WATR for water bodies; and URB for urban land. The main land cover types are forestry, farmland, and grassland. The land use transfer matrix obtained in section 3.3.2.1 and 3.3.2.2 are used for analyzing the historical changes of land use structure, which shows the dynamic transfer information for different time periods. The procedures of the establishment of land use transfer matrix include (1) to prepare the land use status map (SHP format) in 1990 and 2015 with Arc- GIS software, in which each map attribute table should have a field representing the land use type; (2) to use the solver tool in ArcGIS software to fuse the data; (3) the area is calculated and the attribute table is derived; and (4) to load the property sheet in Excel, and calculate the matrix automatically.

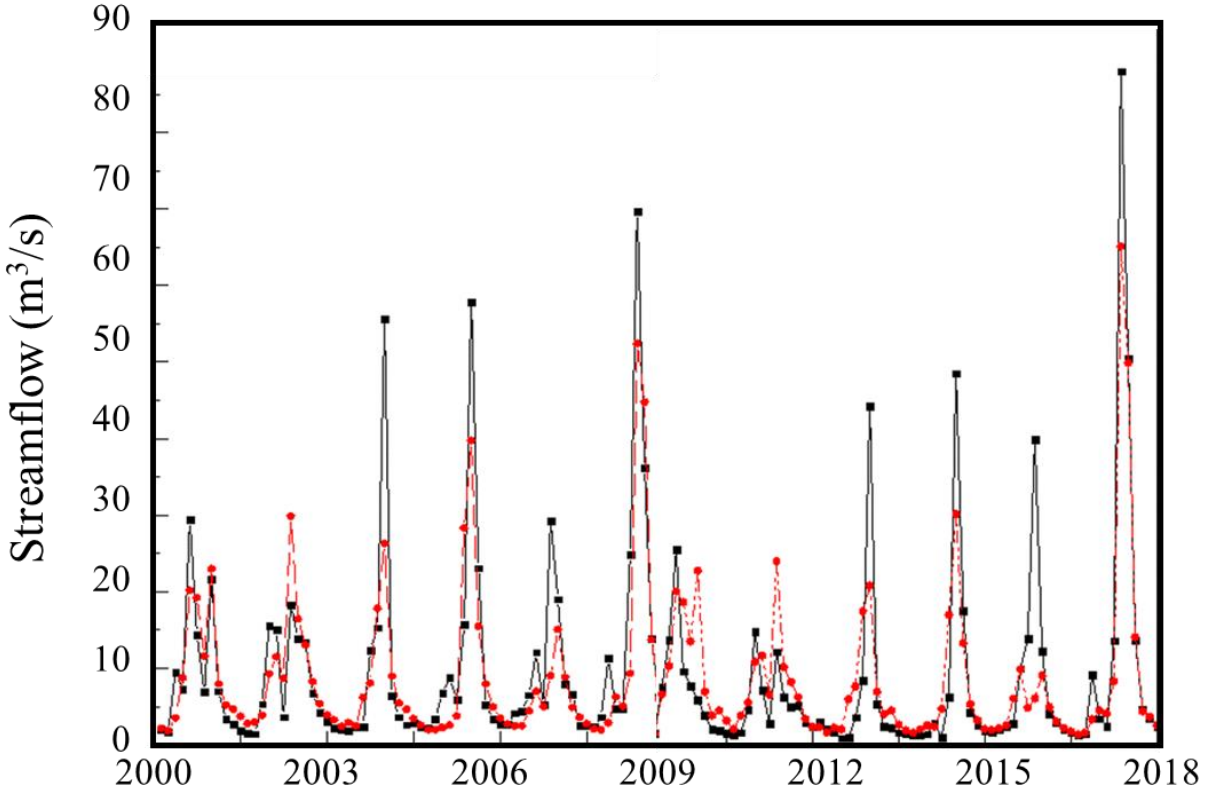

Fig. 3.13: Comparison between simulated and observed streamflow across 2000 to 2018.

As both climate change and land use/cover change will affect the regional runoff production, we studied the streamflow responses to the land use changes with the fixed meteorological forgings for the studied area. Among the 1088 mm (the long-term annual average for the period of 2000–2018) precipitation in Selangor river basin, the annual average evapotranspiration and annual average runoff are about 530 mm and 392 mm, respectively. Then, the streamflow using calibrated model was simulated with the different land use data. Compared to the situation in 1990, as shown in Fig. 3.14, the streamflow in 2030 and 2050 is decreased by 7.4% when urban area is increased by 3.59%, agricultural increased by 3.44%, and forest decreased by 3.44%. Meanwhile, as the studied area is dominated by forestry, the slight changes of the forestry area will not show obvious streamflow changes. Accordingly, the main driver for the streamflow reduction is the reductions of forest and agricultural area, and the increase of urban areas have shown to may slightly increase the streamflow.

For monthly simulation, it could be observed that the future variation of streamflow for 2050 is very dynamic, ranging very high flow rate up to 0 m^3/s to 90 m^3/s, indicating the importance of water usage and irrigation management. It could be observed that the variation during the dry season (June to September) are frequently facing low or no streamflow. This phenomenon has been alarming the community in this region as prolonged dry season might be occurring. Therefore, the application of hydrological model (*i.e.*, the SWAT model here) facilitates to examine the streamflow responses to land use changes, as it is possible land use change scenarios for the future. Although the past land use change had no significant impacts, the effects of future possible changes remain unfolded. The future land use changes (for example, the forestry is converted to agricultural or urban land) are possible with the local policy changes. This study provided some valuable information in this regard, which is very useful for designing future sustainable development strategies.

The obtained results on the streamflow responses to land use changes are basically consistent with the reported studies for other studied area. The high and low flow responses to the extreme land cover alterations are consistent with the study of Niu & Sivakumar (2014) for the Langat basin in Selangor. The urbanization increases the runoff generation, which is consistent with the study of Jatin *et al.*, (2018). Certainly, the magnitudes of these changes are different due to the different regional climate, geographical features, and local land surface backgrounds, which also highlight the importance of the regional study for local water resources' management.

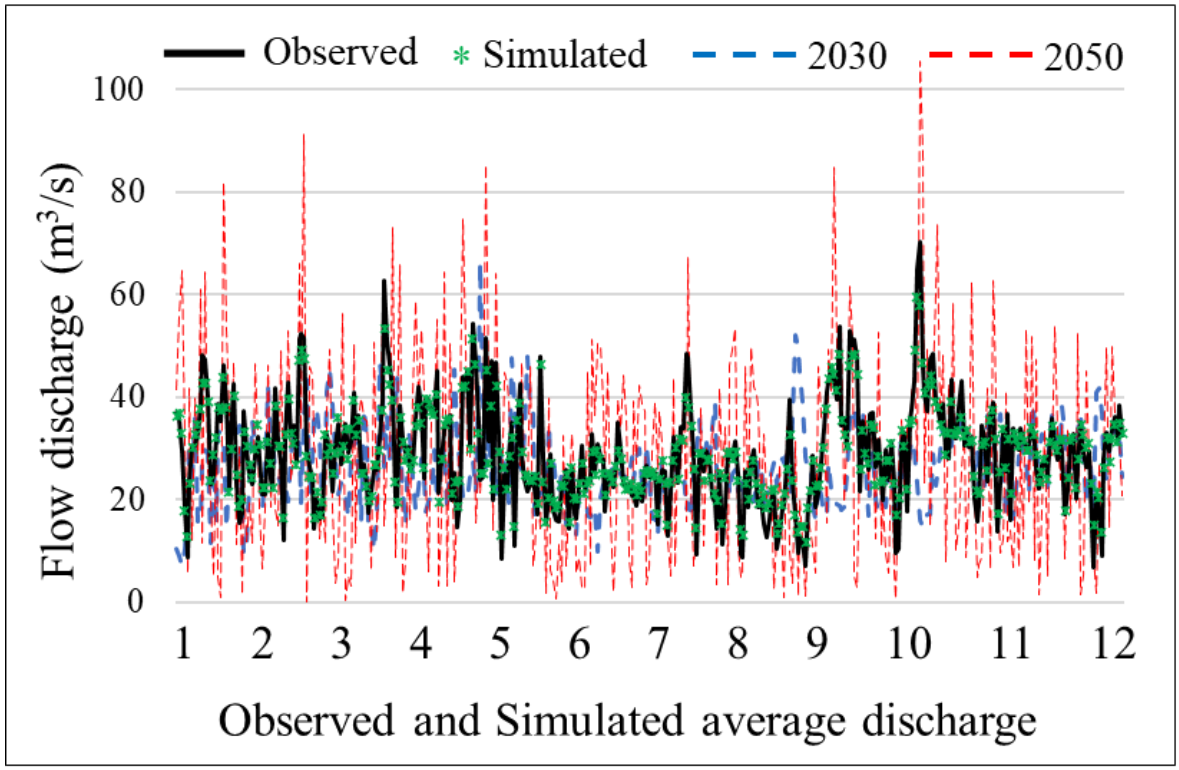

Fig. 3.14: Monthly streamflow simulation for 2030 and 2050 compared the overall observed and simulated dataset.

3.4 Conclusions

In this chapter, the future streamflow utilizing the application of remote sensing and artificial intelligence techniques for detecting the LULC changes is performed using SWAT model. To address the current research gap on identifying the land use from satellite using artificial intelligence methods, a systematic trial-and-error approach was adopted to optimize the network structure for both ANN and SVM models. LCM in Terrset was used to simulate the BAU future land use change in 2030 and 2050 by capturing the present land use changes observed from 1990 to 2016.

It could be observed that network optimization played an important role in improving the prediction accuracy of the land use type classification from satellite images. Compared to ANN, SVM has lesser sensitivity on the hyperparameter, but higher variation is observed across different training algorithms/membership functions. This is mainly due to SVM is

rule-based algorithm where the characteristics among parameters must be well understood before making the predictions. Therefore, in this study, ANN might be more suitable for predicting the land use type from the satellite images.

For future land use simulation, the prediction accuracy for utilizing the present land use maps (1990 and 2000) to simulate 2016 land use maps could reach up to 97%, indicating the accuracy of the LCM. The forestry in the region experienced drastic loss up to 300% in 2050 as compared to 1990, and the urban area expanded up to 200% over 60 years. The simulated land use is used to simulate the future streamflow. Extreme streamflow such as no flow rate or very high flow rate up to 100 m^3/s is more commonly encountered in the future. Through the simulation, it is important to have proper management for water resources to prevent prolonged drought or extreme rainfall induced flood events. Based on the findings, valuable information on designing future sustainable urban development strategies can be provided.

References

Abbasi, T., & Abbasi, S. A. (2012). *Water Quality Indices*: Elsevier Science.

Akkoyunlu, A., & Akiner, M. E. (2012). Pollution evaluation in streams using water quality indices: A case study from Turkey's Sapanca Lake Basin. *Ecological Indicators, 18*, 501-511, doi:10.1016/j.ecolind.2011.12.018.

Ali, Z. M., Ibrahim, N. A., Mengersen, K., Shitan, M., & Juahir, H. Robust principal component analysis in water quality index development. In *AIP Conference Proceedings, 2014* (Vol. 1602, pp. 1091-1097, Vol. 1): AIP

Alves, M. T. R., Teresa, F. B., & Nabout, J. C. (2014). A global scientific literature of research on water quality indices: trends, biases and future directions. *Acta Limnologica Brasiliensia, 26*(3), 245-253.

Aqeel Ashraf, M., Maah, M., Yusoff, I., Wajid, A., & Mahmood, K. (2011). Sand Mining Effects, Causes and Concerns: A Case Study from Bestari Jaya, Selangor, Peninsular Malaysia. *Scientific Research and Essays, 6*(6), 16, doi:10.5897/SRE10.690

ASEAN Secretariat (2017). Fifth ASEAN State of the Environment Report. Jakarta: Association of Southeast Asian Nations (ASEAN).

ASEAN Working Group on Water Resources Management (2012). ASEAN Water Data Management and Reporting System. http://rhn.water.gov.my/awgwrm/.

Basheer, A. O., Hanafiah, M. M., & Abdulhasan, M. J. (2017). A study on water quality from Langat River, Selangor. *Acta Scientifica Malaysia*, *1*(2), 4.

Bassi, N., & Kumar, M. D. (2017). Water quality index as a tool for wetland restoration. *Water Policy*, wp2017099.

Bharti, N., & Katyal, D. (2011). *Water Quality Indices Used for Surface Water Vulnerability Assessment* (Vol. 2).

Brown, R. M., McClelland, N. I., Deininger, R. A., & Tozer, R. G. (1970). A WATER QUALITY INDEX- DO WE DARE.

CCME (2001). Canadian water quality guidelines for the protection of aquatic life: CCME Water Quality Index 1.0 Technical Report *Canadian Environmental Quality Guidelines, 1999*. Winnipeg: Canadian Council of Ministers of the Environment.

Chowdhury, M. S., Othman, F., W.Z, W., Adham, M., & Ema, N. (2018). Assessment of Pollution and Improvement Measure of Water Quality Parameters using Scenarios

Modeling for Sungai Selangor Basin. *Sains Malaysiana, 47*, doi:10.17576/jsm-2018-4703-05.

Corcoran, E., Nellemann, C., Baker, E., Bos, R., Osborn, D., & Savelli, H. (2010). Sick Water? The central role of wastewater management in sustainable development. *A Rapid Response Assessment*: United Nations Environment Programme, UN-HABITAT, GRID-Arendal.

Cude, C. G. (2001). Oregon Water Quality Index a Tool for Evaluating Water Quality Management Effectiveness. *American Water Resources Association, 37*(1), 125-137, doi:doi:10.1111/j.1752-1688.2001.tb05480.x.

Department of Statistic (2016). Current Population Estimates, Malaysia, 2014-2016.

Dezfooli, D., Hosseini-Moghari, S.-M., Ebrahimi, K., Araghinejad, S. J. M. E. S., & Environment (2018). Classification of water quality status based on minimum quality parameters: application of machine learning techniques. [journal article]. *4*(1), 311-324, doi:10.1007/s40808-017-0406-9.

Dunnette, D. A. (1979). A Geographically Variable Water Quality Index Used in Oregon. *Journal of the Water Pollution Control Federation, 51*, 53-61.

Elmore, H., & Hayes, T. Solubility of atmospheric oxygen in water. In *Proc. Am. Sot. Civil Engrs, 1960* (Vol. 86, pp. 41-53)

Faridah Othman, M., Chowdhury, S., & Sakai, N. (2014). Assessment of microorganism pollution of Selangor River, Malaysia. *Advances in Agricultural & Environmental Engineering, 1*(2).

Fathi, E., Zamani-Ahmadmahmoodi, R., & Zare-Bidaki, R. J. A. W. S. (2018). Water quality evaluation using water quality index and multivariate methods, Beheshtabad River, Iran. [journal article]. *8*(7), 210, doi:10.1007/s13201-018-0859-7.

Fukushi, K., Kurisu, F., Oguma, K., Furumai, H., & Fontanos, P. (2010). *Southeast Asian Water Environment 4*: IWA Publishing.

Gholizadeh, M. H., Melesse, A. M., & Reddi, L. (2016). A Comprehensive Review on Water Quality Parameters Estimation Using Remote Sensing Techniques. *Sensors (Basel, Switzerland), 16*(8), 1298, doi:10.3390/s16081298.

Gorde, S., & Jadhav, M. (2013). Assessment of water quality parameters: a review. *J Journal of Engineering Research Applications, 3*(6), 2029-2035.

Gupta, A. (1996). Erosion and sediment yield in Southeast Asia: a regional perspective. *IAHS Publications-Series of Proceedings Reports-Intern Assoc Hydrological Sciences, 236*, 215-222.

Horton, R. K. (1965). An index number system for rating water quality. *Journal of Water Pollution Control Federation, 37*(3), 300-306.

Jing, C., Jianmin, Z., Zhongyu, W., Xiaohong, L., & Xiaolan, Z. (2007). *Application of grey relational analysis in water quality evaluation* (Vol. 19).

Kannel, P. R., Lee, S., Kanel, S. R., Khan, S. P., & Lee, Y.-S. (2007). Spatial–temporal variation and comparative assessment of water qualities of urban river system: a case study of the river Bagmati (Nepal). [journal article]. *Environmental Monitoring and Assessment, 129*(1), 433-459, doi:10.1007/s10661-006-9375-6.

Khan, F., Husain, T., & Lumb, A. (2003). Water Quality Evaluation and Trend Analysis in Selected Watersheds of the Atlantic Region of Canada. [journal article]. *Environmental Monitoring Assessment, 88*(1), 221-248, doi:10.1023/a:1025573108513.

Khanna, D., Bhutiani, R., Tyagi, B., Tyagi, P. K., & Ruhela, M. (2013). Determination of water quality index for the evaluation of surface water quality for drinking purpose. *International journal of Science and Engineering, 1*(1).

Khuong, P. M., McKenna, R., & Fichtner, W. (2019). Analyzing drivers of renewable energy development in Southeast Asia countries with correlation and decomposition methods. *Journal of Cleaner Production, 213*, 710-722, doi:10.1016/j.jclepro.2018.12.192.

Koh, K.-L. (2009). ASEAN Environmental Law, Policy, and Governance. World Scientific.

Koklu, R., Sengorur, B., & Topal, B. (2010). Water Quality Assessment Using Multivariate Statistical Methods—A Case Study: Melen River System (Turkey). [journal article]. *Water Resources Management, 24*(5), 959-978, doi:10.1007/s11269-009-9481-7.

Letchumanan, R. (2010). Climate change: is Southeast Asia up to the challenge?: is there an ASEAN policy on climate change? London, UK: LSE IDEAS, London School of Economics and Political Science.

Li, R., Dong, M., Zhao, Y., Zhang, L., Cui, Q., & He, W. (2007). Assessment of water quality and identification of pollution sources of plateau lakes in Yunnan (China). *Environmental Quality, 36*(1), 291-297.

Lumb, A., C. Sharma, T., & Bibeault, J.-F. (2011). *A Review of Genesis and Evolution of Water Quality Index (WQI) and Some Future Directions* (Vol. 3).

Magyar, N., Hatvani, I. G., Székely, I. K., Herzig, A., Dinka, M., & Kovács, J. (2013). Application of multivariate statistical methods in determining spatial changes in water quality in the Austrian part of Neusiedler See. *Ecological Engineering*, *55*, 82-92, doi:10.1016/j.ecoleng.2013.02.005.

Mahazar, A., Shuhaimi-Othman, M., Kutty, A., & Desa, M. (2013). Monitoring Urban River Water Quality Using Macroinvertebrate and Physico-Chemical Parameters: Case study of Penchala River, Malaysia. *Journal of Biological Sciences, 13*, doi:10.3923/jbs.2013.474.482.

Ministry of Environment and Forestry (2001). Government Regulation No. 82: Water Quality Management and Water Pollution Control

Ministry of Environment and Forestry (2003). Guidelines for Determination of Water Quality Status. In Ministry of Environment and Forestry (Ed.). Indonesia.

Ministry of Natural Resources and Environment (2011). Guidelines and Handbook for Calculation of Water Quality Index. Hanoi, Vietnam.

Mohamad, J., & Goh, H. C. (2015). *Land Use Dynamics and Governance in the Sungai Selangor Watershed*: University of Malaya Press.

Mohamed, I., Othman, F., Ibrahim, A. I. N., Alaa-Eldin, M. E., & Yunus, R. M. (2014). Assessment of water quality parameters using multivariate analysis for Klang River basin, Malaysia. [journal article]. *Environmental Monitoring and Assessment, 187*(1), 4182, doi:10.1007/s10661-014-4182-y.

Mohd Ali, Z., Ibrahim, N. A., Mengersen, K., Shitan, M., & Juahir, H. The Langat River water quality index based on principal component analysis. In *AIP Conference Proceedings, 2013* (Vol. 1522, pp. 1322-1336, Vol. 1): AIP

Nada, B., & Kirton, L. (2004). The secret life of fireflies. *IRBM Updates, 3*(December 2004), 2-4.

Nemerow, N., & Sumitomo, H. (1970). Benefits of water quality enhancement. New York: Syracuse University, .

Noori, R., Berndtsson, R., Hosseinzadeh, M., Adamowski, J. F., & Abyaneh, M. R. (2019). A critical review on the application of the National Sanitation Foundation Water

Quality Index. *Environmental Pollution, 244*, 575-587, doi:10.1016/j.envpol.2018.10.076.

Ogwueleka, T. C. (2015). Use of multivariate statistical techniques for the evaluation of temporal and spatial variations in water quality of the Kaduna River, Nigeria. [journal article]. *Environmental Monitoring and Assessment, 187*(3), 137, doi:10.1007/s10661-015-4354-4.

Othman, F., Chowdhury, M. S., Sakai, N., Shaaban, M., & Shimizu, Y. (2014). *Identification of pollution loading in a tropical river basin: A case study of Selangor River, Malaysia.* Paper presented at the International Conference on Environmental Science and Biological Engineering Beijing, China,

Pham, H., Rahman, M. M., Nguyen, N. C., Vo, P., Le Van, T., & Ngo, H. (2017). *Assessment of Surface Water Quality Using the Water Quality Index and Multivariate Statistical Techniques-A Case Study: The Upper Part of Dong Nai River Basin, Vietnam* (Vol. 7).

Pollution Control Department (2016). Water Quality Index Calculation- Manual.

Rohmad Barokah, G., Ariyani, F., & Siregar, T. (2017). Comparison of Storet and Pollution Index Method to Assess the Environmental Pollution Status: A Case Study from Lampung Bay, Indonesia. *Squalen Bulletin of Marine and Fisheries Postharvest and Biotechnology, 12*, 67-74, doi:10.15578/squalen.v12i2.287.

Saraswati, S., Sunyoto, B. A. K., & BA, H. (2014). Assessment of the Forms and Sensitivity of the Index Formula PI, Storet, CCME for the Determination of Water Quality Status of A Tropical Stream in Indonesia. *Human and Environmental, 21*, 129-142.

Selvam, S., Manimaran, G., Sivasubramanian, P., Balasubramanian, N., & Seshunarayana, T. J. E. E. S. (2014). GIS-based Evaluation of Water Quality Index of groundwater resources around Tuticorin coastal city, south India. [journal article]. *71*(6), 2847-2867, doi:10.1007/s12665-013-2662-y.

Singh, R. P., Nath, S., Prasad, S. C., & Nema, A. K. (2008). Selection of suitable aggregation function for estimation of aggregate pollution index for river Ganges in India. *Environmental Engineering, 134*(8), 689-701.

Subramaniam, V. (2004). Managing water supply in Selangor and Kuala Lumpur. *Buletin Ingenieur, 22*, 9.

Sutadian, A. D., Muttil, N., Yilmaz, A. G., & Perera, B. (2016). Development of river water quality indices—a review. *Environmental Monitoring Assessment, 188*(1), 58.

Suwandana, E., Kawamura, K., Tanaka, K., Sakuno, Y., & Raharjo, P. (2011). Escherichia coli and biophysicochemical relationships of seawater and water pollution index in the Jakarta Bay. *American Journal of Environmental Sciences, 7*(3), 12.

Tripathi, M., & Singal, S. K. (2019). Use of Principal Component Analysis for parameter selection for development of a novel Water Quality Index: A case study of river Ganga India. *Ecological Indicators, 96*, 430-436, doi:10.1016/j.ecolind.2018.09.025.

Tyagi, S., Sharma, B., Singh, P., & Dobhal, R. (2013). Water Quality Assessment in Terms of Water Quality Index. *American Journal of Water Resources, 1*(3), 34-38.

WWAP (United Nations World Water Assessment Programme) (2015). The United Nations World Water Development Report 2015: Water for a Sustainable World. Paris,UNESCO.

Xu, G., Jiao, L., Liu, J., Shi, Z., Zeng, C., & Liu, Y. (2019). Understanding urban expansion combining macro patterns and micro dynamics in three Southeast Asian megacities. *Science of The Total Environment, 660*, 375-383, doi:10.1016/j.scitotenv.2019.01.039.

Zhila, H., Mahmood, H., & Rozainah, M. Z. (2014). Biodiversity and biomass of a natural and degraded mangrove forest of Peninsular Malaysia. [journal article]. *J Environmental Earth Sciences, 71*(11), 4629-4635, doi:10.1007/s12665-013-2853-6.

Zhu, C., & Hao, Z. (2009). *Application of Grey Relation Analysis in Evaluation of Water Quality*.

Chapter 4

Climate Change impacts on Extreme Floods across Taiwan River Basins using RRI model

In this chapter, the impacts of climate change on extreme floods across Taiwan river basins were studied using RRI model and super-high-resolution AGCM ensemble developed by the Meteorological Research Institute of the Japan Meteorological Agency version 3.2 (hereinafter referred to as MRI-AGCM3.2s). Prior to the RRI model construction, bias correction was performed on the climate products and the observed climate dataset. To verify the performance of the dataset, flow rate of river basins during three extreme flood events induced by typhoon was studied. Last but not least, the average annual peak discharge in future (2020-2040), mid future (2050-2070), and far future periods (2079-2099) were simulated using the super-high-resolution AGCM ensemble.

4.1 Introduction

Since 1970, the number of global disasters has increased fivefold, resulting in at least 2 million deaths and approximately 3.64 trillion USD economic losses (World Meteorological Organization, 2021). Among these, floods are regarded as the most recurrent and destructive disaster worldwide, accounting for 44% of all natural disasters (United Nations Office for Disaster Risk Reduction, 2020). Also, associated with the impact of anthropogenic climate change, the occurrence of extreme downpour and flooding has drastically increased and is expected to become more frequent, with intensified severity and prolonged duration, which may lead to unprecedented consequences in both economy and society (Hirabayashi *et al.*, 2021), particularly in Asia Pacific region (Hashim *et al.*, 2016). As with several other regions, Taiwan, a continental island in the Asia Pacific, located on the hub of seasonal typhoon route in the West Pacific Ocean and earthquake-prone circum-Pacific belt (Su *et al.*, 2017), was indicated as the most vulnerable area to natural hazards in the world (Arnold *et al.*, 2005), as more than 99% of its land and population are exposed to 2 or more hazards and is particularly susceptible to climate change (Lin *et al.*, 2017).

Over the past decade, the mean air temperature in Taiwan was observed to have increased twice (0.14 °C per decade) as much as the global mean warming rate per decade (°C per decade) (Hsu & Chen, 2002). This may have exacerbated the trend of heavy precipitation phenomenon (Tu & Chou, 2013), resulting in a significant impact on the hydrological system and inducing the occurrence of extreme floods in Taiwan (Chiang, 2018). The frequency of increased intensity of precipitation (>3,500 mm within 48h) (Lin *et al.*, 2018) has been gradually escalating (Yeh & Huang, 2019). In 2009, the flood induced by Typhoon Morakot with accumulated rainfall of 2,777 mm, one of the most catastrophic flooding, has caused nearly 700 deaths and direct loss of up to 4.7 billion USD (Chjeng *et al.*, 2009; Ge *et al.*, 2010). Although numerous flood risk management frameworks have been proposed and developed for minimizing the potential losses and ensuring public safety, for instance, identifying flood risk zone through flood inundation maps utilizing historical precipitation data (Chen *et al.*, 2011; Doong *et al.*, 2016); however, due to the complex and heterogeneous climate variability, the distribution and intensity of precipitation varied spatiotemporally, which has been supported by both historical observations and model simulations (Rajah *et al.*, 2014). Therefore, it is fundamental to develop robust and reliable future climate simulations to identify the future flow regime and allow decision-makers to formulate corresponding prevention policies for the emerging risk.

To simulate and access the impact of climate change on the hydrological system, the application of hydrological models with outputs of atmospheric general circulation models (AGCMs) (*e.g.*, mean surface temperature and precipitation) under the framework of different coupled model intercomparison projects (CMIPs), which are driven by different emission scenarios are commonly adopted (Usman *et al.*, 2021). The accuracy of the hydrological model simulations is highly dependent on the reliability of the dataset. However, most of the available AGCMs has coarse horizontal resolutions (approximately 100 to 400 km) to sufficiently describe the hydrological processes (*e.g.*, flow regime) at regional scales (Guo *et al.*, 2018; Sun *et al.*, 2016). Although different downscaling methods (*e.g.*, statistical and dynamic approach; Usman *et al.*, 2021) were proposed to acquire finer resolution climate simulations from coarse AGCMs, there exists a debate over the reliability and robustness of

the downscaled climate simulation continues, in part due to the underlying assumptions and limitations which may affect the conclusion drawn over the regional characteristics (Giorgi, 2019). With this backdrop, to address the aforementioned challenges, the development of high-resolution AGCM was ought to be a plausible solution for simulating reliable future climate simulation at the regional scale.

In recent, extensive research has been carried out in employing multi-AGCM ensemble techniques to enhance the model's resolution (Rahman *et al.* 2019). As reported by Duan & Phillips (2010), a multi-AGCM ensemble that adopts different physical parameterizations (*e.g.,* multiple cumulus convection schemes and different patterns of future seas surface temperature projections) has substantially surmounted the uncertainties and is capable to produce more reliable predictions (Ito *et al.,* 2020). Among these, super-high-resolution AGCM ensemble developed by the Meteorological Research Institute of the Japan Meteorological Agency version 3.2 (hereinafter referred to as MRI-AGCM3.2s) is regarded as the most widely adopted AGCM for regional climate simulation (Mizuta *et al.,* 2012). MRI-AGCM3.2s allows realistic simulations of regional climate without requiring dynamic/statistical downscaling due to their high spatial resolution (with a horizontal grid size of approximately 20 km and 60 vertical layers). MRI-AGCM3.2s outputs are generated based on representative concentration pathway (RCP) 8.5 (highest greenhouse gas emission pathway) introduced by Intergovernmental Panel on Climate Change (IPCC), such that the most extreme climate change scenario can be analyzed. As aforementioned, Taiwan is one of the most intense typhoon prone areas in the world (Lin & Chan, 2015); therefore climate data generated by MRI-AGCM3.2s which have successfully simulated the global distribution of typhoons as well as the seasonal march of East Asian Monsoons (Yoshida *et al.,* 2017) are particularly suitable for assessing climate change impacts in Taiwan.

At present, various conceptual-based and/or physically-based hydrological models have been developed, for instance, Soil and Water Assessment Tool, Hydrologiska Byrans Vattenavdelning, Variable Infiltration Capacity and Rainfall-Runoff-Inundation (RRI), to investigate the climate change impacts on hydrological processes of river basins. Among

them, the RRI model, an integrated two-dimensional grid cell-based hydrodynamic model for rainfall-runoff and inundation simulations from areas encompassing downstream flood plains and upstream mountain zones is selected in this research. RRI has been widely adopted and applied in different nations (*e.g.*, Thailand (Sayama *et al.,* 2017), Myanmar (Bhagabati & Kawasaki, 2017), Pakistan (Siddiqui *et al.,* 2018), Japan (Shakti *et al.,* 2020)) for various hydrological applications. The flow on the floodplain slope grid cell and channel flow are calculated independently, through 2D and 1D diffusive wave models, respectively. The complicated flow interactions between river channel and slope are computed through different overflowing formulae (refer to Sayama *et al.* (2012) for detailed explanation). On top of these, to better represent the RRI processes, lateral subsurface (particularly important for the mountainous region), vertical infiltration, and surface flows are also considered in the model, thereby increasing the reliability and accuracy of the simulation in Taiwan.

Although there has been ongoing research on the flood risk simulation utilizing climate data in Taiwan (Hsiao *et al.,* 2021; Hsu *et al.,* 2017b; Chang *et al.,* 2021), most of the research focused only on certain cities or regions and reported the extreme precipitation volume. As aforementioned, climate change impact may be varied across regions, therefore, it is crucial to identify the possible high-risk zones for decision-makers or relevant authorities to implement corresponding prevention measures to minimize the impacts. Indeed, identifying the future precipitation trend and its extreme volume is crucial for flood risk management, it is more important to understand the river flow discharge as the river channel geometries/characteristics vary locally, which will significantly alter the flood hazard across regions. Comprehensive studies detailing super-high-resolution climate data to understand the climate change impacts on extreme streamflow across Taiwan are lacking in the literature and considering possible devastating flood-related damage in the future, it is crucial to understand its hydrological changes. In light of these, the main research objectives of this research were (i) to evaluate and verify the reliability of the developed RRI model by comparing peak discharge during severe flood events across Taiwan; (ii) to improve MRI-AGCM 3.2s simulated climate data through bias-correction method using observed data; (iii) to simulate spatial distribution of the ratio of changes in average annual peak discharge for

near-future (2020-2040), mid-future (2050-2070) and far-future (2080-2100) scenarios. To the best of authors knowledge, this is the first research conducted to simulate future extreme flood events utilizing a super-high resolution AGCM dataset using the RRI model. The findings of this research are expected to provide compendious information, including practical implications, to relevant authorities for policy planning and implementation for better water resources and risk management according to regions.

4.2 Data Collection and Methodology

4.2.1 Research area

Taiwan is a densely populated island, with 23.8 million people spread across a total land area of approximately 36,000 km^2 in Eastern Asia, on the west edge of the Pacific Ocean. As Taiwan is situated at the transition between tropical and temperate latitudes (21.5 – 25.2 °N and 120.0 – 122.0 °E), its climate is strongly influenced by the East Asian Monsoons (southwesterly monsoon during the wet-warm season (May–August) and northeasterly monsoon during the dry-cold season (September–April) (Henny *et al.*, 2021).

The mean annual temperature for the subtropical region is about 23.4 ºC (highest: 35.8 ºC and lowest: 7.4 ºC) whereas for the tropical region is about 25.4 ºC (highest: 35.0 ºC and lowest: 9.3ºC) (Chen *et al.*, 2010). Approximately 90% of the total precipitation (~ 2,000 mm) are contributed during the wet-warm season (Ding *et al.*, 2020) associated with the episodic typhoon impact (mid-July to August). The magnitude and scale of a typhoon hitting Taiwan have increased over the past decades (Hsu *et al.*, 2017a), bringing extremely heavy rain and strong wind, and might eventually cause disastrous flooding, particularly in the coastal area. The complicated and steep topography is also one of the key drivers that have substantially increased the total rainfall accumulation and affected its distribution over Taiwan, especially due to the north-south oriented Central Mountain Range (CMR) (Fig. 4.1). Lin *et al.* (2020) demonstrated the distribution of rainfall in Taiwan is strongly modulated by the topography of CMR due to orographic forcing over mountains, in which the southwest region receives a large amount of rain. Therefore, the inundation susceptibility varied across the region.

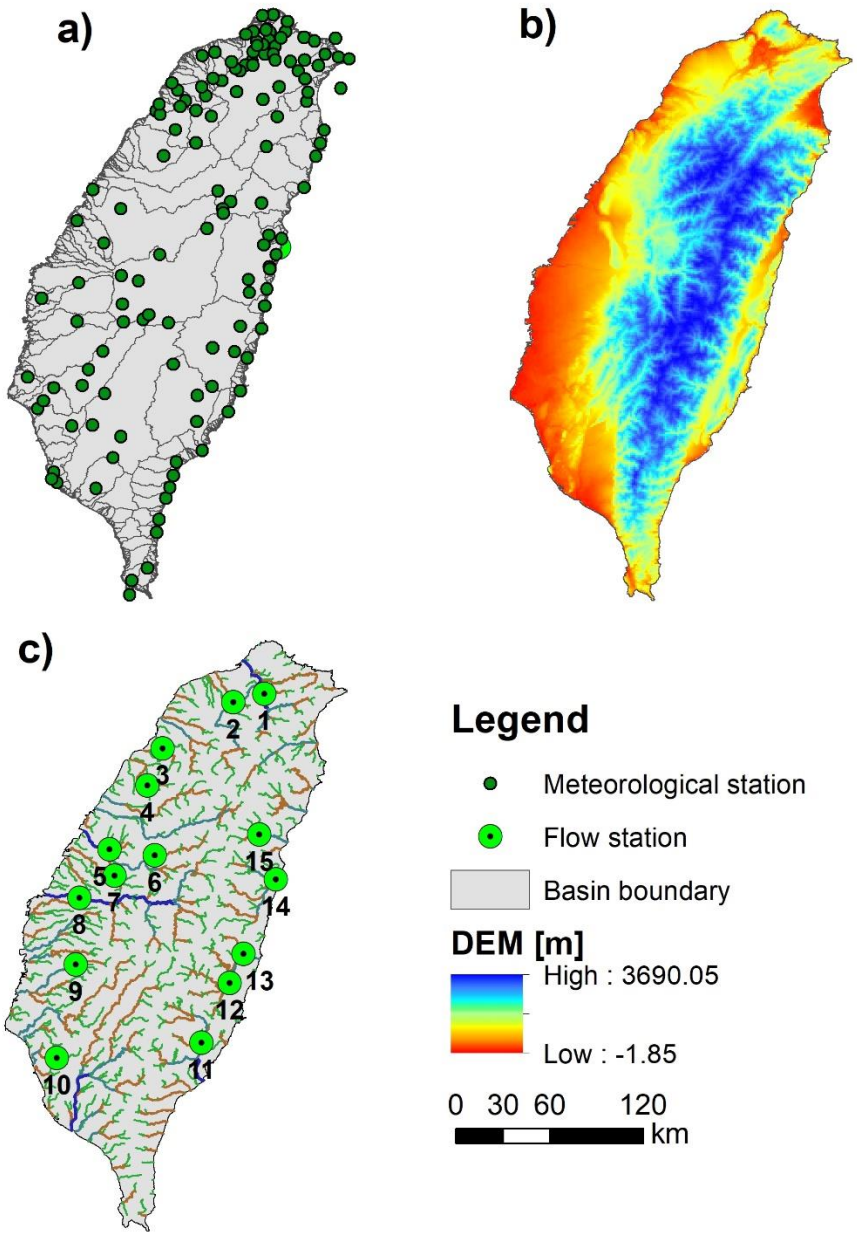

Fig. 4.1: Map of the research area: a) meteorological station, b) digital elevation model (DEM), and c) river flow station.

4.2.2 Model Development

4.2.2.1 Model Input

The methodology flowchart of the research is schematically illustrated in Fig. 4.2. To construct the model, rasterized topographic (river geometry and topological data) and meteorological (precipitation and evapotranspiration) data are required. Twenty-one years (2000-2020) of daily meteorological (n=143) and daily discharge stations (n=15) that located widespread across the region were acquired from Taiwan Central Weather Bureau and Water Resources Agency, respectively, to investigate and evaluate the impact of future extreme floods in Taiwan. Due to data unavailability, the surface evapotranspiration, ET_0 was calculated using the observed temperature and relative humidity, as shown in Eq. (4.1) (Schendel, 1967).

$$ET_0 = 16 \times \frac{T}{RH} \tag{4.1}$$

In Eq. (4.1), ET_0 is the evapotranspiration (mm/day), T is the daily average temperature, and RH is the relative humidity (%).

The 3-arc second (~90 m) resolution digital elevation model (DEM) was obtained from Multi-Error-Removed Improved-Terrain (MERIT) DEM (Yamazaki *et al.*, 2017), as it showed better performance in flood modelling (Hirt, 2018; McClean *et al.*, 2020) and has fewer artefacts (Chen *et al.*, 2018) as compared to other global DEMs (*e.g.*, Shuttle Radar Topography Mission DEM, Ordnance Survey Terrain 50 DEM and Advanced Land Observing Satellite DEM). Other topographic data including flow direction, flow accumulation and river networks were prepared using MERIT DEM using ArcHydro tools in ArcGIS 10.8.

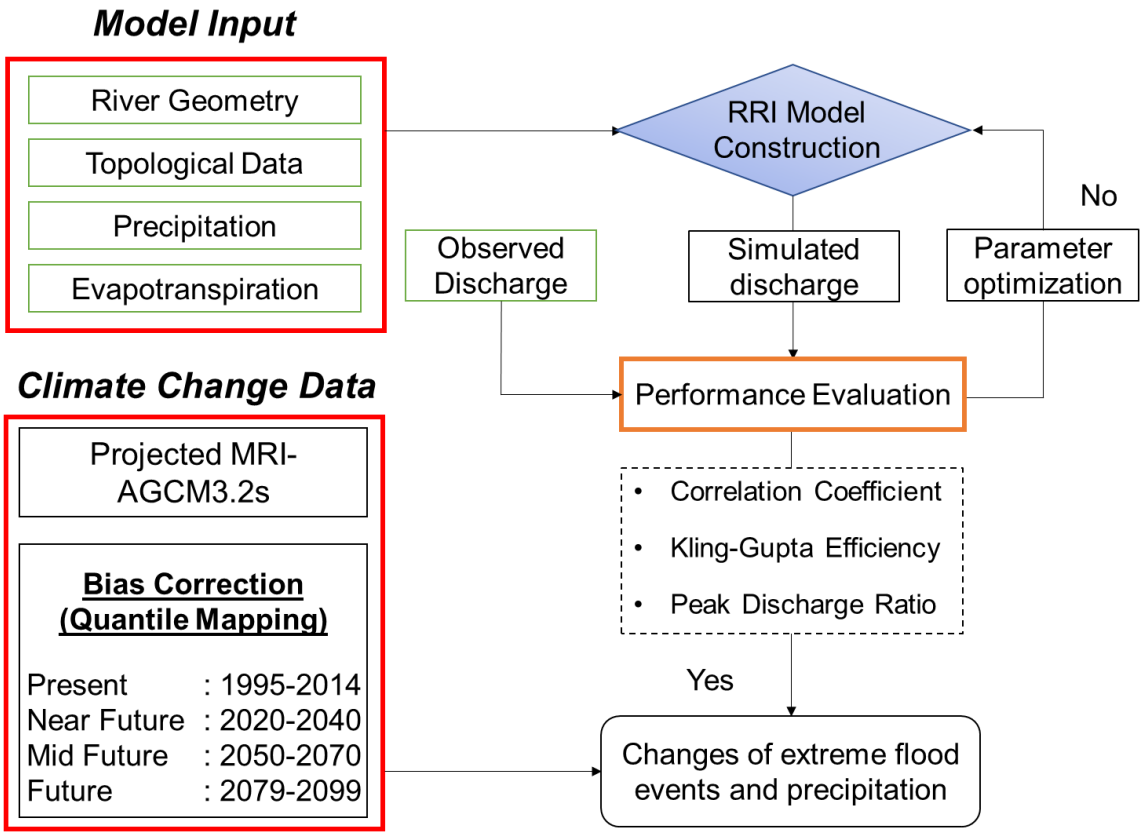

Fig. 4.2**:** Flowchart of modelling process used in this research

As there is no available surveyed data on river geometry, the river cross-sections of the research area were assumed as rectangular, wherein, the river width (W) and depth (D) in the function of upstream contributing area (A) are estimated using Eqs. (4.2) and (4.3).

$$W = C_W A^{S_W} \tag{4.2}$$

$$D = C_D A^{S_D} \tag{4.3}$$

In Eqs (4.2) and (4.3), $C_W = 5$, $C_D = 0.1$, $S_W = 0.1$, $S_D = 0.1$ represent geometry hyperparameters, and their coefficient are determined through a systematic trial-and-error approach.

4.2.2.2 Model Optimization and Performance Evaluation

To obtain the optimal RRI model structure for simulation, six out of nine tuning parameters of the RRI model were found to be sensitive for Taiwan, including Manning's

coefficient for the river (n_{river}), Manning's coefficient for slope (n_{slope}), Soil depth (d), Soil porosity (φ), Lateral saturated hydraulic conductivity (k_a) and unsaturated hydraulic conductivity (β). Optimization of these parameters is performed through systematic trial and error method and validated using five different scenarios; wherein, three of them are super typhoon events (i) Typhoon Morakot: Aug, 2-13, 2009, (ii) Typhoon Jangmi: Sep. 23, Oct. 5, 2008, (iii) Typhoon Nari: Sep. 5-21, 2001, and (iv) Long-term simulation: 2000-2020 across 15 discharge stations (Fig. 4.1(b)). The optimized and calibrated tuning parameters coefficient/values are summarized in Table 4.1.

Table 4.1: Optimized RRI model tuning parameters.

Parameter	Unit	Value
n_{river}	$m^{-1/3}/s$	0.06
n_{slope}	$m^{-1/3}/s$	0.60
d	m	4.00
φ	-	0.05
k_a	m/s	0.10
β	-	8.00

To evaluate the performance of model simulation, three performance indicators were applied, namely Kling-Gupta efficiency (KGE) (Gupta *et al.*, 2009), correlation coefficient (r) and peak discharge ratio (PDR), expressed mathematically as in Eqs. (4.4) to (4.6).

$$\text{KGE} = 1 - \sqrt{(r-1)^2 + (\beta-1)^2 + (\alpha-1)^2};\ \beta = \frac{\overline{Q_s}}{\overline{Q_o}},$$

$$\alpha = \frac{\sqrt{\frac{1}{n}\sum_{t=1}^{n}(Q_s^t - \overline{Q_s})^2}}{\sqrt{\frac{1}{n}\sum_{t=1}^{n}(Q_o^t - \overline{Q_o})^2}} \qquad (4.4)$$

$$r = \frac{\sum_{t=1}^{n}(Q_s^t - \overline{Q_s})(Q_o^t - \overline{Q_o})}{\sqrt{(\sum_{t=1}^{n}(Q_o^t - \overline{Q_o})^2)(\sum_{t=1}^{n}(Q_s^t - \overline{Q_s})^2)}} \quad (4.5)$$

$$\text{PDR} = \frac{Q_s^p}{Q_o^p} \quad (4.6)$$

In Eqs (4.4) to (4.6), Q_s^t and Q_o^t are simulated and observed discharge at time step t respectively; $\overline{Q_s}$ and $\overline{Q_o}$ are the mean simulated and observed discharge in the flood event; β and α are the measures of bias and variability; and Q_s^p and Q_o^p are simulated and observed peak discharge.

4.2.2.3 Bias Correction

Although the resolution of MRI-AGCM3.2s is satisfactory for regional-scale hydrological modelling; at basin scale, due to limited knowledge of physical processes in the real climate system (Zhuan *et al.,* 2019) and/or derivation error due during convective parameterization schemes (Yano *et al.,* 2012), the outputs usually suffer from systematic errors or biases. Therefore, a nonparametric quantile mapping bias correction approach is performed by adjusting the cumulative distribution function (CDF) of the simulated discharge to bridge the gap with the observed discharge, as expressed in Eq. (4.7).

$$Q_m(t) = F_o^{-1}(F_s(Q_s(t))) \quad (4.7)$$

In Eq (4.7), $Q_m(t)$ and $Q_s(t)$ are t^{th} bias-corrected and simulated data from MRI-AGCM3.2s during the reference period in the baseline, respectively. F_s and F_o^{-1} are the CDF of raw data and the inverse CDF of observed data, respectively. For the future projected climate data, this research assumed the probability distribution of observed data to be the same.

The reference period selected for calibrating the observed and simulated discharge was 1995-2014 (baseline period). The projection period is divided into three-time slices, (i) near future (2020-2040), mid future (2050-2070) and far future (2079-2099) to take into account the near, future and long-term changes in the discharge characteristics and flood

regimes for assisting relevant authorities to make appropriate decision making and designing long-term plans/policies/adaptation strategies for future changes.

4.2.3 Major Typhoon Events

Three major flood events together with a long-term simulation (2000-2020) were used to validate the RRI model using the datasets obtained from the Ministry of Environment. Follows are details of major flood events.

- Typhoon Nari: Sep. 5-21, 2001
- Typhoon Jangmi: Sep. 23, Oct. 5, 2008
- Typhoon Morakot: Aug, 2-13, 2009
- Long-term simulation: 2000-2020

4.2.3.1 Typhoon Nari

On August 31, 2001, a weak low-pressure area formed south of Guam. By September 5, it merged with a monsoonal trough feeding it with moisture and strengthened into the 26th tropical depression of the season northeast of Taiwan. A large, dry flow of air from the northwestward caused the storm to drift to the northeast where it became a tropical storm on the September 6th. It made a small burst of convection, as wind shear lowered, and rapidly intensified into a category 3 typhoon. The peaking reached 185 km/h winds before weakening to a tropical storm (Shawn, 2021). It restrengthened to a typhoon, and as it continued southwestward, Nari reached 160 km/h winds before hitting northeastern Taiwan on the 16th. Numerous landslides triggered by the storm's rain destroyed homes and buried people. At least 94 people were killed on the island due to the storm and 10 others were listed as missing. Agricultural losses from Nari were estimated at 84 million USD. In mountainous regions, more than 1,225 mm of rain fell over a two-day span, leading to many rivers overflowing their banks (Nik Maya *et al.*, 2021).

4.2.3.2 Typhoon Jangmi

Tropical Storm Jangmi, which means "rose" in Korean, formed in a low-pressure area south of Guam on September 22, 2008. Undergoing the same process as Nari, the storm developed into a tropical storm on September 24. Jangmi made impact in Taiwan, thousands were evacuated, rainfall, up to 994mm were recorded, and thousands of acres of farmland were destroyed. Jangmi killed 2 people and caused about 77.8 million USD in damage in Taiwan, as well as the typhoon also made operations of Taiwan suspended due to erosion around a pillar, until March 30, 2010 (Nik Maya *et al.*, 2021).

4.2.3.3 Typhoon Morakot

Typhoon Morakot struck Taiwan during August 6–10, 2009, and had a slowly moving path accompanied by a strong southwesterly monsoon with a radius of over 1,000 km. Typhoon Morakot dumped nearly 2,000mm of rainfall, over 70% of the average annual rainfall, on southwestern and southeastern Taiwan. The accumulated rainfall during the Typhoon Morakot were roughly 2,142 mm and 2,355mm respectively, *i.e.*, 75% and 72% of the mean average annual rainfall. Moreover, nearly 3,000 mm of rainfall fell in some mountainous areas of southwestern Taiwan over a period of 4 days during the typhoon. It should be mentioned that the increasing frequency of high intensity rainfall events in recent decades has induced many landslides in southwestern Taiwan. The rainfall during Typhoon Morakot can be characterized as heavy, high-intensity rainfall with a long duration. Rainfall exceeding 2,000 mm during the typhoon was concentrated in the upstream areas of the watershed. The maximum flood discharge during Typhoon Morakot set a new record by reaching 27,445m^3/s at 1:00 am on August 9, 2009. This discharge was approximately 1,000 times greater than the normal discharge.

4.3. Results and Discussion

4.3.1 Descriptive Analysis of Meteorological Data

Descriptive statistics of the meteorological variables in Taiwan between the years of 2000 and 2020 were summarized in Table 4.2. The country received annual precipitation between 1,718 mm/year and 3,484 mm/year (average of 2,632 ± 30 mm/year), with a high

annual relative humidity on average of 80% (range of 77–83%). The spatial distribution of precipitation showed that high precipitation occurs in the high elevation areas than that of the plains (Fig. 4.3(a)).

Throughout the investigation period from 2000 to 2020, four extreme events occurred, namely Typhoon Nari (5–21 September, 2001), Typhoon Jangmi (23 September–5 October, 2008), Typhoon Morakot (2–13 August, 2009), Typhoon Nesat (25–31, July 2017), bringing a cumulative precipitation of 1,430 mm, 2,780 mm, 1,134 mm, 886mm per event, respectively. The daily mean temperature varied substantially from 7.8 °C in winter to 31.2 °C in summer (average of 21.0 ± 0.8 °C). Over the course of the investigated period, the minimal daily temperature reached as low as 4.3 °C while the maximal temperature reached 32.0 °C.

Table 4.2. Descriptive of statistical metrics of meteorological variables across Taiwan during the investigated period (2000–2020). Note: Min: minimum, Avg: average, Max: maximum, SD: standard deviation.

Meteorological Parameters	**Min**	**Avg**	**Max**	**SD**
Annual precipitation (mm/year)	1,718.0	2,632.0	3,484.0	30.0
Daily min. temperature (°C)	4.3	7.8	11.2	0.3
Daily mean temperature (°C)	20.5	21.0	21.6	0.8
Daily max. temperature (°C)	29.9	31.2	32.0	1.3
Relative humidity (%)	77.0	80.0	83.0	6.2

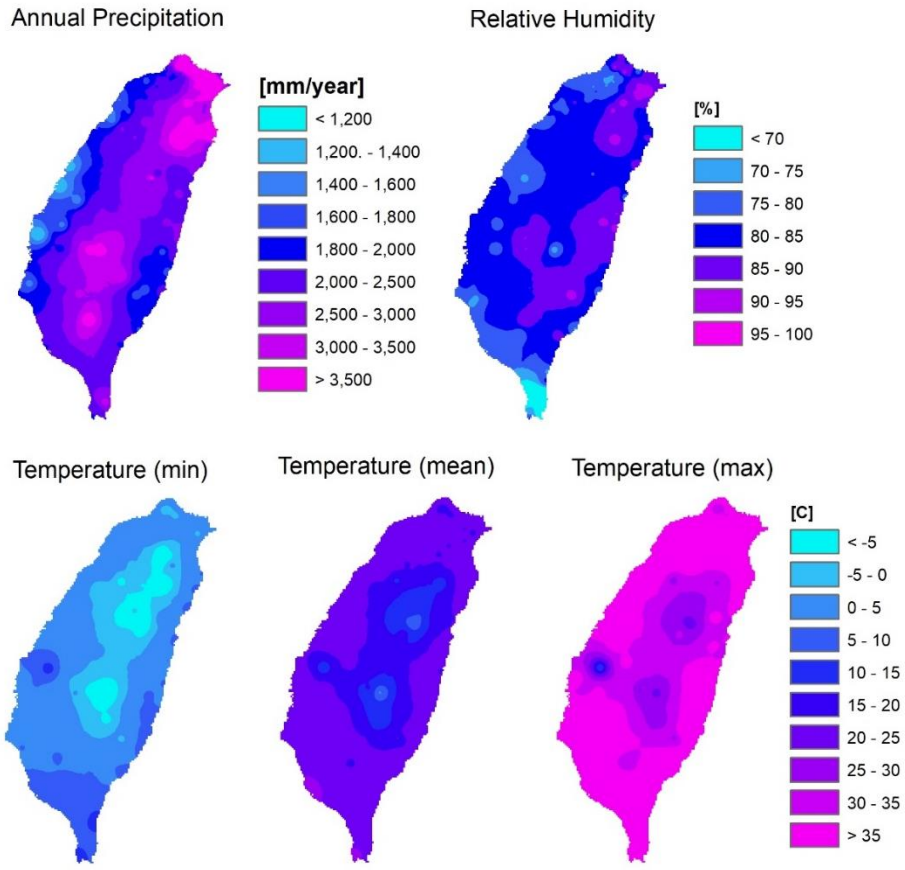

Fig. 4.3: Spatial distribution of Meteorological parameter across Taiwan

4.3.2 Performance of RRI Models

The RRI model for river discharge and flood inundation extent simulated for 2000–2020 performance indices of KGE, r, and PDR were calculated at 15 stations across Taiwan. Figs. S1-S4 shows the comparison of the major typhoon events and the long-term simulation and observation of monthly discharge at the 15 selected stations throughout 2000–2020.

In some stations, *e.g.*, stations 1 and 2, due to the limitation of the dataset which might be caused by the flood or technical errors before or during the event, no observed data was provided. Therefore, some stations only have the simulated dataset as shown in the supplementary figures at the end of this chapter. Figs. S1–S4 for the major flood events. Based on Fig. S1, it could be observed that most of the simulation result could fit the observed data. Based on the findings of the simulation, the observed flow rate in some stations could

reached over 8,000 m^3/s, indicating the disastrous power of the flood in the area during the Typhoon Nari. Daily precipitation from AGCM-MRI was used as input to the calibrated and validated RRI model to assess river flow and annual peak flood discharge. Spatiotemporal performance of the models across different major flood events and the long-term simulation were illustrated in Fig. 4.4 in a comparison of the gauged observation and simulated discharge across different stations on monthly basis. The results of river discharge showed a satisfactory performance with R = 0.91 (0.96,0.87) and KGE= 0.86 (0.95, 0.89) for 2001 (2008,2009, 2000-2020) flooding, respectively.

4.3.3 Bias Correction Performance of Climate Dataset

The bias correction performance was checked by comparing the precipitation and simulated discharge of historical AGCMs before and after bias correction. Fig. 4.5 shows average daily precipitation and simulated discharge comparing between GPCC and AGCMs before and after the bias correction. As compared to uncorrected dataset, closer relationship of the AGCMs data between the corrected and observed datasets on extreme flow (max 1-day) was observed in this research. According to Fig. 4.5, the difference between the raw AGCM and gauge daily maximum discharge has relatively big variations, ranging up to 50 to 1,500 m^3/s. With the huge difference, the simulated results without bias correction will be inaccurate for future streamflow simulation. This has highlighted the importance of applying bias correction in Taiwan region prior to performing simulation using the raw AGCM dataset. Most studies, for instance Wang *et al.*, 2021, Sophal *et al.*, 2020 and Shantini & Makmud, 2021 have utilized the AGCM dataset in understanding the flooding issues in Taiwan. However, based on the findings in this chapter, the reported results might have lower sensitivity and accuracy.

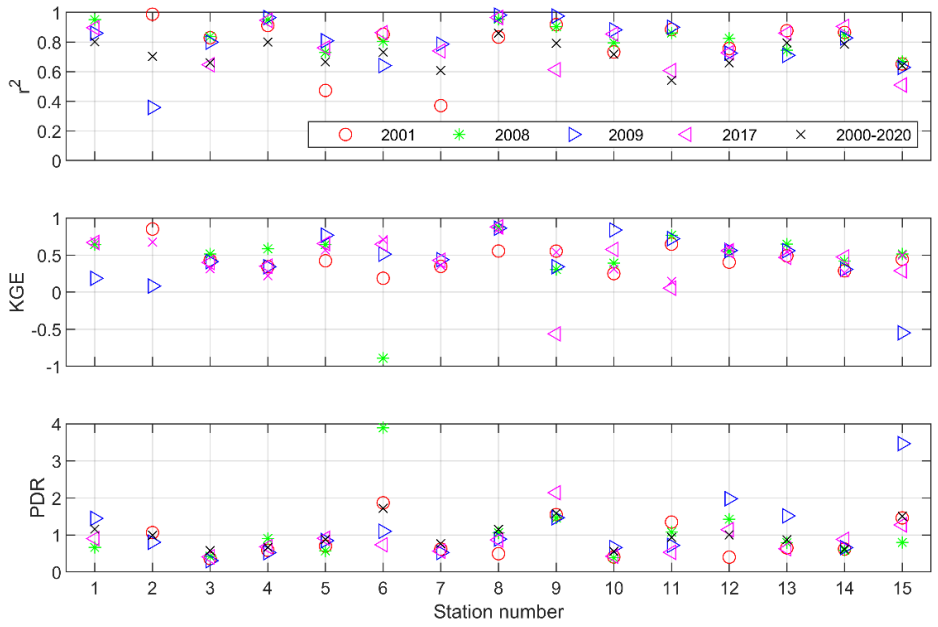

Fig. 4.4: Simulation performance Indices of r^2, KGE, and PDR for river flow in 2001, 2008, 2009, 2017, and total 21-year simulation during 2000-2020.

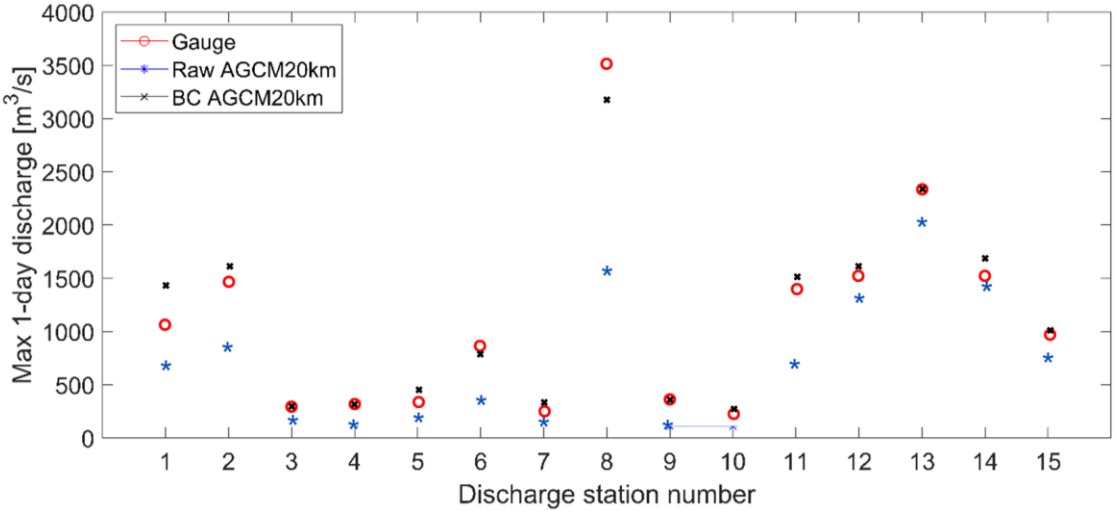

Fig. 4.5: The comparison of average annual peak flow between raw and bias corrected AGCM datasets.

4.3.4 Climate Change

In this section, the effects of climate change on precipitation and temperature patterns across different regions in Taiwan will be discussed. The summarized results are illustrated in Fig. 4.6.

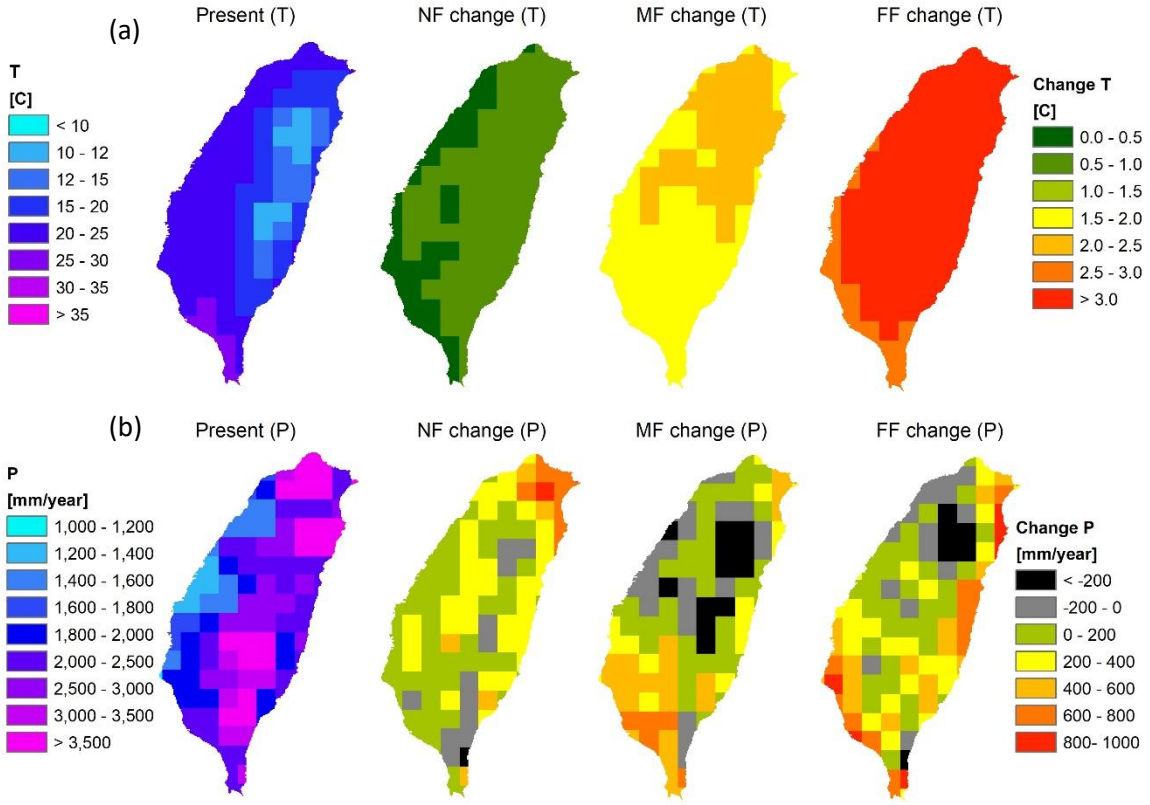

Fig. 4.6: Annual temperature (T) and precipitation (P) in present climate and their relative change in near future (NF), mid future (MF) and far future (FF).

4.3.4.1 Temperature Change

The spatiotemporal variation of present, near future, mid future and far-future temperature are illustrated in Fig. 4.6(a). For present spatiotemporal temperature variation, it could be observed that higher temperature is observed in the southern area, whereas lower temperature is observed in the eastern region. This is due to the geographical difference and location of the stations installed. Southern area is located at tropical region, leading the humidity and temperature are slightly higher compared to other regions. For Eastern region,

due to the latitudes are relatively higher as compared to other regions, the temperature are generally lower than other regions. Based on the simulation, a steady increasing trend is observed throughout the near future, future and far future, and expected to increase by more than 3 ℃ by end of 21st century under current conditions, highlighting the importance to combat or slow down the increasing temperature trend in the region.

4.3.4.2 Precipitation Change

Daily precipitation from the GCMs was used as input to the calibrated and validated RRI model to assess river flow and annual peak flood discharge. Fig. 4.6(b) shows the present, near future, future and far-future precipitation pattern across Taiwan. In present, the Eastern and Central regions are usually experiencing higher precipitation amount, up to 3,500mm per year. This is mainly due to significant amount of rainfall was brought by monsoon and typhoon seasons in these regions. As compared to temperature variation, the future precipitation change trend are different. In the near future, most regions are experiencing increasing trend, ranging between 200 mm to 1,000 mm increment throughout the research period. However, for both future and far future, significant decreasing trend up to -200 mm/year is observed mainly in the central region. These results have provided a significant finding for the responsible authority for more proper water resources management in this region. As reported in most studies and observed in recent rainfall events, extreme rainfall or drought has becoming more normal in nowadays. Therefore, more proper, and sustainable management are required to properly manage the flood issues as well as the water rationing issues.

4.3.5 Future Change of Extreme River Flow

The peak discharge for future flood projections was evaluated and compared with the baseline period. Fifteen main hydrological stations across mainstreams in different Taiwan cities were investigated. The maximum annual peak discharge across different stations showed an increase in discharge by 55, 47, and 57% for MRI-AGCM 3.2 at the projected periods in the near, mid, and far future, respectively (Fig. 4.7). These increases were notable with the K–S test at a significance level of 1% with p-values < 0.01.

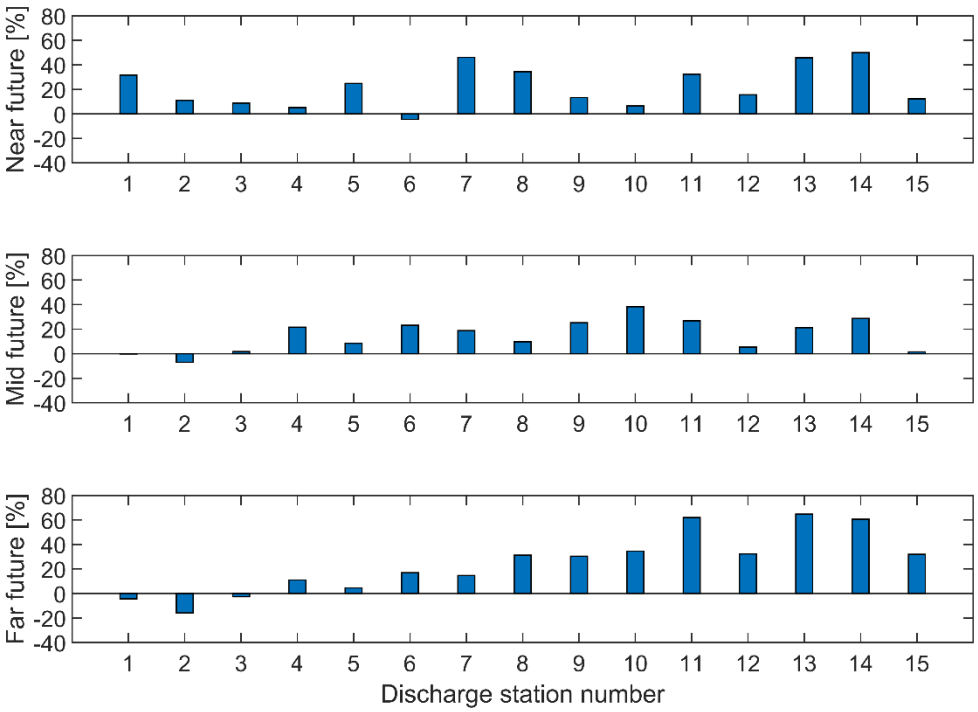

Fig. 4.7: Changes in average annual peak discharge in near future (2020–2040), mid future (2050–2070), and far future periods (2079-2099) at 15 river flow stations.

Among different Taiwan regions, for near-and-mid future, the maximum river flood rate is expected to increase more than 20%. However, for the future, the simulated conditions are slightly different. For East and South regions, it is expected to face severe flooding issues as the PDR more than five times are expected (Fig. 4.8). Most regions during these two periods are expected to face extreme flooding issues and proper flood prevention management are required. On the other hand, on top of the severe flooding issues, for far future, prolonged draught and water stress issues are expected in the Central and Northern regions. The responsible authorities have to have rationale water storage and management.

Nevertheless, few limitations are present in this research. This research primarily evaluated historical simulation from climate datasets and future projections of GCMs under future climate change impacts. Only future climate change impact perspectives on flooding were considered while leaving important variables untouched. The sources of uncertainties in flood projections under the impacts of climate change could be associated with emission scenarios, GCMs, downscaling methods, and hydrological models (Hoan *et al.*, 2020). This research evaluated only considered the worst-case scenario (SSP 8.5) from MRI-AGCM 3.2. Other future projection scenarios (*e.g.*, SSP1-2.6, SSP2-4.5 and SSP3-7.0) could also possibly happen, and they should be considered in further studies. Moreover, different downscaling methods should be investigated to capture the topographic characteristics' complexity, particularly in the more regional-scale studies. Only the RRI model was used to project floods in this research, while different hydrological models and their input parameters could associate with flood projection uncertainties. In addition, land use was assumed to be constant from baseline throughout the projected periods in the RRI model simulation. The changes in topography due to soil erosion and deposition were not considered in the RRI model as well. Moreover, the influence of hydropower and irrigation reservoirs on the river basin's seasonal hydrology and flow have not yet been analyzed. The future projections of flooding in this research focused only on annual peak discharge using MRI-AGCM 3.2. Further studies are needed to assess the cumulative impacts of climate change associated with these land-use changes and the impacts of water infrastructure development.

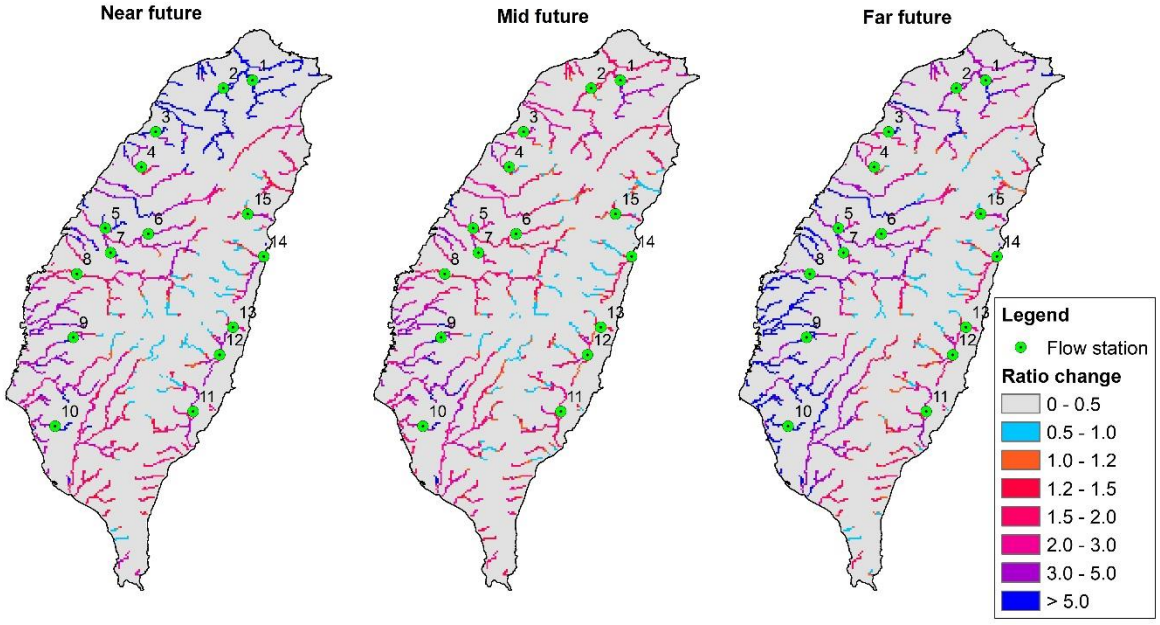

Fig. 4.8: The spatial distribution of ratio of changes in average annual peak discharge in near future (2020-2040), mid future (2050-2070), and far future periods (2079-2099).

4.4 Conclusions

This research has simulated the present, near-, mid- and far future of extreme flooding events across different cities in Taiwan using high resolution MRI-AGCM 3.2s dataset under RRI model. Based on the findings of the research, it could be observed that bias-correction using MRI-AGCM 3.2s dataset is crucial as huge variation are observed between uncorrected and gauge datasets. The precipitation and temperature trends are observed to vary dynamically in the future, with increment of temperature more than 3 °C and rainfall volume change spatiotemporally across different cities. For near-and-mid future simulation, the maximum river flood rate is expected to increase more than 20%. However, for the far future, the East and South regions are expected to face severe flooding issues; whereas prolonged draught and water stress issues are expected in the Central and Northern regions, providing insightful findings to the responsible authorities to have better water storage and management.

The application of high resolution GCM and regional downscaled climate data would be able to capture the complexity of land surface and local topographic characteristics in the small river basin, such as tributaries across Taiwan. The s1tudies on climate change impacts on hydrology changes such as floods and droughts using MRI-AGCM 3.2s could provide additional analysis to the responsible authorities for better water balance management. Moreover, further studies should focus on downscaling GCM to catch up with regional climate change by obtaining a higher spatial resolution; this might be more suitable for spatial distribution, particularly for studies in small-scale river basins. To reduce the possibility of severe damage caused by extreme flooding, adequate water resource management, flood adaptation and mitigation strategies, flood prevention infrastructure, and efficient real-time flood early warning and forecasting systems are required.

Supplementary Materials

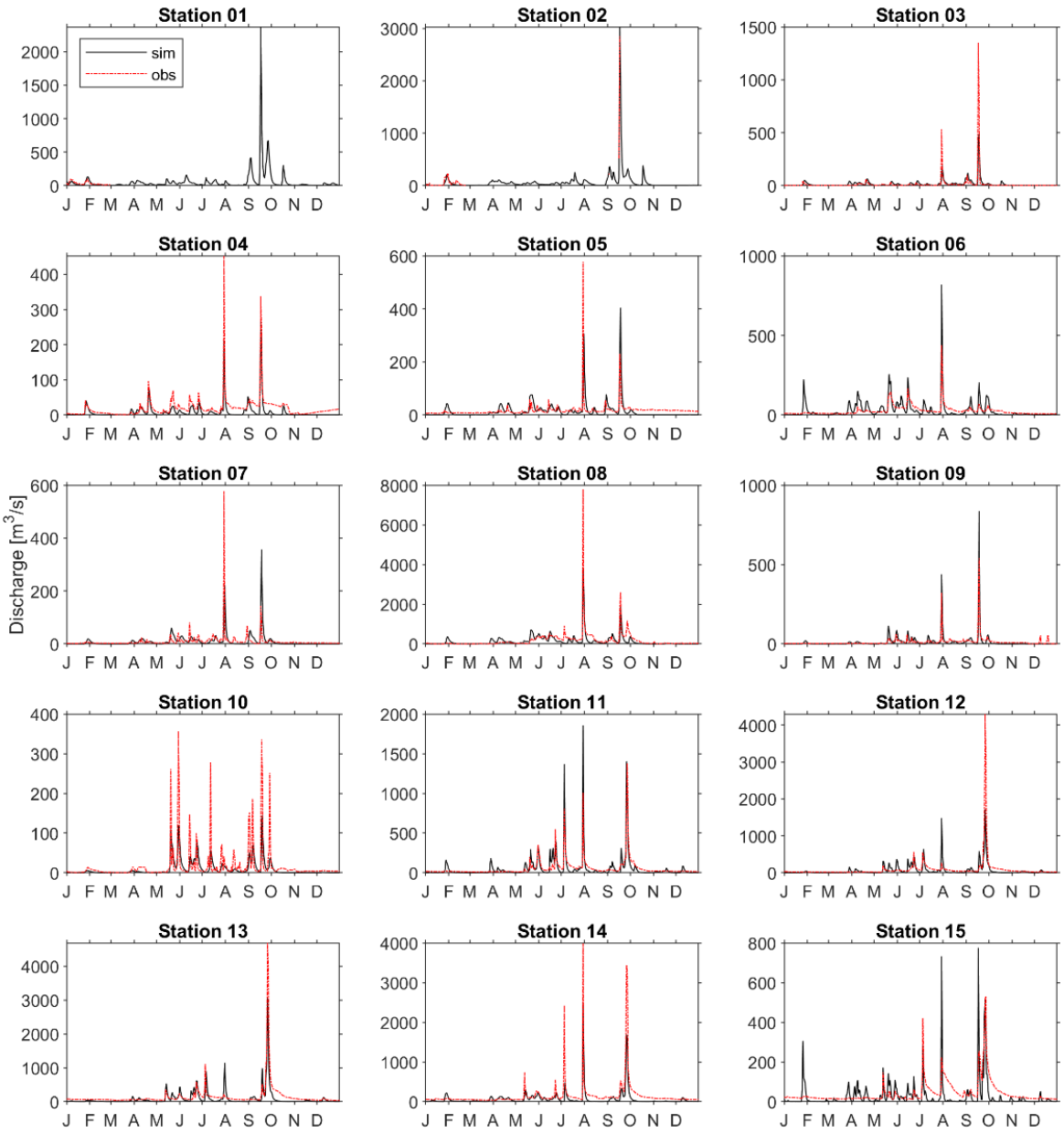

Fig. S1 Simulation performance in 2001 with Typhoon Nari: Sep. 5-21, 2001.

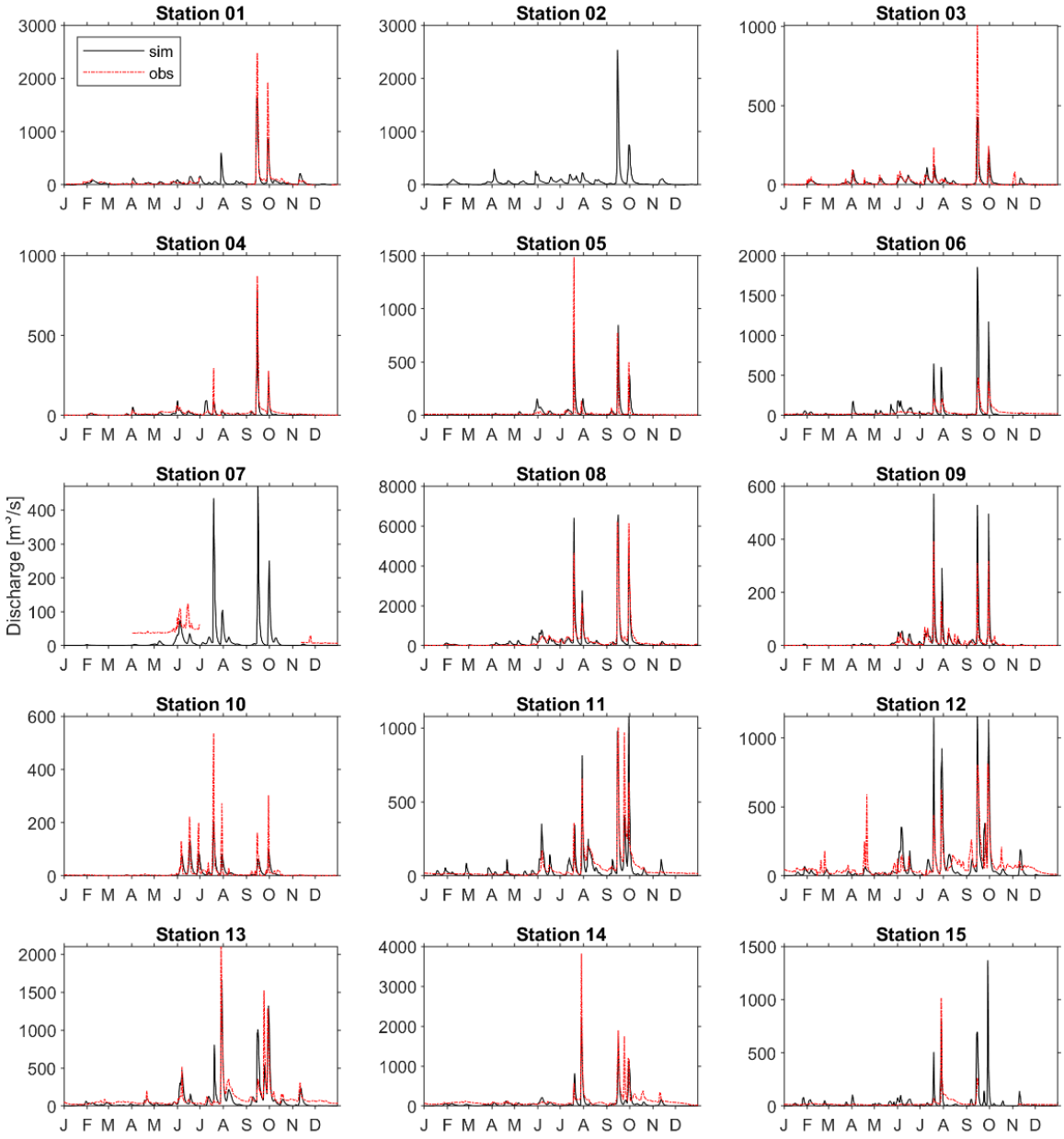

Fig. S2: Simulation performance in 2008 with Typhoon Jangmi: Sep. 23, Oct. 5, 2008

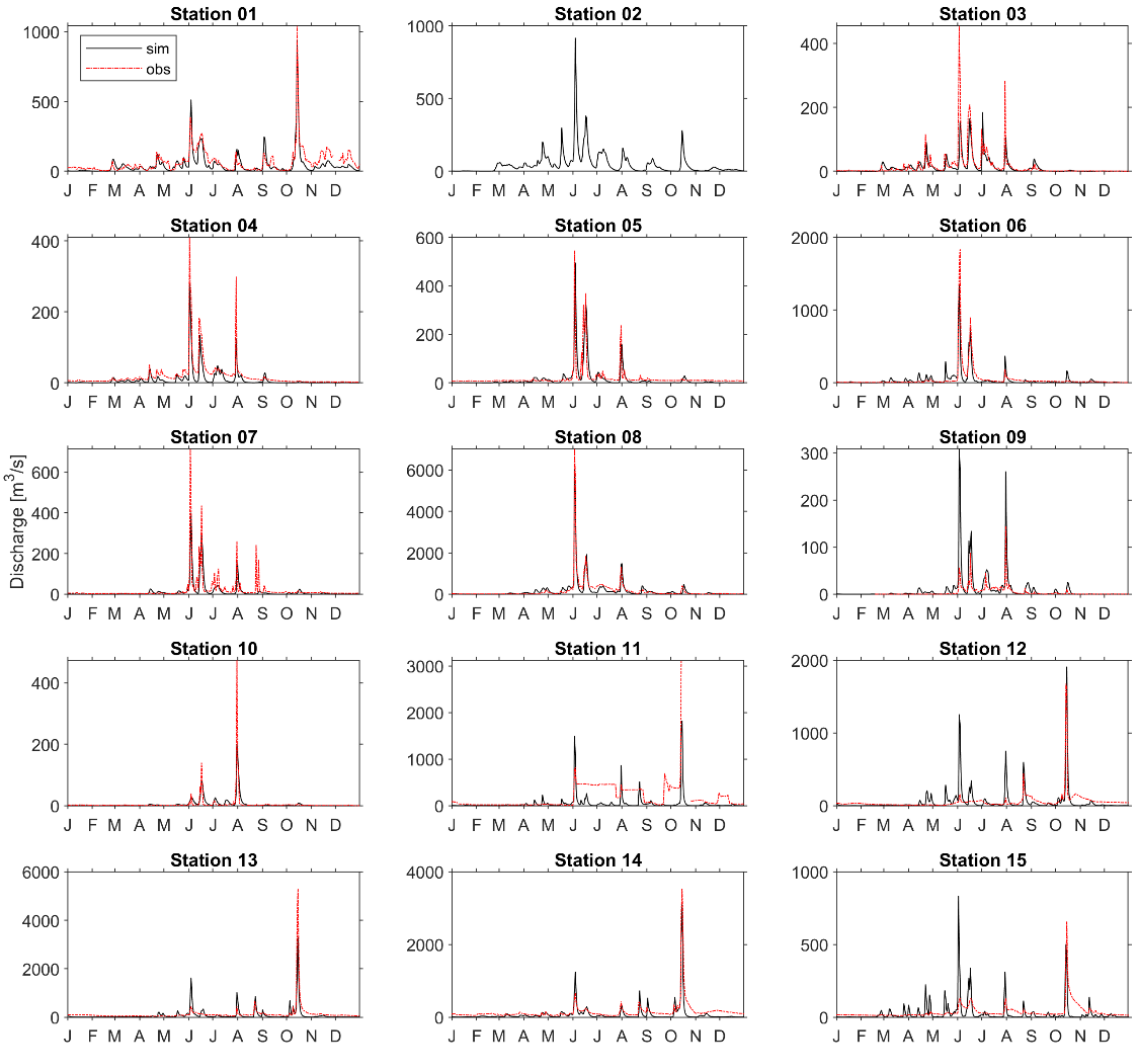

Fig. S3: Simulation performance in 2009 with Typhoon Morakot: Aug, 2-13, 2009

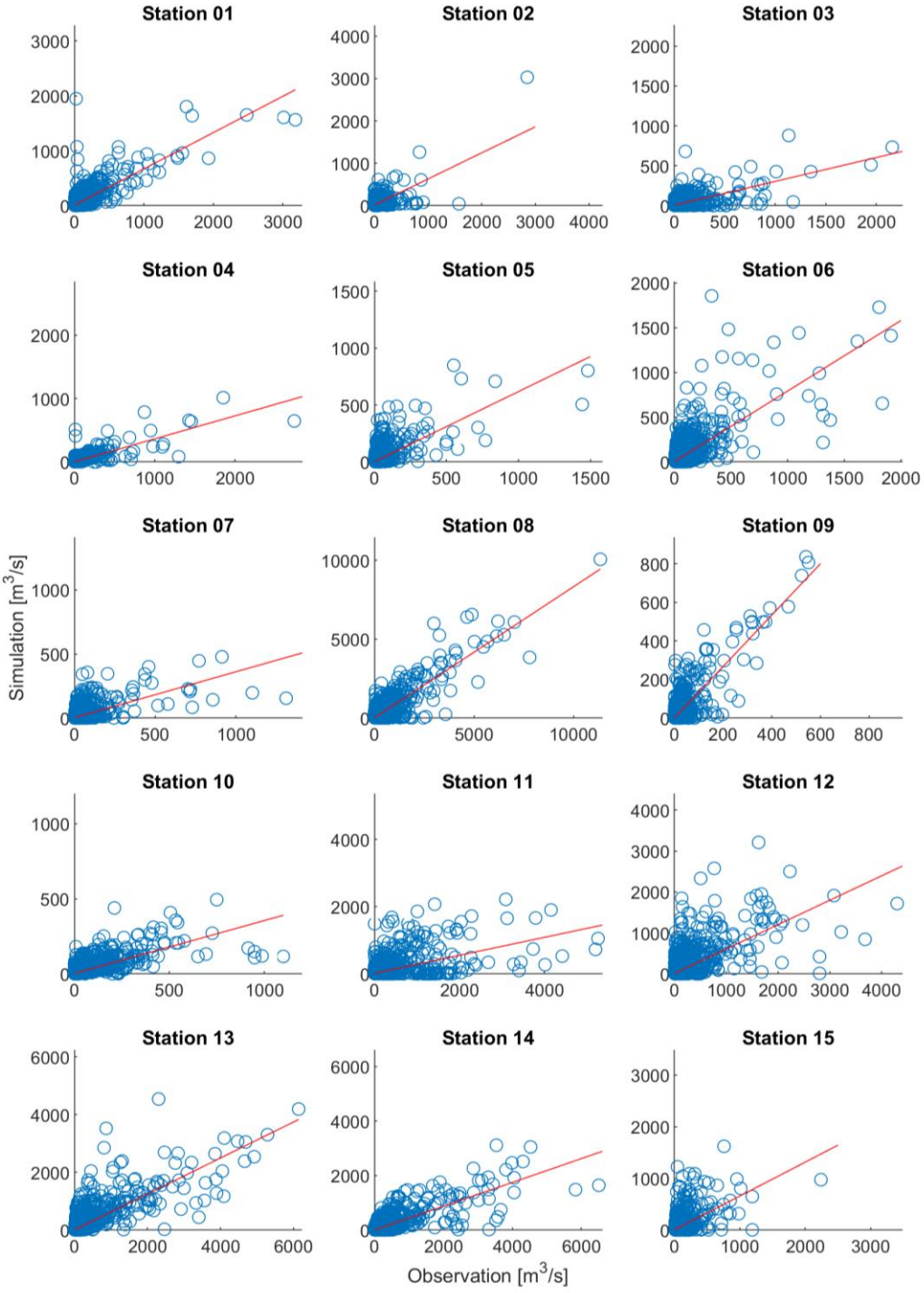

Fig. S4**:** Comparison of long-term simulation and observation of discharge flowrate at 15 stations during 2000–2020.

List of References

Arnold, M., Dilley, M., Deichmann, U., Chen, R. S., & Lerner-Lam, A. L. J. W. B., Washington, DC (2005). Natural disaster hotspots: a global risk analysis.

Chang, H.-S., Su, Q., & Katayama, T. (2021). Research on establishment of the region flood protection standard - a case of watershed of Dajiaxi, Taiwan. *Urban Water Journal, 18*(3), 173-182, doi:10.1080/1573062X.2020.1864831.

Chen, H., Liang, Q., Liu, Y., & Xie, S. (2018). Hydraulic correction method (HCM) to enhance the efficiency of SRTM DEM in flood modeling. *Journal of Hydrology, 559*, 56-70, doi:10.1016/j.jhydrol.2018.01.056.

Chen, S.-C., Liao, C.-M., Chio, C.-P., Chou, H.-H., You, S.-H., & Cheng, Y.-H. (2010). Lagged temperature effect with mosquito transmission potential explains dengue variability in southern Taiwan: Insights from a statistical analysis. *Science of The Total Environment, 408*(19), 4069-4075, doi:10.1016/j.scitotenv.2010.05.021.

Chen, Y.-R., Yeh, C.-H., & Yu, B. (2011). Integrated application of the analytic hierarchy process and the geographic information system for flood risk assessment and flood plain management in Taiwan. *Natural Hazards, 59*(3), 1261-1276, doi:10.1007/s11069-011-9831-7.

Chiang, Y.-C. (2018). Exploring community risk perceptions of climate change - A case study of a flood-prone urban area of Taiwan. *Cities, 74*, 42-51, doi:10.1016/j.cities.2017.11.001.

Chjeng-Lun, S., Chun-Ming, W., Wen-Chi, L., Yun-Chung, T., & Shin-Ping, L. (2009). The composite hazard resulted from Typhoon Morakot in Taiwan. *砂防学会誌, 62*(4), 61-65, doi:10.11475/sabo.62.4_61.

Ding, X., Zheng, L., Zheng, X., & Kao, S.-J. (2020). Holocene East Asian Summer Monsoon Rainfall Variability in Taiwan. [Original Research]. *Frontiers in Earth Science, 8*(234), doi:10.3389/feart.2020.00234.

Doong, D.-J., Lo, W., Vojinovic, Z., Lee, W.-L., & Lee, S.-P. (2016). Development of a New Generation of Flood Inundation Maps—A Case Study of the Coastal City of Tainan, Taiwan. *8*(11), 521.

Duan, Q., & Phillips, T. J. (2010). Bayesian estimation of local signal and noise in multimodel simulations of climate change. *115*(D18), doi:10.1029/2009JD013654.

Ge, X., Li, T., Zhang, S., & Peng, M. (2010). What causes the extremely heavy rainfall in Taiwan during Typhoon Morakot (2009)? *Atmospheric Science Letters, 11*(1), 46-50, doi:10.1002/asl.255.

Giorgi, F. (2019). Thirty Years of Regional Climate Modeling: Where Are We and Where Are We Going next? , *124*(11), 5696-5723, doi:10.1029/2018JD030094.

Guo, Y., Fang, G., Wen, X., Lei, X., Yuan, Y., & Fu, X. (2018). Hydrological responses and adaptive potential of cascaded reservoirs under climate change in Yuan River Basin. *Hydrology Research, 50*(1), 358-378, doi:10.2166/nh.2018.165 %J Hydrology Research.

Hashim, J. H., & Hashim, Z. (2016). Climate Change, Extreme Weather Events, and Human Health Implications in the Asia Pacific Region. *Asia Pac J Public Health, 28*(2 Suppl), 8s-14s, doi:10.1177/1010539515599030.

Henny, L., Thorncroft, C. D., Hsu, H.-H., & Bosart, L. F. (2021). Extreme Rainfall in Taiwan: Seasonal Statistics and Trends. *Journal of Climate, 34*(12), 4711-4731, doi:10.1175/JCLI-D-20-0999.1.

Hirabayashi, Y., Tanoue, M., Sasaki, O., Zhou, X., & Yamazaki, D. (2021). Global exposure to flooding from the new CMIP6 climate model projections. *Scientific Reports, 11*(1), 3740, doi:10.1038/s41598-021-83279-w.

Hirt, C. (2018). Artefact detection in global digital elevation models (DEMs): The Maximum Slope Approach and its application for complete screening of the SRTM v4.1 and MERIT DEMs. *Remote Sensing of Environment, 207*, 27-41, doi:10.1016/j.rse.2017.12.037.

Hsiao, S.-C., Chiang, W.-S., Jang, J.-H., Wu, H.-L., Lu, W.-S., Chen, W.-B., et al. (2021). Flood risk influenced by the compound effect of storm surge and rainfall under climate change for low-lying coastal areas. *Science of The Total Environment, 764*, 144439, doi:10.1016/j.scitotenv.2020.144439.

Hsu, H. H., & Chen, C. T. (2002). Observed and projected climate change in Taiwan. *Meteorology and Atmospheric Physics, 79*(1), 87-104, doi:10.1007/s703-002-8230-x.

Hsu, T.-W., Shih, D.-S., Li, C.-Y., Lan, Y.-J., & Lin, Y.-C. (2017a). A Study on Coastal Flooding and Risk Assessment under Climate Change in the Mid-Western Coast of Taiwan. *Water, 9*(6), 390.

Hsu, T.-W., Shih, D.-S., Li, C.-Y., Lan, Y.-J., & Lin, Y.-C. (2017b). A Study on Coastal Flooding and Risk Assessment under Climate Change in the Mid-Western Coast of Taiwan. *9*(6), 390.

Ito, R., Nakaegawa, T., & Takayabu, I. (2020). Comparison of regional characteristics of land precipitation climatology projected by an MRI-AGCM multi-cumulus scheme and multi-SST ensemble with CMIP5 multi-model ensemble projections. *Progress in Earth and Planetary Science, 7*(1), 77, doi:10.1186/s40645-020-00394-4.

Lin, C.-Y., Chien, Y.-Y., Su, C.-J., Kueh, M.-T., & Lung, S.-C. (2017). Climate variability of heat wave and projection of warming scenario in Taiwan. *Climatic Change, 145*(3), 305-320, doi:10.1007/s10584-017-2091-0.

Lin, I. I., & Chan, J. C. L. (2015). Recent decrease in typhoon destructive potential and global warming implications. *Nature Communications, 6*(1), 7182, doi:10.1038/ncomms8182.

Lin, M.-Y., Sun, W.-Y., Chiou, M.-D., Chen, C.-Y., Cheng, H.-Y., & Chen, C.-H. (2018). Development and evaluation of a storm surge warning system in Taiwan. *Ocean Dynamics, 68*(8), 1025-1049, doi:10.1007/s10236-018-1179-z.

Lin, Y.-F., Wu, C.-C., Yen, T.-H., Huang, Y.-H., & Lien, G.-Y. (2020). Typhoon Fanapi (2010) and Its Interaction with Taiwan Terrain – Evaluation of the Uncertainty in Track, Intensity and Rainfall Simulations. *気象集誌. 第2 輯, advpub*, doi:10.2151/jmsj.2020-006.

McClean, F., Dawson, R., & Kilsby, C. (2020). Implications of Using Global Digital Elevation Models for Flood Risk Analysis in Cities. *Water Resources Research, 56*(10), e2020WR028241, doi:10.1029/2020WR028241.

Mizuta, R., Yoshimura, H., Murakami, H., Matsueda, M., Endo, H., Ose, T., et al. (2012). Climate Simulations Using MRI-AGCM3.2 with 20-km Grid. *Journal of the Meteorological Society of Japan. Ser. II, 90A*, 233-258, doi:10.2151/jmsj.2012-A12.

Rahman, M. M., Ferdousi, N., Abdullah, S. M. A., Kusunoki, S., & Islam, A. (2019). Recent Climate Simulation over SAARC Region Including Bangladesh Using High Resolution AGCM. *Asia-Pacific Journal of Atmospheric Sciences, 55*(2), 115-134, doi:10.1007/s13143-018-0077-0.

Rajah, K., O'Leary, T., Turner, A., Petrakis, G., Leonard, M., & Westra, S. (2014). Changes to the temporal distribution of daily precipitation. *41*(24), 8887-8894, doi:10.1002/2014GL062156.

S. Bhagabati, S., & Kawasaki, A. (2017). Consideration of the rainfall-runoff-inundation (RRI) model for flood mapping in a deltaic area of Myanmar. *Hydrological Research Letters, 11*(3), 155-160, doi:10.3178/hrl.11.155.

Sayama, T., Ozawa, G., Kawakami, T., Nabesaka, S., & Fukami, K. (2012). Rainfall–runoff–inundation analysis of the 2010 Pakistan flood in the Kabul River basin. *Hydrological Sciences Journal, 57*(2), 298-312, doi:10.1080/02626667.2011.644245.

Sayama, T., Tatebe, Y., & Tanaka, S. (2017). An emergency response-type rainfall-runoff-inundation simulation for 2011 Thailand floods. *Journal of Flood Risk Management, 10*(1), 65-78, doi:10.1111/jfr3.12147.

Schendel, U. (1967). Vegetationswasserverbrauch und-wasserbedarf. *Habilitation, Kiel, 137*, 1-11.

Shakti, P. C., Kamimera, H., & Misumi, R. (2020). Inundation Analysis of the Oda River Basin in Japan during the Flood Event of 6–7 July 2018 Utilizing Local and Global Hydrographic Data. *Water, 12*(4), 1005.

Su, Y.-F., Wu, C.-H., & Lee, T.-F. (2017). Public Health Emergency Response in Taiwan. *Health security, 15*(2), 137-143, doi:10.1089/hs.2016.0108.

Sun, Q., Miao, C., & Duan, Q. (2016). Extreme climate events and agricultural climate indices in China: CMIP5 model evaluation and projections. *36*(1), 43-61, doi:10.1002/joc.4328.

Tu, J.-Y., & Chou, C. (2013). Changes in precipitation frequency and intensity in the vicinity of Taiwan: typhoon versus non-typhoon events. *Environmental Research Letters, 8*(1), 014023, doi:10.1088/1748-9326/8/1/014023.

United Nations Office for Disaster Risk Reduction (2020). Human cost of disasters: an overview of the last 20 years.

Usman, M., Ndehedehe, C. E., Farah, H., & Manzanas, R. (2021). Impacts of climate change on the streamflow of a large river basin in the Australian tropics using optimally selected climate model outputs. *Journal of Cleaner Production, 315*, 128091, doi:10.1016/j.jclepro.2021.128091.

World Meteorological Organization (2021). WMO Atlas of Mortality and Economic Losses from Weather, Climate and Water Extremes (1970–2019).

Yamazaki, D., Ikeshima, D., Tawatari, R., Yamaguchi, T., O'Loughlin, F., Neal, J. C., et al. (2017). A high-accuracy map of global terrain elevations. *Geophysical Research Letters, 44*(11), 5844-5853, doi:10.1002/2017GL072874.

Yano, J. I., Cheedela, S. K., & Roff, G. L. (2012). A compressed super-parameterization: test of NAM-SCA under single-column GCM configurations. *Atmos. Chem. Phys. Discuss., 2012*, 28237-28303, doi:10.5194/acpd-12-28237-2012.

Yeh, H.-F., & Huang, C.-C. (2019). Evaluation of basin storage–discharge sensitivity in Taiwan using low-flow recession analysis. [10.1002/hyp.13411]. *Hydrological Processes, 33*(10), 1434-1447, doi:10.1002/hyp.13411.

Yoshida, K., Sugi, M., Mizuta, R., Murakami, H., & Ishii, M. (2017). Future Changes in Tropical Cyclone Activity in High-Resolution Large-Ensemble Simulations. *Geophysical Research Letters, 44*(19), 9910-9917, doi:10.1002/2017GL075058.

Zhuan, M., Chen, J., Xu, C.-Y., Zhao, C., Xiong, L., & Liu, P. (2019). A method for investigating the relative importance of three components in overall uncertainty of climate projections. *International Journal of Climatology, 39*(4), 1853-1871, doi:10.1002/joc.5920.

Chapter 5

Spatiotemporal impact of COVID-19 on Taiwan air quality in the absence of lockdown

In this chapter, a novel research framework is proposed to evaluate the long-term monthly spatiotemporal impact of COVID-19 on Taiwan air quality through different statistical analyses, including geostatistical analysis, change detection analysis and identification of nonattainment pollutant occurrence between the average mean air pollutant concentrations from 2018-2019 and 2020, considering both meteorological and public transportation impacts. Reduced public transportation use had a more significant impact than meteorology on air quality improvement in Taiwan, highlighting the importance of proper public transportation management for air pollution control and paving a new path for sustainable air quality management even in the absence of a lockdown.

5.1 Introduction

Air pollution has been recognized as one of the deadliest environmental issues worldwide and has been reported to cause more than 7 million deaths annually (WHO 2021) by inducing long-term health problems such as lung cancer, heart diseases, asthma, and other chronic respiratory diseases (Landrigan *et al.*, 2018). Tremendous efforts to combat air pollution have been made across the globe, such as formulating numerous frameworks/laws/policies at both the national (Li *et al*., 2017; Amann *et al*., 2017) and international levels (Shapiro & Yarime, 2021). Nevertheless, large gaps have been observed in implementation, financing and enforcement capacity (United Nations Environment Programme 2021), causing air pollution to remain a major health threat worldwide. However, the unprecedented outbreak of fatal 2019 coronavirus disease (COVID-19) has made a remarkable breakthrough in unresolved air pollution management.

Since the end of 2019, COVID-19 has tremendously disrupted the normal rhythm of livelihood and has led to dramatic loss of human life worldwide, with infections and deaths exceeding 242 million and 4.9 million, respectively, as of October 2021 (Worldometer, 2021). COVID-19 is caused by the novel severe acute respiratory syndrome coronavirus 2 that can

be transmitted through the air, particularly in crowded areas or poorly ventilated indoor areas (Dinoi *et al.* 2022) and can survive on a variety of surfaces for hours (van Doremalen *et al.*, 2020). Due to its high infectivity and transmissibility, it was classified as a global pandemic by the World Health Organization (WHO) on March 11, 2020 (WHO 2020). Therefore, most governments across the globe have imposed restrictive/preventive measures, such as lockdowns, travel restrictions, shelter-at-home policies, social distancing, and mandatory mask wearing in public places, to contain or slow down the spread of COVID-19. These timely and strict measures have effectively slowed virus transmission among people. Concurrently, these measures also reduced emissions from major anthropogenic and economic activities due to the disruption of anthropogenic emissions. Consequently, a remarkable change in air pollutant concentrations was observed throughout the world, particularly in countries that imposed lockdown, creating a silver lining in the dark cloud of COVID-19 (Jephcote *et al.,* 2021; Nakada & Urban 2020; Kanniah *et al.,* 2020). A significant reduction in air pollutant concentration is observed worldwide, wherein the average concentrations of ground-level nitrogen dioxide (NO_2) and particulate matter with average aerodynamic diameters less than 10 µm and 2.5 µm (PM_{10} and $PM_{2.5}$) declined by approximately 30% and 20%, respectively, compared to 2019 (Yang *et al.,* 2021). Since then, there has been growing attention to utilizing both high-resolution satellite images and/or ground-based monitoring data to quantify the impact of COVID-19 on the local atmospheric environment, particularly to compare the differences before and after lockdown implementation, for instance, in India (Mahato *et al.,* 2020), China (Shen *et al.,* 2021), Singapore (Li and Tartarini 2020), Malaysia (Abdullah *et al.,* 2020), Iran (Broomandi *et al.*, 2020), Bangladesh (Rahman *et al.,* 2020), Brazil (Nakada & Urban, 2020), and Turkey (Ghasempour *et al.*, 2021).

Most of the studies hypothesized that strict lockdowns were the major contributors to air pollution reduction during the early stages of the pandemic and highlighted that these environmental changes were only temporary due to the small respite before industrial activities resumed (Nigam *et al.,* 2021); however, contradictory findings were reported by Dinoi *et al.* (2021). Due to the disruption of local economic activities, *e.g.,* transportation and

tourism, as well as the reduced emissions from local private travel due to the enforcement of smart working in Italy, the authors showed that the concentration of ultrafine particles decreased more rapidly after the lockdown than during the lockdown. Moreover, to date, only a few studies have focused on the air quality changes in cities that did not impose lockdowns, such as Taiwan. Credit must be given to the established public health response mechanism and Taiwanese government's timely and accurate decision (*e.g.*, border restriction). COVID-19 was contained without imposing lockdown or implementing work-from home policies, and its impact on people's daily lives was minimized in 2020 (Chen & Fang, 2021). Consequently, in contrast with most of the reported studies, insignificant changes or higher concentrations of major pollutants (carbon monoxide (CO), sulfur dioxide (SO_2), ozone (O_3), $PM_{2.5}$ and PM_{10}) were observed in Taipei and New Taipei cities (major cities in northern Taiwan) at the early stages of COVID-19 (Chang *et al.*, 2021). However, according to the report from Taiwan's Environmental Protection Administration (TEPA), a substantial improvement in air quality was observed in Taiwan for 2020 compared to 2019 (TEPA 2021), which may indicate a delayed improvement in the COVID-19 impact on the cities that did not impose lockdown. Therefore, further studies are required to evaluate the long-term COVID-19 impact on the environment and identify possible "new normal lifestyles" that can be practiced for future pollution reduction.

Recently, growing attention has been given to investigating the influencing factors of air quality changes during the COVID-19 period, for which the impacts of meteorology and public transportation are most reported. Since meteorological parameters also play a significant role in affecting the dynamics of pollutants (such as dispersion rate, transportation, and transformation) (Singh & Tyagi, 2021), various methods have been introduced, *e.g.,* the application of black-box models to eliminate the associated effects caused by meteorological variability (Grange *et al.,* 2018; Solberg *et al.,* 2021). For instance, Petetin *et al.* (2020) and Talbot *et al.* (2021) performed a random forest machine learning algorithm to estimate the business-as-usual (BAU) pollutant concentration based on the emission scenario and meteorological parameters in the absence of COVID-19 in Spain and New Zealand, respectively. Although it is undeniable that black-box models usually have high prediction

accuracy, white-box models are still preferred compared to black-box models due to their transparency; additionally, the relative importance of the predictor variables, which are necessary for decision making in air quality management, can be recognized (Fung *et al.*, 2021). Compared to black-box models, white-box models require fewer datasets for model construction and are commonly adopted for practical application due to their simplicity and robustness (Wong *et al.*, 2021; Loyola- González, 2019). However, to the best of the authors' knowledge, most studies have applied only black-box models to simulate the BAU air pollutant concentration by utilizing meteorological parameters during the lockdown period (Petetin *et al.*, 2020; Querol *et al.*, 2021). In addition, the majority of current studies have considered only the impact of public roadway transportation reduction during the lockdown period (Gao *et al.*, 2021; Tian *et al.*, 2021), but according to the annual transportation report of Taiwan, the use of public urban transportation, including different transportation modes (*e.g.*, railway, air and waterway), in 2020 declined and dropped to almost the lowest level of the past decade (Ministry of Transportation and Communication, 2021). Significant concentrations of air pollutants have been reported in railways (Moreno *et al.*, 2015), air (Psanis *et al.*, 2017) and waterways (Solomon *et al.*, 2021), as different transportation modes have different features and may constitute divergent air pollutants to the environment. Therefore, to provide a comprehensive evaluation of the impact of public urban transportation on air quality during the study period, four transportation modes were included in this study.

In light of these findings and to better understand the impact of COVID-19 on atmospheric quality in the absence of a lockdown, this study proposed a novel research framework to evaluate the spatiotemporal impacts of COVID-19 across five regions in Taiwan through comparative analysis between mean air pollutant concentrations of 2018-2019 averaged and 2020, considering both meteorological and public transportation effects. In this study, to bridge the aforementioned research gaps, the research objectives are set to:

1. evaluate, compare and illustrate the spatiotemporal variations in air pollutants between 2020 and the base year utilizing a geographical information system;

2. identify the major health risk air pollutants;
3. identify the changes in different public transportation modes and their impact on air quality;
4. evaluate the impact of meteorological parameters and formulate a white-box model to simulate the meteorological normalized business-as-usual concentration; and
5. identify the underlying reasons during anomalous months (*i.e.,* local emissions or transboundary pollution) through backward trajectory analysis.

Although the impact of lockdown has driven the significant improvement in air quality, as shown in many regions, it is impossible to impose lockdown indefinitely, as it would lead to tremendous losses for the economy and human liberty. Therefore, these findings are expected to reveal the long-term COVID-19 impacts (monthly analysis throughout 2020) on the atmospheric environment associated with public transportation and meteorological impacts in the absence of lockdown and provide comprehensive information to relevant authorities for future sustainable planning of air quality management.

5.2 Data Collection and Methodology

5.2.1 Study Area

Taiwan is geographically located in East Asia (21.5–25.2 °N and 120.0–122.0 °E) with altitudes ranging from -10–3880 m above sea level. As Taiwan straddles the Tropic of Cancer, the northern part of Taiwan belongs to the subtropical climate zone, while the very southern part belongs to the tropical climate zone. The mean annual precipitation of Taiwan ranges from 2,000 mm to 4,000 mm, with approximately 70% of the precipitation occurring during the wet-warm season (May to October), primarily driven by monsoon and typhoon events; therefore, lower concentrations of pollutants are usually observed during this period and higher concentrations in the dry cold season (November to April) (Hsu *et al.,* 2020a; Wu *et al.,* 2019).

To ascertain the impact of COVID-19 on air quality in 2020, different base years, *e.g.,* single year (2019) (Naqvi *et al.,* 2021; Mesas-Carrascosa *et al.,* 2020), two years averaged

(2018-2019) (Hu *et al.,* 2021; Tian *et al.,* 2021), and five years averaged (2015-2019) (Nakada & Urban, 2020; Zangari *et al.,* 2020), were proposed. Continual improvements in the overall air quality conditions in Taiwan have been observed owing to effective pollution control strategies implemented by the government (Tsai *et al.,* 2021), and coal use for power generation is gradually being reduced and replaced by liquefied natural gas since the end of 2017 (TEPA, 2021). In light of these findings, for a better and more precise comparison between business-as-usual (BAU) and COVID-19 scenarios, the 2018-2019 average was selected as the base year in this study.

To evaluate the spatiotemporal impacts of COVID-19 on air quality across Taiwan, air pollutants and meteorological stations distributed in different cities were acquired from the TEPA and Central Weather Bureau, respectively. The daily data for both air pollutants and meteorological parameters were used to calculate the mean concentrations/values for each month. Due to certain technical errors (*i.e.,* power failure, machine error or under maintenance) (Benis *et al.,* 2015), some data were missing (approximately 5% of the overall data). Therefore, the numbers of usable air quality and meteorological parameter stations were 69 and 224, respectively, as shown in Fig. 5.1. The air pollutants included in this study were CO, SO_2, NO_2, O_3, PM_{10} and $PM_{2.5,}$ whereas the meteorological parameters included were station pressure (P_{sta}), sea-level atmospheric pressure (P_{sea}), atmospheric temperature (T_{atm}), dew temperature (T_{dew}), class-A pan evaporation (Evap), wind speed (WS), wind direction (WD), rainfall (RF), relative humidity (RH), sunshine hours (SH), global radiation (GR) and cloud cover (CC).

The monthly passenger volumes (2018-2020) for roadway, railway, air and waterway transportation modes were acquired from the Taiwan Ministry of Transportation and Communication to evaluate the impact of traffic volume on air quality (Ministry of Transportation and Communication 2020). To better understand public mobility behavior in 2020, each transportation mode has been further categorized into intercity/international and local routes, except for waterway transportation. Detailed information on the data used in this study is summarized in Table 5.1.

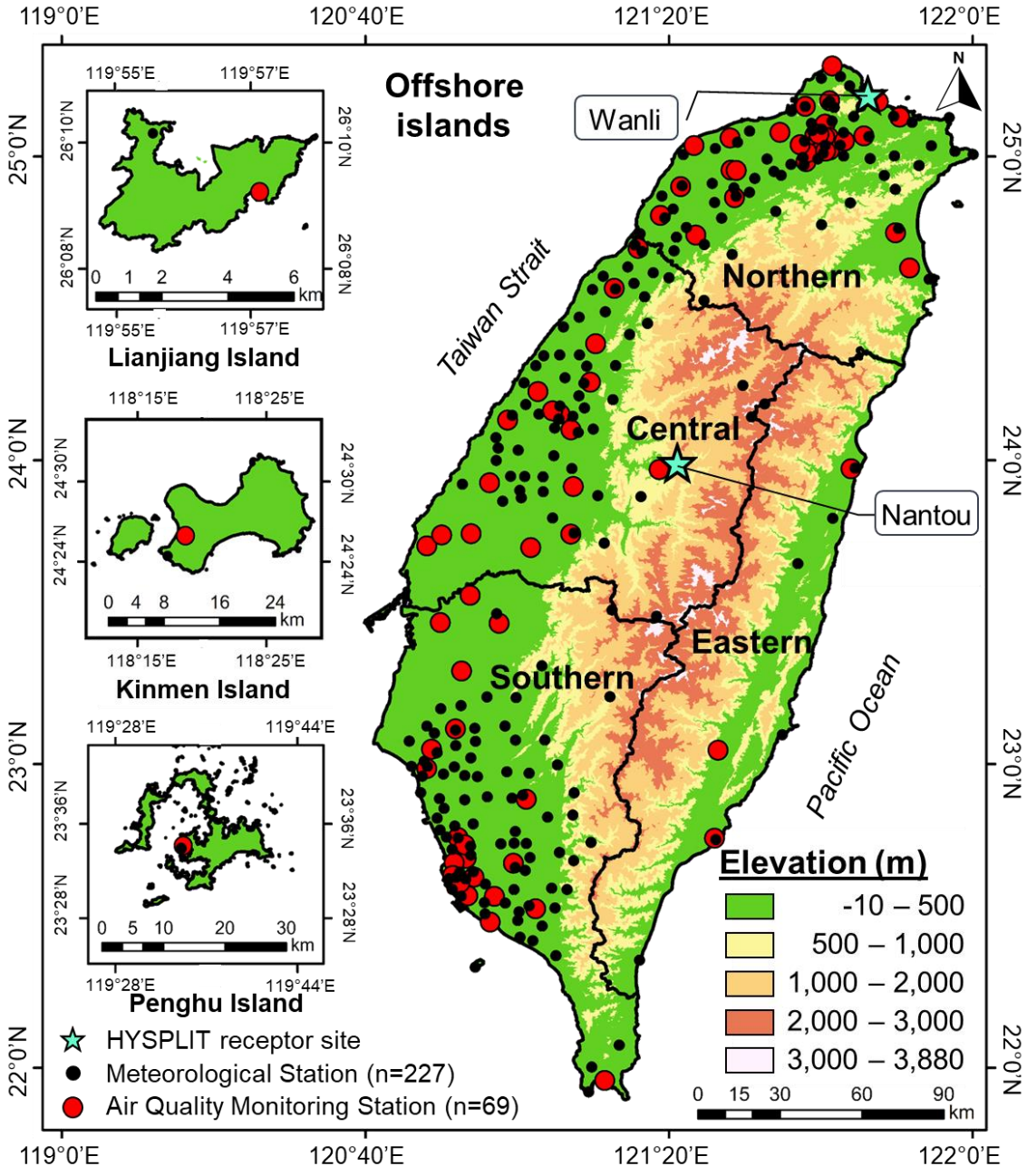

Fig. 5.1: Topography and geographical location of Taiwan with meteorological and air quality monitoring stations as well as receptor sites for back-trajectory analysis.

Table 5.1: Summary of the dataset used in the study

Type	Parameter/Variable		Unit	No. of Monitoring Station	Duration	Source
Air Quality	Carbon monoxide (CO)		$\mu g/m^3$	69	2018-2020 (Daily)	Taiwan Environmental Protection Administration
	Sulfur dioxide (SO_2)		$\mu g/m^3$			
	Nitrogen dioxide (NO_2)		ppm			
	Ozone (O_3)		ppb			
	Particulate matter 2.5 ($PM_{2.5}$)		ppb			
	Particulate matter 10 (PM_{10})		ppb			
Meteorological	Station pressure (P_{sta})		hPa	224	2018-2020 (Daily)	Taiwan Central Weather Bureau
	Sea-level pressure (P_{sea})		hPa			
	Atmospheric temperature (T_{atm})		˚C			
	Dew temperature (T_{dew})		˚C			
	Class-A pan evaporation (Evap)		mm			
	Wind speed (WS)		m/s			
	Wind direction (WD)		℃			
	Rainfall (RF)		Mm			
	Relative humidity (RH)		%			
	Sunshine hours (SH)		hour			
	Global radiation (GR)		MJ/m^3			
	Cloud Cover (CC)		-			
Traffic Volume	Roadway	Local	person	*	2018-2020 (Monthly)	Ministry of Transportation and Communication
		Intercity				
	Railway	Local				
		Intercity				
	Air	Local				
		International				
	Waterway	Local				

* Total number of passengers across Taiwan

5.2.2 Research Framework

In this section, the architecture of an integrated research framework for identifying the impacts of public transportation usage and meteorology on air quality during the COVID-19 period in the absence of lockdown is introduced, as shown in Fig. 5.2. Different statistical analyses were performed and effectively illustrated using a geospatial information system (GIS) to quantify the spatiotemporal variation change in each air pollutant between 2018-2019 and 2020. Correlation and trend analyses were performed to assess the degree of association and temporal changes between public transportation usage and meteorological parameters and air pollutants. A stepwise regression model (SRM) was adopted to simulate the concentration of air pollutants under the meteorological-normalized BAU scenario by utilizing meteorological parameters. To identify the underlying reasons during the anomalous months (*i.e.*, local emissions or transboundary pollution), backward trajectory analysis using the hybrid single-particle Lagrangian integrated trajectory (HYSPLIT) model was applied. A detailed discussion of each step is provided as follows:

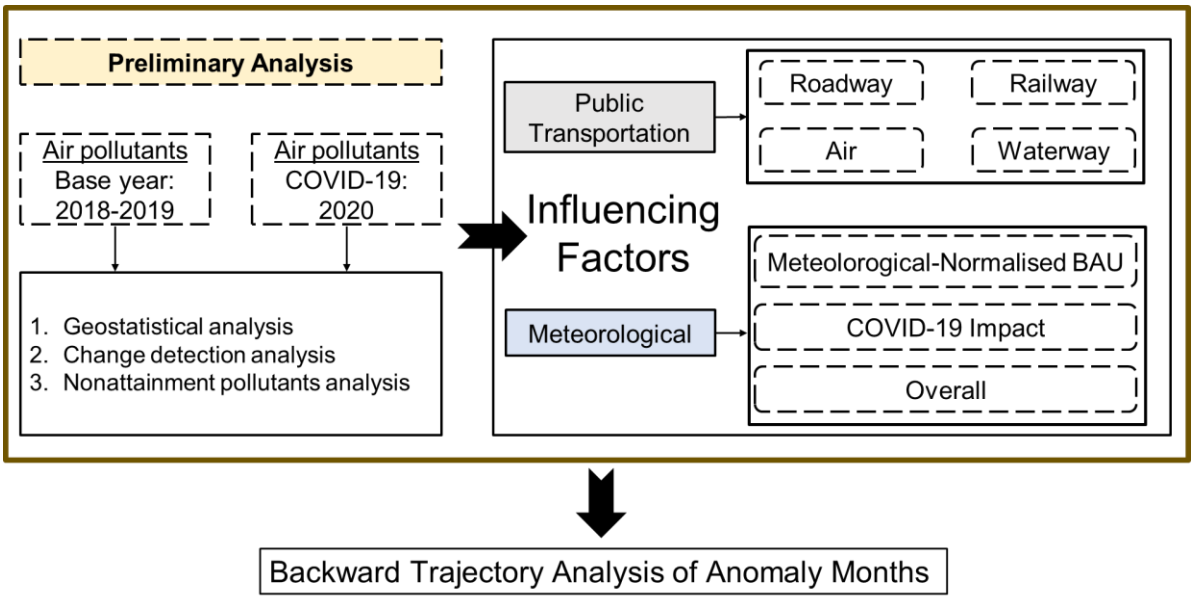

Fig. 5.2: Schematic overview of the proposed framework for evaluating the spatiotemporal impacts of COVID-19 with consideration given to the impacts of public transportation users and meteorology.

5.2.2.1 Geostatistical Analysis

The descriptive statistics (range and mean ± standard deviation) for air pollutants are summarized in Table 5.2. To analyze the data distribution of the variables included in this study, the Shapiro–Wilk (SW) normality test was applied due to its robustness and suitability for complicated atmospheric interactions (Ventura *et al.,* 2018). One-way analysis of variance (ANOVA) was performed to evaluate the significant differences between the air pollutants in 2018-2019 and 2020. All statistical tests were performed using the Statistical Package and Service Solutions (IBM SPSS version 22). The spatial distribution of the monthly mean concentration and mean percentage difference in air pollutants across Taiwan were determined using the spatial analyst module in the ArcGIS 10.8 platform. To visualize the spatiotemporal variation in air pollutants, the deterministic interpolation technique inverse distance weighting (IDW) method was selected due to its wide application for temporal climate and environmental data analysis (Chen & Liu, 2012; Wong *et al.,* 2020).

5.2.2.2 Change Detection Analysis

The monthly mean percentage difference between air pollutants between 2018-2019 averaged and 2020 was computed using Eq. (5.1) (Hu *et al.,* 2021).

$$Percentage\ Change\ (\%) = \frac{Conc_{2020} - Conc_{2018-2019}}{Conc_{2018-19}} \times 100\% \qquad (5.1)$$

where $Conc_{2018-19}$ and $Conc_{2020}$represent the mean monthly concentration of pollutants for 2018-2019 and 2020.

5.2.2.3 Nonattainment Pollutants Analysis

The current Taiwan AQI framework was revised in 2016 (formerly known as the pollutant standard index) by Taiwan's Environmental Protection Administration to have stricter standards and a more detailed classification of the concentration of each pollutant for air quality evaluation. The Taiwan AQI consists of six air pollutants. Pollutant concentrations are converted into individual dimensionless subindex values () (scaled from 0 to 500) using Eq. (5.2). The overall AQI is determined as the maximum of among pollutants and is regarded as the major pollutant, expressed mathematically in Eq. (5.3).

Table 5.2: Summary of the descriptive statistics of air quality parameters for 2018-2019 averaged and 2020 across different stations in Taiwan

Parameters	Range		Mean ± Standard Deviation		Shapiro–Wilk		ANOVA
	Average 2018-2019	2020	Average 2018-2019	2020	Average 2018-2019	2020	
$PM_{2.5}$	5.00–37.00	2.00–33.00	18.46 ± 6.08	15.32 ± 7.01	*	*	#
PM_{10}	11.50–79.50	6.00–65.00	39.54 ± 12.70	30.61 ± 13.05	*	*	#
CO	0.11–0.95	0.05–0.95	0.37 ± 0.12	0.33 ± 0.13	*	*	
NO_2	0.25–28.12	0.30–27.20	12.25 ± 5.10	10.88 ± 5.10	0.12	*	
O_3	16.05–58.75	12.60–62.00	32.23 ± 6.17	30.89 ± 8.58	*	*	
SO_2	1.15–5.85	0.60–5.20	2.42 ± 0.67	2.16 ± 0.61	*	*	#

For Shapiro–Wilk test: * $p < 0.05$

For ANOVA test: # $p < 0.05$

$$AQI_i = \frac{SI_{high} - SI_{low}}{Conc_{high} - Conc_{low}} (Conc_i - Conc_{low}) + SI_{low} \quad (5.2)$$

$$AQI = max\ (AQI_1, AQI_2, \dots, AQI_i) \quad (5.3)$$

where AQI_i represents the subindex value of air pollutant i; $Conc_i$ represents the measured concentration of air pollutant i; $Conc_{high}$ and $Conc_{low}$ denote the upper and lower limit concentrations corresponding to the health category encompassing $Conc_i$, respectively; and SI_{high} and SI_{low} denote the upper and lower subindex scores corresponding to $Conc_{high}$ and $Conc_{low}$, respectively.

The reference concentrations of pollutants and corresponding subindex scores are divided into six categories, from Class I (Good): 1–50 to Class VI (Hazardous): 301–500, in association with their impacts on human health (TEPA 2006). Class I and Class II (AQI < 100) are attainment grades, while others are regarded as nonattainment, which may cause adverse health effects (Ma *et al.*, 2019).

5.2.2.4 Meteorological Normalization

To eliminate meteorological biases, a backward SRM that successively excluded nonsignificant ($p > 0.05$) meteorological variables was adopted. The monthly mean concentration of each pollutant and meteorological variable from 2018 to 2019 was used as the training dataset to formulate the best fit equations and to simulate the monthly mean BAU concentration for each pollutant in 2020 for given meteorological conditions and temporal structures (Querol *et al.*, 2021; Jephcote *et al.*, 2021). Through this process, the monthly percentage change for (i) meteorological-normalized BAU, (ii) COVID-19 (observed – meteorological-normalized BAU) and (iii) overall (total percentage change combining scenarios (i) and (ii)) for each air pollutant could be identified.

5.2.2.5 Backward Trajectory Analysis

The HYSPLIT model developed with the National Oceanic and Atmospheric Administration Air Resources Laboratory was extensively used to compute backward trajectories of air masses (Draxler & Hess, 1998; Stein *et al.*, 2015). The meteorological

fields used in the calculation of 120-h backward trajectory data are driven by the National Centers for Environmental Prediction Global Data Assimilation System (GDAS 1°x1°). The vertical transport was modeled using the isobaric option of HYSPLIT. The backward trajectories were computed every 6 h at 200 m arrival heights. The clustering method using Euclidean distance is used to reveal the dominant trajectories of air pollution events and thus help to identify the possible causes of pollution (Wang *et al.,* 2010).

5.3. Results and Analysis

5.3.1 Descriptive Analysis of Air Pollutants

The descriptive statistics for the 2018-2019 and 2020 air pollutant concentrations obtained from 69 stations across Taiwan are summarized in Table 5.2. Among the six pollutants, both PM_{10} and $PM_{2.5}$ showed the highest annual mean concentration reduction in 2020 relative to 2018-2019, by 24% and 18%, respectively, followed by SO_2, NO_2, CO and O_3, with reductions of 15%, 9.6% and 7.4% and 1.3%, respectively. Significant differences between 2018-2019 and 2020 using one-way ANOVA were observed in the parameters with remarkable improvement, which were PM_{10}, $PM_{2.5}$ and SO_2. Since NO_2 was not normally distributed ($p < 0.05$) according to the SW normality test, Spearman correlation was used to examine the bivariate association between air pollutants and meteorological factors. To better understand the impacts of COVID-19 on the atmospheric environment, spatiotemporal analysis of each pollutant was performed.

5.3.1.1 Spatiotemporal Variations in PM Concentrations

The mean concentrations of $PM_{2.5}$ and PM_{10} ranged between 5.0–37.0 μg/m^3 and 1.5–79.5 μg/m^3 in 2018-2019 and 2.0–33.0 μg/m^3 and 6.0–65.0 μg/m^3 in 2020, respectively. As shown in Figs. 5.S1 and 5.S2, high concentrations of $PM_{2.5}$ (>20.0 μg/m^3) and PM_{10} (> 30.0 μg/m^3) are usually detected in the southern region. For both PMs, a contradictory phenomenon was observed, where a deteriorating trend was shown from January to April, even after the declaration of the COVID-19 pandemic. In most of the reported literature, the impact of COVID-19 on particulate matter in other countries/major cities is significant, for instance, India ($PM_{2.5}$: ~-41%, PM_{10}: ~-52%) by Jain and Sharma (2020), Malaysia ($PM_{2.5}$:

~-30%, PM_{10}: ~-31%) by Kanniah *et al.* (2020), the Yangtze River Delta of China ($PM_{2.5}$: ~-37%, PM_{10}: ~-32%) by Li *et al.* (2020), and Bangkok, Thailand ($PM_{2.5}$: ~-41%, PM_{10}: ~-52%) by Dejchanchaiwong & Tekasakul (2021). However, in the absence of a lockdown, although some anthropogenic activities were restricted, the major industrial and economic activities were not severely disrupted (Summers *et al.,* 2020; Wu *et al.,* 2021). Thus, the improvement was less significant (< 20%) for both PMs during the first quarter of 2020 compared to other countries (Fig. 5.3). A slight increase in $PM_{2.5}$ and PM_{10} concentrations was observed in April, which might be attributed to forest fires from China (Yang *et al.,* 2020) and Indochina (Chuang *et al.,* 2020) or caused by local emissions; the underlying reasons are to be verified in the following section using HYSPLIT.

The rainy season in conjunction with the COVID-19 restrictions showed significant improvements, with mean percentage changes of up to -87% and -81% for $PM_{2.5}$ and PM_{10}, respectively. The highest improvement observed during the rainy season was in the central (mean percentage change: $PM_{2.5}$: ~-37% and PM_{10}: ~-33%) and southern (mean percentage change: $PM_{2.5}$: ~-35% and PM_{10}: ~-32%) regions, which are highly urbanized and heavily industrialized (Chen *et al.,* 2019; Huang & Hsieh, 2019). The associated meteorological impacts coupled with government measures and public awareness (such as reduced mobility and human activity) have resulted a significant improvement in PM across Taiwan.

An abnormal increase in the mean percentage change up to 42% for $PM_{2.5}$ and 37% for PM_{10} was observed in the southern region in October 2020. This month marks the start of the Asian winter monsoon, where the cold high-pressure system exits the continent toward Taiwan as the northeast wind system. This wind system enters Taiwan in the north and gradually moves southeastwards, where a turbulent wake is formed. The latter is conducive to pollution accumulation and is often linked to wind-blown dust, which increases the local PM_{10} level. During 2020, a major dust storm event arose and swept over Taiwan; which maybe caused by a strong pressure gradient, originated from the deserts of Mongolia and Kazakhstan and carried large masses of PM (Keoni, 2020; Hsu & Cheng, 2019). Under high pressure and low wind speed conditions, the atmospheric conditions are relatively stable,

causing pollutants to not thoroughly disperse and leading to the occurrence of pollutant accumulation (Maurer *et al.*, 2019). Nevertheless, due to the blocking effects of the Central Mountain Range, large concentrations of air pollutants accumulate predominantly over the central and southern regions; thus, higher concentrations (up to 70.0 μg/m^3 and 40.0 μg/m^3 for PM_{10} and $PM_{2.5}$, respectively) were observed over these two regions.

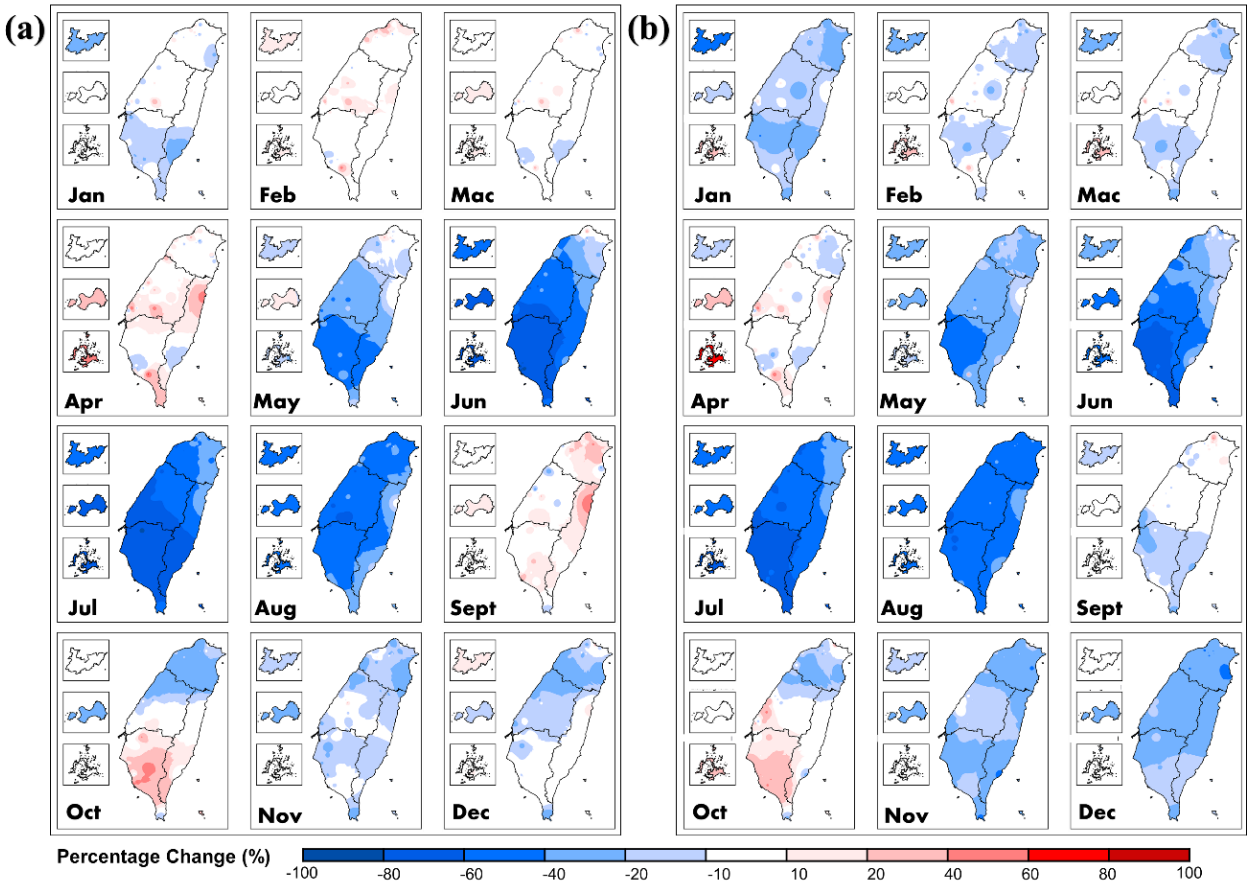

Fig. 5.3: Spatiotemporal change detection analysis for (a) $PM_{2.5}$ and (b) PM_{10} across Taiwan between 2018-2019 and 2020.

5.3.1.2 Spatiotemporal Variations in CO and NO_2 Concentrations

For CO and NO_2, the mean concentrations in 2018-2019 ranged between 0.1–1.0 ppm and 0.3–28.1 ppb, whereas in 2020, they ranged between 0.1–1.0 ppm and 0.3–27.2 ppb, respectively. As illustrated in Figs. 5.S3 and 5.S4, the mean concentrations of CO and NO_2

are usually in compliance with the Taiwan national standard (CO: ≤ 4.4 ppm and NO_2: ≤ 30 ppb). In agreement with most of the reported literature, an improving trend across Taiwan from January to April 2020 for CO and NO_2 was observed, with mean percentage reductions of up to -11%, particularly in the northern region (Fig. 5.4). The decreases in CO and NO_2 were found to be highly associated with reduced mobility and transportation emissions as a result of government measures for combating COVID-19 transmission. As the northern region is the most densely populated region in Taiwan (with a population of more than 10 million or approximately 40% of the whole Taiwan population), improvement due to reduced mobility is particularly remarkable in this region. Therefore, to investigate and validate the impact of traffic volume, a detailed transportation usage rate was collected and discussed in section 3.2.

During the rainy season, a similar phenomenon with PMs occurred, where significant improvements in CO and NO_2 concentrations associated with meteorological impacts were observed, with reductions of up to 62% and 47%, respectively. However, a substantial increase in CO in September 2020 over northern and central western Taiwan was observed. This month is the transition period between the rainy summer and the dry winter season, which explains the mixed changes in different air pollutants. The increase in CO and NO_2 concentrations during September 2020 might be due to the diminishing wet deposition ability of precipitation. In early October, the strong winter monsoon cleared out the pollutants in the north, and these pollutants began to accumulate over the southwestern region (concentrations of CO and NO_2 up to 0.58 ppm and 28 ppb, respectively). This might be due to the long-range transportation pollution from East Asia as an effect of the summer-winter transition period.

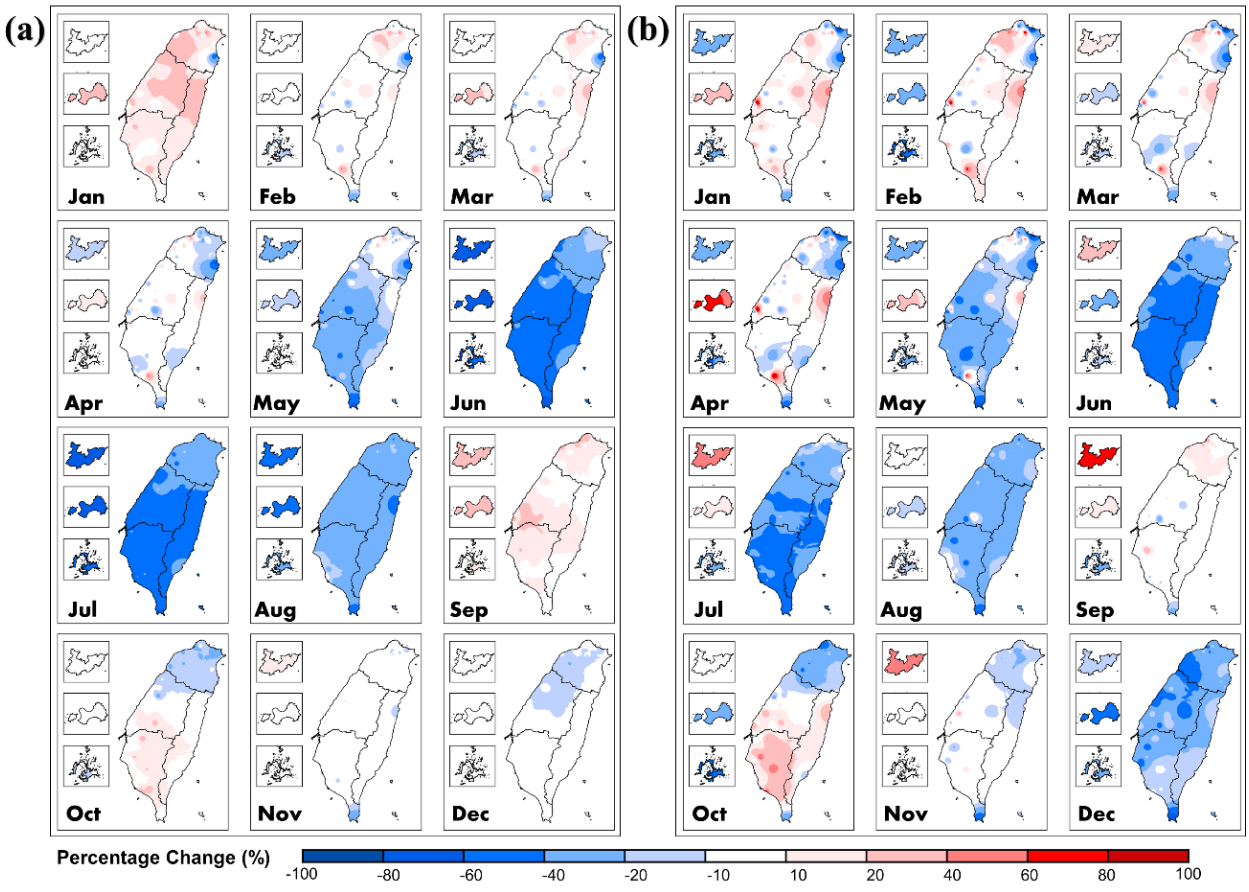

Fig. 5.4: Spatiotemporal change detection analysis for (a) CO and (b) NO_2 across Taiwan between 2018-2019 and 2020.

5.3.1.3 Spatiotemporal variations in the O_3 and SO_2 concentrations

The mean concentrations of O_3 and SO_2 in 2018-2019 ranged between 16.1–58.8 ppb and 1.2–5.9 ppb, whereas in 2020, they ranged between 12.6–62.0 ppb and 0.6–5.2 ppb, respectively. O_3 has emerged as one of the major pollutants in Taiwan and has been addressed effectively, and it has progressively increased in the past decade (Qiu *et al.*, 2021). As shown Fig. 5.5(a), in contrast to the NO_2 observation, the mean concentration of O_3 showed a significant increase (approximately 20-30%) with a mean concentration ranging between 40.0-60.0 ppb (Fig. 5.S5) in 2020 April, and similar observations have been reported worldwide (Li *et al.*, 2020; Siciliano *et al.*, 2020; Cazorla *et al.*, 2021). O_3 is a secondary atmospheric pollutant that is formed during the complex photochemical reactions between

oxides of nitrogen and volatile organic compounds; therefore, the reduction in NO_2 subsequently leads to an increased ozone concentration.

The main sources of SO_2 are formed by burning sulfur-containing fossil fuels (particularly coal) and residual fuels used in shipping and by metal smelting or other industrial processes (Merico *et al.,* 2016). Due to continuous efforts of the Taiwanese government to deploy combinations of policies and legislative initiatives to boost the execution of renewable energy sources and gas-fired plants in order to replace coal-fired power generation (Kung & McCarl, 2020), the mean concentration of SO_2 is always in compliance with the Taiwanese national standard (≤20.0 ppb), as illustrated in Fig. 5.S6, and continuous improvement/reduction is observed in Fig. 5.5(b).

During the rainy season, wet deposition is less significant for both O_3 and SO_2 than for other air pollutants, with mean percentage changes of -7.4% and -15%, respectively. An abnormal increase up to 52% was observed in O_3 in September and October, which may have been caused by the similar factors mentioned in sections 5.3.1.1 and 5.3.1.2. In contrast, because SO_2 is a short-lived gas (Wang *et al.,* 2018), the impact of its long-range transport was insignificant; therefore, no abnormal phenomenon was observed compared to other air pollutants.

5.3.2 Contribution of the Nonattainment Pollutants

The contribution of major pollutants to the nonattainment days across Taiwan for 2018-2019 and 2020 is presented in Fig. 5.6(a). A significant improvement was observed, where the total nonattainment days decreased from 3,736 in 2018-2019 to 2,470 in 2020, with a total reduction of 34%. In both 2018-2019 and 2020, the occurrence of nonattainment days in the central and southern regions was observed to be much higher than that in other regions, accounting for 80% and 78% in 2018-2019 and 2020, respectively. Among the six air pollutants, $PM_{2.5}$ and O_3 were observed as the major pollutants, with total nonattainment days of 1,894 and 1,812 (775 and 1,695), contributing 51% and 49% (31% and 69%) in 2018-2019 (2020), respectively, whereas the remaining pollutants had almost negligible contributions (<1%) to the total nonattainment days.

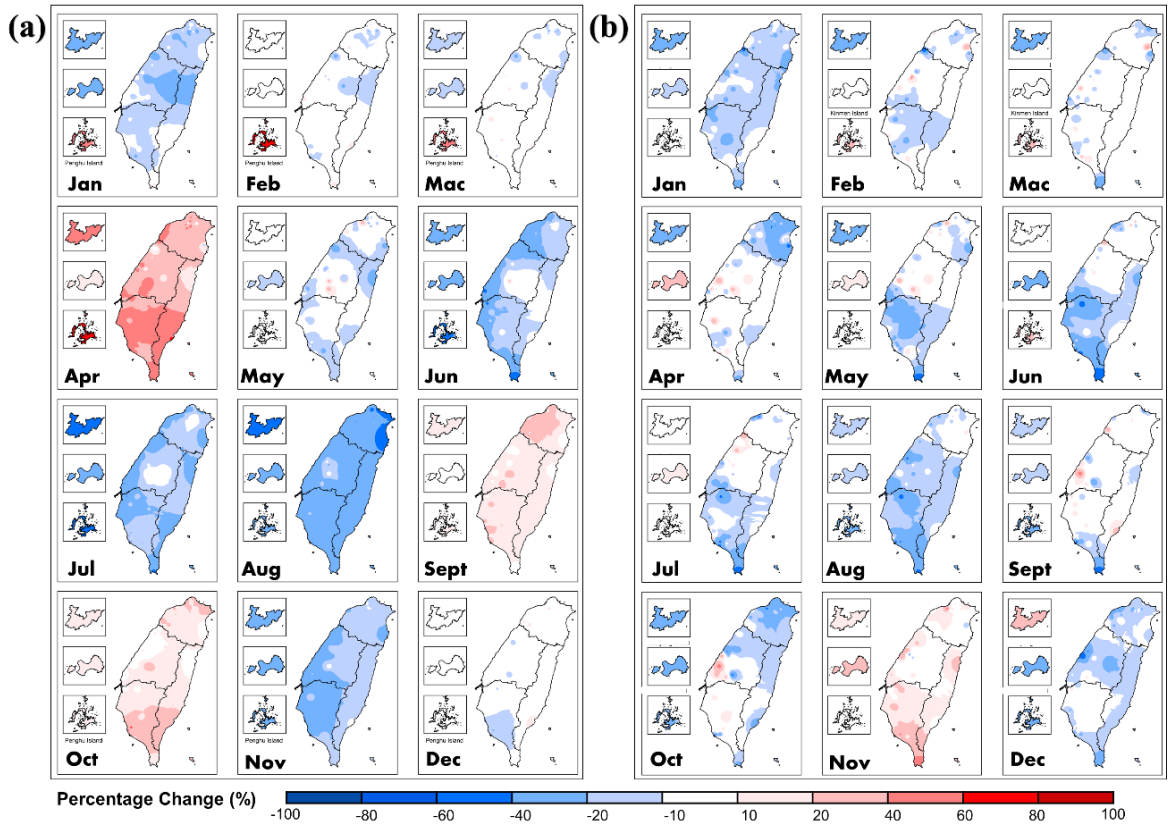

Fig. 5.5: Spatiotemporal change detection analysis for (a) O_3 and (b) SO_2 across Taiwan between 2018-2019 and 2020.

Compared to 2018-2019, a significant improvement was observed, where the total nonattainment days decreased by 33.8% in 2020, and the nonattainment days caused by $PM_{2.5}$ decreased significantly by 59.1%, while ozone decreased by 6.0%. Seasonal meteorological impacts on air pollutants have been studied extensively (Yousefian *et al.*, 2020; Liu *et al.*, 2020); however, due to their complex, coupled, and adaptive interactions and dynamic characteristics, the reported findings may vary according to geographical region and intensity of meteorological parameters (Tfwala *et al.*, 2017). As shown in Fig. 5.6(b), the worst air quality (mainly due to $PM_{2.5}$) across Taiwan usually occurred during the dry cold season, with a total number of nonattainment days of 2,517 and 1,602 in 2018-2019 and 2020 (accounting for approximately 60% in both periods), respectively. High $PM_{2.5}$ concentrations were usually detected during the dry cold season, which may have been due to the strong

thermal inversion and low mixing layer height, leading PMs to be trapped and accumulate in the troposphere (Sanguineti *et al.,* 2020). During the wet season, PM concentrations were effectively decreased through wet deposition (Wang & Ogawa, 2015). In contrast, nonattainment days caused by O_3 were observed to occur mainly during the wet–warm season, as meteorological parameters (*e.g.,* $T_{\_atm}$, GR, SH) are more suitable for photochemical reactions (Cheng *et al.*, 2022). However, an unprecedented spike in O_3 was observed in April and September 2020, with an almost 2-fold increase as compared to base year. To identify the possible reasons, backward trajectory simulation using the HYSPLIT model was constructed and performed (Sari *et al.,* 2020; Shan *et al.,* 2009).

5.4 Discussion of Findings

5.4.1 Impact of the Traffic Volume

The monthly passenger volume and percentage change between 2018-2019 and 2020 for roadway, railway, air, and waterway transportation are presented in Fig. 5.7. While most of the people were largely unaware of the emerging crisis, the Taiwanese government had implemented strict enforcement of border control measures for immigration entry since January 2020, which resulted in a conspicuous and significant downward trend in all transportation modes in 2020 compared to 2018-2019 (Cheng *et al.,* 2020). The official declaration of the COVID-19 outbreaks as a pandemic, which was made by the WHO on 11 March, promoted restrictive measures (*e.g.,* closure of bars and nightclubs and crowd control at hotspots); these measures were eventually imposed by the Taiwanese government to prevent cross-infection transmission within the community and led to minimal community mobility in April for all transportation modes. The use rates of roadway, railway, air, and waterway transportation were reduced by 32%, 34%, 82%, and 64%, respectively.

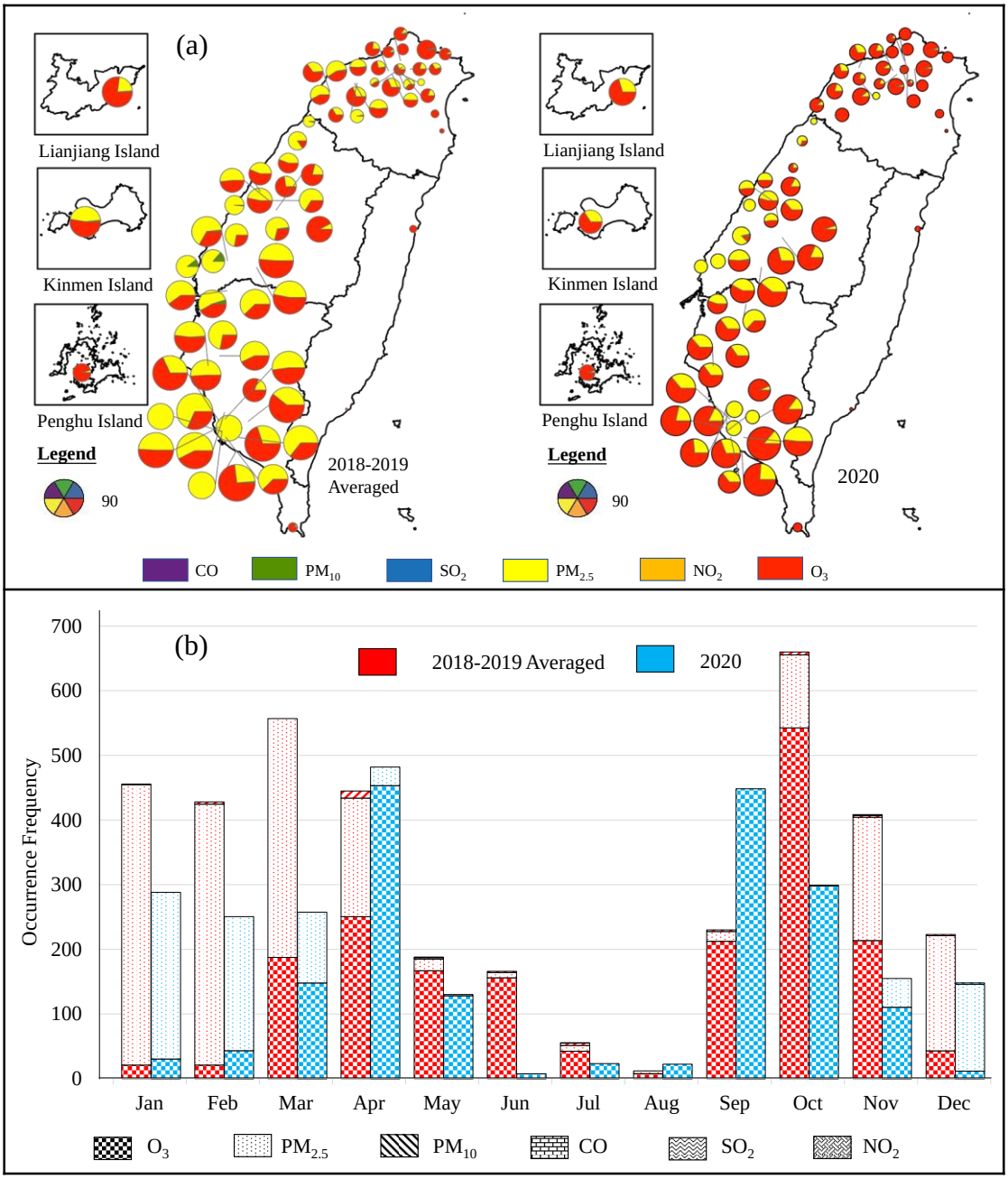

Fig. 5.6: Average nonattainment frequency of air pollutants in Taiwan for 2018-2019 and 2020 (a) according to region and (b) according to month. The relative size of the pie chart corresponds to the occurrence of nonattainment frequency. The purple, green, blue, yellow, orange, and red pie chart sectors represent the occurrence of nonattainment days caused by CO, PM_{10}, SO_2, $PM_{2.5}$, NO_2 and O_3, respectively.

As the nationwide COVID-19 condition became relatively more stable, the government eased the restrictions, and a steady upward trend for roadway and railway transportation was observed from May to July; the trend remained relatively stable from August to December. Although international flights were severely disrupted (almost at a standstill after April), the Taiwanese government focused on promoting domestic tourism to boost the local economy and business with support programs and safety measures, which resulted in a strong upward trend in both local flights and water transportation from May to September, reaching a peak during the summer holiday season (August) and gradually decreasing until December.

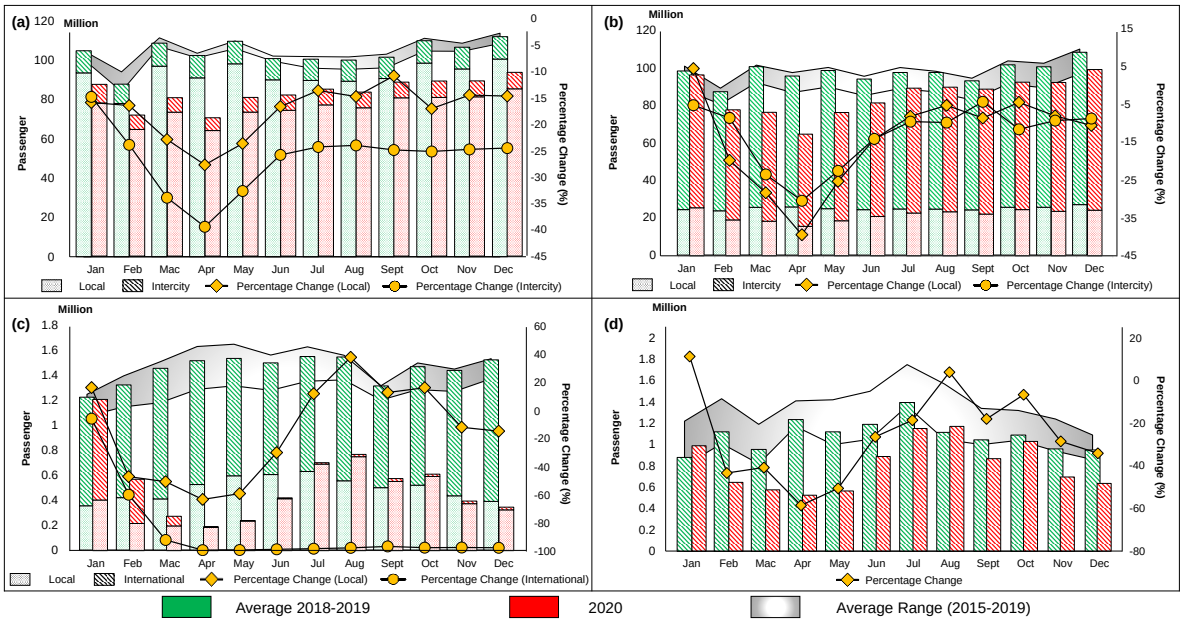

Fig. 5.7 Monthly variation in public transportation passenger volume for (a) roadway, (b) railway, (c) air and (d) waterway transportation across Taiwan.

Spearman correlation was performed to investigate the relationship between transportation volume and air pollutants, as presented in Fig. 5.8. Although there were no lockdowns or enforced human mobility restrictions imposed by the Taiwan Government during 2020, as shown in Fig. 5.7, significant changes in traffic volume were observed. Therefore, to incorporate these observed changes to provide a comprehensive evaluation of the nexus of air pollutants with traffic volume, the monthly mean data between 2018 and

2020 were used. Most of the air pollutants were positively correlated with different transportation modes, except for local flights. Although SO_2, PM_{10} and $PM_{2.5}$ showed high correlations with different transportation modes, the changes were inconsistent with the transportation usage volume. Conversely, the change trends of the NO_2 and CO concentrations (major pollutants emitted from transportation) that demonstrate substantial correlations with roadway and air transportation were congruent with the transportation usage volume, except during the wet season (May to August). Similar findings were reported by Gao *et al.* (2021) and Tian *et al.* (2021) in China and Canada during the COVID-19 period, respectively, where NO_2 and CO were fairly correlated with the traffic volume, advocating for the importance of proper public transportation planning/design to address NO_2 and CO pollution. There was no statistical correlation observed between O_3 and traffic volume; however, the abnormally high concentration up to 62 ppm observed in April may have been caused by reduced mobility (Siciliano *et al.,* 2020). As most of the monitoring stations are located in urban areas, ozone production may be VOC-limited; therefore, the increase in O_3 concentrations might have been caused by reduced NO_2 concentrations due to reduced mobility (Sicard *et al.,* 2020; Cazorla *et al.,* 2021).

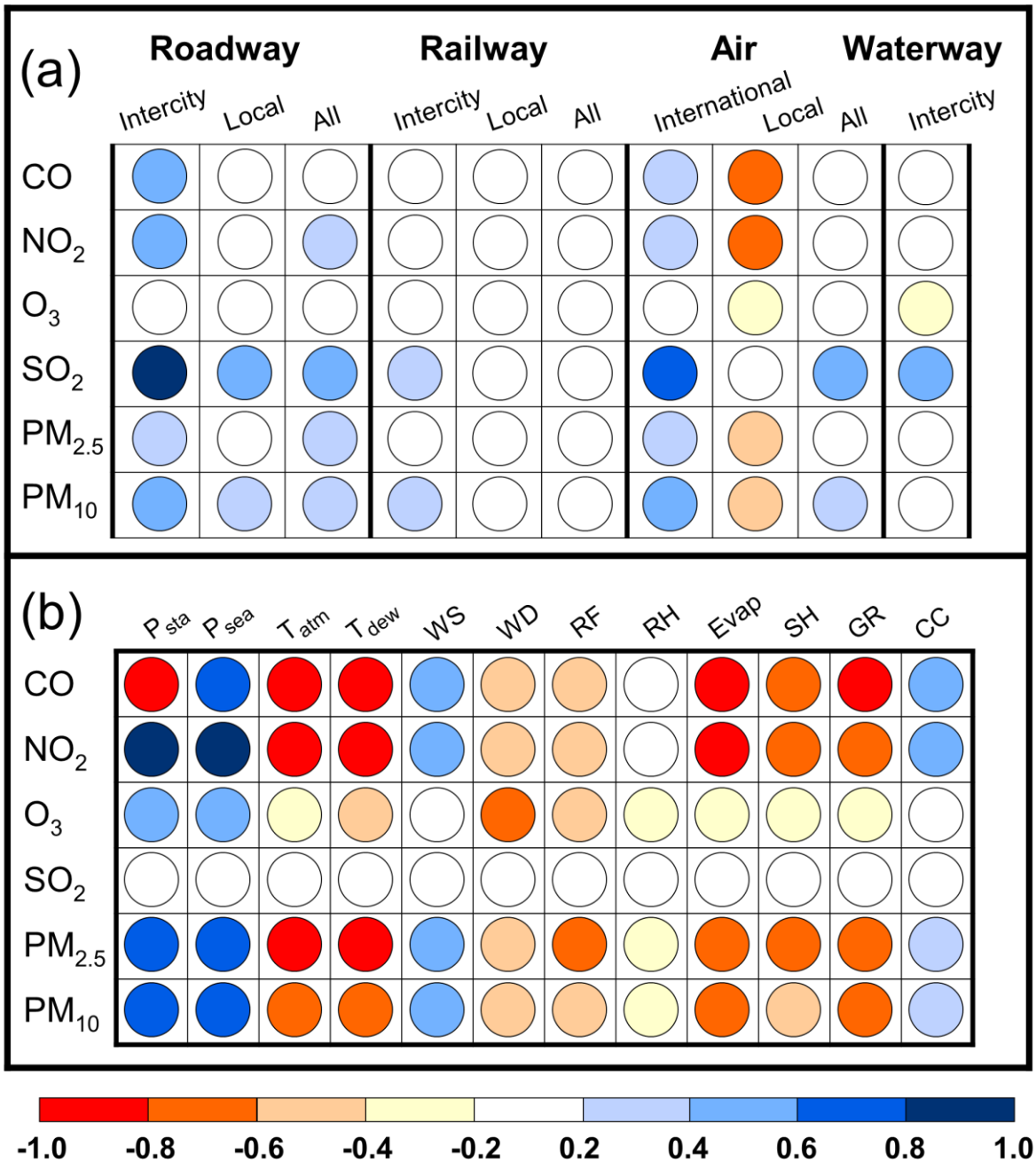

Fig 5.8: Spearman correlation heatmap between air pollutants and (a) traffic volume and (b) meteorological parameters across Taiwan.

5.4.2 Meteorological-normalized BAU Scenario

To eliminate meteorological biases during the quantification of COVID-19 impacts on air quality (improvement/degradation), this study constructed SRM models by utilizing 12 meteorological parameters for each studied air pollutant. The correlations between air pollutants and selected meteorological parameters are presented in Fig. 5.8(b). The mean values at all available air pollutants and meteorological stations were used (Teng *et al.* 2018), as the focus of the study is to find the overall relationship among them across Taiwan despite the different numbers of air quality (n=69) and meteorological stations (n=224). Similar approaches were also reported by He *et al.* (2020), Kwon *et al.* (2020) and Zhu *et al.* (2021). Therefore, the representative air pollutant concentration and meteorological parameter value were defined by averaging the monthly mean concentration/value of all the available monitoring stations from 2018 to 2020. Meteorological parameters have a stronger correlation with air pollutants (except for SO_2) than traffic volume for different transportation modes in Taiwan; however, contradictory findings were reported by Gao *et al.* (2021) for China, as the magnitude of the impact may vary across regions. Most of the meteorological parameters were negatively correlated with air pollutants, except for pressures, WS and CC, in agreement with the majority of the literature (Peng *et al.,* 2020; Liu *et al.,* 2020; Talbot *et al.,* 2021).

Radar diagrams were used to illustrate and compare the mean annual percentage change between 2018-2019 and 2020 among different scenarios, as shown in Fig. 5.9b. Under the meteorologically normalized BAU scenario, slight increases in the concentrations of CO, NO_2, O_3, $PM_{2.5}$, PM_{10}, and SO_2 were observed in 2020, where the mean percentage changes relative to 2018-2019 were 2.5%, 4.4%, 0.5%, 1.0%, 5.4% and 2.0%, respectively. This implied that the meteorological conditions in 2020 might have been unfavorable for the dispersion and transportation of air pollutants. Similar findings have also been reported in neighboring areas, such as cities in China (Hu *et al.* 2021; Bai *et al.* 2022). On the other hand, under the COVID-19 scenario, a significant reduction was observed for PM_{10}, $PM_{2.5}$, SO_2, and NO_2, with mean percentage changes relative to 2018-2019 of -36%, -26%, -27%, and -20%, respectively. The maximum reduction of these four pollutants was observed in the

wet season, contributing a 40–60% reduction in concentration. For CO, a satisfactory reduction was observed, with percentage changes of -16%, and a slight increment was observed for O_3, with 1.3%. Despite the unfavorable meteorology of 2020, significant improvements were observed among air pollutants (except for O_3) due to the reduction of anthropogenic emissions even in the absence of a lockdown. Overall, for 2020, the total change associated with the meteorological-normalized simulated air pollutant concentrations and COVID-19 scenarios, a significant reduction was observed in the mean percentage change relative to 2018-2019, with -13% and -16%, -25%, -30%, and -25% for CO NO_2, $PM_{2.5}$, PM_{10}, and SO_2, respectively, and a slight increment was observed for O_3, with 1.8%.

Table 5.3: Performance and equation of the constructed SRM for each air pollutant

Parameter	R^2	Standard Error
CO	0.843	3.317
NO_2	0.867	1.080
O_3	0.827	2.315
$PM_{2.5}$	0.875	2.235
PM_{10}	0.830	4.585
SO_2	0.634	0.186

$$CO = -0.016T_{atm} - 0.116WS + 0.003P_{sea} - 3.0411 \quad (4)$$

$$NO_2 = -4.910P_{sea} - 0.292RH + 0.348P_{sta} + 2.376CC + 0.051SH - 0.021GR - 312.689 \quad (5)$$

$$O_3 = -0.124WD - 8.218CC - 0.373SH + 0.168Evap - 0.009RF + 0.058GR - 0.469RH + 148.078 \quad (6)$$

$$PM_{2.5} = -2.963P_{sta} - 0.053WD + 1.419P_{sea} - 9.831WS - 2.366T_{dew} - 0.0060RF + 1331.758 \quad (7)$$

$$PM_{10} = 1.01P_{sta} - 0.091WD - 13.530WS - 1.534RH - 776.544 \quad (8)$$

$$SO_2 = -0.189T_{atm} - 1.469WS + 0.264P_{sea} - 0.091RH - 0.523P_{sta} + 0.463CC + 0.014SH - 0.004GR + 217.791 \quad (9)$$

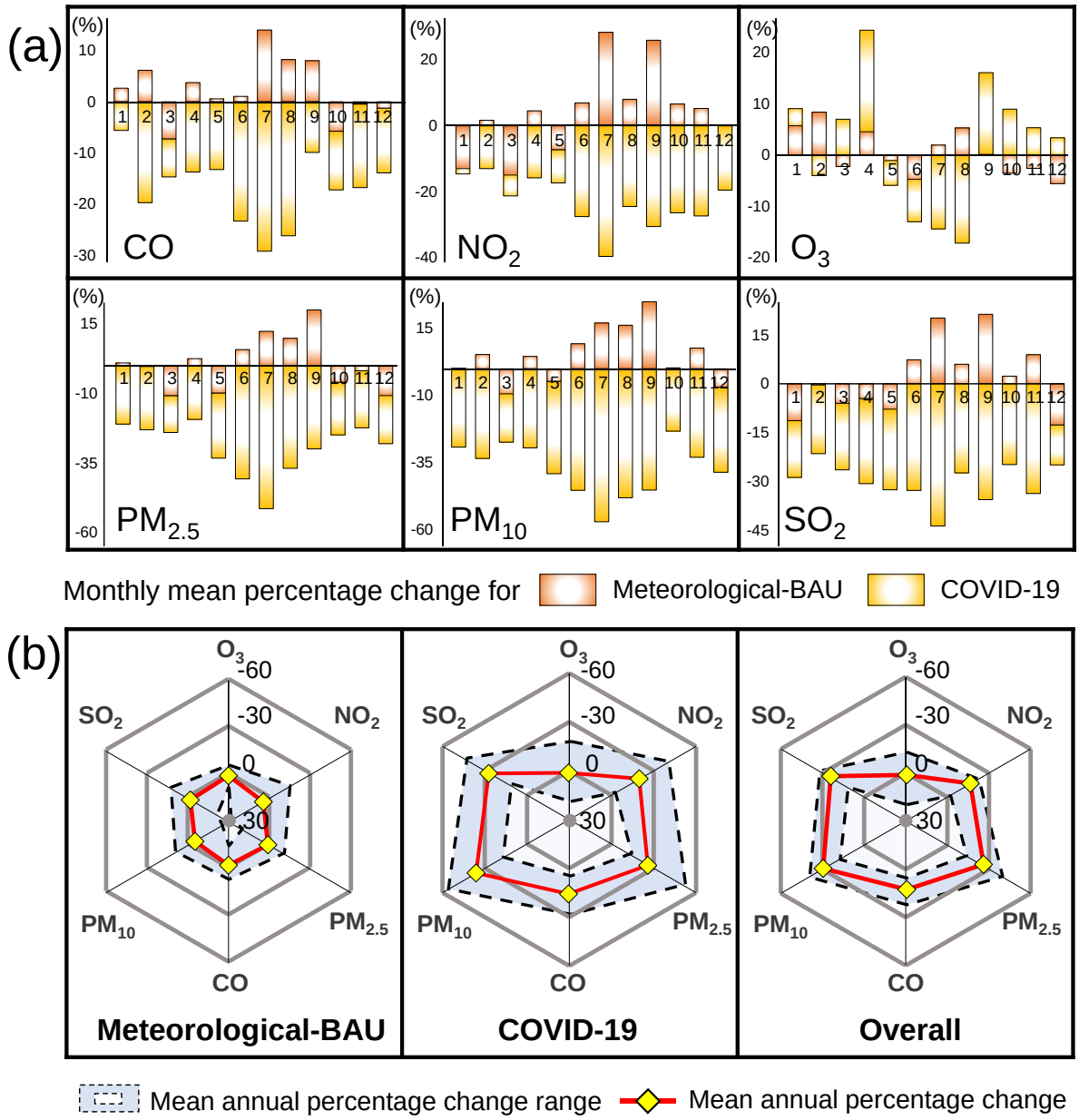

Fig. 5.9: Percentage change of six air pollutants both (a) monthly and (b) annually based on meteorological-normalized BAU, COVID-impact and actual observed scenarios between 2018-2019 and 2020.

5.4.3 Backward Trajectory Analysis of the Anomaly Months

In this section, backward trajectory HYSPLIT analysis is used to identify the possible air mass origin affecting the air quality over Taiwan during April and September, as abnormal increments of up to 80% in pollutants were observed in 2020 compared to 2018-2019 despite the reduced mobility and implementation of restrictive measures. Applying a similar approach in section 3.1, 2018-2019 was selected to represent the BAU scenario, whereas 2020 was selected as the COVID-19 scenario. For the April scenario, Nantou station in central Taiwan was selected as the receptor site due to the unusually high $PM_{2.5}$ and PM_{10} recorded in the spatiotemporal change percentage between 2018-2019 and 2020 (see Fig. 5.3). For the September scenario, Wanli station in northern Taiwan was selected as the receptor site due to the substantial increase in CO and NO_2 (see Fig. 5.4). This station is also a background station that is often used to identify the transboundary pollution scenario from East China. Fig. 5.10 presents the clustered 120-h trajectory pathways driven by the GDAS meteorological dataset at 1.0° x 1.0° in April and September.

As shown in Fig. 5.10 (a), the air mass reaching Nantou station in April 2020 is mostly from the northeast direction, with the highest proportion accounting for C1 (88%), followed by C3 (8.0%) and C2 (4.0%). These three clusters shared a very similar trajectory pathway, indicating that they might be driven by the same synoptic weather pattern. This weather pattern features a weak anticyclone over the Asian continent and the Pacific subtropical high-pressure system that does not have an apparent influence in Taiwan, which frequently occurs during the seasonal transition period in April (Hsu & Cheng, 2019). Although the trajectories do not originate directly from the continent, the prevailing northeasterly winds associated with the eastward-propagating anticyclone from the Taiwan Strait make it possible to inject long-range transported pollutants into Taiwan. In addition, as the lockdown measures and travel restrictions of neighboring major cities were gradually lifted in early April for economic recovery, an apparent rebound effect was detected (Gao *et al.,* 2021; Hasnain *et al.,* 2021), and trajectories of polluted air masses to central Taiwan were observed originating from neighboring major cities (Wu & Huang, 2021). When the prevailing northeasterly wind is obstructed by the Central Mountain Range, low wind speeds and strong subsidence occur

over the leeside of the mountain, often leading to serious $PM_{2.5}$ accumulations in central and southern Taiwan. In contrast, the backward trajectories in April 2018-2019 clearly demonstrated the mixture of oceanic air masses from the western Pacific Ocean, C2 (10%), and South China Sea, C3 (18%). The westward stretching of the Pacific subtropical high-pressure system slightly changed the prevailing wind in Taiwan to southeasterly and southerly flows, bringing more pristine air to Taiwan and eventually reducing the PM and gas pollutant concentrations.

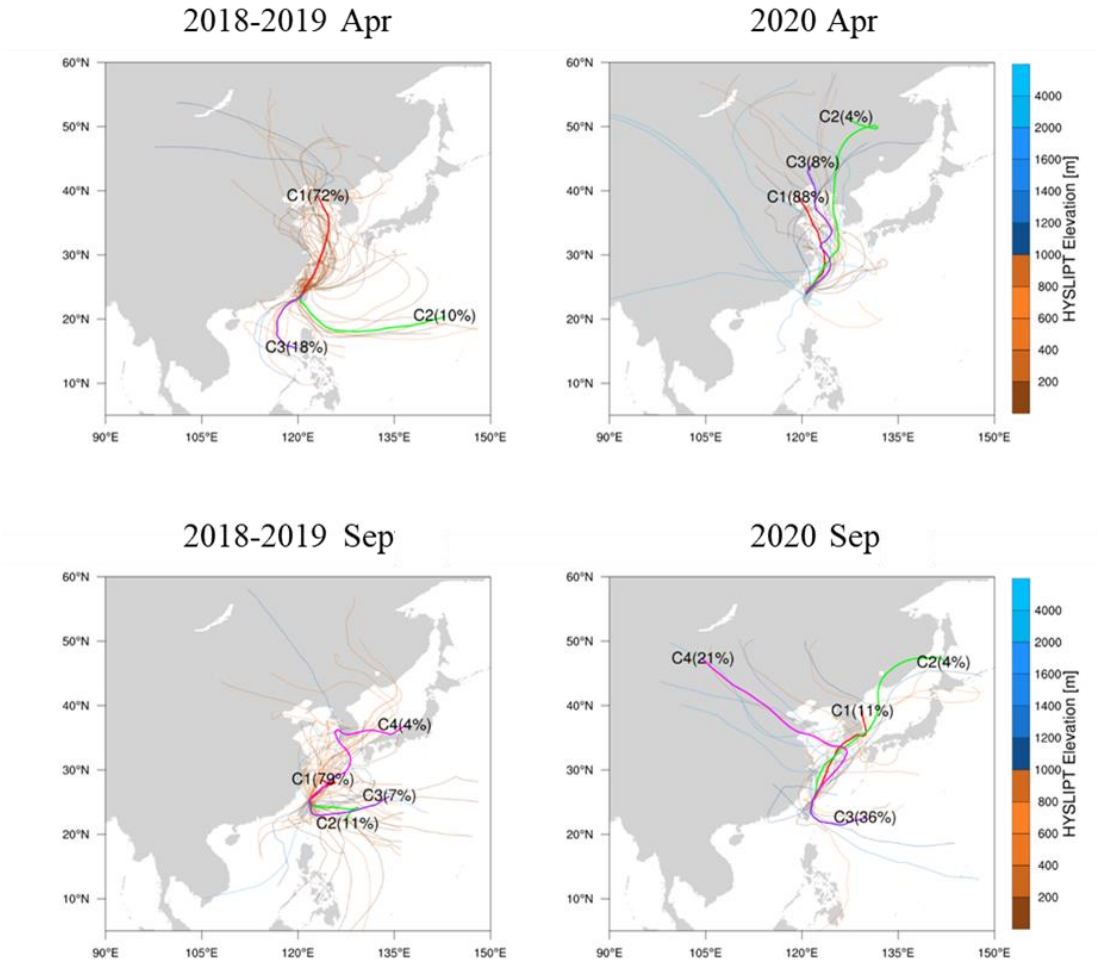

Fig. 5.10: 120-h HYSPLIT backward trajectory driven by GDAS meteorological data at 1.0°x1.0° in April and September separated for the BAU scenario in 2018-2019 and the COVID-19 scenario in 2020.

For the September scenario, the backward trajectories C4 (21%) at Wanli station in 2020 clearly show that the possible air mass trajectories are different compared to 2018-2019. Unprecedented elevated ozone concentrations associated with Asian high-pressure ridge incidents were reported and carried from the continent toward Taiwan in high-level (>1 km) trajectories, particularly in northern and eastern Taiwan, contributing to long-range transboundary air pollution in September 2020 (Keoni, 2020; Wang *et al.,* 2016; Tseng *et al.*, 2019). Meanwhile, backward trajectories in September 2018-2019 were mainly dominated by oceanic air masses from the East China Sea (C1: 79%) and the western Pacific Ocean (C2: 11% & C3: 7%), which are typically cleaner than continental air masses, resulting in lower observed air pollution concentrations during this period (Golubeva *et al.,* 2013).

5.4.4 Implications and Limitations

The drastic disruption in normal routine due to the COVID-19 pandemic has provided a unique opportunity to explore the impact of transportation and meteorology on air quality. According to the findings, it could be observed that the impact of reduced transportation usage and a "new normal lifestyle", such as social distancing, has a more significant impact than meteorology on air quality improvement, in agreement with the findings reported by Nguyen *et al.* (2020). As demonstrated in Taiwan, although the emission scenario from industries has insignificant changes, an approximately 52% reduction was observed in public transportation usage and may be the key driver of air quality improvements. It may be ambitious to implement policies restricting traffic mobility to sustain long-term improvements (Sokhi *et al.,* 2021); however, proper transportation system management and alternative greener fuel may be one of the most emerging topics at present that should be considered and adopted by governments worldwide for sustainable air quality management. The reduced precipitation in 2020 might have been due to climate change (Yeh & Huang, 2019), and this phenomenon is expected to continue and may worsen air quality over the long-term (Kinney, 2021). There have been ongoing global and regional efforts to address climate change impacts on air quality (*e.g.,* Kyoto Protocol, Paris Agreement, Gothenburg Protocol). However, climate change-driven air pollution mortality has not yet been addressed (Hong *et al.,* 2019) and further contributes to the degradation of the environment and human

health. Therefore, decision makers must consider these important implications when formulating and implementing sustainable air quality policies in response to unavoidable climate change in order to maintain/improve air quality in the absence of lockdowns and prevent adverse impacts on the economy and society.

Nevertheless, there are several limitations in this study that must be acknowledged. Due to the limitation of the dataset available, this study utilized only public transportation users. According to the Ministry of Transportation and Communication of Taiwan, the public transportation use rate was approximately 35% for urban cities, while the overall use rate across Taiwan was 18% (Department of Statistics, 2016). Therefore, the impact of private transportation may not be reflected in this study. Second, as the intention of the study was to evaluate the impact of COVID-19 under the meteorological-normalized scenario, this study utilized only the mean monthly concentrations of air pollutants and meteorological parameters across Taiwan, which may not be capable of providing accurate simulations at high temporal (such as daily or hourly) or spatial (according to station) variations. For the meteorologically normalized BAU scenario, this study assumes that there are insignificant changes in the environmental protection activities/policies performed by the government and the public, as well as the technologies for electricity generation, industrial processes, etc. Based on the Taiwan Energy Statistic Handbook, the average total domestic energy consumption in 2018-2019 was 86.1 million kiloliter of oil equivalent (KLOE), whereas in 2020, it was 85.4 million KLOE, with less than a 1% difference. The difference in coal and coal product usage for electricity generation (known to be more polluting than any other fossil fuel) in 2018-2019 and 2020 is insignificant, with an approximately 1% difference. Therefore, in this study, the emissions in 2020 are assumed to be consistent with those in 2018-2019. In addition, there are no detailed data available on the local emissions (industrial, domestic) and sudden/accidental pollution, which may have further limited the ability to identify the underlying reasons for the improvements in the study. Although HYSPLIT was applied, but it may not be sufficient for identifying the factors underlying the abnormal increase of up to 80% in pollutants that was observed in April and September of 2020 compared to 2018-2019.

5.5 Conclusion

With the current need to decrease air pollution risks in regard to public health and the environment, air quality management is an emerging issue that has attracted global attention. The occurrence of the COVID-19 pandemic has indeed had a profound impact on many aspects of life and the economy; notably, due to the new normal lifestyle, nature has been reclaiming itself even in the absence of a strict lockdown (Muhammad *et al.*, 2020). This study demonstrated and contributed to the spatiotemporal impact of COVID-19 on air quality variation across different regions in Taiwan and provided a preliminary monthly comparative analysis between air pollutant concentrations in 2020 and 2018-2019.

In this study, substantial improvements were observed in the studied air pollutants, wherein both PM_{10} and $PM_{2.5}$ showed the highest annual mean concentration reduction in 2020 relative to 2018-2019, by 24% and 18%, respectively, followed by SO_2, NO_2, CO and O_3, with reductions of 15%, 9.6% and 7.4% and 1.3%, respectively, even in the absence of lockdown. The occurrence frequency of air pollutants that may cause adverse health effects decreased by more than 30% in 2020 compared to 2018-2019, particularly in O_3 and $PM_{2.5}$. This study makes an important contribution to the literature as it is the first to investigate the impact and patterns of different modes of public transportation (*i.e.*, including roadway, railway, air, and waterway) on air quality improvements in 2020. The change trends of CO and NO_2, the major pollutants emitted from the public transportation sector, were found to be in parallel with the shift in traffic volume patterns in 2020.

Similar to other reported studies, the seasonal variation in air pollutants (Figs. 5.4-5.6) and their correlations with meteorological parameters (Fig. 5.9) were found to be significant in this study. However, in 2020, although a significant improvement in air quality was observed during the rainy season, the simulated meteorologically normalized BAU air pollutant concentrations were observed to be higher than those in 2018-2019 due to reduced precipitation (approximately 240 mm) and an approximately 5% reduction in the frequency of wind speeds of less than 1.5 m/s. This may imply a delayed COVID-19 effect on the

improvement in the air quality of Taiwan compared to the immediate improvements observed in countries that imposed lockdown, a phenomenon that has yet to be reported elsewhere.

This study has revealed the long-term COVID-19 impacts on the atmospheric environment in Taiwan, incorporating public transportation use and meteorological impacts in the absence of lockdowns. The findings of this study are expected to provide comprehensive information to relevant authorities for sustainable planning on air quality management. All of these findings imply that public urban transportation sector emissions have a more significant impact than meteorological conditions in Taiwan. It is expected that the development of public transportation facilities will be further promoted in the future; therefore, to maintain or further improve the current situation, the use of energy-saving, cleaner fuel, and emission-reducing vehicles should be considered (Tian *et al.,* 2021; Muhammad *et al.,* 2020). Additionally, strategic transportation network design associated with proper traffic planning and traffic light operation for reducing traffic congestion issues (Hsieh and You 2021; Zhai *et al.* 2022), could be one of the key drivers to maintain/improve air quality. Nevertheless, although anthropogenic activity and public transportation use seem to have more significant impacts in improving air quality than meteorological parameters, the impact of climate change should be considered when formulating future policies, as increased climate variability is expected. This variability will consequently project incremental changes to air pollution concentrations that may lead to adverse effects on both the environment and human health.

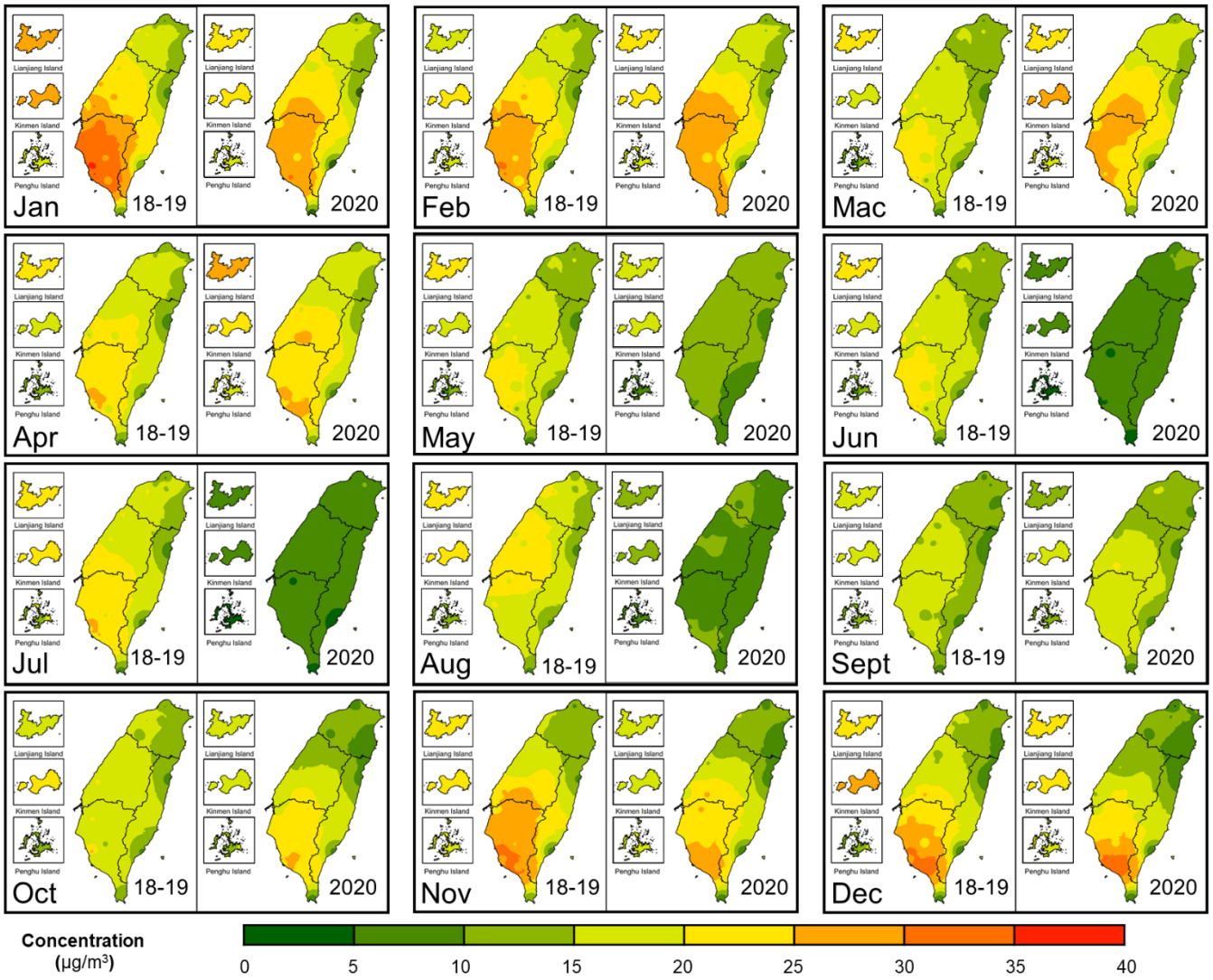

Fig. 5.S1: Spatiotemporal distribution of monthly $PM_{2.5}$ mean concentrations across Taiwan for 2018-2019 and 2020

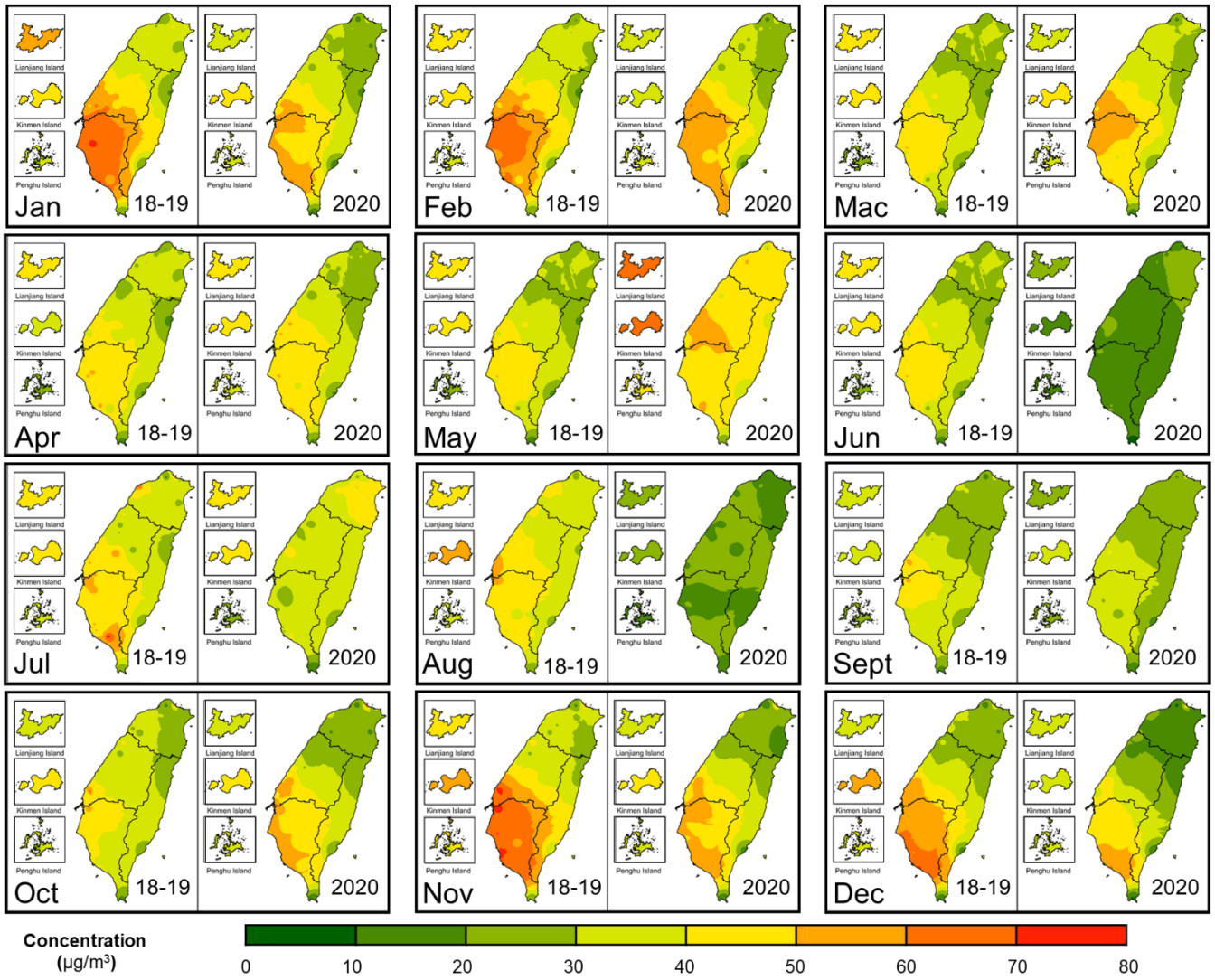

Fig. 5.S2: Spatiotemporal distribution of monthly PM_{10} mean concentrations across Taiwan for 2018-2019 and 2020

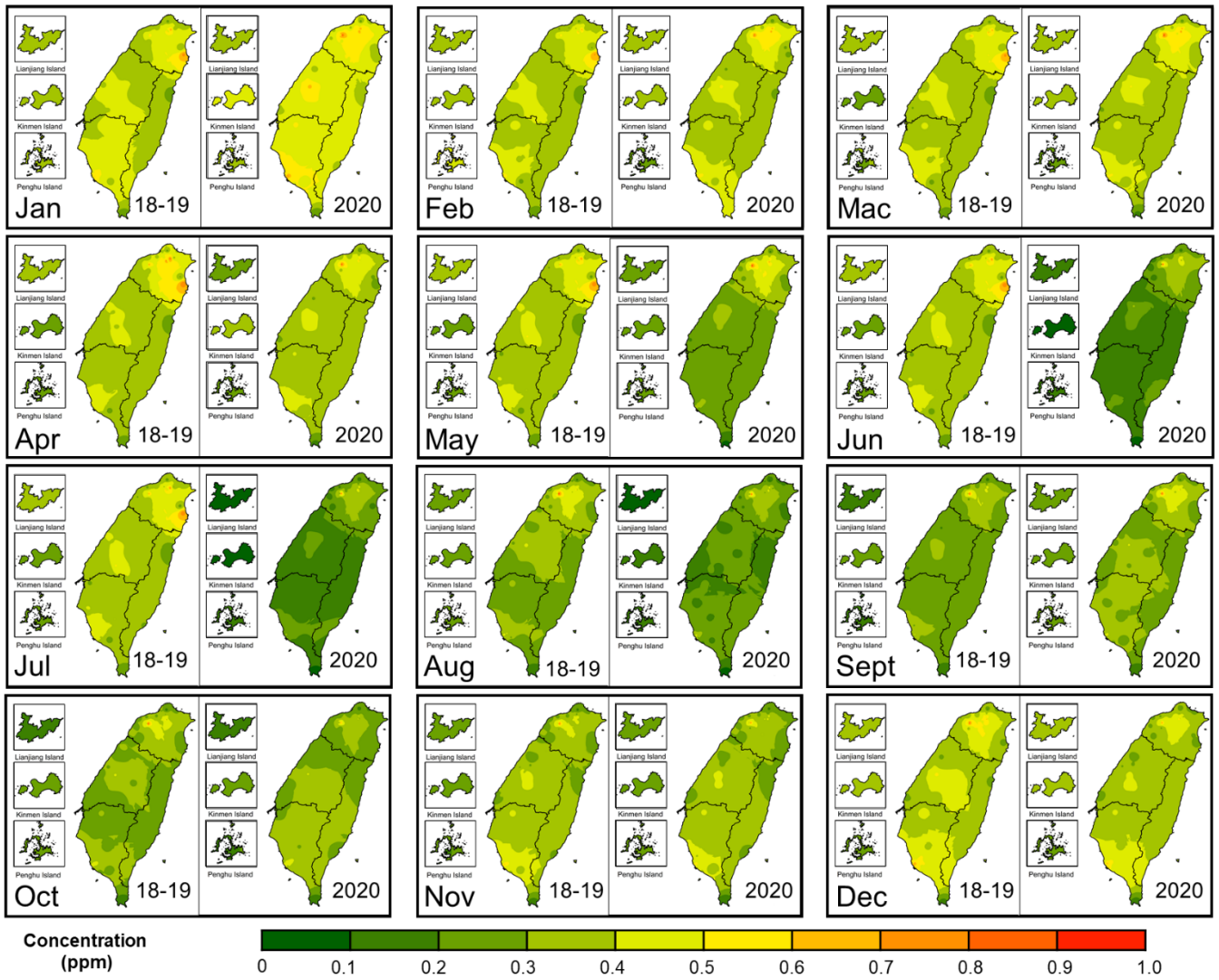

Fig. 5.S3: Spatiotemporal distribution of monthly CO mean concentrations across Taiwan for 2018-2019 and 2020

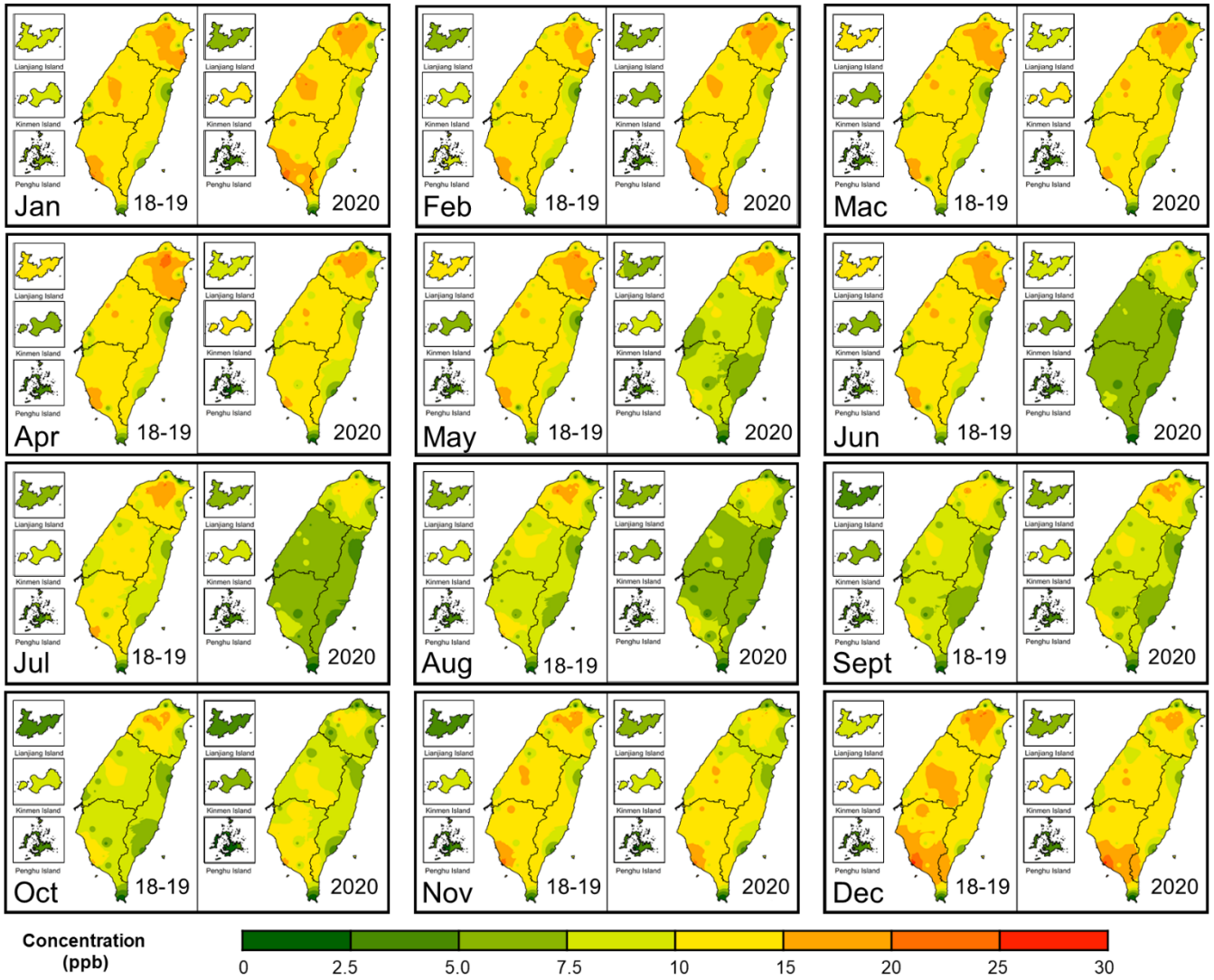

Fig. 5.S4: Spatiotemporal distribution of monthly NO_2 mean concentrations across Taiwan for 2018-2019 and 2020

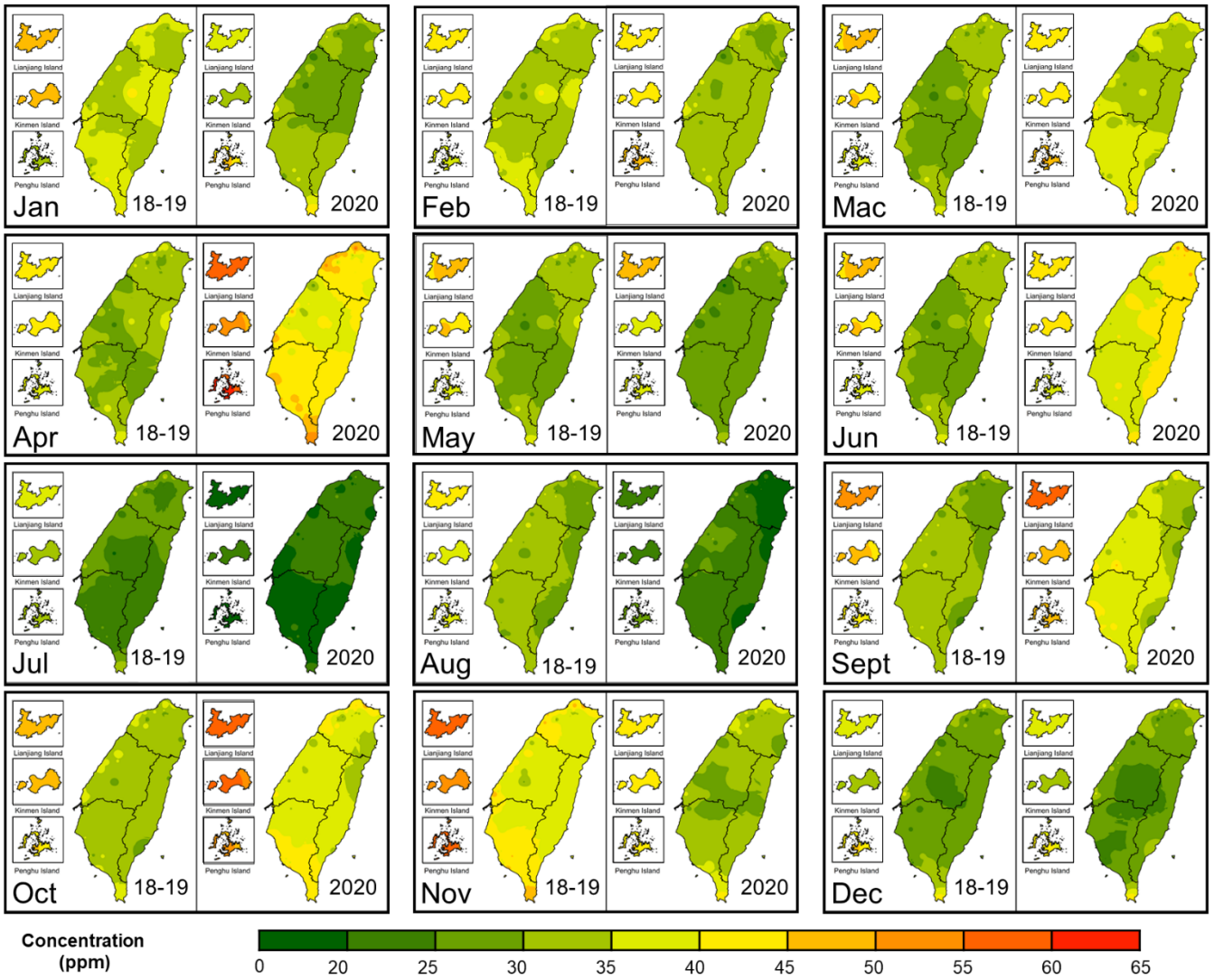

Fig. 5.5: Spatiotemporal distribution of monthly O_3 mean concentrations across Taiwan for 2018-2019 and 2020

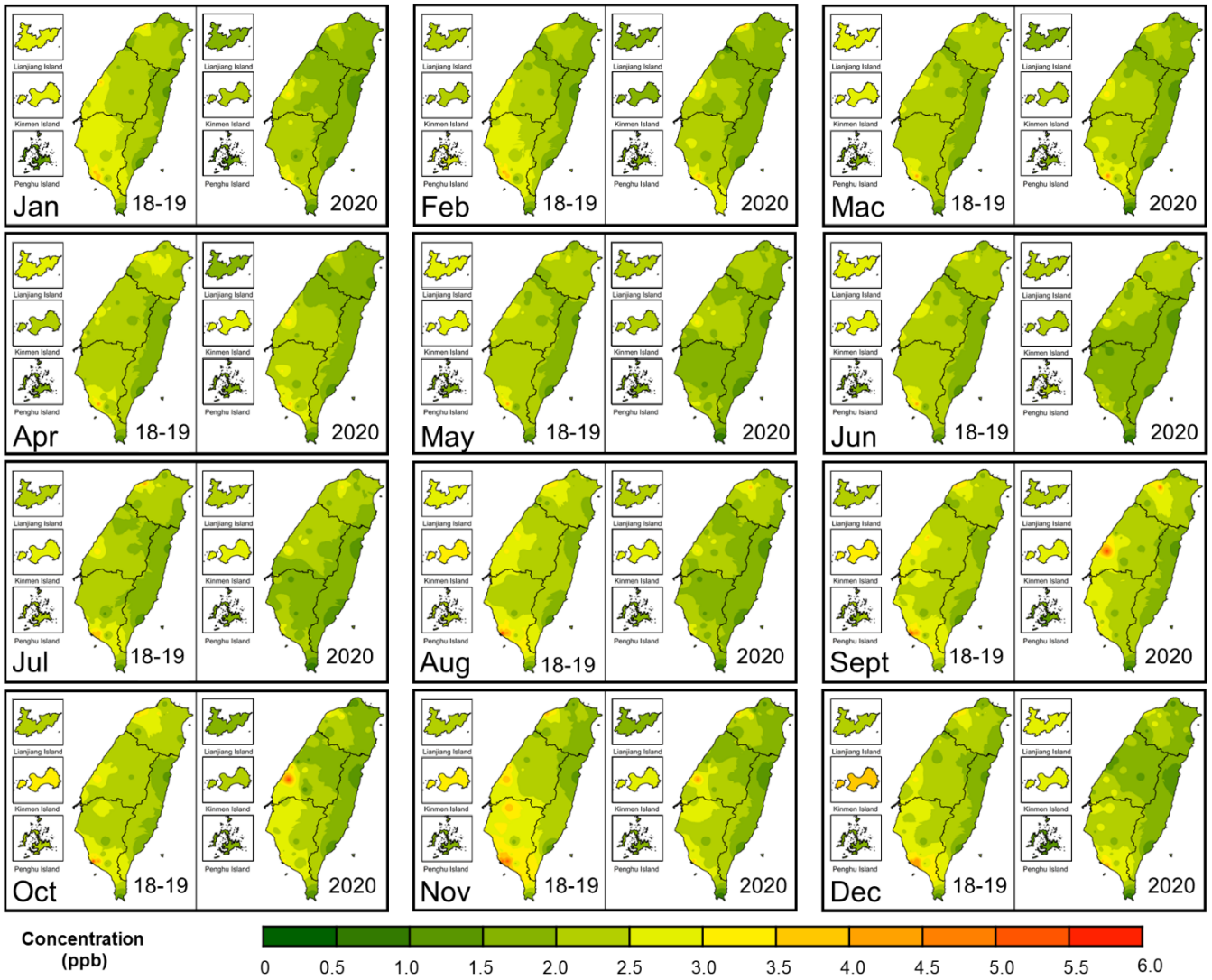

Fig. 5.S6: Spatiotemporal distribution of monthly SO_2 concentrations across Taiwan for 2018-2019 and 2020

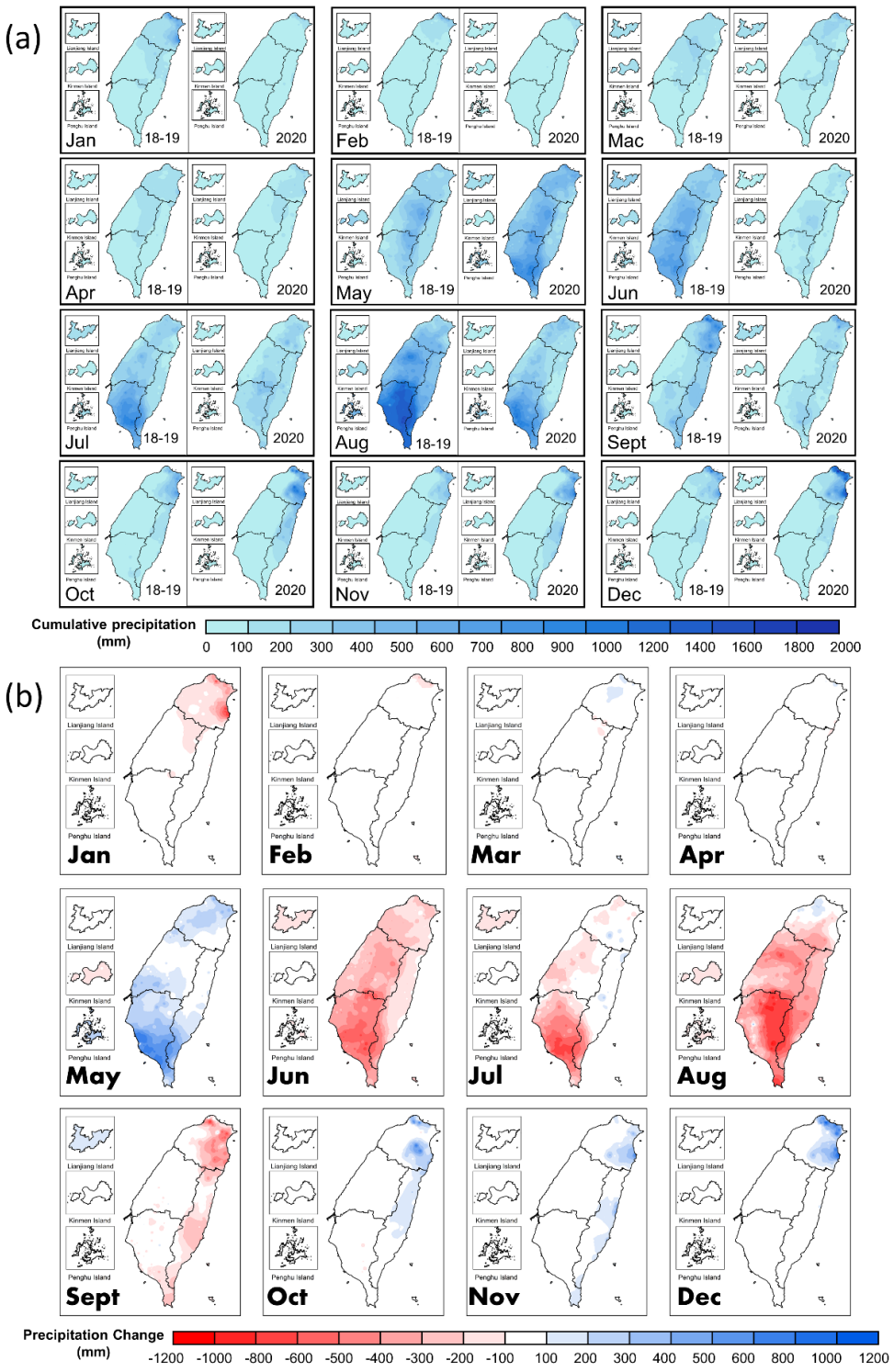

Fig. 5.S7: Spatiotemporal distribution of (i) monthly cumulative precipitation volume and (ii) precipitation change across Taiwan for 2018-2019 and 2020.

List of References

Abdullah, S., Mansor, A. A., Napi, N. N. L. M., Mansor, W. N. W., Ahmed, A. N., Ismail, M., et al., (2020). Air quality status during 2020 Malaysia Movement Control Order (MCO) due to 2019 novel coronavirus (2019-nCoV) pandemic. Science of The Total Environment, 729, 139022, doi.org/10.1016/j.scitotenv.2020.139022.

Amann, M., Purohit, P., Bhanarkar, A. D., Bertok, I., Borken-Kleefeld, J., Cofala, J., et al., (2017). Managing future air quality in megacities: A case study for Delhi. Atmospheric Environment, 161, 99-111, doi.org/10.1016/j.atmosenv.2017.04.041.

Bai, H., Gao, W., Zhang, Y., & Wang, L. (2022). Assessment of health benefit of PM2.5 reduction during COVID-19 lockdown in China and separating contributions from anthropogenic emissions and meteorology. *Journal of Environmental Sciences, 115*, 422-431, doi:10.1016/j.jes.2021.01.022.

Benis, K. Zoroufchi, Fatehifar, E., Ahmadi, J., & Rouhi, A. (2015). Optimal design of air quality monitoring network and its application in an oil refinery plant: an approach to keep health status of workers. Health Promot Perspect, 5(4), 269-279, doi:10.15171/hpp.2015.032.

Broomandi, P., Karaca, F., Nikfal, A., Jahanbakhshi, A., Tamjidi, M., & Kim, J. R. (2020). Impact of COVID-19 event on the air quality in Iran. Aerosol and Air Quality Research, 20(8), 1793-1804, doi:10.4209/aaqr.2020.05.0205.

Cazorla, M., Herrera, E., Palomeque, E., & Saud, N. (2021). What the COVID-19 lockdown revealed about photochemistry and ozone production in Quito, Ecuador. Atmospheric Pollution Research, 12(1), 124-133, doi.org/10.1016/j.apr.2020.08.028.

Chang, H.H., Meyerhoefer, C. D., & Yang, F.A. (2021). COVID-19 prevention, air pollution and transportation patterns in the absence of a lockdown. Journal of Environmental Management, 298, 113522, doi.org/10.1016/j.jenvman.2021.113522.

Chen, F.W., & Liu, C.W. (2012). Estimation of the spatial rainfall distribution using inverse distance weighting (IDW) in the middle of Taiwan. Paddy and Water Environment, 10(3), 209-222, doi:10.1007/s10333-012-0319-1.

Chen, S., Cui, K., Yu, T.Y., Chao, H.R., Hsu, Y.C., Lu, I. C., et al., (2019). A big data analysis of PM2.5 and PM10 from low cost air quality sensors near traffic areas. Aerosol and Air Quality Research, 19(8), 1721-1733, doi:10.4209/aaqr.2019.06.0328.

Chen, Y.H., & Fang, C.T. (2021). Combined interventions to suppress R0 and border quarantine to contain COVID-19 in Taiwan. Journal of the Formosan Medical Association, 120(2), 903-905, doi.org/10.1016/j.jfma.2020.08.003.

Cheng, F.-Y., Wang, Y.-T., Huang, M.-Q., Lin, P.-L., Lin, C.-H., Lin, P.-H., et al. (2022). Boundary Layer Characteristics Over Complex Terrain in Central Taiwan: Observations and Numerical Modeling. *127*(2), e2021JD035726, doi:10.1029/2021JD035726

Cheng, H.Y., Li, S.Y., & Yang, C.H. (2020). Initial rapid and proactive response for the COVID-19 outbreak - Taiwan's experience. Journal of the Formosan Medical Association, 119(4), 771-773, doi:10.1016/j.jfma.2020.03.007.

Chinese air pollution to blow into Taiwan on Friday. (2020), Taiwan News. https://www.taiwannews.com.tw/en/news/4035517. Accessed 15 Sept 2021.

Chuang, M. T., Ooi, M. C. G., Lin, N. H., Fu, J. S., Lee, C. T., Wang, S. H., et al., (2020). Study on the impact of three Asian industrial regions on PM2.5 in Taiwan and the process analysis during transport. Atmospheric Chemistry and Physics, 20(23), 14947-14967, doi:10.5194/acp-20-14947-2020.

Dejchanchaiwong, R., & Tekasakul, P. (2021). Effects of coronavirus induced city lockdown on PM2.5 and gaseous pollutant concentrations in Bangkok. Aerosol and Air Quality Research, 21(4), 200418, doi:10.4209/aaqr.200418.

Department of Statistics (2016). Investigation report on the daily use of transportation, Republic of China (Taiwan).

Dinoi, A., Feltracco, M., Chirizzi, D., Trabucco, S., Conte, M., Gregoris, E., et al. (2022). A review on measurements of SARS-CoV-2 genetic material in air in outdoor and indoor environments: Implication for airborne transmission. *Science of The Total Environment*, *809*, 151137, doi:10.1016/j.scitotenv.2021.151137.

Dinoi, A., Gulli, D., Ammoscato, I., Calidonna, C. R., & Contini, D. (2021). Impact of the Coronavirus Pandemic Lockdown on Atmospheric Nanoparticle Concentrations in Two Sites of Southern Italy. *12*(3), 352.

Draxler, R., & Hess, G. (1998). An overview of the HYSPLIT_4 modeling system for trajectories, dispersion, and deposition. Australian Meteorological Magazine, 47, 295-308.

Fung, P. L., Zaidan, M. A., Timonen, H., Niemi, J. V., Kousa, A., Kuula, J., et al., (2021). Evaluation of white-box versus black-box machine learning models in estimating ambient black carbon concentration. Journal of Aerosol Science, 152, 105694, doi.org/10.1016/j.jaerosci.2020.105694.

Gao, C., Li, S., Liu, M., Zhang, F., Achal, V., Tu, Y., et al., (2021). Impact of the COVID-19 pandemic on air pollution in Chinese megacities from the perspective of traffic volume and meteorological factors. Science of The Total Environment, 773, 145545, doi.org/10.1016/j.scitotenv.2021.145545.

Gao, H., Wang, J., Li, T., & Fang, C. (2021). Analysis of air quality changes and influencing factors in Changchun during the COVID-19 pandemic in 2020. Aerosol and Air Quality Research, 21(9), 210055, doi:10.4209/aaqr.210055.

Ghasempour, F., Sekertekin, A., & Kutoglu, S. H. (2021). Google Earth Engine based spatio-temporal analysis of air pollutants before and during the first wave COVID-19 outbreak over Turkey via remote sensing. Journal of Cleaner Production, 319, 128599, doi.org/10.1016/j.jclepro.2021.128599.

Golubeva, N. I., Burtseva, L. V., Matishov, G. G., & Il'in, G. V. (2013). The results of measurements of heavy metals in atmospheric aerosols in the open areas of the Arctic Seas in 2009–2010. Doklady Earth Sciences, 453(1), 1090-1093, doi:10.1134/S1028334X13110019.

Grange, S. K., Carslaw, D. C., Lewis, A. C., Boleti, E., & Hueglin, C. (2018). Random forest meteorological normalisation models for Swiss PM10 trend analysis. Atmospheric Chemistry and Phyicss, 18(9), 6223-6239, doi:10.5194/acp-18-6223-2018.

Hasnain, A., Hashmi, M. Z., Bhatti, U. A., Nadeem, B., Wei, G., Zha, Y., et al., (2021). Assessment of air pollution before, during and after the COVID-19 pandemic lockdown in Nanjing, China. Atmosphere, 12(6), 743.

He, G., Pan, Y., & Tanaka, T. (2020). The short-term impacts of COVID-19 lockdown on urban air pollution in China. *Nature Sustainability*, *3*(12), 1005-1011, doi:10.1038/s41893-020-0581-y.

Hong, C., Zhang, Q., Zhang, Y., Davis, S. J., Tong, D., Zheng, Y., et al., (2019). Impacts of climate change on future air quality and human health in China. Proceedings of the National Academy of Sciences of the United States of America, 116(35), 17193-17200, doi: 10.1073/pnas.1812881116

Hsieh, Y.-C., & You, P.-S. (2021). Evolutionary artificial intelligence algorithms for the one-way road orientation planning problem with multiple venues: An example of evacuation planning in Taiwan. *104*(3_suppl), 00368504211063258, doi:10.1177/00368504211063258.

Hsu, C.-H., & Cheng, F.-Y. (2019). Synoptic weather patterns and associated air pollution in Taiwan. Aerosol and Air Quality Research, 19(5), 1139-1151, doi:10.4209/aaqr.2018.09.0348.

Hsu, Y.-J., Fu, Y., Bürgmann, R., Hsu, S.-Y., Lin, C.C., Tang, C.H., et al., (2020). Assessing seasonal and interannual water storage variations in Taiwan using geodetic and hydrological data. Earth and Planetary Science Letters, 550, 116532, doi.org/10.1016/j.epsl.2020.116532.

Hu, J., Pan, Y., He, Y., Chi, X., Zhang, Q., Song, T., et al. (2021). Changes in air pollutants during the COVID-19 lockdown in Beijing: Insights from a machine-learning technique and implications for future control policy. *Atmospheric and Oceanic Science Letters, 14*(4), 100060, doi:10.1016/j.aosl.2021.100060.

Hu, M., Chen, Z., Cui, H., Wang, T., Zhang, C., & Yun, K. (2021). Air pollution and critical air pollutant assessment during and after COVID-19 lockdowns: Evidence from pandemic hotspots in China, the Republic of Korea, Japan, and India. Atmospheric Pollution Research, 12(2), 316-329, doi.org/10.1016/j.apr.2020.11.013.

Huang, Y. S., & Hsieh, C. C. (2019). Ambient volatile organic compound presence in the highly urbanized city: source apportionment and emission position. Atmospheric Environment, 206, 45-59, doi.org/10.1016/j.atmosenv.2019.02.046.

Jain, S., & Sharma, T. (2020). Social and travel lockdown impact considering coronavirus disease (COVID-19) on air quality in Megacities of India: present benefits, future challenges and way forward. Aerosol and Air Quality Research, 20, 1222-1236, doi:10.4209/aaqr.2020.04.0171.

Jephcote, C., Hansell, A. L., Adams, K., & Gulliver, J. (2021). Changes in air quality during COVID-19 'lockdown' in the United Kingdom. Environmental Pollution, 272, 116011, doi.org/10.1016/j.envpol.2020.116011.

Kanniah, K. D., Kamarul Zaman, N. A. F., Kaskaoutis, D. G., & Latif, M. T. (2020). COVID-19's impact on the atmospheric environment in the Southeast Asia region. Science of The Total Environment, 736, 139658, doi.org/10.1016/j.scitotenv.2020.139658.

Kinney, P. L. (2021). How can we solve our air quality problem in the face of climate change? JAMA Network Open, 4(1), e2035010, doi: 10.1001/jamanetworkopen.2020.35010.

Kung, C.C., & McCarl, B. A. (2020). The potential role of renewable electricity generation in Taiwan. Energy Policy, 138, 111227, doi.org/10.1016/j.enpol.2019.111227.

Kwon, S.-H., Kim, J., Shim, S., Seo, J., & Byun, Y.-H. (2020). Analysis of Weather Patterns Related to Wintertime Particulate Matter Concentration in Seoul and a CMIP6-Based Air Quality Projection. *11*(11), 1161.

Lai, I. C., & Brimblecombe, P. (2021). Long-range transport of air pollutants to Taiwan during the COVID-19 lockdown in Hubei Province. Aerosol and Air Quality Research, 21(2), 200392, doi:10.4209/aaqr.2020.07.0392.

Landrigan, P. J., Fuller, R., Acosta, N. J. R., Adeyi, O., Arnold, R., Basu, N., et al., (2018). The Lancet Commission on pollution and health. The Lancet, 391(10119), 462-512, doi:10.1016/S0140-6736(17)32345-0.

Li, J., & Tartarini, F. (2020). Changes in air quality during the COVID-19 lockdown in Singapore and associations with human mobility trends. Aerosol and Air Quality Research, 20(8), 1748-1758, doi:10.4209/aaqr.2020.06.0303.

Li, L., Li, Q., Huang, L., Wang, Q., Zhu, A., Xu, J., et al., (2020). Air quality changes during the COVID-19 lockdown over the Yangtze River Delta Region: An insight into the impact of human activity pattern changes on air pollution variation. Science of The Total Environment, 732, 139282, doi.org/10.1016/j.scitotenv.2020.139282.

Li, Y., Chang, M., Ding, S., Wang, S., Ni, D., & Hu, H. (2017). Monitoring and source apportionment of trace elements in PM2.5: implications for local air quality management. Journal of Environmental Management, 196, 16-25, doi.org/10.1016/j.jenvman.2017.02.059.

Liu, Y., Zhou, Y., & Lu, J. (2020). Exploring the relationship between air pollution and meteorological conditions in China under environmental governance. Scientific Reports, 10(1), 14518, doi:10.1038/s41598-020-71338-7.

Loyola-González, O. (2019). Black-box vs. white-box: understanding their advantages and weaknesses from a practical point of view. Institute of Electrical and Electronics Engineers Access, 7, 154096-154113, doi:10.1109/ACCESS.2019.2949286.

Ma, T., Duan, F., He, K., Qin, Y., Tong, D., Geng, G., et al., (2019). Air pollution characteristics and their relationship with emissions and meteorology in the Yangtze River Delta region during 2014–2016. Journal of Environmental Sciences, 83, 8-20, doi.org/10.1016/j.jes.2019.02.031.

Mahato, S., Pal, S., & Ghosh, K. G. (2020). Effect of lockdown amid COVID-19 pandemic on air quality of the megacity Delhi, India. Science of The Total Environment, 730, 139086, doi.org/10.1016/j.scitotenv.2020.139086.

Maurer, M., Klemm, O., Lokys, H. L., & Lin, N.H. (2019). trends of fog and visibility in Taiwan: climate change or air quality improvement? Aerosol and Air Quality Research, 19(4), 896-910, doi:10.4209/aaqr.2018.04.0152.

Merico, E., Donateo, A., Gambaro, A., Cesari, D., Gregoris, E., Barbaro, E., et al. (2016). Influence of in-port ships emissions to gaseous atmospheric pollutants and to particulate matter of different sizes in a Mediterranean harbour in Italy. *Atmospheric Environment*, *139*, 1-10, doi:10.1016/j.atmosenv.2016.05.024.

Mesas-Carrascosa, F.J., Pérez Porras, F., Triviño-Tarradas, P., García-Ferrer, A., & Meroño-Larriva, J. E. (2020). Effect of lockdown measures on atmospheric nitrogen dioxide during SARS-CoV-2 in Spain. Remote Sensing, 12(14), 2210.

Ministry of Transportation and Communication (2020). Commonly used transportation statistics. https://stat.motc.gov.tw/mocdb/stmain.jsp?sys=100&funid=emenu. Accessed 28 April 2021.

Ministry of Transportation and Communication (2021). Overview of public transportation passenger services in 2020, Republic of China (Taiwan).

Moreno, T., Martins, V., Querol, X., Jones, T., BéruBé, K., Minguillón, M. C., et al., (2015). A new look at inhalable metalliferous airborne particles on rail subway platforms. Science of The Total Environment, 505, 367-375, doi:10.1016/j.scitotenv.2014.10.013.

Muhammad, S., Long, X., & Salman, M. (2020). COVID-19 pandemic and environmental pollution: A blessing in disguise? Science of The Total Environment, 728, 138820, doi.org/10.1016/j.scitotenv.2020.138820.

Nakada, L. Y. K., & Urban, R. C. (2020). COVID-19 pandemic: Impacts on the air quality during the partial lockdown in São Paulo state, Brazil. Science of The Total Environment, 730, 139087, doi.org/10.1016/j.scitotenv.2020.139087.

Naqvi, H. R., Datta, M., Mutreja, G., Siddiqui, M. A., Naqvi, D. F., & Naqvi, A. R. (2021). Improved air quality and associated mortalities in India under COVID-19 lockdown. Environmental Pollution, 268, 115691, doi.org/10.1016/j.envpol.2020.115691.

Nguyen, G. T. H., Shimadera, H., Uranishi, K., Matsuo, T., & Kondo, A. (2020). Numerical assessment of PM2.5 and O3 air quality in Continental Southeast Asia: Impacts of future projected anthropogenic emission change and its impacts in combination with potential future climate change impacts. Atmospheric Environment, 226, 117398, doi.org/10.1016/j.atmosenv.2020.117398.

Nigam, R., Pandya, K., Luis, A. J., Sengupta, R., & Kotha, M. (2021). Positive effects of COVID-19 lockdown on air quality of industrial cities (Ankleshwar and Vapi) of Western India. Scientific Reports, 11(1), 4285, doi:10.1038/s41598-021-83393-9.

Peng, L., Zhao, X., Tao, Y., Mi, S., Huang, J., & Zhang, Q. (2020). The effects of air pollution and meteorological factors on measles cases in Lanzhou, China. Environmental Science and Pollution Research, 27(12), 13524-13533, doi:10.1007/s11356-020-07903-4.

Petetin, H., Bowdalo, D., Soret, A., Guevara, M., Jorba, O., Serradell, K., et al., (2020). Meteorology-normalized impact of the COVID-19 lockdown upon NO2 pollution in Spain. Atmospheric Chemistry and Phyicss, 20(18), 11119-11141, doi:10.5194/acp-20-11119-2020.

Psanis, C., Triantafyllou, E., Giamarelou, M., Manousakas, M., Eleftheriadis, K., & Biskos, G. (2017). Particulate matter pollution from aviation-related activity at a small airport of the Aegean Sea Insular Region. Science of The Total Environment, 596-597, 187-193, doi:10.1016/j.scitotenv.2017.04.078.

Qiu, H., Bai, C.H., Chuang, K.J., Fan, Y.C., Chang, T.P., Yim, S. H.L., et al., (2021). Association of cardiorespiratory hospital admissions with ambient volatile organic compounds: Evidence from a time-series study in Taipei, Taiwan. Chemosphere, 276, 130172, doi.org/10.1016/j.chemosphere.2021.130172.

Querol, X., Massagué, J., Alastuey, A., Moreno, T., Gangoiti, G., Mantilla, E., et al., (2021). Lessons from the COVID-19 air pollution decrease in Spain: Now what? Science of The Total Environment, 779, 146380, doi.org/10.1016/j.scitotenv.2021.146380.

Rahman, M. S., Azad, M. A. K., Hasanuzzaman, M., Salam, R., Islam, A. R. M. T., Rahman, M. M., et al., (2021). How air quality and COVID-19 transmission change under different lockdown scenarios? A case from Dhaka city, Bangladesh. Science of The Total Environment, 762, 143161, doi.org/10.1016/j.scitotenv.2020.143161.

Sanguineti, P. B., Lanzaco, B. L., López, M. L., Achad, M., Palancar, G. G., Olcese, L. E., et al., (2020). PM2.5 monitoring during a 10-year period: relation between elemental concentration and meteorological conditions. Environmental Monitoring and Assessment, 192(5), 313, doi:10.1007/s10661-020-08288-0.

Sari, D., Incecik, S., & Ozkurt, N. (2020). Analysis of surface ozone episodes using WRF-HYSPLIT model at Biga Peninsula in the Marmara region of Turkey. Atmospheric Pollution Research, 11(12), 2361-2378, doi.org/10.1016/j.apr.2020.09.018.

Shan, W., Yin, Y., Lu, H., & Liang, S. (2009). A meteorological analysis of ozone episodes using HYSPLIT model and surface data. Atmospheric Research, 93(4), 767-776, doi.org/10.1016/j.atmosres.2009.03.007.

Shapiro, M. A., & Yarime, M. (2021). Effects of national affiliations and international collaboration on scientific findings: The case of transboundary air pollution in Northeast Asia. Environmental Science & Policy, 118, 71-85, doi.org/10.1016/j.envsci.2021.01.005.

Shen, L., Wang, H., Zhu, B., Zhao, T., Liu, A., Lu, W., et al., (2021). Impact of urbanization on air quality in the Yangtze River Delta during the COVID-19 lockdown in China. Journal of Cleaner Production, 296, 126561, doi.org/10.1016/j.jclepro.2021.126561.

Sicard, P., De Marco, A., Agathokleous, E., Feng, Z., Xu, X., Paoletti, E., et al., (2020). Amplified ozone pollution in cities during the COVID-19 lockdown. Science of The Total Environment, 735, 139542, doi.org/10.1016/j.scitotenv.2020.139542.

Siciliano, B., Dantas, G., da Silva, C. M., & Arbilla, G. (2020). Increased ozone levels during the COVID-19 lockdown: Analysis for the city of Rio de Janeiro, Brazil. Science of The Total Environment, 737, 139765, doi.org/10.1016/j.scitotenv.2020.139765.

Singh, J., & Tyagi, B. (2021). Transformation of air quality over a coastal tropical station Chennai during COVID-19 lockdown in India. Aerosol and Air Quality Research, 21(4), 200490, doi:10.4209/aaqr.200490.

Sokhi, R. S., Singh, V., Querol, X., Finardi, S., Targino, A. C., Andrade, M. d. F., et al., (2021). A global observational analysis to understand changes in air quality during exceptionally low anthropogenic emission conditions. Environment International, 157, 106818, doi.org/10.1016/j.envint.2021.106818.

Solberg, S., Walker, S.-E., Schneider, P., & Guerreiro, C. J. A. (2021). Quantifying the impact of the Covid-19 lockdown measures on nitrogen dioxide levels throughout Europe. Atmosphere, 12(2), 131.

Solomon, B., Otoo, E., Boateng, A., & Ato Koomson, D. (2021). Inland Waterway Transportation (IWT) in Ghana: A case study of Volta Lake Transport. International Journal of Transportation Science and Technology, 10(1), 20-33, doi:10.1016/j.ijtst.2020.05.002.

Stein, A. F., Draxler, R. R., Rolph, G. D., Stunder, B. J. B., Cohen, M. D., & Ngan, F. (2015). NOAA's HYSPLIT atmospheric transport and dispersion modeling system. Bulletin of the American Meteorological Society, 96(12), 2059-2077, doi:10.1175/BAMS-D-14-00110.1.

Summers, J., Cheng, H.Y., Lin, H.H., Barnard, L. T., Kvalsvig, A., Wilson, N., et al., (2020). Potential lessons from the Taiwan and New Zealand health responses to the COVID-19 pandemic. The Lancet Regional Health - Western Pacific, 4, 100044, doi.org/10.1016/j.lanwpc.2020.100044.

Taiwan Central Weather Bureu (2020). CWB Observation Data Inquiry System. https://e-service.cwb.gov.tw/HistoryDataQuery/. Accessed 28 April 2021.

Taiwan Environmental Protection Administration (2006). Air Quality Index. https://airtw.epa.gov.tw/ENG/Information/Standard/AirQualityIndicator.aspx.

Taiwan Environmental Protection Administration (2021). Environmental Protection Administration Open Data. Accessed 14 February 2021.

Talbot, N., Takada, A., Bingham, A. H., Elder, D., Lay Yee, S., & Golubiewski, N. E. (2021). An investigation of the impacts of a successful COVID-19 response and meteorology on air quality in New Zealand. Atmospheric Environment, 254, 118322, doi.org/10.1016/j.atmosenv.2021.118322.

TEPA (2021). Air Quality Annual Report of Republic of China (Taiwan), 2020.

Teng, M., Yang, K., Shi, Y., & Luo, Y. Study on the Temporal and Spatial Variation of $PM_{2.5}$ in Eight Main Cities of Yunnan Province. In *2018 26th International Conference on Geoinformatics, 28-30 June 2018 2018* (pp. 1-7). doi:10.1109/GEOINFORMATICS.2018.8557198.

Tfwala, C. M., van Rensburg, L. D., Schall, R., Mosia, S. M., & Dlamini, P. (2017). Precipitation intensity-duration-frequency curves and their uncertainties for Ghaap plateau. Climate Risk Management, 16, 1-9, doi.org/10.1016/j.crm.2017.04.004.

Tian, X., An, C., Chen, Z., & Tian, Z. (2021). Assessing the impact of COVID-19 pandemic on urban transportation and air quality in Canada. Science of The Total Environment, 765, 144270, doi.org/10.1016/j.scitotenv.2020.144270.

Tsai, J.-H., Lee, M.Y., & Chiang, H.L. (2021). Effectiveness of SOx, NOx, and primary particulate matter control strategies in the improvement of ambient PM concentration in Taiwan. Atmosphere, 12(4), 460.

Tseng, Y.L., Yuan, C.S., Bagtasa, G., Chuang, H.L., & Li, T.C. (2019). Inter-correlation of chemical compositions, transport routes, and source apportionment results of atmospheric PM2.5 in southern Taiwan and the northern Philippines. Aerosol and Air Quality Research, 9(12), 2645-2661, doi:10.4209/aaqr.2019.10.0526.

United Nations Environment Programme (2021). The First Global Assessment of Air Pollution Legislation. Air Pollution Series: Regulating Air Quality.

van Doremalen, N., Bushmaker, T., Morris, D. H., Holbrook, M. G., Gamble, A., Williamson, B. N., et al. (2020). Aerosol and Surface Stability of SARS-CoV-2 as Compared with SARS-CoV-1. *N Engl J Med, 382*(16), 1564-1567, doi:10.1056/NEJMc2004973.

Ventura, L. M. B., de Oliveira Pinto, F., Soares, L. M., Luna, A. S., & Gioda, A. (2018). Evaluation of air quality in a megacity using statistics tools. Meteorology and Atmospheric Physics, 130(3), 361-370, doi:10.1007/s00703-017-0517-x.

Wang, F., Chen, D. S., Cheng, S. Y., Li, J. B., Li, M. J., & Ren, Z. H. (2010). Identification of regional atmospheric PM10 transport pathways using HYSPLIT, MM5-CMAQ and synoptic pressure pattern analysis. Environmental Modelling & Software, 25(8), 927-934, doi.org/10.1016/j.envsoft.2010.02.004.

Wang, J., & Ogawa, S. (2015). Effects of Meteorological Conditions on PM2.5 Concentrations in Nagasaki, Japan. 12(8), 9089-9101.

Wang, S.H., Hung, W.T., Chang, S.C., & Yen, M.C. (2016). Transport characteristics of Chinese haze over northern Taiwan in winter, 2005–2014. Atmospheric Environment, 126, 76-86, doi.org/10.1016/j.atmosenv.2015.11.043.

Wang, Z., Zheng, F., Zhang, W., & Wang, S. (2018). Analysis of SO2 pollution changes of Beijing-Tianjin-Hebei region over China based on OMI observations from 2006 to 2017. Advances in Meteorology, 2018, 8746068, doi:10.1155/2018/8746068.

WHO (2020). Timeline of WHO's Response to COVID-19. https://www.who.int/news-room/detail/29-06-2020-covidtimeline. Accessed 25 June 2021.

WHO (2021). Air pollution. https://www.who.int/health-topics/air-pollution#tab=tab_1. Accessed 6 June 2021.

Wong, Y. J., Shimizu, Y., He, K., & Nik Sulaiman, N. M. (2020). Comparison among different ASEAN water quality indices for the assessment of the spatial variation of surface water quality in the Selangor river basin, Malaysia. Environmental Monitoring and Assessment, 192(10), 644, doi:10.1007/s10661-020-08543-4.

Wong, Y. J., Shimizu, Y., Kamiya, A., Maneechot, L., Bharambe, K. P., Fong, C. S., et al. (2021). Application of artificial intelligence methods for monsoonal river classification in Selangor river basin, Malaysia. Environmental Monitoring and Assessment, 193(7), 438, doi:10.1007/s10661-021-09202-y

Worldometer (2021). COVID-19 Coronavirus Pandemic. https://www.worldometers.info/coronavirus/. Accessed 15 Oct 2021.

Wu, C.H., Tsai, I. C., Tsai, P.C., & Tung, Y.S. (2019). Large–scale seasonal control of air quality in Taiwan. Atmospheric Environment, 214, 116868, doi.org/10.1016/j.atmosenv.2019.116868.

Wu, L.-F., Achyldurdyyeva, J., Jou, W.-P., Foung, W.-T., & Jaw, B.-S. (2021). Relief, recovery, and revitalization measures for tourism and hospitality industry during covid-19 pandemic: case study from Taiwan. SAGE Open, 11(3), 21582440211040805, doi:10.1177/21582440211040805.

Wu, P.C., & Huang, K.F. (2021). Tracing local sources and long-range transport of PM10 in central Taiwan by using chemical characteristics and Pb isotope ratios. Scientific Reports, 11(1), 7593, doi:10.1038/s41598-021-87051-y.

Yang, J., Zhou, F., & Zhang, K. (2020). Efforts to fight forest fire continue in SW China. https://news.cgtn.com/news/2020-04-02/Efforts-to-fight-forest-fire-continue-in-SW-China-PmbgCSLHI4/index.html. Accessed 15 April 2021.

Yang, Q., Wang, B., Wang, Y., Yuan, Q., Jin, C., Wang, J., et al., (2021). Global air quality change during COVID-19: a synthetic analysis of satellite, reanalysis and ground station data. Environmental Research Letters, 16(7), 074052, doi:10.1088/1748-9326/ac1012.

Yeh, H.F., & Huang, C.C. (2019). Evaluation of basin storage–discharge sensitivity in Taiwan using low-flow recession analysis. [10.1002/hyp.13411]. Hydrological Processes, 33(10), 1434-1447, doi.org/10.1002/hyp.13411.

Yousefian, F., Faridi, S., Azimi, F., Aghaei, M., Shamsipour, M., Yaghmaeian, K., et al., (2020). Temporal variations of ambient air pollutants and meteorological influences on their concentrations in Tehran during 2012–2017. Scientific Reports, 10(1), 292, doi:10.1038/s41598-019-56578-6.

Zangari, S., Hill, D. T., Charette, A. T., & Mirowsky, J. E. (2020). Air quality changes in New York City during the COVID-19 pandemic. Science of The Total Environment, 742, 140496, doi.org/10.1016/j.scitotenv.2020.140496.

Zhai, Z., Fu, X., Yi, M., Sheng, M., & Guang, F. (2022). Haze management: is urban public transportation priority effective? *Environmental Science and Pollution Research*, doi:10.1007/s11356-021-17871-y.

Zhu, L., Zhang, Y., Wu, Z., & Zhang, C. (2021). Spatio-Temporal Characteristics of SO2 across Weifang from 2008 to 2020. *18*(22), 12206.

Chapter 6

Change analysis of machine learning-based meteorological-normalized NO_2 and O_3 during COVID-19 pandemic in the absence of lockdown

In this study, a novel research framework is proposed to investigate the observed and meteorological-normalized concentrations of nitrogen dioxide (NO_2) and ozone (O_3) across 62 cities in Taiwan. Four commonly adopted meteorological normalization techniques, namely the generalized additive model (GAM), generalized linear model (GLM), gradient boosting machine (GBM), and random forest (RF), were developed, optimized, and compared using nine meteorological and temporal variables. The models were optimized using systematic trial-and-error for data distribution type in GAM and GLM and using the grid-search approach for tree numbers in GBM and RF. The simulation performance of RF and GBM outperformed GAM and GLM across Taiwan, highlighting the importance of model selection and hyperparameter optimization for meteorological normalization.

6.1 Introduction

According to the World Meteorological Organization (WMO, 2021), global premature mortality due to air pollution increased by 2-fold in 2019 (4.5 million deaths) compared to 1990, with approximately 99% of the global population living with air pollution levels exceeding the World Health Organization (WHO, 2021) guidelines. Although numerous blueprints/actions have been proposed and implemented across different nations such as the Global Clean Air Initiative, Climate and Clean Air Coalition, and Clean Air Fund, the cross-cutting challenges, including the lack of financial resources, government transparency, and institutional and expert capacity, have resulted in outdoor air pollution remaining an unresolved problem (UNEP, 2021) until the emergence of coronavirus disease (COVID-19). The COVID-19 pandemic has prompted significant changes in the normal rhythm of livelihood, leading to most countries implementing lockdowns or imposing a range of stringent policies, such as compulsory mask-wearing and social distancing, to retard and

contain the transmission of the infectious virus. These restrictive measures associated with rapid vaccination rates have not only substantially reduced COVID-19 morbidity and mortality (Vasileiou *et al.*, 2021) but have also led to significant reductions in anthropogenic emissions of air pollutants, shedding light on the sources of global air pollution.

Throughout 2020, significant improvements in air pollution have been observed worldwide, with an approximately 30% reduction observed in major air pollutants e.g., carbon monoxide (CO), sulfur dioxide (SO_2), nitrogen monoxide (NO), nitrogen dioxide (NO_2), ozone (O_3), and particulate matter with average aerodynamic diameters < 10 and 2.5 µm (PM_{10} and $PM_{2.5}$) (Addas and Maghrabi 2021). Numerous studies have investigated the impact of lockdown on air pollution and performed change analyses of air pollutant concentrations between pre-lockdown and lockdown periods (Rodríguez-Urrego and Rodríguez-Urrego 2020; Tobías *et al.*, 2020) or in relation to the selected base year (Abdullah *et al.*, 2020; Nakada and Urban 2020). Based on findings observed using the high-resolution Sentinel-5P/TROPOMI satellite and Google Community Mobility Reports over 164 countries, Dang and Trinh (2021) concluded that reduced mobility and transportation use were factors influencing air quality improvement during the COVID-19 period. Similar findings utilizing station-based data have been reported in China (Zhu *et al.*, 2020), Malaysia (Ash'aari *et al.*, 2020), Brazil (Rudke *et al.*, 2021), the United States of America *(Archer et al.*, 2020), Italy (Gualtieri *et al.*, 2020) and many other regions worldwide (Baysan *et al.*, 2021; Tian et al., 2021; Wetchayont, 2021; Anugerah *et al.*, 2021).

Nevertheless, few studies have focused on changes in air quality in regions that did not impose lockdowns, such as Taiwan. Compared to regions that imposed lockdown, contradictory findings were reported in Taiwan (Wong *et al.*, 2022; Chang *et al.*, 2021), in which there were insignificant changes or even higher concentrations of air pollutants despite the reduced mobility. One of the possible reasons for this extraordinary phenomenon may be the dynamic climate variability (Pei *et al.*, 2020). Therefore, some researchers have adopted different meteorological-normalization approaches to decouple meteorological impacts and assess the impact of COVID-19-induced changes on air quality (Fu *et al.*, 2021; Zhai *et al.*,

2019; Petetin *et al.*, 2020). Among these, machine-learning models are the most popular due to their reliability and robustness in capturing the complex and non-linear relationships between air pollutant concentrations and various meteorological and temporal variables (Petetin *et al*., 2020; Qu *et al*., 2020). Key relevant studies are summarized and the most commonly used modelling techniques and input parameter combinations are presented in Table 1.

As shown in Table 6.1, all reported studies focus on identifying the impact of lockdown based on the difference between the observed and simulated business-as-usual (BAU) air pollutant concentrations. Commonly adopted meteorological parameters are station pressure ($P_{\_sta}$), atmospheric temperature (T_{atm}), wind speed (WS), wind direction (WD), rainfall (RF), and relative humidity (RH) whereas time-related variables are Julian day (JD), Unix time (UT), and weekday values (WV). Although most of the developed models presented good to very good performance in the training dataset (Munir *et al*., 2021a; Lovrić *et al.*, 2021; Brancher 2021), most studies did not perform model verification for simulating meteorologically normalized BAU air pollutant concentrations. Model verification is essential to ensure that the executable model provides a sufficiently accurate representation of the system in the presence of unseen data to evaluate the robustness of the system (Trensch *et al.*, 2018). Therefore, based on the previous studies, although significant differences of up to 150% were observed between the simulated and observed data (Petetin *et al.*, 2020), the reliability of the developed models may be limited.

Model-type selection and hyperparameter optimization are vital to improving their robustness and accuracy. Depending on the characteristics of the dataset, network hyperparameter optimization and the type of model also influence the accuracy of the simulated results. Imbalanced datasets are common in environmental datasets, particularly for atmospheric studies (Ramos-López and Maldonado 2021; Ketu and Mishra 2021; Asgari et al., 2017). As reported by Wong *et al.* (2021), network structures and model selection play important roles regarding distinct learning capacities and computational formulae. Despite some studies reporting the relative importance of variables, to the best of our knowledge,

optimal parameter combination, optimized network structures, and performance comparison between different models have not been performed.

In light of these findings, and considering the effect of climate variability across Taiwan in the absence of lockdown, this study proposes a novel research framework for constructing robust models in quantifying the impact of COVID-19 on air pollutant concentrations. The research objectives were set as follows:

i. To select and evaluate optimal hyperparameters for each constructed model;
ii. To compare, verify, and adopt an optimized model for predicting air pollutant concentration; and
iii. To perform spatiotemporal change analysis between observed and simulated data.

To achieve these objectives, the concentrations of NO_2 and O_3, emerging air pollutants due to increasing traffic exhaust emissions, were simulated and compared *(Tsai et al.,* 2021; Li *et al*., 2016). This research adopted the most commonly used modelling techniques and input parameter combinations (including meteorological and temporal variables), as summarized in Table 1. Four machine-learning techniques, namely, the generalized additive model (GAM), gradient boosting machine (GBM), generalized linear model (GLM), and random forest (RF), were constructed, evaluated, and compared. In this research, the daily concentrations/values of the studied parameters from 2015–2018 were selected as the training dataset, and 2019 was selected as the base year to verify and test the capability of the model for application under the BAU scenario. The output of the best-performing model during the verification stage was used to quantify the COVID-19 impacts associated with the meteorological normalized BAU scenario through a geographic information system (GIS) platform. These findings are expected to support decision-making, guide future development, address air quality management issues, and bridge the current research gaps.

Table 6.1. Summary of meteorological-normalization modelling techniques for COVID-19 BAU simulation

Authors (year)	Country/City	Modelled Air Pollutant(s)	Input Variable(s)	Data Period	Model Type	Model Verification	Performance Criteria
Rybarczyk & Zalakeviciute (2021)	Ecuador	NO_2, SO_2, CO, and $PM_{2.5}$	*Meteorological:* RH, RF, T_{atm}, SR, P_{sta}, WS, and WD *Temporal:* JD, WV, H, DI	Training: 1 Jan. 2016 to 15 Jan. 2020 Testing: 16 Jan. to 30 Jun. 2020	Gradient Boosting Machine	No	RMSE PCC
Petetin *et al.* (2020)	Spain	NO_2	*Meteorological:* mean/min/max 2m T_{atm}, normalized 10 m zonal and meridian WS components, WS, P_{sta}, SR, downward SR, downward UVR, BLH, *Temporal:* JD, WV, DI	Training: 1 Jan. to 31 Dec. 2016-2019 & 1 Jan. to 31 Dec. 2020 Testing: 1 Jan. to 23 Apr. 2016-2019 & 1 Jan. to 13 Mac. 2020	Gradient Boosting Machine	No	MB nMB RMSE nRMSE PCC

Table 6.1. Summary of meteorological-normalization modelling techniques for COVID-19 BAU simulation (continued)

Barré *et al.* (2021)	European	NO_2	*Meteorological* mean/min/max 2m T_{atm}, normalized 10 m zonal and meridian WS components, WS, P_{sta}, SR, downward SR, downward UVR, BLH, *Temporal:* JD, WV, DI	Training: 2017-2019 Testing: 1 Jan. to 15 Mac. 2020	Gradient Boosting Machine	No	MB nMB RMSE nRMSE PCC
Jephcote *et al.* (2021)	United Kingdom	NO_2, NO_X, O_3, and $PM_{2.5}$	*Meteorological:* T_{dew}, T_{atm}, P_{sta}, WS, WD, RH, CCH	Training: 75% of 1 Jan. to 31 Dec. 2017-2019 Testing: 25% of 1 Jan. to 31 Dec. 2017-2019 Prediction: 30 Mac. to 3 May. 2020	Gradient Boosting Machine	Yes	F^2 IOA COE R^2

Table 6.1. Summary of meteorological-normalization modelling techniques for COVID-19 BAU simulation (continued)

Granella *et al.* (2021)	Lombardy, Italy	NO_2 and $PM_{2.5}$	*Meteorological* min/max T_{atm}, WS, WD, and RH, *Temporal:* DI, WD, MD	Training: 2012-2019 Testing: 1 Jan. to 31 Mac. 2020	Gradient Boosting Machine	No	MB nMB RMSE cRMSE ncRMSE PCC
Wang *et al.* (2020)	Megacities of China (Beijing, Chengdu, Shenzhen, Xi'an, Shanghai, and Wuhan)	NO_2, O_3, CO, and $PM_{2.5}$	*Meteorological:* RH, WD, WS, P_{sta}, and T_{atm} *Temporal:* JD, Y, WV, H, LD	Training: 1 Jan. 2019 to 31 Apr. 2019 Testing: 1 Jan. to 31 Apr. 2020	Random Forest	No	F^2 MB NMB R^2 RMSE
Shi *et al.* (2021)	Beijing, Wuhan, Milan, Rome, Madrid, London, Paris, Berlin, New York, Los Angeles, Delhi	NO_2, O_3, O_x, and $PM_{2.5}$	*Meteorological:* RH, WD, WS, P_{sta}, and T_{atm}, AMC, BLH, CC, SR, RF *Temporal:* UT, JD, WD, H	Training: 70% of Dec. 2015 to May. 2020 Testing: 30% of Dec. 2015 to May. 2020	Random Forest	No	F^2 MB NMB PCC IOA MGE NMGE

Table 6.1. Summary of meteorological-normalization modelling techniques for COVID-19 BAU simulation (continued)

Diémoz *et al.* (2021)	Aosta Valley, Italy	NO, NO_2, O_3, $PM_{2.5}$ and PM_{10}	*Meteorological:* RH, WD, WS, P_{sta}, T_{tm}, SR and RF *Temporal:* UT, JD, WD	Training: 2015-2019 Testing: 2020	Random Forest	No	PCC MB
Grange *et al.* (2021)	European	NO_2, O_X, and O_3	*Meteorological:* RH, WD, WS, P_{sta}, and T_{atm} *Temporal:* UT, JD, WD and H	Training: 80% of 1 Jan. 2018 to 14 Feb. 2020 Testing: 20 % of 1 Jan. 2018 to 14 Feb. 2020	Random forest	No	PCC MB NMB NRMSE
Velders *et al.* (2021)	Netherland	NO_2, NO_x, O_3, $PM_{2.5}$, and PM_{10}	*Meteorological:* RH, WD, WS, P_{sta}, T_{atm}, SR, CC and RF *Temporal:* DI and H	Training: 1 Jan. 2017 to 29 Feb. 2020 Testing: 1 Mac. 2020 to 30 May. 2020	Random Forest	No	-
Dobson and Semple (2020)	Scotland	NO_2, and $PM_{2.5}$,	*Meteorological:* RH, WD, WS, P_{sta}, and T_{atm} *Temporal:* JD, Y, WV, H, LD	24 Mac. to 23 Apr. in 2017-2020 (Details of training/testing data not provided)	Random Forest	No	-

Table 6.1. Summary of meteorological-normalization modelling techniques for COVID-19 BAU simulation (continued)

Fenech *et al.* (2021)	Malta	NO_2, and O_3	*Meteorological:* RH, WD, WS, and T_{atm} *Temporal:* UT, JD, and WV	Training: 2008–2017 Testing: 1 Jan. 2020 to 15 Oct. 2020	Random Forest	No	RMSE R^2
Brancher (2021)	Vienna, Austria	NO_2, O_X, and O_3	*Meteorological:* RH, WD, WS, P_{sta}, and T_{atm} *Temporal:* UT, JD, WV and H	Training 1 Jan. 2015 to 15 Feb. 2020 Testing: 16 Feb. to 29 Feb. 2020 Prediction: 16 Feb. to 30 Sep. 2020	Random Forest	Yes	F^2 MB RMSE PCC IOA
Lovrić *et al.* (2021)	Graz, Austria	NO_2, O_3, and $PM_{2.5}$	*Meteorological:* RH, WD, WS, P_{sta},T_{atm} and RH *Temporal:* M, JD, WV and DI	Training 3 Jan. 2014 to 31 Dec. 2019 Testing: 3 Jan. to 10 Mac. 2020 Prediction: 10 Mac. to 2 May. 2020	Random Forest	Yes	R^2 RMSE nRMSE

Table 6.1. Summary of meteorological-normalization modelling techniques for COVID-19 BAU simulation (continued)

Dai *et al.* (2021)	31 major cities of China	SO_2, NO_2, O_3, CO, $PM_{2.5}$, and PM_{10}	*Meteorological:* RH, WD, WS, P_{sta}, and T_{atm}, BLH, CC, SR, AMC and RF *Temporal:* UT, GD, WV and H, LD	Training 70% of 2015 to 2020 Testing: 70% of 2015 to 2020	Random Forest	No	F2 MB NMB MGE NMGE RMSE PCC COE IOA
Talbot *et al.* (2021)	New Zealand	NO_2, $PM_{2.5}$, and PM_{10}	*Meteorological:* RH, WD, WS, and T_{atm} *Temporal:* UT, WN, and WV	Training 80% of 2015 to 2019 Testing: 20% of 2015 to 2019 Prediction: 2020	Random Forest	Yes	MAE NRMSE R^2
Solberg *et al.* (2021)	Europe	NO_2	*Meteorological:* RH, WD, WS, BLH and T_{atm} *Temporal:* JD, WN, and WV	Training 2015 to 2019 Testing: 2020	Generalized adaptive model	No	PCC NMGE

Table 6.1. Summary of meteorological-normalization modelling techniques for COVID-19 BAU simulation (continued)

Munir *et al.* (2021b)	Reading, United Kingdom	NO_2, NO_X, O_3, and $PM_{2.5}$	*Meteorological:* RH, WD, WS, P_{atm} and T_{atm} *Temporal:* H, MD, and WN	Training and Validation: 2018-2019 Prediction: 2020	Generalized adaptive model	Yes	FAC2 MB RMSE PCC MAE
Munir *et al.* (2021a)	Northern United Kingdom	NO_2, NO_X, O_3, and $PM_{2.5}$	*Meteorological:* WD, WS and T_{atm} *Temporal:* H, MD, and WN	Training: 80% of 2019-2020 Testing: 20% of 2019-2020	Generalized adaptive model	No	-

Abbreviation:

Input Variables: station pressure (P_{sta}), atmospheric temperature (T_{atm}), dew temperature (T_{dew}), class-A pan evaporation, (Evap), wind speed (WS), wind direction (WD), rainfall (RF), relative humidity (RH), sunshine hours (SH), global radiation (GR) and cloud cover (CC) ,atmospheric mass cluster (AMC), boundary layer height (BLH), Julian day (JD), unix time (UT) and weekday values (WV), Gregorian day (GD), Lunar day (LD), week number (WN), month number (MN), hour (H).

Performance Criteria: root mean square error (RMSE), Pearson correlation coefficient (PCC), mean bias (MB), normalized mean bias (nMB), normalized RMSE (nRMSE), factor-of-two (F^2), index of agreement (IOA), coefficient of determination (R^2), centered RMSE (cRMSE), normalized centered RMSE (ncRMSE), mean gross error (MGE), normalized MGE (nMGE).

6.2. Materials and Methodology

6.2.1 Research Area and Data Collection

Taiwan is a densely populated island in East Asia (21.5–25.2 °N and 120.0–122.0 °E), with an average population density of 647 per km^2 (National Statistics, 2021) and a land area of approximately 36,000 km^2. Over half of Taiwan is mountainous and heavily forested, with the highest peak at an elevation of 3,880 m (Fig 6.1). Being located at the hub of the typhoon route, its climate is strongly affected by seasonal monsoons and typhoons, with more than 70% of the mean annual precipitation (approximately 1,800 mm) occurring during the wet-warm season (May-August) (Wu *et al*., 2019). High and steep topography leads to pronounced spatiotemporal variations in rainfall distribution (Hsu *et al*., 2020). Recently, the uneven distribution of precipitation across Taiwan has become more serious and frequent due to climate change, creating meteorological conditions that increase air pollutant dispersion, particularly in central and southern Taiwan (Cheng *et al*., 2021; Cheng and Hsu, 2019). Therefore, to comprehensively evaluate COVID-19 in Taiwan's atmospheric environment, 62 daily air quality measurements were obtained at air quality monitoring stations across the regions (23 in Northern; 14 in Central; 2 in Eastern; 20 in Southern; and 3 in Offshore) and data was collected from the corresponding meteorological stations.

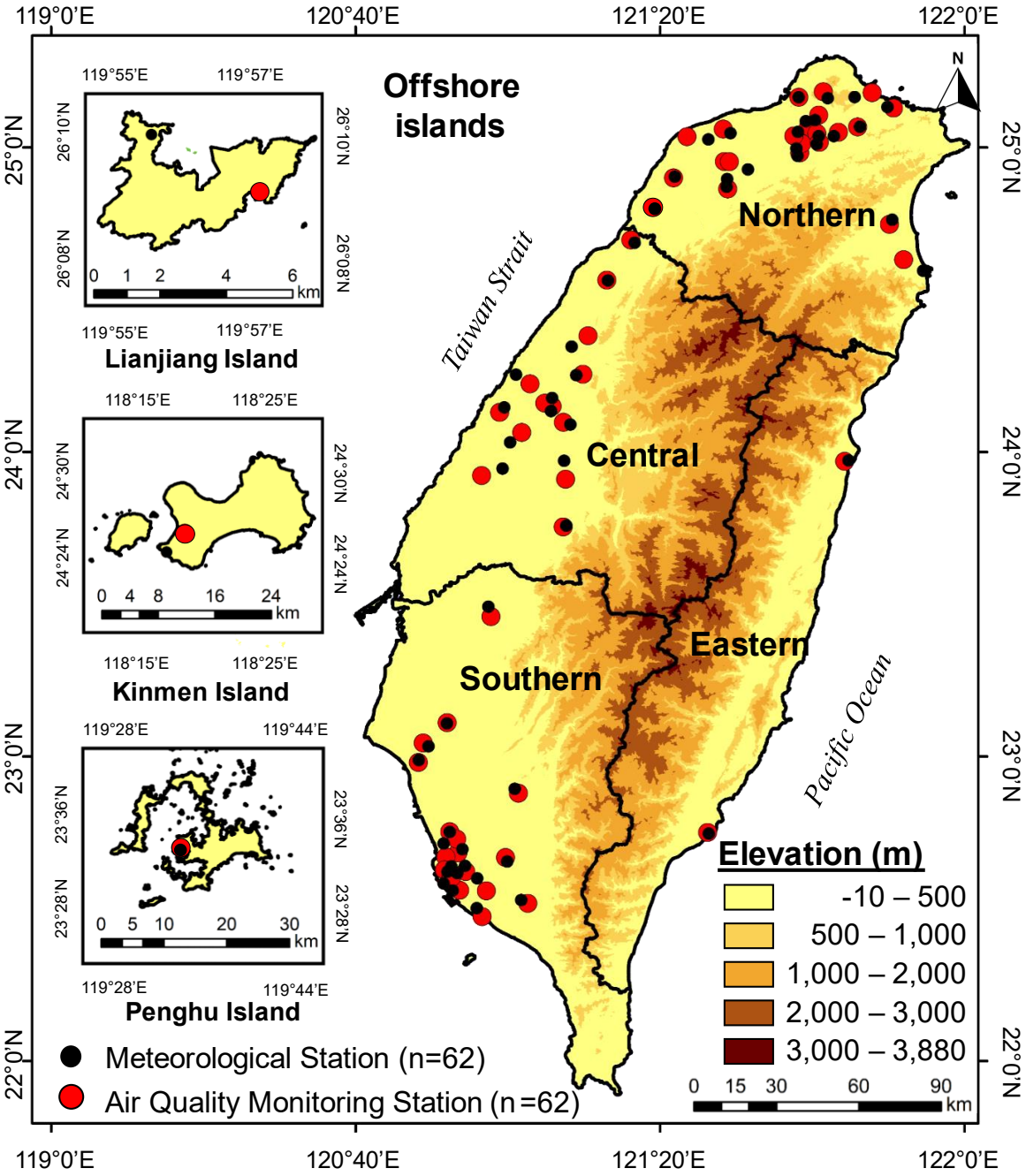

Fig. 6.1: Topography and geographical location of Taiwan with locations of meteorological and air quality monitoring stations

6.2.2 Proposed Research Framework

To eliminate meteorological biases and verify the application of machine learning methods for quantifying the impacts of COVID-19 in the absence of lockdown, a flowchart of the proposed research framework is introduced, as illustrated in Fig 6.2. The framework comprises five major sections: data preprocessing, model construction, hyperparameter optimization, performance evaluation, and change analysis. A detailed discussion of each section is provided below:

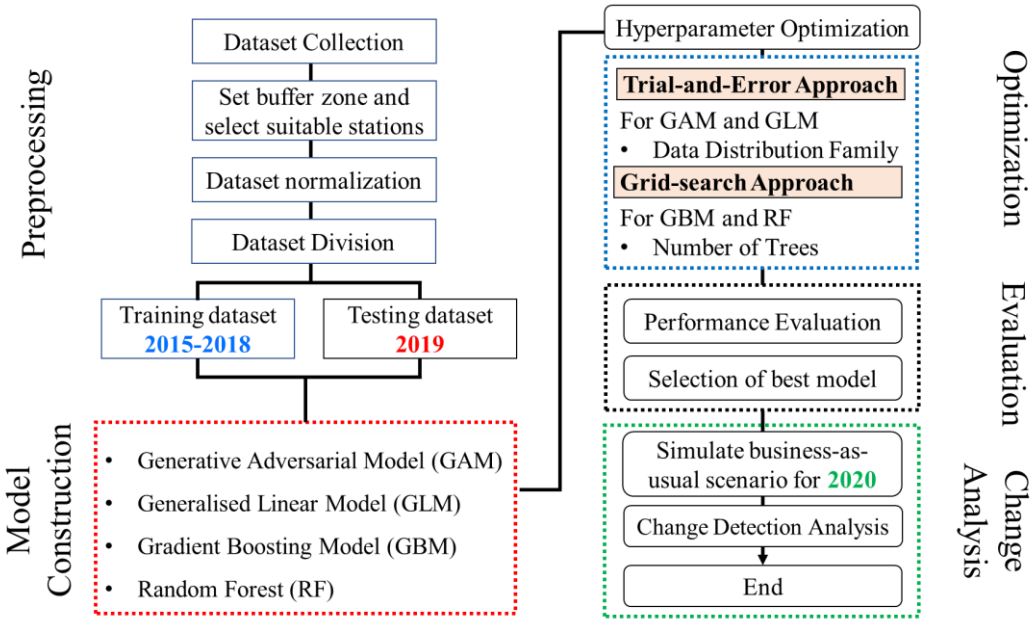

Fig. 6.2: Schematic flowchart of the proposed framework for quantifying the spatiotemporal changes between the meteorological-normalized business-as-usual and COVID-19 scenarios by utilizing different machine learning techniques.

6.2.2.1 Data Preprocessing

The 24-h averaged concentration/values of air pollutants and meteorological parameters between 1 January 2015 and 31 December 2020 were collected from the Taiwan Environment Protection Agency (TEPA 2021) and Central Weather Bureau (CWB 2020), respectively (except for precipitation for which a 24-h accumulated value was used). The upper limit of the buffer distance between the meteorological and air quality stations was set as 5 km to minimize spatial variability in the meteorological parameters of the air pollutants

(Peña Quiñones *et al.*, 2019). Temporal variables were incorporated to enhance the accuracy of the model prediction and minimize the temporal variability (e.g., seasonal effect) of air pollutants.

Prior to model construction, the collected dataset was normalized to the range of (0.1, 0.9) to prevent the dominance of larger-value data over smaller-value data, expressed mathematically in Eq. (6.1) (Wong *et al.*, 2021):

$$X_i' = 0.8 \times \frac{x_i - x_{min}}{x_{max} - x_{min}} + 0.1 \qquad (6.1)$$

In Eq. (6.1), x_i and X_i' represent the original and normalized values of the input parameter, respectively, and x_{max} and x_{min} denote the maximum and minimum values of the original input parameter, respectively.

In this research, the complex non-linear relationship between the meteorological parameters and air pollutant concentration was captured, the performance of the models was assessed, and the normalized dataset was divided into training (2015–2018 dataset), and testing and verification (2019 dataset).

6.2.2.2 Model Description

Based on literature review findings summarized in Table 6.1, the commonly adopted GAM, GLM (base model of GAM), GBM, and RF models for quantifying COVID-19 impacts under meteorological-normalized BAU scenario were selected. The detailed schematic diagram of the modelling process is illustrated in Fig. 6.3. A brief description of the selected models is provided as follows.

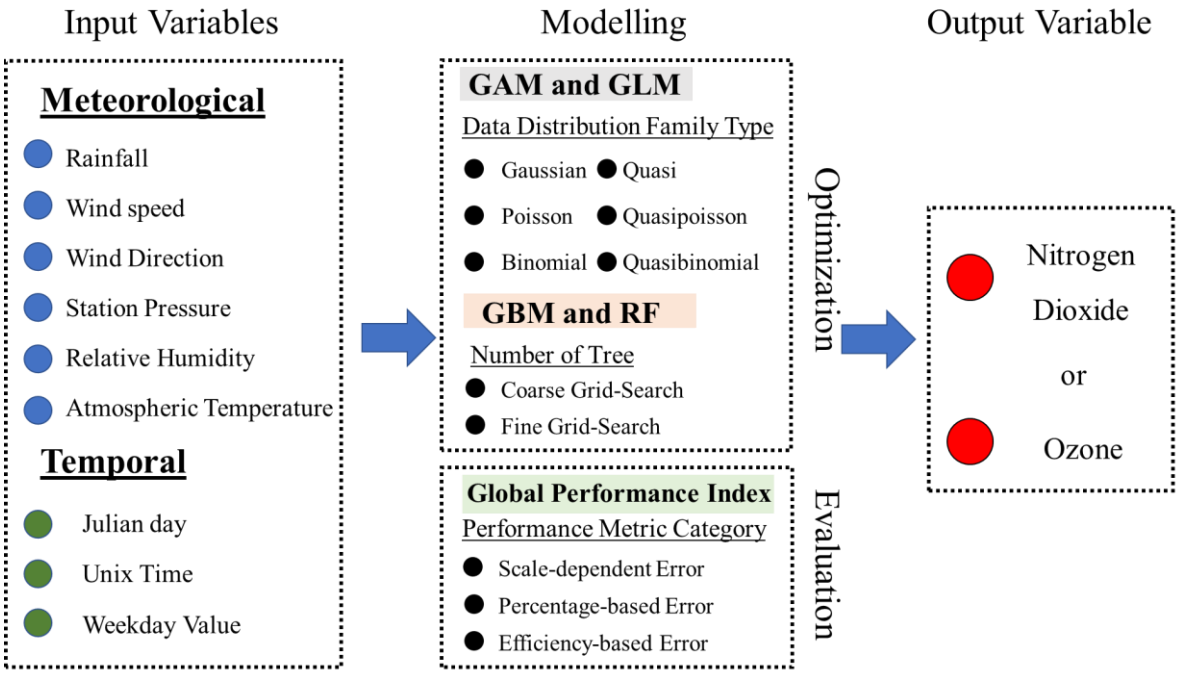

Fig. 6.3: Detailed schematic diagram for modelling meteorological-normalized business-as-usual NO_2 and O_3 concentrations.

6.2.2.2.1 GLM technique

GLM is an extension of the traditional linear regression models that was formulated by Nelder & Wedderburn (1972). The GLM is widely applied in environmental studies due to its simplicity relative to the robust regression (Saggi & Jain, 2019). To establish a linear relationship between response and predictor variables, an exponential family distribution (*e.g.*, Gaussian and Poisson) is assigned for responses along with a predefined link function, as expressed in Eq. (6.2).

$$g(E(y_i)) = \beta_0 + \sum_{j=1}^{k} \beta_j(x_{i,j}) + \varepsilon \qquad (6.2)$$

In Eq. (6.2), y_i represents the measured air pollutants concentration (NO_2/O_3) in i^{th} day at a specific monitoring station, while x_i represents the measured meteorological and temporal parameters value in i^{th} day with β_j, the regression coefficients of x_j; β_0 and ε represent the constant intercept and error term, respectively; g denotes the link function which connect the expected value Y_i to the $x_{i,j}$.

6.2.2.2.2 GAM technique

GAM was proposed and developed by Hastie & Tibshirani (1990), an addendum of GLM, in which non-linear relationship between response and predictor variables are incorporated (Shafizadeh-Moghadam *et al.*, 2018). The semiparametric GAM provides a more flexible structure for the response variable by allowing additivity of non-linear smooth functions (f_j) to replace the defined parametric relationship (β_j) on the covariates x_j, expressed mathematically in Eq. (6.3).

$$g(E(y_i)) = \beta_0 + \sum_{j=1}^{k} f_j(x_{i,j}) + \varepsilon \qquad (6.3)$$

6.2.2.2.3 GBM technique

GBM, an ensemble model that integrated both gradient descent and decision tree methods for minimizing the overfitting issues of traditional ensemble methods, through bagging and boosting algorithms. The learning procedure of GBM consecutively combine and optimize multiple shallow and weak successive classifiers or "trees" to reach the maximum negative gradient of the loss function for a more accurate estimation of the response variable (Alzamzami *et al*., 2020). In this research, as the response variable values (concentrations of NO_2 and O_3) are continuous, squared-error loss function is applied (Natekin & Knoll, 2013). The general mathematical representation of GBM is expressed as follows (Rong *et al*., 2020):

$$Y_i = \sum_{i=1}^{j} \theta_i h_i(x); \qquad (6.4)$$

In Eq. (6.4), Y_i represents the predicted air pollutant concentration; $h_i(x)$ denotes the weak classifier in each iteration while θ_i represents the loss function which can be described:

$$\theta_i = argmin \sum_{m=1}^{M} L(y_i, Y_{i-1}(x_i) + \theta_i h_m(x)) \qquad (6.5)$$

In Eq. (6.5), *argmin* function is the argument of minimum; $Y_{i-1}(x_i)$ denotes the present iteration and L represents a differentiable squared-error loss function. Detailed description can refer to Friedman (2001).

6.2.2.2.4 RF technique

RF model was introduced by Breiman (2001) which utilizes multiple decision trees as base classifier and integrated with bagging method for aggregating a whole forest of trees separated with oblique hyperplanes to obtain the final prediction (expressed mathematically in Eq. (6.6). As each tree is independently grown without pruning using a bootstrap sample of the training data (random data subset and subset of predictor variables), the tree diversity promotes the model stability which in turn reduces the generalization error or overfitting issues in decision tree technique(Ließ *et al.*, 2012; Carranza *et al.*, 2021). Further detailed description of RF technique is provided in by Breiman (2001).

$$Y_{rf,i} = \frac{1}{J}\sum_{j=1}^{J} T_j(x_i); \quad (6.6)$$

In Eq. (6.6), J represents number of trees; $T_j(x_i)$ denotes the output of ensemble of trees in i^{th} day at a specific monitoring station and $Y_{rf,i}$ represents the averaged air pollutant concentrations for random forest.

6.2.2.3 Hyperparameter Optimization

Hyperparameter tuning is crucial in machine learning models to achieving maximum learning capacity during training process and providing highest prediction performance during the testing stage due to the distinct data characteristics. Therefore, to obtain the optimized network structure of the models, as shown in Fig. 6.3, trial-and-error approach and grid-search approach are applied on GLM/ GAM and GBM/RF, respectively.

For GLM and GAM, the critical hyperparameter selected in this research is data distribution family type (Nzediegwu *et al*., 2021; Thompson *et al.*, 2014) whereas for GBM and RF, is number of trees (Oyedele *et al*., 2021; Akbar *et al*., 2021). Six different data distribution from (i) Classical: Binomial, Gaussian, Poisson, and (ii) Quasi-based: Quasi-binomial, Quasi-Gaussian and Quasi-Poisson were tested in both GLM and GAM (Zeileis *et al*., 2008). For GBM and RF, the number of trees ranged between 10 to 10000 and the optimized value is determined using coarse grid-search and followed by fine grid-search methods. During the coarse grid-search, for range between 10 to 100, the interval was set 10 whereas for range between 100 to 10000, the interval was set at 100. Fine-grid search was

conducted at lower interval (minimum 10) around the range of optimized values obtained from coarse grid-search. For instance, if the optimized coarse grid-search value is 2000, at the interval of 100, the number of trees at 1100 to 2900 will be performed, followed by an interval of 10 around the range of optimized values.

6.2.2.4 Evaluation Criteria

Various evaluation criteria have been proposed and formulated to evaluate the model's performance; however, till present, there is no universal evaluation criterion that can provide comprehensive assessment on the model. Therefore, to fairly compare and evaluate the models' performance from different perspectives, this research adopted three evaluation criteria categories: scale-dependent error, percentage-based error, and efficiency-based error (C. Chen *et al.*, 2017; Despotovic *et al.*, 2015).

Scale-dependent error metrics are utilized to compare the dataset within the same scale (Hyndman & Koehler, 2006). However, one of the major limitations of these measures is it cannot be applied to compare accuracy results across dataset under different scale. In this research, two common scale-dependent error metrics, namely mean absolute error (MAE) and root mean square error (RMSE) are adopted, expressed respectively in Eqs. (6.7) and (6.8).

$$MAE = \frac{1}{n}\sum_{i=1}^{n}|Y_i - y_i| \tag{6.7}$$

$$RMSE = \sqrt{\frac{1}{n}\sum_{i=1}^{n}(Y_i - y_i)^2} \tag{6.8}$$

Percentage-based error metrics are dimensionless; therefore, it is commonly used to compare different modelling methods across different datasets. One of the major drawbacks of this metric is its tendency towards infinity when the observed values closed to zero (Soyiri & Reidpath, 2012; Nigitz & Gölles, 2019). Therefore, the data normalization described aforementioned is crucial to avoid this occurrence. The percentage-based error metrics included are mean absolute percentage error (MAPE) and root mean square percentage error (RMSPE), expressed respectively in Eqs. (6.9) and (6.10).

$$MAPE = \frac{1}{n}\frac{\sum_{i=1}^{n}|Y_i - y_i|}{\bar{y}_i} \times 100\% \quad (6.9)$$

$$RMSPE = \sqrt{\frac{1}{n}\frac{\sum_{i=1}^{n}(Y_i - y_i)^2}{\bar{y}_i}} \times 100\% \quad (6.10)$$

In Eqs. (6.9) and (6.10), $\bar{y}_i$ represents mean values of y_i.

Efficiency-based error metrics are crucial in quantifying the variation/goodness-of-fit between the simulated and observed dataset. Although efficiency metrics such as coefficient of determination (R^2) and index of agreement (IOA) (expressed in Eqs. (6.11) and (6.12), respectively) are commonly adopted to evaluate the model's performance, these metrics are insensitive to over- or under-prediction (Krause *et al.*, 2005).

$$R^2 = 1 - \frac{\sum_{i=1}^{n}(y_i - Y_i)^2}{\sum_{i=1}^{n}(y_i - \bar{y}_i)^2} \quad (6.11)$$

$$IOA = 1 - \frac{\sum_{i=1}^{n}(y_i - Y_i)^2}{\sum_{i=1}^{n}(|Y_i - \bar{y}_i| + |y_i - \bar{y}_i|)^2} \quad (6.12)$$

6.2.2.4.1 Global Performance Index

To comprehensively evaluate the model's performance, this research adopted global performance index (GPI) which integrated different perspective statistical evaluations aforementioned into a single index (Eq. 6.13) (Despotovic *et al.*, 2015).

$$GPI_i = \sum_{j=1}^{6} \alpha_j(\tilde{\beta}_j - \beta_{ij}) \quad (6.13)$$

In order to prevent the dominance effects of larger error value over the smaller error value, all indicators are normalized using Eq. (6.1). In Eq. (6.13), α_j represents the weight factor (α_j equals -1 for R^2 and IOA, and equals to 1 for other evaluation criteria); $\tilde{\beta}_j$ represents the median of normalized values of evaluation criterion j whereas β_{ij} represents the normalized value of evaluation criterion j for model i.

6.2.2.4.2 Average Rank Score

Since the hyperparameter optimization for GAM and GLM is categorical based, an average rank score (ARS) was adopted to identify the optimized data distribution type (Chia *et al.,* 2021). Specifically, for each monitoring station, 12 models were compared (6 data distribution family type x 2 (Training dataset and Testing Dataset)). The model with the lowest GPI value was assigned the ranking score=1 (Worst), whereas the model with the highest GPI value was assigned with ranking score=12 (Best). The sum of ARS for all monitoring stations were adopted for evaluating the optimized data distribution in this research (Huang *et al.,* 2019).

6.2.2.5 Spatiotemporal Change Detection Analysis

The monthly mean percentage change between the observed and simulated air pollutants was computed using Eq. (6.14) (Hu *et al.,* 2021). The spatiotemporal variation of monthly mean concentration and percentage difference between the observed and simulated NO_2 and O_3 concentrations were performed using ArcGIS 10.8 platform, utilizing inverse distance weighting method under spatial analyst module (Wong *et al*., 2020)

$$\text{Percentage Change } (\%) = \frac{\text{Conc}_{2020\_obs} - \text{Conc}_{2020\_sim}}{\text{Conc}_{2020\_obs}} \times 100\% \quad (6.14)$$

In Eq. (6.14), $Conc_{2020\_obs}$ and $Conc_{2020\_sim}$ represent the observed and simulated mean monthly concentration of pollutants in 2020.

6.3 Results and Discussions

6.3.1 Optimized GLM and GAM models

A total of 744 GLMs and GAMs (2 models × 62 sites × 6 data distributions family type) were developed for simulating the BAU concentration of each air pollutant in this research. To select the optimized distribution family type for GLM and GBM, the average rank score for NO_2 and O_3 under different data distribution are presented in Fig. 6.4 (a) and (b), respectively.

For GLM, according to Fig. 6.4, the performance of GLMs under classical data distribution are same as the Quasi-based data distribution for both NO_2 and O_3 simulations (*e.g.*, results obtained between Gaussian and Quasi-Gaussian). Quasi-based data distribution was developed to overcome the overdispersion in computation, in which a dispersion parameter was considered by specifying the relationship on the mean and variance of dataset according to the type of distribution selected. In this research, for GLM models developed utilizing classical data distributions, the dispersion ratio was approximately equal to 1 , indicating no overdispersion occurred (Payne *et al.*, 2018). Therefore, only conventional data distribution will be discussed for GLM. As shown in Table 6.2, for GLM, the optimal data distribution type for both NO_2 and O_3 is Gaussian, with ARS_{test_NO2} and ARS_{test_O3} of 10.661 and 9.581, respectively; followed by Binomial, with mean ARS_{test_NO2} and ARS_{test_O3} of 5.306 and 3.742, respectively; and Binomial, with mean ARS_{test_NO2} and ARS_{test_O3} of 4.629 and 3.613, respectively.

On the other hand, for GAM models, it was noticed that the ψ was larger than 1.1, indicating the occurrence of overdispersion. A possible reason for the observation might be due to the more complicated non-linear smooth function adopted in GAM as compared to the constant regression coefficient adopted in the GLM, leading the residual deviance was larger than the residual degrees of freedom utilizing conventional distributions *(Guikema et al.*, 2010; Lee & Nelder, 2000). For NO_2 simulation, the top three data distributions type for GAM are Quasi-Gaussian (ARS_{test_NO2}=7.064), Gaussian (ARS_{test_NO2}=7.064), and Binomial (ARS_{test_NO2}=7.064); whereas for O_3 simulation, the top three data distribution type for GAM

are Poisson (ARS_{test_O3}=6.968), Binomial (ARS_{test_O3}=5.710) and Gaussian (ARS_{test_O3}=4.758). Although it could be observed that most Quasi-based models illustrated relatively better performance in training dataset; however, the testing results are much poorer than conventional data distributions, particularly in O_3 simulation. Although the dispersion ratio in GAM is larger than two in all conventional data distributions, it was just slightly beyond the limit (ranging between 1.2-1.4). The further adjustment of the dispersion parameter in Quasi-based data distribution may have caused poorer simulation for testing dataset due to overfitting in training data (Zhang *et al*., 2012; Zou *et al.*, 2017).

As reported by Lorenzo *et al.* (2021) and Ravindra *et al.* (2019), Poisson-based data distribution was selected as the most suitable distribution type for air pollution modelling for GAM and GLM, respectively; however different findings were found in this research. For GLM, the optimal data distribution for both NO_2 and O_3 modelling is Gaussian data distribution, whereas for GAM, the optimal data distribution for NO_2 and O_3 simulation is Quasi and Poisson, respectively. Based on these findings, the importance of performing optimal data distribution selection for GLM and GAM are shown. Although the optimal data distribution selection may be varied in different monitoring stations under the influence of the geographical and climate variations; still, associated with the application of ARS, it serves as a basis of proper data distribution type selection, especially for studies incorporating large research area.

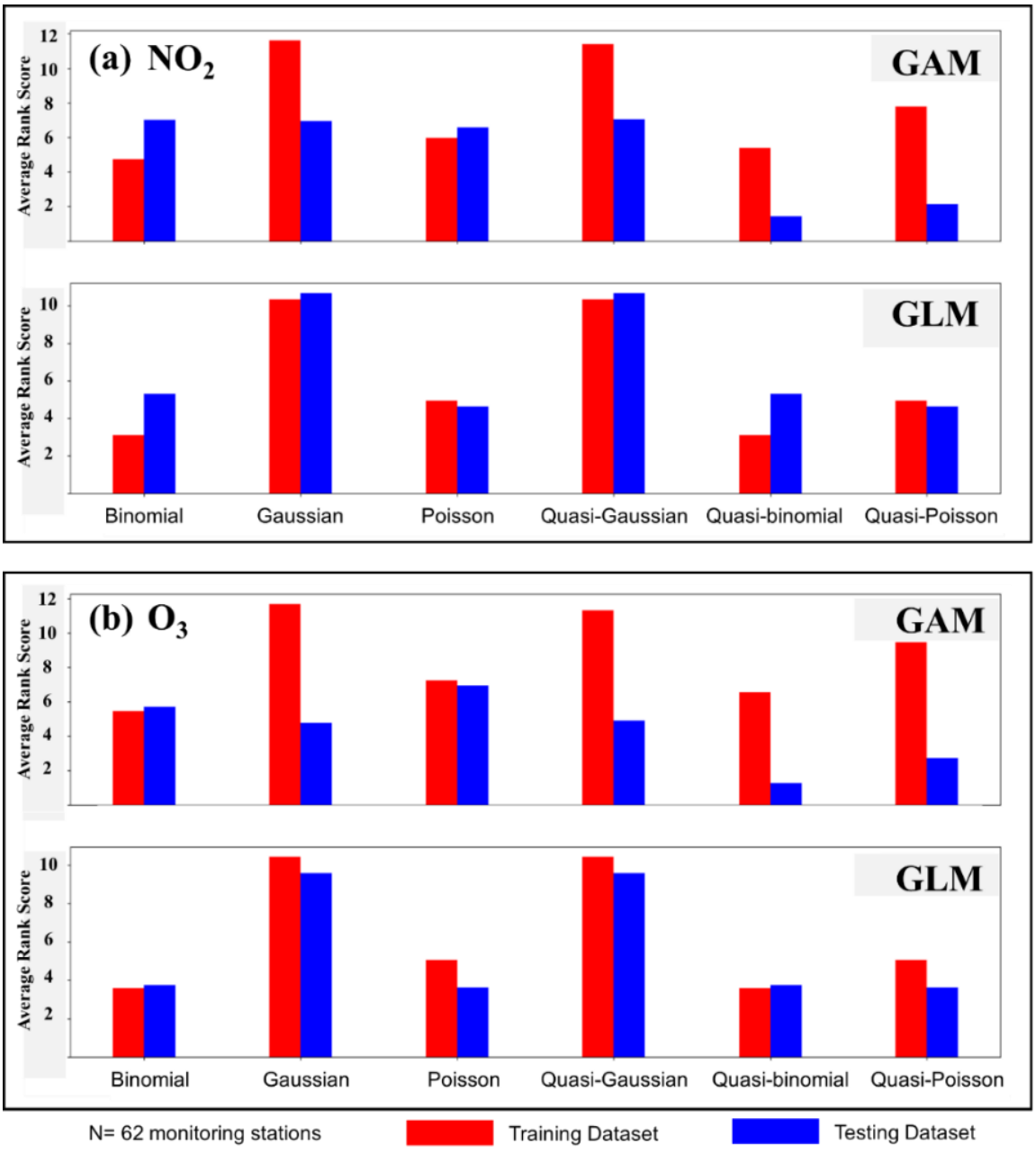

Fig. 6.4: Mean average rank score of GLR and GAM for 62 monitoring stations under different data distribution family type

Table 6.2: Mean average rank score of GLR and GAM for 62 monitoring stations under different data distribution family type

For NO_2 simulation						
Distribution Family Type	Generalized Linear Model (GLR)		Dispersion ratio	Generalized Additive Model (GAM)		Dispersion ratio
	Training	Testing		Training	Testing	
Binomial	3.113	5.306	1.003	4.742	7.000	1.153
Gaussian	10.339	10.661	1.004	11.605	6.935	1.126
Poisson	4.952	4.629	1.003	5.968	6.565	1.129
Quasi-Gaussian	10.339	10.661	1.003	11.395	7.065	1.168
Quasi-Binomial	3.113	5.306	1.004	5.387	1.452	1.115
Quasi-Poisson	4.952	4.629	1.003	7.774	2.113	1.134

For O_3 simulation						
Distribution Family Type	Generalized Linear Model (GLR)		Dispersion ratio	Generalized Additive Model (GAM)		Dispersion ratio
	Training	Testing		Training	Testing	
Binomial	3.581	3.742	1.008	5.452	5.710	1.374
Gaussian	10.419	9.581	1.006	11.677	4.758	1.269
Poisson	5.065	3.613	1.005	7.258	6.968	1.315
Quasi-Gaussian	10.419	9.581	1.008	11.323	4.903	1.442
Quasi-Binomial	3.581	3.742	1.006	6.532	1.258	1.389
Quasi-Poisson	5.065	3.613	1.005	9.452	2.710	1.234

6.3.2 Optimized GBM and RF models

In most reported studies summarized in Table 6.1, the number of trees in GBM and RF models were usually fixed by default or adopted from published references. However, referring to Figs. 6.5 and 6.6 (model's performance of NO_2 and O_3 in coarse grid-search, respectively) the optimal tree number varied significantly across the monitoring stations as well as the pollutant type. The optimized GBM and RF models through fine grid-search will be discussed in Section 6.3.3.

During the training (testing) stage, GBM shows much higher variation in model's performance (> ± 200%) under different number of trees as compared to RF, with GPI ranging from -4.2 to 4.2 (-5.0 to 1.0) and -1.3 to 4.2 (-2.3 to 0.0) for NO_2 and O_3 simulation, respectively. The results demonstrate that the GBM has higher sensitivity and dependency towards the number of trees included in the model. Structurally, although both RF and GBM

appear to be similar as their learning are based on decision tree algorithm, nonetheless, the models differed significantly in tree-building/learning process. The GBM sequentially build each tree at a time and improves relying on the prior trees, causing it to be non-parallelizable (Natekin & Knoll, 2013) and has high sensitivity to noises in dataset (Cortes-Ciriano *et al.*, 2015) as compared to RF. As the relationship between air pollutant and meteorological data are stochastic and dynamic (González-Recio *et al.*, 2013), therefore large variation of generalization performance in GBM was observed at different number of tree.

On the other hand, RF shows relatively more stable simulation performance (approximately ± 25%), for training (testing) dataset even under large range number of tree, with GPI ranging from 1.8 to 2.9 (-3.5 to -2.0) and 2.6 to 2.9 (-3.3 to 2.7) for NO_2 and O_3 simulation, respectively. This is due to RF has higher parallelization compared to GBM as all trees are built independently by maximizing the information from randomized dataset (Probst *et al.*, 2019). According to Fig. 6.6(b), although it could be observed that most of the models' performance increase as the number of trees increases in the training dataset for NO_2 simulation, poorer performance is observed in the testing dataset, which might be due to the occurrence of overfitting (Richter *et al.*, 2016). However, for O_3 simulation (Fig. 6.5(b)), this phenomenon is inconspicuous. As reported in Probst & Boulesteix (2017), these contradicted phenomenon might due to the characteristics of variables (both input and output) in the dataset, highlighted the importance of testing large range of tree in order to more precisely optimizing the model.

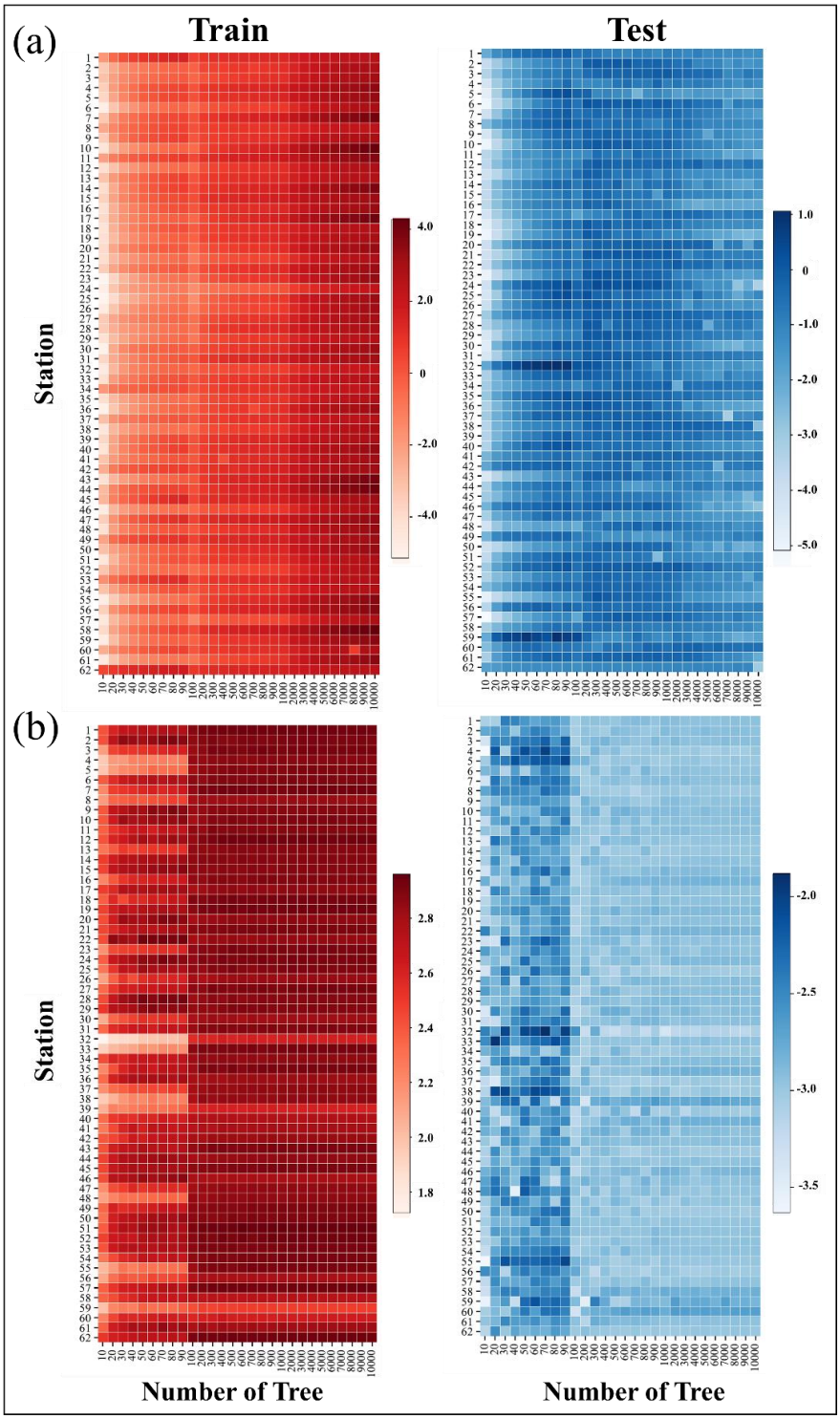

Fig. 6.5: Effects of number of trees on (a) GBM and (b) RF for NO_2 simulation across 62 monitoring stations. Heatmap representations illustrate the GPI values for both training and testing dataset

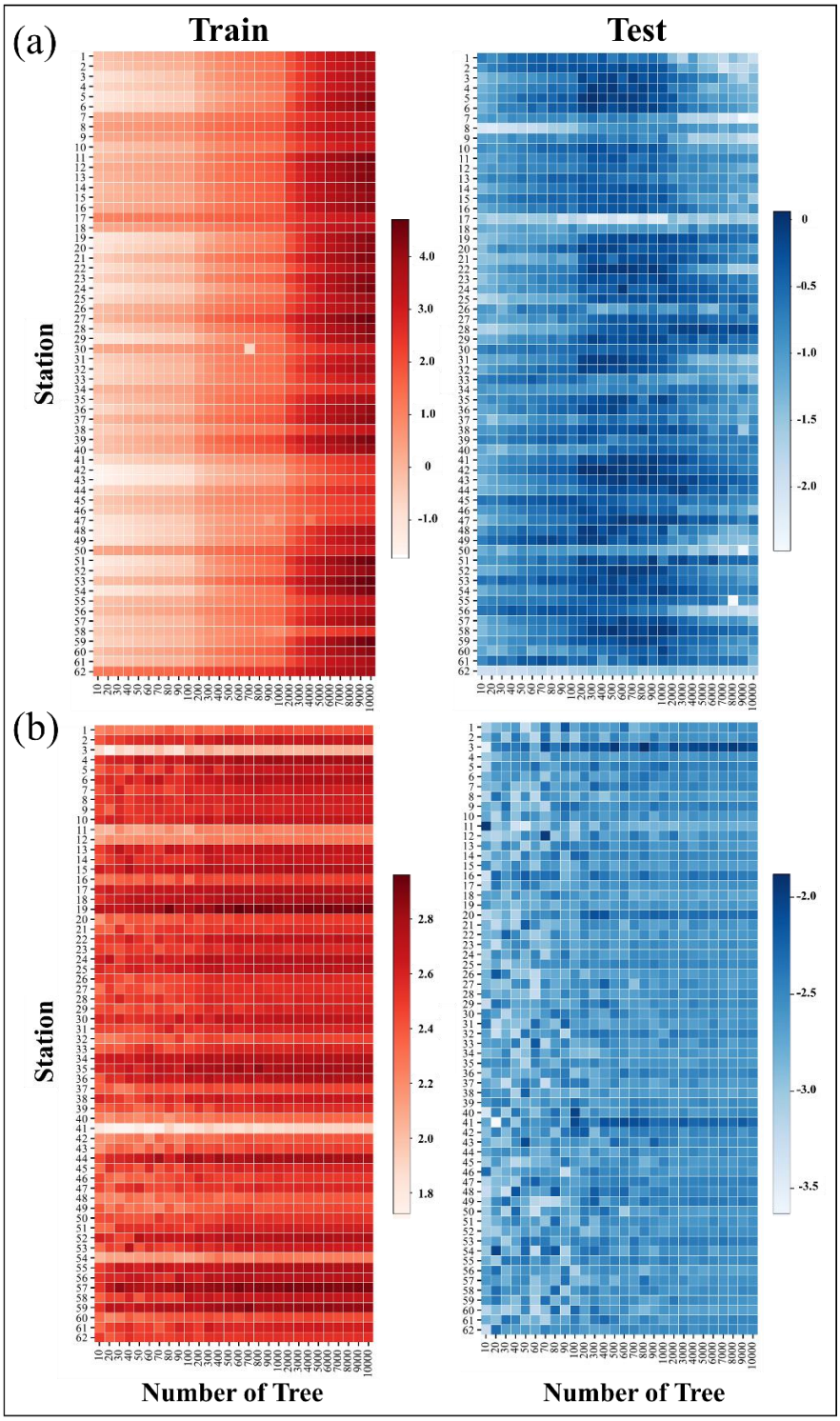

Fig. 6.6: Effects of number of trees on (a) GBM and (b) RF for O_3 simulation across 62 monitoring stations. Heatmap representations illustrate the GPI values for both training and testing dataset

6.3.3 Selection of Optimized Modelling Type

A robust and accurate model is an important pre-requisite for reliable simulation of air pollutants' concentrations. In previous sections, the performance of the optimized GLM, GAM, GBM and RF for simulating the concentrations of NO_2 and O_3 during the training (2015-2018) the testing period (2019) was evaluated in terms of various criteria and the comprehensive GPI. In this section, the most suitable modelling technique of each monitoring station for NO_2 and O_3 simulation will be selected based on the performance of the models as summarized in Tables 6.S1 and 6.S2, respectively.

Fig. 6.7 illustrates the boxplots of the six performance criteria and the Taylor diagram that shows the average GPI as well as the standard deviation of GPI for NO_2 and O_3 simulations using the four aforementioned machine learning techniques. The boxplots serve to visualise the performance variance of different models at different stations across Taiwan, whereas the Taylor diagrams provides a more comprehensive view of the overall performance. It is noteworthy to mention that the performance deterioration was very drastic for the case of GAM and RF. Not only had their simulation accuracies became lower, at the same time the expansion of the boxplots for the two models indicated that the performance variance across the whole Taiwan had increased, resulting in less stable performance. Potts & Rose (2018) had suggested that both GLM and GAM share mutual framework, in which the GAM considers additional smoothing function for at least one covariate. This has resulted in the GAM to be able to model non-linear processes to the better extent, and outperformed GLM when it was used for the training dataset. However, due to the dynamic climate variability, the GAM models seem unable to capture the essential relationship among parameters, leading to the poor testing performance. Despite many literatures claiming that the GAM is a more powerful model than the GLM, however, contradicted phenomenon was reported in this research (Fig. 6.7).

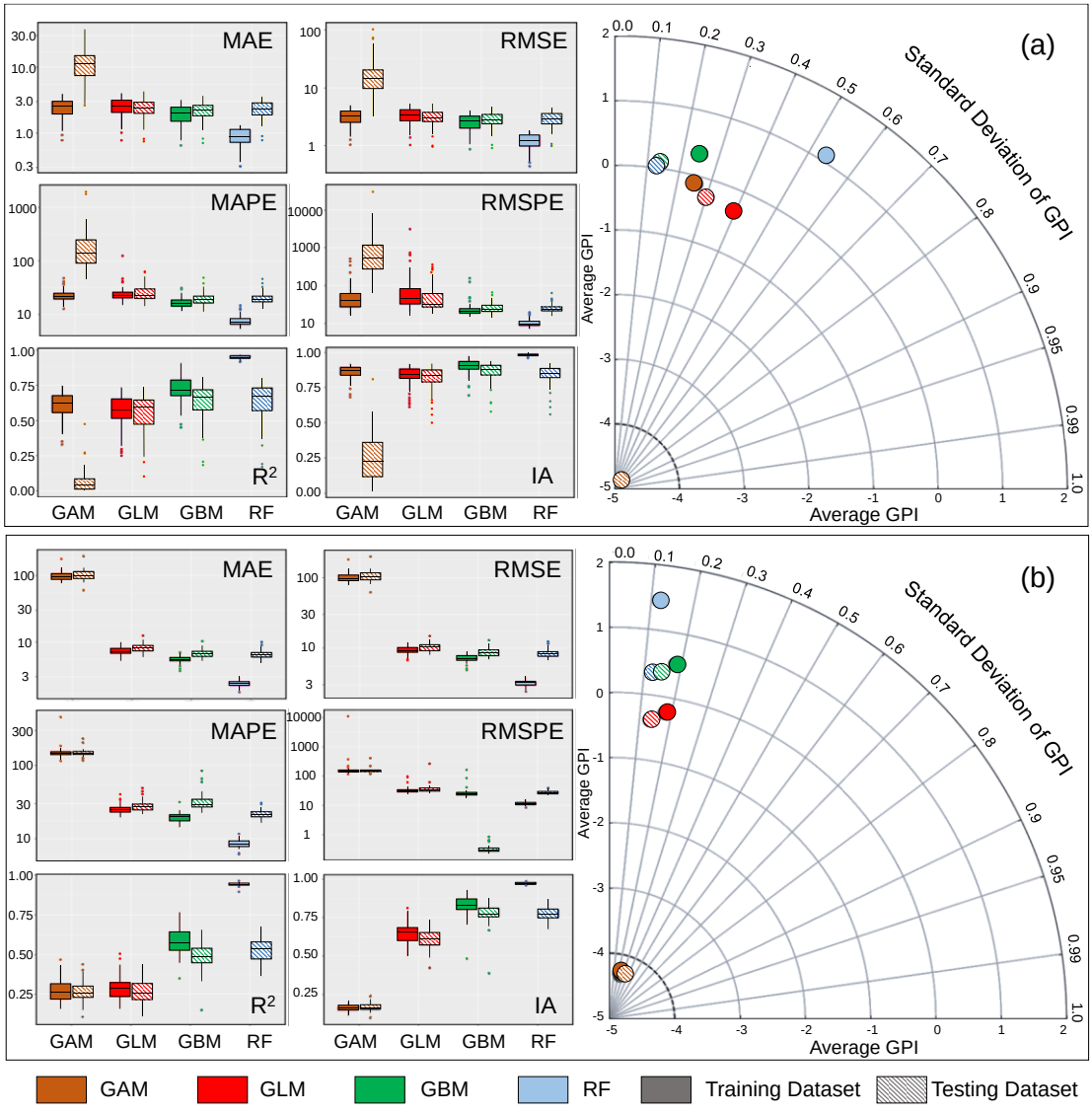

Fig. 6.7: Boxplots for six performance criteria (MAE, RMSE, MAPE, RMSPE, R^2 and IA) and Taylor diagram of average GPI and standard deviation of GPI under four machine learning techniques for (a) NO_2 and (b) O_3 simulations. The brown, red, green, and blue colour indicates performance of GAM, GLM, GBM and RF, respectively; whereas the solid and striped colours represent performance for training dataset and testing dataset, respectively.

Similar issue was faced by the RF for NO_2 simulation whereby the RF could simulate well for the training data but not for the testing data. While both the GBM and RF are tree-based, such phenomenon was not observed for the GBM. The core difference between the GBM and RF is that the former is trained progressively by working on the residual of previous tree, leading to the minimisation of the bias. On the other hand, trees of the RF are trained in parallel and independent on each other. The randomness is the key factor of the RF performance, and poor randomization or insufficient could lead to higher bias (Barthwal *et al.*, 2021*)*. This could explain the difference in performance of the GBM and RF.

Despite having poorer performance than the GBM, the RF still managed to perform better than the GAM and GLM. The Taylor diagram in Fig. 6.7(a) indicates that the GBM and RF had the highest average GPI across the 62 selected stations. RF with training dataset had higher standard deviation of GPI, probably due to the bias of the model to certain regions. Fig. 6.S1 illustrates the optimal modelling techniques for both NO_2 and O_3 across each monitoring station for the whole Taiwan. The model selection at the individual station was based on the GPI value. It can be seen that only the GBM and RF were selected as they achieved better GPI score. For NO_2 simulation, based on Fig. 6.S1(a), GBM dominated most of the areas in Taiwan as the selected models for O_3 concentration simulation, including the Northern (13/23 stations), Central (11/14 stations) and Southern (14/20 stations) regions whereas the RF was only favoured in the Offshore (3/3 stations).

The same approach was used to select the best model of O_3 concentration. In this case, the GAM exhibited notable difference in performance as compared to the other three machine learning techniques. As illustrated in Fig. 6.S1 (b), similar to NO_2 simulation, the GBM dominated in the Northern (20/23 stations), Central (9/14 stations), Eastern (2/2 stations) and Southern (16/20 stations) whereas the RF was only favoured in the Offshore (3/3 stations). It is worth to mention that the domination of the GBM for O_3 concentration simulation was much decisive than the NO_2 concentration simulation, whereby higher number of stations opted for GBM in the Northern and Southern regions.

From the currents research, it can be inferred that the GAM is not suitable for NO_2 and O_3 concentration simulation in Taiwan. As for the GLM, despite having high stability with low performance variance, its accuracy in terms of the six evaluation criteria and GPI was still slightly lower than the GBM and RF. With high computational capacity, different models could be used to simulate NO_2 concentration at different regions of Taiwan, however, the GBM, with its outstanding balance accuracy and generalization shall be opted if only one model is to be used over the whole Taiwan.

6.3.4 Change Detection Analysis

By utilizing the meteorological normalized data simulated from best performing models, the impact of COVID-19 on air quality can be better quantified by identifying the spatiotemporal trend of monthly mean percentage change for NO_2 and O_3 concentration between BAU scenario with the observed data. The observed and simulated daily mean concentration of NO_2 ranged between 0.8–27.0 and 1.8–29.8 ppb, whereas for O_3, they ranged 12.6–87.2 and 14.6–67.8 ppb, respectively (Figs. 6.S1 and 6.S2).

For NO_2 and O_3 simulation, the observed and simulated meteorological normalized BAU scenario utilizing best performing models across Taiwan is illustrated in Fig. 6.8. Referring to Fig. 6.8(a), although in the absence of a lockdown, the observed NO_2 concentrations in 2020 were usually lower than the simulated BAU concentrations across different cities, with mean concentration reduced by approximately 14.9%. For both observed and simulated BAU concentrations, the daily mean concentrations of NO_2 are in compliance with the Taiwan national standard where NO_2 is always $\leq$ 30 ppb. Due to different socioeconomic and urbanization level across Taiwan, the NO_2 concentration change varied spatially, ranging between reduction up to 60% and increment up to 80% (observed in the offshore islands). Keller *et al.*, (2021) performed XGBoost machine learning algorithm to access the 6-month (January to June 2020) change of NO_2 and O_3 in 46 countries at over 5,700 monitoring stations. It was reported that the observed NO_2 concentration declined by 18% as compared to BAU scenario, similar improvement shown in Taiwan. This implies that

the reduced human activity and mobility under the government measures and public awareness might played a major role for the improvement instead of the climate.

On contrary to NO_2 continual improvement throughout 2020, significant reduction up to 78% of O_3 concentration was only observed in June to August 2020 and an abnormal increment up to 45% was observed in April and September. The meteorologically normalized daily O_3 across all cities in Taiwan was below the standard (O_3: $\leq$ 71 ppb), however for the observed dataset, abnormally high O_3 was detected, particularly in Northern and Southern regions (frequency = 43 times). Throughout 2020, eliminating the meteorological impacts, the mean O_3 concentration was observed to have reduced by approximately 5.8%. The significant increment of O_3 concentration in April 2020 was observed globally, primarily due to the effects of reduced mobility and anthropogenic emissions, after the declaration of pandemic by WHO (Tang *et al.*, 2021). Although there was no lockdown imposed in Taiwan; Taiwan Government imposed restrictive measures such as border restriction and crowd control at travel hotspots, which has subsequently led to minimal community mobility in all forms of transportation in April and drastically reduced the NO_x ($NO+NO_2$) and volatile organic chemicals (VOCs) emissions (Zhang *et al*., 2021). Similar to most regions, most of the monitoring stations are installed in urban areas, where the O_3 production are usually VOC-limited. Therefore, the decrease in NO_x might have led to its abnormal increment in April (Fenech *et al*., 2021). In September, due to the effects of unprecedented transboundary pollution associated with the Asian high-pressure ridge, an elevated ozone concentration was observed in the North and Southern regions (Keoni, 2020).

Referring to the Fig. 6.8, substantial improvement in NO_2 and O_3 could be observed after eliminated the meteorological impacts (except for O_3 in September). Their results presented implied that the reduction/disruption of anthropogenic emissions even in the absence of a lockdown is more pronounced as compared to the meteorological impacts in Taiwan. The findings are in consistent with most of the reported literature where lockdown was imposed, only with a smaller magnitude of improvement (Liu *et al.*, 2022, Petetin *et al*., 2020), highlighting a new insight/approach for air quality management.

6.4. Implications and Limitations

The utilization of different modelling techniques for quantifying the COVID-19 impacts is imperative, and extensive research has been carried out across the globe; however, the modelling framework has not yet been clearly established. Based on the findings, this research has proven the importance of modelling method chosen and the necessity to perform hyperparameter optimization for each monitoring station during the simulation of BAU concentrations of air pollutants. In addition, most studies reported poorer simulation performance of O_3 simulation due to complex photochemical reactions with NO_x, VOCs and meteorology (Brancher, 2021, Fenech *et al.*, 2021, Lee *et al.*, 2020). Under systematic optimization and proper modelling method selection, it could be observed that the developed models not only performed well in simulating the primary pollutant (NO_2), but also for the secondary pollutant (O_3). Therefore, the proposed framework in this research could be useful to facilitate and investigate the meteorological-normalized scenario over air pollutants for special incidence.

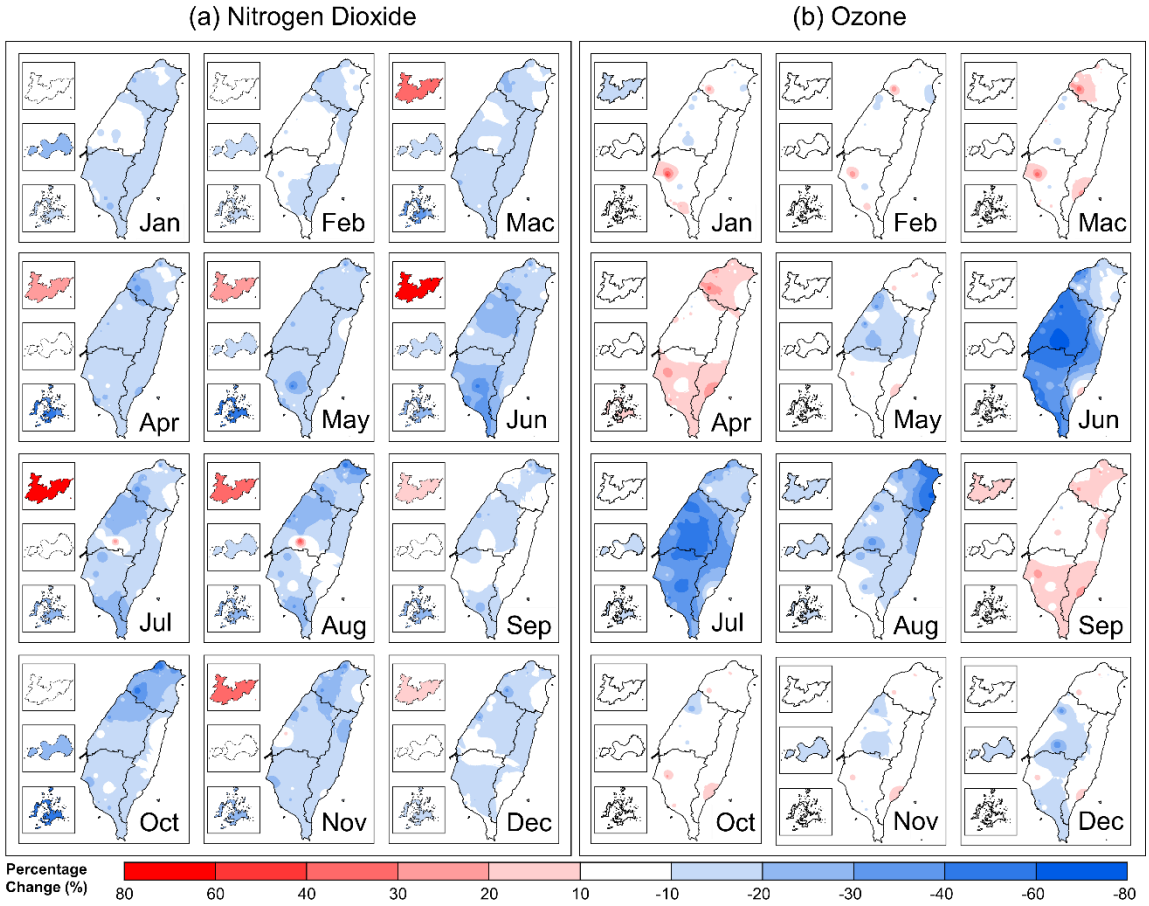

Fig. 6.8: Spatiotemporal change detection analysis for (a) NO_2 and (b) O_3 concentration in Taiwan between observed and simulated meteorological normalized BAU scenario.

Ozone has been identified as the major health-threating air pollutant worldwide, and recognized as the emerging air pollutant in Taiwan due to increasing detection of non-attainment frequency, with O_3 concentration > 71 ppb (Chen *et al.*, 2021). Despite the ubiquitous decrease in NO_2 observed throughout 2020, however insignificant improvement for O_3 or worse, significant increment of O_3 could be observed, which might be attributed to the higher VOC/NO_x ratio. This might increase the mortality burden from cardiorespiratory diseases, especially to the vulnerable population (Li *et al.*, 2021). Based on this phenomenon, for better management of O_3 pollution, stringent emission control is crucial, not only on the primary pollutants but also the precursors like VOCs.

Several limitations of this research that must be acknowledged. Due to intensive computation required during model selection and hyperparameter optimization across 62 monitoring stations, this research only simulate the daily mean concentrations of NO_2 and O_3. Phenomenon such as downpour or sudden pollution might not be reflected in this research. In addition, the long-range transportation of pollutants sourcing was not performed, therefore underlying reasons (local emission or transboundary emission) for the changes of concentration in NO_2 and O_3 between observed and simulated data might not be clearly evaluated in this research.

6.5 Conclusions and Future Recommendations

With the increasing popularity on quantifying the impacts of COVID-19 induced lockdown on the air quality utilizing different modelling techniques, this research has a marked importance to provide an insight of COVID-19 on air pollutants to region without lockdown imposed. This research has utilized and compared four different AI methods, namely GAM, GLM, GBM and RF to quantify the spatiotemporal impacts of COVID-19 on NO_2 and O_3 concentrations across 62 cities in Taiwan under meteorological-normalized BAU conditions.

Based on the findings, the selection of modelling method and the optimization of hyperparameter is crucial for each studied monitoring station for simulating the BAU concentrations of air pollutants. For GLM, the optimal data distribution for both NO_2 and O_3 modelling is Gaussian data distribution, whereas for GAM, the optimal data distributions for NO_2 and O_3 simulation are Quasi and Poisson, respectively. Meanwhile, for RF and GBM, the optimized number of trees is highly site dependent. Due to the complicated and non-linear characteristics between the air pollutants with temporal and meteorological parameters, regression-based models (GAM and GLM) have the poorest performance. For Taiwan, it could be observed that tree-based models (RF and GBM) are more suitable for simulating the NO_2 and O_3 BAU concentrations.

Throughout 2020, even in the absence of a lockdown, the daily mean meteorological-normalized NO_2 and O_3 across Taiwan were observed to reduce by 14.9 and 5.8%,

respectively with significant spatiotemporal variation. Due to the frequent occurrence of downpour in recent decades, further studies on higher temporal resolution such as hourly are required to better understand the meteorological impacts to the air pollutants. Furthermore, to sustainably maintain the air quality management, future studies should also identify the possible pollution sources (*e.g.*, type of industry, local emission, or transboundary pollution) so that the corresponding mitigations can be performed by relevant authorities. This unexpected "global experiment" provided an opportunity to assess the weight of anthropogenic activity and the changing climate on enhancing the environment (Rybarczyk & Zalakeviciute, 2021). However, measures like lockdown will be unlikely to be imposed indefinitely. Therefore, based on the findings in this research, it is expected to provide a new insight/approach for better air quality management.

Table 6.S1: Summary of optimized modelling techniques for NO_2 simulation and its corresponding GPI values

Station number	GLM			GAM			GBM			RF		
	Distribution Family	GPI_Train	GPI_Test	Distribution Family	GPI_Train	GPI_Test	Number of Tree	GPI_Train	GPI_Test	Number of Tree	GPI_Train	GPI_Test
1	Gaussian	-0.249	-0.312	Poisson	-4.437	-4.415	120	0.228	0.391	90	1.388	0.379
2	Gaussian	-0.220	-0.386	Poisson	-4.334	-4.397	560	0.439	0.363	170	1.478	0.361
3	Gaussian	-0.300	-0.394	Poisson	-4.669	-4.779	770	0.476	0.446	290	1.146	0.360
4	Gaussian	-0.327	-0.424	Poisson	-4.437	-4.432	570	0.381	0.454	1130	1.400	0.490
5	Gaussian	-0.363	-0.323	Poisson	-4.392	-4.363	420	0.319	0.430	300	1.433	0.454
6	Gaussian	-0.335	-0.350	Poisson	-4.364	-4.361	310	0.356	0.462	490	1.443	0.438
7	Gaussian	-0.228	-0.444	Poisson	-4.251	-4.357	310	0.497	0.374	250	1.532	0.394
8	Gaussian	0.090	-0.559	Poisson	-4.002	-4.334	910	0.825	0.468	130	1.569	-0.003
9	Gaussian	-0.121	-0.419	Poisson	-4.282	-4.430	180	0.344	0.282	710	1.462	0.425
10	Gaussian	-0.257	-0.495	Poisson	-4.165	-4.237	320	0.462	0.485	430	1.607	0.480
11	Gaussian	-0.237	-0.425	Poisson	-4.160	-4.139	670	0.700	0.419	10	1.650	0.493
12	Gaussian	-0.162	-0.310	Poisson	-4.212	-4.350	1050	0.715	0.312	70	1.533	0.217
13	Gaussian	-0.177	-0.348	Poisson	-4.248	-4.414	120	0.318	0.322	250	1.501	0.384
14	Gaussian	-0.155	-0.415	Poisson	-4.299	-4.413	280	0.435	0.342	220	1.446	0.239
15	Gaussian	-0.180	-0.405	Poisson	-4.334	-4.437	340	0.450	0.309	240	1.445	0.362
16	Gaussian	-0.213	-0.358	Poisson	-4.423	-4.538	460	0.521	0.368	460	1.382	0.318
17	Gaussian	0.502	-0.123	Poisson	-3.798	-4.082	10	-0.015	-0.355	50	1.691	0.257
18	Gaussian	-0.108	-0.475	Poisson	-4.291	-4.484	1210	0.639	0.245	80	1.420	0.220
19	Gaussian	-0.277	-0.301	Poisson	-4.466	-4.432	1310	0.638	0.419	730	1.418	0.368
20	Gaussian	-0.237	-0.259	Poisson	-4.506	-4.033	460	0.457	0.334	370	1.418	0.360
21	Gaussian	-0.171	-0.409	Poisson	-4.669	-3.101	410	0.476	0.171	50	1.244	0.264
22	Gaussian	-0.150	-0.287	Poisson	-4.416	-4.502	580	0.425	0.299	30	1.398	0.228
23	Gaussian	-0.232	-0.257	Poisson	-4.517	-4.478	470	0.482	0.366	130	1.397	0.337
24	Gaussian	-0.265	-0.330	Poisson	-4.327	-4.285	600	0.459	0.415	370	1.549	0.352
25	Gaussian	-0.152	-0.219	Poisson	-4.339	-4.281	630	0.578	0.452	110	1.517	0.160

26	Gaussian	-0.065	-0.172	Poisson	-4.341	-4.325	120	0.292	0.181	20	1.478	0.230
27	Gaussian	-0.200	-0.439	Poisson	-4.241	-4.373	630	0.692	0.389	330	1.544	0.234
28	Gaussian	-0.253	-0.381	Poisson	-4.251	-4.378	620	0.659	0.495	180	1.522	0.286
29	Gaussian	-0.318	-0.293	Poisson	-4.423	-4.396	660	0.536	0.456	150	1.392	0.377
30	Gaussian	0.229	-1.038	Poisson	-3.636	-3.817	1540	0.362	0.306	110	1.622	0.413
31	Gaussian	-0.203	-0.449	Poisson	-4.318	-4.412	350	0.470	0.386	90	1.487	0.262
32	Gaussian	-0.315	-0.442	Poisson	-4.286	-4.306	340	0.517	0.454	160	1.513	0.394
33	Gaussian	-0.397	-0.205	Poisson	-4.375	-4.312	130	0.257	0.363	60	1.495	0.337
34	Gaussian	-0.166	-0.582	Poisson	-3.977	-4.127	1700	1.064	0.342	110	1.719	0.342
35	Gaussian	-0.310	-0.290	Poisson	-4.384	-4.420	860	0.717	0.392	120	1.462	0.373
36	Gaussian	-0.327	-0.440	Poisson	-4.420	-4.380	540	0.595	0.461	130	1.487	0.476
37	Gaussian	-0.150	-0.438	Poisson	-3.607	-3.924	830	0.786	0.344	120	1.548	0.256
38	Gaussian	-0.333	-0.449	Poisson	-4.239	-4.346	920	0.660	0.423	50	1.500	0.496
39	Gaussian	-0.256	-0.435	Poisson	-4.178	-4.253	220	0.545	0.388	140	1.614	0.401
40	Gaussian	-0.488	-0.450	Poisson	-4.005	-4.110	1260	0.973	0.594	100	1.712	0.513
41	Gaussian	-0.347	-0.477	Poisson	-4.090	-4.022	1260	0.775	0.551	230	1.529	0.437
42	Gaussian	-0.581	-0.398	Poisson	-4.314	-4.366	400	0.448	0.634	130	1.401	0.438
43	Gaussian	-0.527	-0.404	Poisson	-4.406	-4.377	1220	0.656	0.263	50	1.389	0.394
44	Gaussian	-0.325	-0.603	Poisson	-4.075	-4.264	1830	0.771	0.371	280	1.458	0.410
45	Gaussian	-0.285	-0.183	Poisson	-4.156	-4.214	230	0.464	0.305	310	1.506	0.204
46	Gaussian	-0.660	-0.344	Poisson	-4.251	-4.044	270	0.435	0.387	330	1.433	0.383
47	Gaussian	-0.298	-0.368	Poisson	-4.142	-4.261	640	0.616	0.489	60	1.576	0.360
48	Gaussian	-0.295	-0.365	Poisson	-4.057	-4.380	470	0.545	0.419	540	1.444	0.466
49	Gaussian	-0.429	-0.461	Poisson	-4.254	-4.296	240	0.409	0.502	890	1.491	0.544
50	Gaussian	0.077	-0.355	Poisson	-4.545	-4.645	1080	0.741	0.195	170	1.286	0.021
51	Gaussian	-0.327	-0.314	Poisson	-4.543	-4.516	670	0.514	0.393	260	1.272	0.366
52	Gaussian	-0.352	-0.465	Poisson	-4.622	-4.645	530	0.491	0.495	770	1.235	0.458
53	Gaussian	-0.283	-0.297	Poisson	-4.587	-4.453	300	0.357	0.333	230	1.322	0.415
54	Gaussian	-0.364	-0.220	Poisson	-4.606	-4.509	640	0.455	0.399	260	1.234	0.250

55	Gaussian	-0.172	-0.363	Poisson	-4.272	-4.345	250	0.400	0.371	380	1.536	0.299
56	Gaussian	-0.141	-0.212	Poisson	-4.270	-4.371	240	0.427	0.270	240	1.529	0.220
57	Gaussian	-0.232	-0.337	Poisson	-4.405	-4.457	810	0.515	0.408	800	1.394	0.443
58	Gaussian	-0.565	-0.116	Poisson	-4.015	-4.142	410	0.279	0.739	80	1.638	0.619
59	Gaussian	-0.251	-0.356	Poisson	-4.283	-4.302	510	0.585	0.518	310	1.576	0.276
60	Gaussian	-0.238	-0.541	Poisson	-4.478	-4.591	1000	0.608	0.374	280	1.279	0.261
61	Gaussian	-0.218	-0.274	Poisson	-4.473	-4.543	710	0.491	0.290	210	1.350	0.406
62	Gaussian	0.088	-0.347	Poisson	-4.256	-3.877	560	0.858	0.020	390	1.394	0.036

Table 6.S2: Summary of optimized modelling techniques for O_3 simulation and its corresponding GPI values

Station number	GLM			GAM			GBM			RF		
	Distribution Family	GPI_Train	GPI_Test	Distribution Family	GPI_Train	GPI_Test	Number of Tree	GPI_Train	GPI_Test	Number of Tree	GPI_Train	GPI_Test
1	Gaussian	-0.235	-1.052	Quasi	-0.539	-1.853	210	1.426	0.155	30	4.050	0.197
2	Gaussian	-0.149	-0.209	Quasi	-0.114	-4.995	510	0.348	0.198	60	1.005	0.091
3	Gaussian	-0.109	-0.245	Quasi	0.077	-4.757	1010	0.536	0.113	20	1.243	-0.111
4	Gaussian	-1.023	-0.618	Quasi	-0.030	-4.757	950	0.571	0.101	70	1.243	0.056
5	Gaussian	-0.350	-0.169	Quasi	-0.085	-4.949	110	0.162	0.085	40	1.051	0.054
6	Gaussian	-0.408	-0.159	Quasi	-0.094	-4.657	240	0.329	0.313	70	1.343	-0.023
7	Gaussian	-0.202	-0.248	Quasi	-0.614	-4.960	1140	0.527	0.198	20	1.040	0.083
8	Gaussian	-1.721	-0.054	Quasi	-0.003	-3.900	210	0.214	-0.040	70	1.312	-0.012
9	Gaussian	-0.396	-1.802	Quasi	-0.161	-3.655	410	0.603	0.228	210	1.901	0.173
10	Gaussian	-0.325	-0.323	Quasi	-0.033	-4.808	310	0.288	0.189	70	1.192	0.033
11	Gaussian	-0.347	-0.639	Quasi	0.032	-4.554	710	0.704	0.070	90	1.446	0.053
12	Gaussian	-0.795	-0.636	Quasi	-0.285	-4.326	310	0.465	0.263	40	1.674	0.207
13	Gaussian	-0.322	-0.121	Quasi	0.060	-4.772	260	0.352	0.102	20	1.228	-0.087
14	Gaussian	-0.085	0.010	Quasi	-0.044	-4.829	520	0.400	0.065	40	1.171	0.024
15	Gaussian	-0.161	-0.029	Quasi	-0.147	-5.085	230	0.247	0.037	50	0.915	-0.009
16	Gaussian	-0.225	0.016	Quasi	-0.083	-4.901	460	0.299	0.038	70	1.099	0.005
17	Gaussian	-1.369	-1.015	Quasi	-0.035	-4.469	1220	0.385	0.129	60	0.855	0.008
18	Gaussian	-0.114	-0.028	Quasi	-0.109	-5.254	230	0.148	0.065	60	0.746	-0.041
19	Gaussian	-0.154	-0.112	Quasi	-0.015	-5.199	260	0.155	0.071	70	0.801	0.011
20	Gaussian	-0.169	-0.287	Quasi	-0.025	-5.407	1510	0.263	0.051	50	0.593	0.072
21	Gaussian	-0.455	-0.753	Quasi	-0.072	-4.622	530	0.402	0.241	80	1.378	0.002
22	Gaussian	-0.444	-0.402	Quasi	-0.998	-3.589	2310	1.020	0.353	90	1.765	0.226

23	Gaussian	-0.196	-0.067	Quasi	-0.070	-5.323	310	0.120	0.136	30	0.677	0.037
24	Gaussian	-0.658	-0.551	Quasi	-0.839	-4.655	310	0.362	0.565	60	1.201	0.468
25	Gaussian	-0.276	-0.124	Quasi	-0.120	-5.258	210	0.056	0.199	50	0.742	0.248
26	Gaussian	-0.429	-0.093	Quasi	-0.143	-5.103	320	0.106	0.150	60	0.897	0.129
27	Gaussian	-0.259	-0.155	Quasi	-0.101	-5.244	810	0.213	0.134	720	0.756	0.195
28	Gaussian	-0.149	-0.073	Quasi	-0.063	-5.104	280	0.145	0.055	90	0.896	0.090
29	Gaussian	-0.174	0.008	Quasi	-1.023	-5.126	430	0.153	0.048	2030	0.874	0.011
30	Gaussian	-0.186	-0.061	Quasi	-0.115	-5.344	240	0.113	0.089	550	0.656	0.070
31	Gaussian	-0.210	-0.135	Quasi	-0.117	-4.928	310	0.293	0.120	50	1.072	0.051
32	Gaussian	-0.151	-0.021	Quasi	-0.193	-5.469	100	0.048	0.147	50	0.531	0.051
33	Gaussian	-0.441	-0.121	Quasi	-0.059	-5.178	90	0.085	0.059	80	0.822	0.104
34	Gaussian	-0.034	-0.085	Quasi	-0.117	-4.819	60	0.559	0.061	90	1.181	-0.358
35	Gaussian	-0.110	-0.139	Quasi	-0.096	-5.231	220	0.119	0.092	3510	0.769	0.114
36	Gaussian	-0.119	-0.130	Quasi	-0.110	-5.300	260	0.183	0.130	80	0.700	0.062
37	Gaussian	-1.830	0.119	Quasi	-0.059	-3.787	80	0.185	0.123	70	1.557	-0.129
38	Gaussian	-0.248	-0.218	Quasi	-0.192	-4.688	2410	0.664	0.351	60	1.312	0.084
39	Gaussian	-1.016	-0.466	Quasi	-0.050	-4.556	1620	0.486	0.128	70	0.866	0.028
40	Gaussian	-0.161	-0.018	Quasi	-0.013	-5.456	90	0.125	0.024	810	0.544	0.007
41	Gaussian	-0.094	-0.683	Quasi	-0.080	-5.021	510	0.149	0.123	50	0.979	0.092
42	Gaussian	-0.047	-0.363	Quasi	-0.805	-5.186	510	0.293	0.050	80	0.814	0.165
43	Gaussian	-0.073	-0.335	Quasi	-0.053	-5.197	310	0.286	0.099	230	0.803	0.048
44	Gaussian	-0.130	-0.140	Quasi	0.026	-5.037	3520	0.601	0.079	70	0.963	0.028
45	Gaussian	0.021	-0.221	Quasi	0.015	-5.170	320	0.336	-0.032	1120	0.830	-0.061
46	Gaussian	-0.671	-0.206	Quasi	0.029	-5.392	420	0.187	0.050	60	0.608	-0.042
47	Gaussian	-0.036	-0.234	Quasi	0.000	-5.309	230	0.237	-0.010	50	0.691	0.010

48	Gaussian	-0.095	-0.205	Quasi	-0.009	-5.360	730	0.281	0.095	50	0.640	-0.099
49	Gaussian	-0.023	-0.138	Quasi	-0.014	-5.216	6130	0.573	-0.085	90	0.784	-0.004
50	Gaussian	-0.037	-0.091	Quasi	-0.012	-5.029	610	0.337	0.037	70	0.971	-0.092
51	Gaussian	0.071	-0.290	Quasi	-0.022	-5.097	220	0.237	0.000	90	0.903	-0.026
52	Gaussian	-0.441	-0.167	Quasi	-0.022	-4.219	920	0.484	0.065	930	1.781	-0.006
53	Gaussian	-0.046	-0.406	Quasi	-0.217	-4.125	410	0.747	-0.068	920	1.875	-0.153
54	Gaussian	-0.059	-0.290	Quasi	0.140	-4.599	310	0.402	0.014	80	1.401	-0.134
55	Gaussian	-0.198	-0.228	Quasi	0.023	-5.223	310	0.166	0.082	30	0.777	-0.018
56	Gaussian	-0.244	-0.260	Quasi	-0.010	-5.274	310	0.201	0.013	70	0.726	0.104
57	Gaussian	-0.357	-0.216	Quasi	-0.106	-5.166	510	0.256	0.278	810	0.834	0.080
58	Gaussian	-0.085	-0.111	Quasi	0.007	-5.386	410	0.247	0.022	1210	0.614	-0.037
59	Gaussian	-0.204	-0.213	Quasi	-0.163	-4.870	70	0.138	0.338	60	1.130	0.201
60	Gaussian	-0.143	-0.283	Quasi	0.213	-4.379	1670	0.106	-0.144	80	1.621	0.290
61	Gaussian	-1.253	-0.284	Quasi	-0.016	-4.933	1210	0.372	0.004	70	1.067	0.123
62	Gaussian	0.254	-0.754	Quasi	0.542	-3.585	90	0.903	-0.505	220	2.415	-0.404

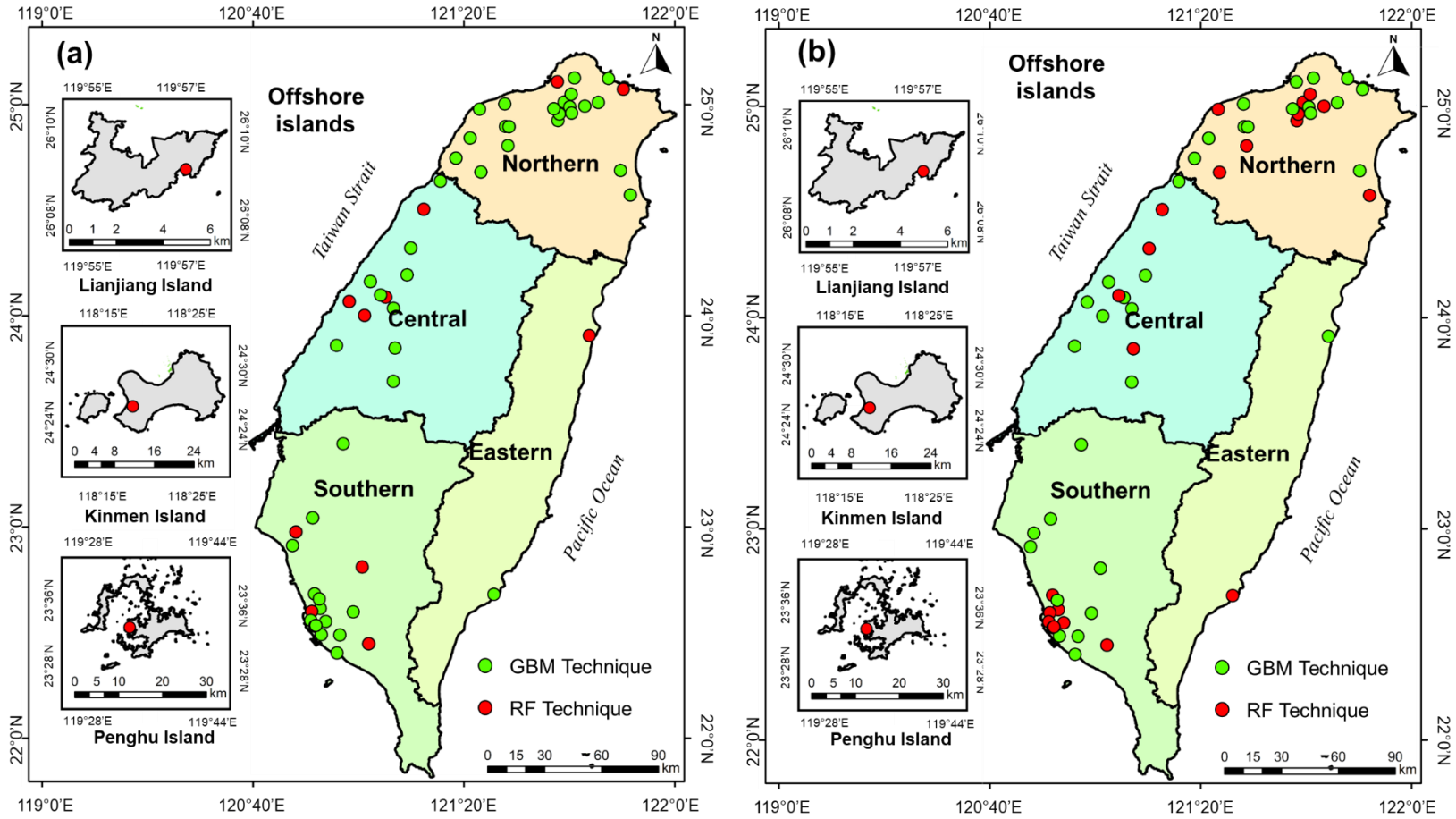

Fig 6.S1: Optimal modelling techniques for (a) NO_2 and (b) O_3 across different air quality monitoring stations in Taiwan

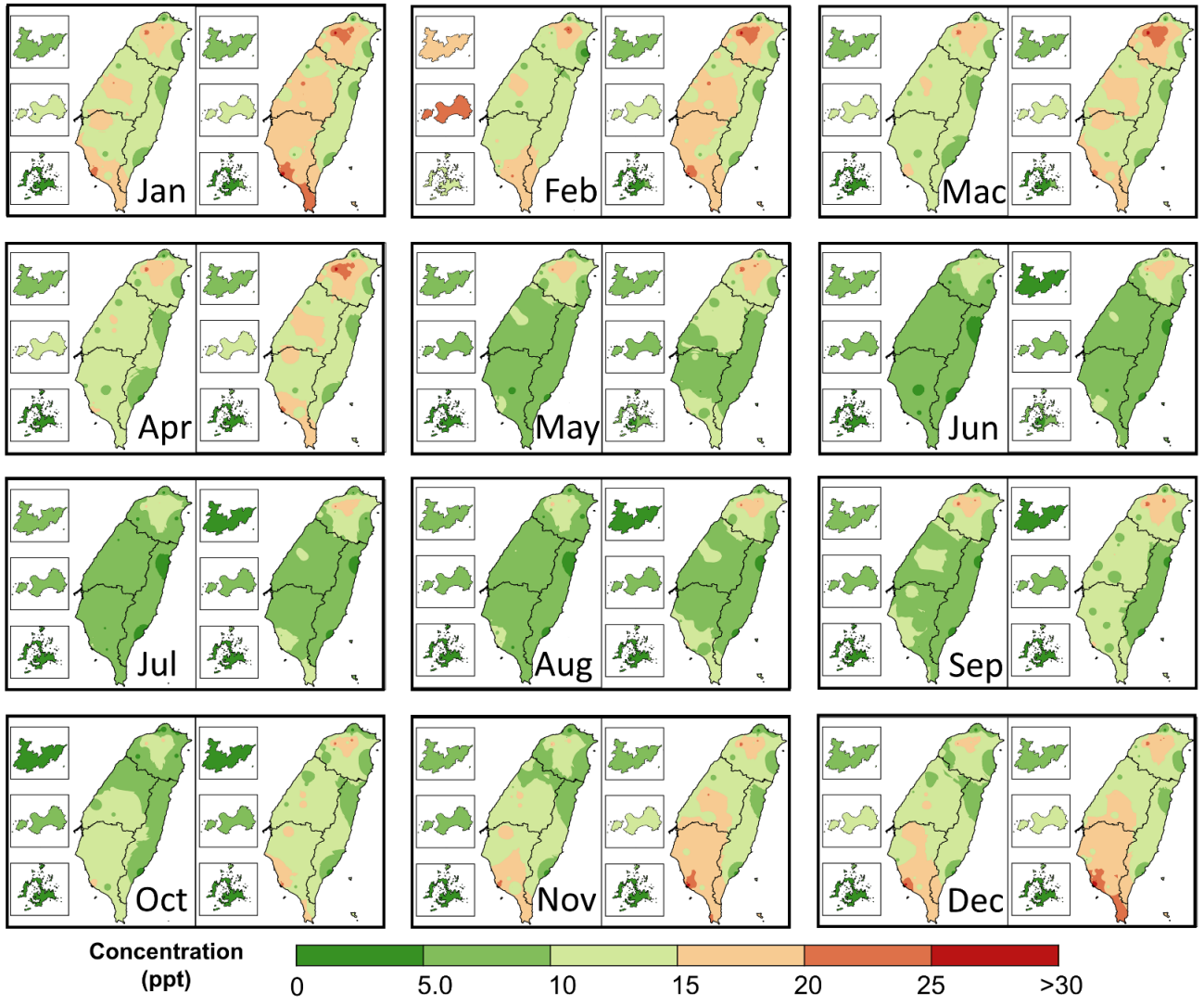

Fig 6.S2: Spatiotemporal distribution of monthly NO_2 mean concentration across Taiwan for observed (left) and meteorological-normalized simulated (right) for 2020

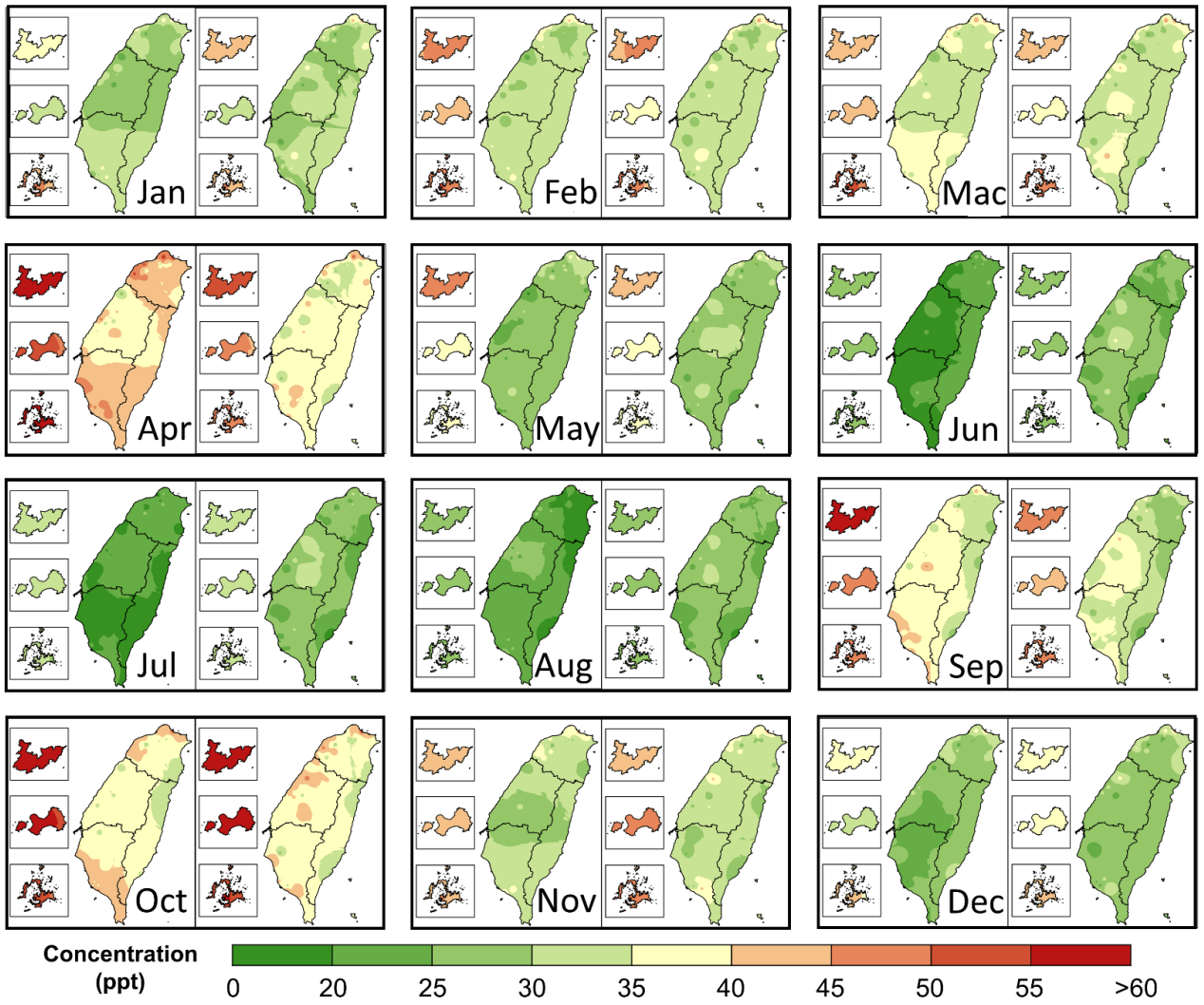

Fig 6.S3: Spatiotemporal distribution of monthly O_3 mean concentration across Taiwan for observed (left) and meteorological-normalized

List of References

Abdullah, S., Mansor, A. A., Napi, N. N. L. M., Mansor, W. N. W., Ahmed, A. N., Ismail, M., et al. (2020). Air quality status during 2020 Malaysia Movement Control Order (MCO) due to 2019 novel coronavirus (2019-nCoV) pandemic. *Science of The Total Environment, 729*, 139022, doi:10.1016/j.scitotenv.2020.139022.

Addas, A., & Maghrabi, A. (2021). The Impact of COVID-19 Lockdowns on Air Quality—A Global Review. *13*(18), 10212.

Akbar, C., Li, Y., & Sung, W. L. (2021). Machine Learning Aided Device Simulation of Work Function Fluctuation for Multichannel Gate-All-Around Silicon Nanosheet MOSFETs. *IEEE Transactions on Electron Devices, 68*(11), 5490-5497, doi:10.1109/TED.2021.3084910.

Alzamzami, F., Hoda, M., & Saddik, A. E. (2020). Light Gradient Boosting Machine for General Sentiment Classification on Short Texts: A Comparative Evaluation. *IEEE Access, 8*, 101840-101858, doi:10.1109/ACCESS.2020.2997330.

Anugerah, A. R., Muttaqin, P. S., & Purnama, D. A. (2021). Effect of large-scale social restriction (PSBB) during COVID-19 on outdoor air quality: Evidence from five cities in DKI Jakarta Province, Indonesia. *Environmental Research, 197*, 111164, doi:10.1016/j.envres.2021.111164.

Archer, C. L., Cervone, G., Golbazi, M., Al Fahel, N., & Hultquist, C. (2020). Changes in air quality and human mobility in the USA during the COVID-19 pandemic. *Bulletin of Atmospheric Science and Technology, 1*(3), 491-514, doi:10.1007/s42865-020-00019-0.

Asgari, M., Farnaghi, M., & Ghaemi, Z. (2017). *Predictive mapping of urban air pollution using Apache Spark on a Hadoop cluster.* Paper presented at the Proceedings of the 2017 International Conference on Cloud and Big Data Computing, London, United Kingdom,

Ash'aari, Z. H., Aris, A. Z., Ezani, E., Ahmad Kamal, N. I., Jaafar, N., Jahaya, J. N., et al. (2020). Spatiotemporal Variations and Contributing Factors of Air Pollutant Concentrations in Malaysia during Movement Control Order due to Pandemic COVID-19. *Aerosol and Air Quality Research, 20*(10), 2047-2061, doi:10.4209/aaqr.2020.06.0334.

Barré, J., Petetin, H., Colette, A., Guevara, M., Peuch, V. H., Rouil, L., et al. (2021). Estimating lockdown-induced European NO2 changes using satellite and surface observations and air quality models. *Atmos. Chem. Phys., 21*(9), 7373-7394, doi:10.5194/acp-21-7373-2021.

Barthwal, A., Acharya, D., & Lohani, D. (2021). Prediction and analysis of particulate matter (PM2.5 and PM10) concentrations using machine learning techniques. *Journal of Ambient Intelligence and Humanized Computing*, doi:10.1007/s12652-021-03051-w.

Baysan, C., Palanbek Yavaş, S., & Çöl, M. (2021). Change in Air Pollution and Human Mobility Trends during COVID-19 Lockdown Measures in Turkey. *The Anatolian Journal of Family Medicine, 4*(2), 170-177, doi:10.5505/anatoljfm.2021.25338.

Brancher, M. (2021). Increased ozone pollution alongside reduced nitrogen dioxide concentrations during Vienna's first COVID-19 lockdown: Significance for air quality management. *Environmental Pollution, 284*, 117153, doi:10.1016/j.envpol.2021.117153.

Breiman, L. (2001). Random Forests. *Machine Learning, 45*(1), 5-32, doi:10.1023/A:1010933404324.

Carranza, C., Nolet, C., Pezij, M., & van der Ploeg, M. (2021). Root zone soil moisture estimation with Random Forest. *Journal of Hydrology, 593*, 125840, doi:10.1016/j.jhydrol.2020.125840.

Chang, H.-H., Meyerhoefer, C. D., & Yang, F.-A. (2021). COVID-19 prevention, air pollution and transportation patterns in the absence of a lockdown. *Journal of Environmental Management, 298*, 113522, doi:10.1016/j.jenvman.2021.113522.

Chen, C., Twycross, J., & Garibaldi, J. M. (2017). A new accuracy measure based on bounded relative error for time series forecasting. *PLOS ONE, 12*(3), e0174202, doi:10.1371/journal.pone.0174202.

Chen, S.-P., Liu, W.-T., Hsieh, H.-C., & Wang, J.-L. (2021). Taiwan ozone trend in response to reduced domestic precursors and perennial transboundary influence. *Environmental Pollution, 289*, 117883, doi:10.1016/j.envpol.2021.117883.

Cheng, F.-Y., Feng, C.-Y., Yang, Z.-M., Hsu, C.-H., Chan, K.-W., Lee, C.-Y., et al. (2021). Evaluation of real-time PM2.5 forecasts with the WRF-CMAQ modeling system and weather-pattern-dependent bias-adjusted PM2.5 forecasts in Taiwan. *Atmospheric Environment, 244*, 117909, doi:10.1016/j.atmosenv.2020.117909.

Cheng, F.-Y., & Hsu, C.-H. (2019). Long-term variations in PM2.5 concentrations under changing meteorological conditions in Taiwan. *Scientific Reports, 9*(1), 6635, doi:10.1038/s41598-019-43104-x.

Chia, M. Y., Huang, Y. F., & Koo, C. H. (2021). Swarm-based optimization as stochastic training strategy for estimation of reference evapotranspiration using extreme learning machine. *Agricultural Water Management, 243*, 106447, doi:10.1016/j.agwat.2020.106447.

Cole, M. A., Elliott, R. J. R., & Liu, B. (2020). The Impact of the Wuhan Covid-19 Lockdown on Air Pollution and Health: A Machine Learning and Augmented Synthetic Control

Approach. *Environmental and Resource Economics, 76*(4), 553-580, doi:10.1007/s10640-020-00483-4.

Cortes-Ciriano, I., Bender, A., & Malliavin, T. E. (2015). Comparing the Influence of Simulated Experimental Errors on 12 Machine Learning Algorithms in Bioactivity Modeling Using 12 Diverse Data Sets. *Journal of Chemical Information and Modeling, 55*(7), 1413-1425, doi:10.1021/acs.jcim.5b00101.

Dai, Q., Hou, L., Liu, B., Zhang, Y., Song, C., Shi, Z., et al. (2021). Spring Festival and COVID-19 Lockdown: Disentangling PM Sources in Major Chinese Cities. [10.1029/2021GL093403]. *Geophysical Research Letters, 48*(11), e2021GL093403, doi:10.1029/2021GL093403.

Dang, H.-A. H., & Trinh, T.-A. (2021). Does the COVID-19 lockdown improve global air quality? New cross-national evidence on its unintended consequences. *Journal of Environmental Economics and Management, 105*, 102401, doi:10.1016/j.jeem.2020.102401.

Despotovic, M., Nedic, V., Despotovic, D., & Cvetanovic, S. (2015). Review and statistical analysis of different global solar radiation sunshine models. *Renewable and Sustainable Energy Reviews, 52*, 1869-1880, doi:10.1016/j.rser.2015.08.035.

Diémoz, H., Magri, T., Pession, G., Tarricone, C., Tombolato, I. K. F., Fasano, G., et al. (2021). Air Quality in the Italian Northwestern Alps during Year 2020: Assessment of the COVID-19 «Lockdown Effect» from Multi-Technique Observations and Models. *12*(8), 1006.

Dobson, R., & Semple, S. (2020). Changes in outdoor air pollution due to COVID-19 lockdowns differ by pollutant: evidence from Scotland. *Occupational and Environmental Medicine, 77*(11), 798, doi:10.1136/oemed-2020-106659.

Fenech, S., Aquilina, N. J., & Vella, R. (2021). COVID-19-Related Changes in NO2 and O3 Concentrations and Associated Health Effects in Malta. [Original Research]. *3*(1), doi:10.3389/frsc.2021.631280.

Friedman, J. H. (2001). Greedy Function Approximation: A Gradient Boosting Machine. *The Annals of Statistics, 29*(5), 1189-1232.

Fu, S., Guo, M., Fan, L., Deng, Q., Han, D., Wei, Y., et al. (2021). Ozone pollution mitigation in guangxi (south China) driven by meteorology and anthropogenic emissions during the COVID-19 lockdown. *Environmental Pollution, 272*, 115927, doi:10.1016/j.envpol.2020.115927.

Fu, Y.-c., & Lee, H.-W. (2020). Daily Contacts Under Quarantine amid Limited Spread of COVID-19 in Taiwan. *International Journal of Sociology, 50*(5), 434-444, doi:10.1080/00207659.2020.1786636.

Galvin, C. J., Li, Y.-C., Malwade, S., & Syed-Abdul, S. (2020). COVID-19 preventive measures showing an unintended decline in infectious diseases in Taiwan.

International Journal of Infectious Diseases, 98, 18-20, doi:10.1016/j.ijid.2020.06.062.

González-Recio, O., Jiménez-Montero, J. A., & Alenda, R. (2013). The gradient boosting algorithm and random boosting for genome-assisted evaluation in large data sets. *Journal of Dairy Science, 96*(1), 614-624, doi:10.3168/jds.2012-5630.

Granella, F., Aleluia Reis, L., Bosetti, V., & Tavoni, M. (2021). COVID-19 lockdown only partially alleviates health impacts of air pollution in Northern Italy. *Environmental Research Letters, 16*(3), 035012, doi:10.1088/1748-9326/abd3d2.

Grange, S. K., Lee, J. D., Drysdale, W. S., Lewis, A. C., Hueglin, C., Emmenegger, L., et al. (2021). COVID-19 lockdowns highlight a risk of increasing ozone pollution in European urban areas. *Atmos. Chem. Phys., 21*(5), 4169-4185, doi:10.5194/acp-21-4169-2021.

Gualtieri, G., Brilli, L., Carotenuto, F., Vagnoli, C., Zaldei, A., & Gioli, B. (2020). Quantifying road traffic impact on air quality in urban areas: A Covid19-induced lockdown analysis in Italy. *Environmental Pollution, 267*, 115682, doi:10.1016/j.envpol.2020.115682.

Guikema, S. D., Quiring, S. M., & Han, S.-R. (2010). Prestorm Estimation of Hurricane Damage to Electric Power Distribution Systems. *30*(12), 1744-1752, doi:10.1111/j.1539-6924.2010.01510.x.

Hastie, T., & Tibshirani, R. (1990). Generalized Additive Models (Chapman & Hall/CRC Monographs on Statistics & Applied Probability). Chapman and Hall/CRC.

Ho, J. Y., Afan, H. A., El-Shafie, A. H., Koting, S. B., Mohd, N. S., Jaafar, W. Z. B., et al. (2019). Towards a time and cost effective approach to water quality index class prediction. *Journal of Hydrology, 575*, 148-165, doi:10.1016/j.jhydrol.2019.05.016.

Hsu, Y.-J., Fu, Y., Bürgmann, R., Hsu, S.-Y., Lin, C.-C., Tang, C.-H., et al. (2020). Assessing seasonal and interannual water storage variations in Taiwan using geodetic and hydrological data. *Earth and Planetary Science Letters, 550*, 116532, doi:10.1016/j.epsl.2020.116532.

Hua, J., Zhang, Y., de Foy, B., Shang, J., Schauer, J. J., Mei, X., et al. (2021). Quantitative estimation of meteorological impacts and the COVID-19 lockdown reductions on NO2 and PM2.5 over the Beijing area using Generalized Additive Models (GAM). *Journal of Environmental Management, 291*, 112676, doi:10.1016/j.jenvman.2021.112676.

Huang, G., Wu, L., Ma, X., Zhang, W., Fan, J., Yu, X., et al. (2019). Evaluation of CatBoost method for prediction of reference evapotranspiration in humid regions. *Journal of Hydrology, 574*, 1029-1041, doi:10.1016/j.jhydrol.2019.04.085.

Hyndman, R. J., & Koehler, A. B. (2006). Another look at measures of forecast accuracy. *International Journal of Forecasting, 22*(4), 679-688, doi:10.1016/j.ijforecast.2006.03.001.

Jephcote, C., Hansell, A. L., Adams, K., & Gulliver, J. (2021). Changes in air quality during COVID-19 'lockdown' in the United Kingdom. *Environmental Pollution, 272*, 116011, doi:10.1016/j.envpol.2020.116011.

Kassam, N. (2020). COVID poll: Lowy Institute polling on Australian attitudes to the coronavirus pandemic.

Keller, C. A., Evans, M. J., Knowland, K. E., Hasenkopf, C. A., Modekurty, S., Lucchesi, R. A., et al. (2021). Global impact of COVID-19 restrictions on the surface concentrations of nitrogen dioxide and ozone. *Atmos. Chem. Phys., 21*(5), 3555-3592, doi:10.5194/acp-21-3555-2021.

Chinese air pollution to blow into Taiwan on Friday. (2020, *Taiwan News*.

Ketu, S., & Mishra, P. K. (2021). Scalable kernel-based SVM classification algorithm on imbalance air quality data for proficient healthcare. *Complex & Intelligent Systems, 7*(5), 2597-2615, doi:10.1007/s40747-021-00435-5.

Krause, P., Boyle, D. P., & Bäse, F. (2005). Comparison of different efficiency criteria for hydrological model assessment. *Adv. Geosci., 5*, 89-97, doi:10.5194/adgeo-5-89-2005.

Lee, J. D., Drysdale, W. S., Finch, D. P., Wilde, S. E., & Palmer, P. I. (2020). UK surface NO2 levels dropped by 42 % during the COVID-19 lockdown: impact on surface O3. *Atmos. Chem. Phys., 20*(24), 15743-15759, doi:10.5194/acp-20-15743-2020.

Lee, Y., & Nelder, J. A. (2000). Two Ways of Modelling Overdispersion in Non-Normal Data. *Journal of the Royal Statistical Society. Series C (Applied Statistics), 49*(4), 591-598.

Li, M., Dong, H., Wang, B., Zhao, W., Zare Sakhvidi, M. J., Li, L., et al. (2021). Association between ambient ozone pollution and mortality from a spectrum of causes in Guangzhou, China. *Science of The Total Environment, 754*, 142110, doi:10.1016/j.scitotenv.2020.142110.

Li, N., Chen, J.-P., Tsai, I. C., He, Q., Chi, S.-Y., Lin, Y.-C., et al. (2016). Potential impacts of electric vehicles on air quality in Taiwan. *Science of The Total Environment, 566-567*, 919-928, doi:10.1016/j.scitotenv.2016.05.105.

Ließ, M., Glaser, B., & Huwe, B. (2012). Uncertainty in the spatial prediction of soil texture: Comparison of regression tree and Random Forest models. *Geoderma, 170*, 70-79, doi:10.1016/j.geoderma.2011.10.010.

Liu, H., Yue, F., & Xie, Z. (2022). Quantify the role of anthropogenic emission and meteorology on air pollution using machine learning approach: A case study of

PM2.5 during the COVID-19 outbreak in Hubei Province, China. *Environmental Pollution, 300*, 118932, doi:10.1016/j.envpol.2022.118932.

Lorenzo, J. S. L., Tam, W. W. S., & Seow, W. J. (2021). Association between air quality, meteorological factors and COVID-19 infection case numbers. *Environmental Research, 197*, 111024, doi:10.1016/j.envres.2021.111024.

Lovrić, M., Pavlović, K., Vuković, M., Grange, S. K., Haberl, M., & Kern, R. (2021). Understanding the true effects of the COVID-19 lockdown on air pollution by means of machine learning. *Environmental Pollution, 274*, 115900, doi:10.1016/j.envpol.2020.115900.

Munir, S., Coskuner, G., Jassim, M. S., Aina, Y. A., Ali, A., & Mayfield, M. (2021a). Changes in Air Quality Associated with Mobility Trends and Meteorological Conditions during COVID-19 Lockdown in Northern England, UK. *12*(4), 504.

Munir, S., Luo, Z., & Dixon, T. (2021b). Comparing different approaches for assessing the impact of COVID-19 lockdown on urban air quality in Reading, UK. *Atmospheric Research, 261*, 105730, doi:10.1016/j.atmosres.2021.105730.

Nakada, L. Y. K., & Urban, R. C. (2020). COVID-19 pandemic: Impacts on the air quality during the partial lockdown in São Paulo state, Brazil. *Science of The Total Environment, 730*, 139087, doi:10.1016/j.scitotenv.2020.139087.

Natekin, A., & Knoll, A. (2013). Gradient boosting machines, a tutorial. *Frontiers in neurorobotics, 7*, 21-21, doi:10.3389/fnbot.2013.00021.

Nelder, J. A., & Wedderburn, R. W. M. (1972). Generalized Linear Models. *135*(3), 370-384, doi:10.2307/2344614.

Nigitz, T., & Gölles, M. (2019). A generally applicable, simple and adaptive forecasting method for the short-term heat load of consumers. *Applied Energy*, *241*, 73-81, doi:10.1016/j.apenergy.2019.03.012.

Nzediegwu, C., Naeth, M. A., & Chang, S. X. (2021). Elemental composition of biochars is affected by methods used for its determination. *Journal of Analytical and Applied Pyrolysis, 156*, 105174, doi:10.1016/j.jaap.2021.105174.

Oyedele, A., Ajayi, A., Oyedele, L. O., Delgado, J. M. D., Akanbi, L., Akinade, O., et al. (2021). Deep learning and Boosted trees for injuries prediction in power infrastructure projects. *Applied Soft Computing, 110*, 107587, doi:10.1016/j.asoc.2021.107587.

Payne, E. H., Gebregziabher, M., Hardin, J. W., Ramakrishnan, V., & Egede, L. E. (2018). An empirical approach to determine a threshold for assessing overdispersion in Poisson and negative binomial models for count data. *Communications in Statistics - Simulation and Computation, 47*(6), 1722-1738, doi:10.1080/03610918.2017.1323223.

Pei, L., Yan, Z., Chen, D., & Miao, S. (2020). Climate variability or anthropogenic emissions: which caused Beijing Haze? *Environmental Research Letters, 15*(3), 034004, doi:10.1088/1748-9326/ab6f11.

Peña Quiñones, A. J., Chaves Cordoba, B., Salazar Gutierrez, M. R., Keller, M., & Hoogenboom, G. (2019). Radius of influence of air temperature from automated weather stations installed in complex terrain. *Theoretical and Applied Climatology, 137*(3), 1957-1973, doi:10.1007/s00704-018-2717-9.

Petetin, H., Bowdalo, D., Soret, A., Guevara, M., Jorba, O., Serradell, K., et al. (2020). Meteorology-normalized impact of the COVID-19 lockdown upon NO2 pollution in Spain. *Atmos. Chem. Phys., 20*(18), 11119-11141, doi:10.5194/acp-20-11119-2020.

Potts, S. E., & Rose, K. A. (2018). Evaluation of GLM and GAM for estimating population indices from fishery independent surveys. *Fisheries Research, 208*, 167-178, doi:10.1016/j.fishres.2018.07.016.

Probst, P., & Boulesteix, A.-L. (2017). To tune or not to tune the number of trees in random forest. *Journal of Machine Learning Research, 18*(1), 6673-6690.

Probst, P., Wright, M. N., & Boulesteix, A.-L. (2019). Hyperparameters and tuning strategies for random forest. *9*(3), e1301, doi:10.1002/widm.1301.

Qu, L., Liu, S., Ma, L., Zhang, Z., Du, J., Zhou, Y., et al. (2020). Evaluating the meteorological normalized PM2.5 trend (2014–2019) in the "2+26" region of China using an ensemble learning technique. *Environmental Pollution, 266*, 115346, doi:10.1016/j.envpol.2020.115346.

Ramos-López, D., & Maldonado, A. D. (2021). Cost-Sensitive Variable Selection for Multi-Class Imbalanced Datasets Using Bayesian Networks. *9*(2), 156.

Ravindra, K., Rattan, P., Mor, S., & Aggarwal, A. N. (2019). Generalized additive models: Building evidence of air pollution, climate change and human health. *Environment International, 132*, 104987, doi:10.1016/j.envint.2019.104987.

Richter, R., Reu, B., Wirth, C., Doktor, D., & Vohland, M. (2016). The use of airborne hyperspectral data for tree species classification in a species-rich Central European forest area. *International Journal of Applied Earth Observation and Geoinformation, 52*, 464-474, doi:10.1016/j.jag.2016.07.018.

Rodríguez-Urrego, D., & Rodríguez-Urrego, L. (2020). Air quality during the COVID-19: PM2.5 analysis in the 50 most polluted capital cities in the world. *Environmental Pollution, 266*, 115042, doi:10.1016/j.envpol.2020.115042.

Rong, G., Alu, S., Li, K., Su, Y., Zhang, J., Zhang, Y., et al. (2020). Rainfall Induced Landslide Susceptibility Mapping Based on Bayesian Optimized Random Forest and Gradient Boosting Decision Tree Models—A Case Study of Shuicheng County, China. *12*(11), 3066.

Rudke, A. P., Martins, J. A., de Almeida, D. S., Martins, L. D., Beal, A., Hallak, R., et al. (2021). How mobility restrictions policy and atmospheric conditions impacted air quality in the State of São Paulo during the COVID-19 outbreak. *Environ Res, 198*, 111255, doi:10.1016/j.envres.2021.111255.

Rybarczyk, Y., & Zalakeviciute, R. (2021). Assessing the COVID-19 Impact on Air Quality: A Machine Learning Approach. *48*(4), e2020GL091202, doi:10.1029/2020GL091202.

Saggi, M. K., & Jain, S. (2019). Reference evapotranspiration estimation and modeling of the Punjab Northern India using deep learning. *Computers and Electronics in Agriculture, 156*, 387-398, doi:10.1016/j.compag.2018.11.031.

Shafizadeh-Moghadam, H., Valavi, R., Shahabi, H., Chapi, K., & Shirzadi, A. (2018). Novel forecasting approaches using combination of machine learning and statistical models for flood susceptibility mapping. *Journal of Environmental Management, 217*, 1-11, doi:10.1016/j.jenvman.2018.03.089.

Shi, Z., Song, C., Liu, B., Lu, G., Xu, J., Van Vu, T., et al. (2021). Abrupt but smaller than expected changes in surface air quality attributable to COVID-19 lockdowns. *Sci Adv, 7*(3), doi:10.1126/sciadv.abd6696.

Solberg, S., Walker, S.-E., Schneider, P., & Guerreiro, C. (2021). Quantifying the Impact of the Covid-19 Lockdown Measures on Nitrogen Dioxide Levels throughout Europe. *12*(2), 131.

Soyiri, I. N., & Reidpath, D. D. (2012). Evolving forecasting classifications and applications in health forecasting. *Int J Gen Med, 5*, 381-389, doi:10.2147/ijgm.S31079.

Talbot, N., Takada, A., Bingham, A. H., Elder, D., Lay Yee, S., & Golubiewski, N. E. (2021). An investigation of the impacts of a successful COVID-19 response and meteorology on air quality in New Zealand. *Atmospheric Environment, 254*, 118322, doi:10.1016/j.atmosenv.2021.118322.

Tang, R., Huang, X., Zhou, D., Wang, H., Xu, J., & Ding, A. (2021). Global air quality change during the COVID-19 pandemic: Regionally different ozone pollution responses COVID-19. *Atmospheric and Oceanic Science Letters, 14*(4), 100015, doi:10.1016/j.aosl.2020.100015.

Thompson, A. J., Newman, W. G., Elliott, R. A., Roberts, S. A., Tricker, K., & Payne, K. (2014). The Cost-Effectiveness of a Pharmacogenetic Test: A Trial-Based Evaluation of TPMT Genotyping for Azathioprine. *Value in Health, 17*(1), 22-33, doi:10.1016/j.jval.2013.10.007.

Tian, X., An, C., Chen, Z., & Tian, Z. (2021). Assessing the impact of COVID-19 pandemic on urban transportation and air quality in Canada. *Science of The Total Environment, 765*, 144270, doi:10.1016/j.scitotenv.2020.144270.

Tobías, A., Carnerero, C., Reche, C., Massagué, J., Via, M., Minguillón, M. C., et al. (2020). Changes in air quality during the lockdown in Barcelona (Spain) one month into the SARS-CoV-2 epidemic. *Science of The Total Environment, 726*, 138540, doi:10.1016/j.scitotenv.2020.138540.

Trensch, G., Gutzen, R., Blundell, I., Denker, M., & Morrison, A. (2018). Rigorous Neural Network Simulations: A Model Substantiation Methodology for Increasing the Correctness of Simulation Results in the Absence of Experimental Validation Data. [Original Research]. *12*(81), doi:10.3389/fninf.2018.00081.

Tsai, I. C., Lee, C.-Y., Lung, S.-C. C., & Su, C.-W. (2021). Characterization of the vehicle emissions in the Greater Taipei Area through vision-based traffic analysis system and its impacts on urban air quality. *Science of The Total Environment, 782*, 146571, doi:10.1016/j.scitotenv.2021.146571.

Vasileiou, E., Simpson, C. R., Shi, T., Kerr, S., Agrawal, U., Akbari, A., et al. (2021). Interim findings from first-dose mass COVID-19 vaccination roll-out and COVID-19 hospital admissions in Scotland: a national prospective cohort study. *The Lancet, 397*(10285), 1646-1657, doi:10.1016/S0140-6736(21)00677-2.

Velders, G. J. M., Willers, S. M., Wesseling, J., den Elshout, S. v., van der Swaluw, E., Mooibroek, D., et al. (2021). Improvements in air quality in the Netherlands during the corona lockdown based on observations and model simulations. *Atmospheric Environment, 247*, 118158, doi:10.1016/j.atmosenv.2020.118158.

Wang, Y., Wen, Y., Wang, Y., Zhang, S., Zhang, K. M., Zheng, H., et al. (2020). Four-Month Changes in Air Quality during and after the COVID-19 Lockdown in Six Megacities in China. *Environmental Science & Technology Letters, 7*(11), 802-808, doi:10.1021/acs.estlett.0c00605.

Wetchayont, P. (2021). Investigation on the Impacts of COVID-19 Lockdown and Influencing Factors on Air Quality in Greater Bangkok, Thailand. *Advances in Meteorology, 2021*, 6697707, doi:10.1155/2021/6697707.

Wong, Y. J., Shimizu, Y., He, K., & Nik Sulaiman, N. M. (2020). Comparison among different ASEAN water quality indices for the assessment of the spatial variation of surface water quality in the Selangor river basin, Malaysia. *Environmental Monitoring and Assessment, 192*(10), 644, doi:10.1007/s10661-020-08543-4.

Wong, Y. J., Shimizu, Y., Kamiya, A., Maneechot, L., Bharambe, K. P., Fong, C. S., et al. (2021). Application of artificial intelligence methods for monsoonal river classification in Selangor river basin, Malaysia. *Environmental Monitoring and Assessment, 193*(7), 438, doi:10.1007/s10661-021-09202-y.

Wu, C.-H., Tsai, I. C., Tsai, P.-C., & Tung, Y.-S. (2019). Large–scale seasonal control of air quality in Taiwan. *Atmospheric Environment, 214*, 116868, doi:10.1016/j.atmosenv.2019.116868.

Zeileis, A., Kleiber, C., & Jackman, S. (2008). Regression Models for Count Data in R. *Journal of Statistical Software, 27*(8), 1 - 25, doi:10.18637/jss.v027.i08.

Zhai, S., Jacob, D. J., Wang, X., Shen, L., Li, K., Zhang, Y., et al. (2019). Fine particulate matter (PM2.5) trends in China, 2013–2018: separating contributions from anthropogenic emissions and meteorology. *Atmos. Chem. Phys., 19*(16), 11031-11041, doi:10.5194/acp-19-11031-2019.

Zhang, K., Liu, Z., Zhang, X., Li, Q., Jensen, A., Tan, W., et al. (2021). Insights into the abnormal increase of ozone during COVID-19 in a typical urban city of China. *Atmos. Chem. Phys. Discuss., 2021*, 1-26, doi:10.5194/acp-2021-834.

Zhang, Y., Xie, Y., & Li, L. (2012). Crash frequency analysis of different types of urban roadway segments using generalized additive model. *Journal of Safety Research, 43*(2), 107-114, doi:10.1016/j.jsr.2012.01.003.

Zhu, Y., Xie, J., Huang, F., & Cao, L. (2020). The mediating effect of air quality on the association between human mobility and COVID-19 infection in China. *Environmental Research, 189*, 109911, doi:10.1016/j.envres.2020.109911.

Zou, B., Chen, J., Zhai, L., Fang, X., & Zheng, Z. (2017). Satellite Based Mapping of Ground PM2.5 Concentration Using Generalized Additive Modeling. *9*(1), 1.

Chapter 7

Comparison, Mitigation and Adaptation Strategies for Global Change

In this chapter, a review of environmental management and monitoring conditions in the developing countries in Asia is discussed. Besides that, the recent technological advances and developments have evolved the application of the Internet of Things (IoT), low-cost sensors, and three-dimensional (3D) printing for near-real-time environmental monitoring; however, these technologies have not yet been widely implemented in field operations. Therefore, in this research, a solar-powered 3D-printed IoT-based water quality monitoring system prototype was developed to measure turbidity and water level every two hours and utilized in a palm oil plantation on Carey Island, Malaysia for two months. Based on the developed prototype, it could be further modified to address the monitoring frequency across wider area for both water and air quality monitoring, paving a new path for the development of cost-effective and reliable systems for near-real-time or real-time monitoring.

7.1 Environmental Management and Monitoring Conditions in Asia

Over the past few decades, industrialization, climate change, and urbanization have disrupted the natural balance of ecosystems, imposing inimical impacts particularly to the aquatic environments through a wide range of pollutants (Arfanuzzaman & Dahiya, 2019). According to the World Water Assessment Program (WWAP, 2021), approximately 70–90% of untreated wastewater is discharged into the environment by middle- and low-income countries. The proliferation of pollutants in the aquatic environments has affected approximately a billion people worldwide, who have no access to safe drinking water, attracting global attention (WHO, 2019). In particular, high levels of suspended solids and turbidity in waterways have been a major concern (Patang & Soegianto, 2020), because these are primary indicators of toxics, heavy metals, and organic matter, which may severely affect

both the aquatic environments and human health. Moreover, the air quality issues in this region have been observed deteriorating as discussed in Chapter 2, especially, the particulate matters (PMs) pollutions.

With the current need to decrease these risks to the environment, among other global challenges, the United Nations Sustainable Development Goals (UNSDGs), introduced in 2015, provide a blueprint for "attaining a better and more sustainable future for all." Among these goals, the third and sixth specify ensuring substantial reduction of health impacts from hazardous air substances and clean accessible water for everyone, respectively. Since then, numerous frameworks have been proposed and developed for sustainable water and air quality management, for example, through collaboration among diverse stakeholders (Medema *et al.,* 2017), and cost-effective classification based on water/air quality index (an aggregated normalized value of multiple water/air quality parameters) (EPA, 2020). However, one of the main challenges that hinder the implementation of these frameworks is the inadequacy in water/air quality monitoring programs, particularly in developing countries of Asia, due to significant difficulties concerning the economy and the workforce (Awan *et al.,* 2019).

In order to solve the water and air crisis issues, Asia countries established water/air quality assessment to regularize the management (Gholizadeh *et al.*, 2016). However, assessment of the surface water and ground air quality is often labor-intensive, costly and time consuming. It is a complex process that requires a large number of samples to characterize a water/air body over multiple parameters including but not limited to physicochemical and bacteriological aspects (Bharti & Katyal, 2011). Conventionally, to evaluate surface water and ground air quality, individually measured parameter will be compared to its existing standard/guidelines set by the local authority. Nevertheless, since there are large number of parameters are included, it is difficult to provide a comprehensive evaluation of water quality status with its scientific basis (Lumb *et al.*, 2011, Noori *et al.*, 2019).

7.1.1 Towards Industrial Revolution 4.0

Recently, the fourth industrial revolution (IR 4.0) paradigm shift has initiated a wave of technological innovation (Cheng *et al.,* 2021) and sustainable transformation in various industries and sectors (Kumar *et al.,* 2020), including water and air quality monitoring *(*Wang *et al.,* 2021). The IR 4.0 has interconnected people, processes, and data via a networked connection, and its utilization has become more prevalent and relevant to the public (Awan *et al.*, 2021). Among the nine main pillars of IR 4.0 (Rüßmann *et al.*, 2015), the integration of the Internet of Things (IoT), cloud computing, and three-dimensional (3D) printing is most commonly adopted for water quality monitoring. Premised on the search for low-cost and reliable water and air quality monitoring systems, there has been a remarkable increase in the use of low-cost sensors and power-efficient integrated on-chip computers (Raspberry Pi and Arduino) (Tushar *et al.,* 2018) for adaptive water and air quality monitoring (*i.e.*, intervals of a few hours) (Prasad, 2015). However, there are trade-offs between certified reference standard sensors and low-cost sensors in terms of measurement accuracy and robustness (Castell *et al.*, 2017). On the other hand, the spatial dynamics of water and air quality could be better understood through the use of low-cost sensors because they are inexpensive in terms of deployment and operation. Thus, the application of low-cost sensors has a marked importance in addressing present challenges with inadequate monitoring.

7.1.2 Low cost and reliable monitoring system

Typically, an IoT-based system is continuously exposed to the environment, and thus the system should be durable and capable of coping with prevailing local weather conditions. Therefore, to minimize potential damage due to harmful environmental influences (such as rainfall, dust, and wind) on the system, the method of fabrication (*e.g.*, machining, laser cutting, and 3D printing) and the durability of the resulting device should be a focus of further research. Among the various techniques currently available, 3D printing is employed in this research because of its infinite possibility and flexibility for producing cost-effective prototypes and customized sensor fabrications (Khosravani & Reinicke, 2020).

With the increasing popularity of low-cost and miniaturized IoT-based system on low-cost sensors, the 3D-printed system architecture has been studied extensively; the relevant recent studies are summarized in Table 7.1. As shown in Table 7.1, both physicochemical parameters (*e.g.*, turbidity, pH, and temperature) and hydrological parameters (*e.g.*, water level and flow rate) are incorporated. In particular, for water quality monitoring, hydrological measurement is necessary for sustainable water resource management because of the significant climatic impact of heavy precipitation, which could potentially cause surface contaminants to overflow into water bodies (Ogata *et al.,* 2018). However, most of these studies have not progressed much beyond the development and validation stages, practicality and to the best of the authors' knowledge, only a few studies have focused on the deployment of the system for continuous monitoring. Some of the major challenges that remain to be addressed, contributing further to the slow deployment of IoT-based systems, include: (i) reliability under harsh environmental conditions, (ii) poor power management, and (iii) complex interoperability among sensors, as summarized by Talavera *et al*., (2017) and Farooq *et al*., (2020), causing major knowledge gaps concerning in the deployment and of IoT-based system. Although rechargeable battery has been connected to solar panels are often utilized as primary energy source for IoT devices, their optimal sampling frequency is not commonly discussed, nor has it been determined, which has restricted the application of photovoltaic devices in field operation of IoT systems. Furthermore, when high numbers of electronics are involved (Arduino, relay module, convertors, *etc.*), syntactical and technical interoperability among the IoT devices becomes more complicated; therefore, further research and development of robust algorithms are required to solve these problems (Farooq *et al*., 2020).

Based on findings from a review of literature, this research intends to design, develop, and deploy a 3D-printed IoT-based system with a high reliability using low-cost sensors that could address the aforementioned challenges. Compared to air quality monitoring using low-cost sensors, the application to water quality monitoring is much limited. Therefore, this research attempted to address the installation of IoT system for water quality monitoring system (WQMS) and the research objectives are set follows:

(i) To design and develop of a cost-effective and standalone 3D-printed IoT-based WQMS that measures turbidity and water level;

(ii) To calibrate and validate sensors according to internationally adopted standards, for obtaining the optimal measurement range; and

(iii) To Demonstrate the applicability of the developed system for water quality monitoring and management through field tests.

The proposed WQMS is compact and portable, consisting of four major modules: energy, time, monitoring, and communication. These modules can be easily assembled and disassembled. To promote the utilization of renewable energy, the WQMS relies on only a photovoltaic system as its primary energy source for operation. The electrical consumption values of the WQMS in the standby, operating, and data transmission modes were calculated to determine the optimal monitoring frequency. The sensors were developed and validated according to international standards (*e.g.,* International Organization for Standardization (ISO) and Environmental Protection Agency (EPA)) to ensure that the measurements are comparable with those of commercial sensors. The developed system was then deployed in a palm oil plantation on Carey Island, Malaysia, for two months (November 28, 2019–January 21, 2020) to evaluate its practicality and durability. The findings of this research are expected to provide comprehensive information, including on practical implications, to relevant authorities and practitioners for decision making, future development and application of 3D-printed IoT-based WQMSs. The ultimate objective is to address the inadequacies in water monitoring programs, particularly in developing countries, to contribute to the fulfillment of the UNSGDs.

The remainder of the chapter is organized as follows: Section 7.2 describes the research area and development of the IoT-based 3D-printed WQMS. Section 7.3 discusses the calibration and application of the WQMS. Section 7.4 reports on the findings, implications, and contributions of the research. Section 7.5 presents pertinent conclusions from the investigations and information regarding relevant future research.

Table 7.1. Related studies on IoT-based WQMS and its characteristics

Authors	Monitoring Frequency	Energy Source	Measurement Parameters	Sensor Type	Data Communication Platform	Deployment duration	Cost (USD)
Nandakumar *et al.* (2020)	Continuous	Direct current supply	pH, conductivity, turbidity	Hybrid**	Firebase Cloud	*	-
Pasika & Gandla (2020)	Every 30s	Direct current supply	pH, turbidity, water level, temperature	Hybrid	ThingSpeak	*	-
Jerom *et al.* (2020)	-	Battery	Dissolved oxygen, pH and temperature	Low cost	Firebase Cloud	*	-
Darmalim *et al*. (2020)	Continuous	Photovoltaic system	pH, turbidity, temperature, TDS	Low cost	PondIOT (Developed by authors)	*	-
Rohit *et al.* (2019)	Continuous	Direct current supply	pH, turbidity and temperature	Hybrid	If This Then That (IFTTT)	*	68.00
Chowdury *et al*. (2019)	Continuous	Direct current supply	pH, turbidity, temperature, ORP	Hybrid	Zigbee module	*	-
Kshirsagar *et al*. (2019)	-	Direct current supply	pH, turbidity, conductivity	Hybrid	ThingSpeak	*	-

Table 7.1. Related studies on IoT-based WQMS and it's characteristics (continued)

Oelen *et al.* (2018)	Every 15 min	Photovoltaic system	pH, turbidity, temperature, TDS, ORP.	Hybrid	Zigbee Module	*	250.00
Koditala & Pandey (2018)	Continuous	Direct current supply	Turbidity, temperature	Low-cost	Power Business Intelligence (BI)	*	-
Mulyana & Hakim (2018)	Continuous	Direct current supply	Turbidity, water level	Low-cost	ThingSpeak	*	
Encinas *et al.* (2017)	Every 15s	Rechargeable 9v battery	Dissolved oxygen, pH and temperature	Hybrid	XBee Module	*	-
Daigavane & Gaikwad (2017)	Continuous	Direct current supply	pH, turbidity, temperature, flowrate	Low-cost	Blynk	*	-
This research	Every 2h	Photovoltaic system	Turbidity, water level	Low-cost	Ambient	2 months	261.20

* Only test runs were performed.

** Hybrid indicates utilizing both certified reference and low-cost sensors.

7.2 Materials and Methodology

7.2.1 Research Area

This research was conducted on Carey Island, the largest ex-promontory island of the Klang Isles in Malaysia, bounded by latitudes 2° 48′ N–2° 59′ N and longitudes 101°16′ E–101 27′ E. Carey Island was selected because its surrounding water quality has been deteriorating (Zakaria *et al.*, 2017); in particular, levels of suspended solids and turbidity are high, and source tracking of these pollutants is necessary to enhance the water condition. The island is located on the west coast of Selangor state, the most developed state in Peninsular Malaysia, within the busy sea lanes of the Strait of Malacca (Fig. 7.1). The total area of Carey Island is approximately 162 km^2, with more than 65% of the island being used for palm oil plantations (Almasi *et al.*, 2018), managed by the largest producer of sustainable palm oil in the world, Sime Darby Plantation. The remaining area comprises settlements and mangrove forest reserves. Therefore, the main economic activities of the island are associated with palm oil-based products, from cultivation to milling and refinement (Sofawi *et al.*, 2017).

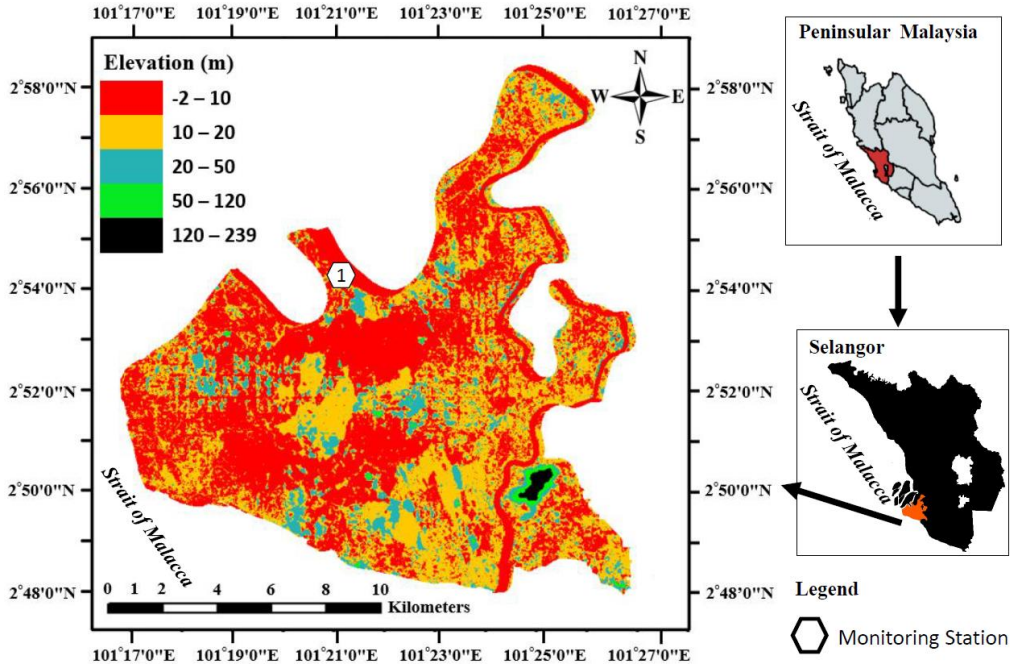

Fig. 7.1: Geographic location of Carey Island and position where water quality monitoring system was deployed

7.2.2 Development of IoT System

In this section, the architecture of the 3D-printed IoT-based WQMS (Fig. 7.2) is introduced. It consists of four major modules: energy, time, monitoring, and communication. A detailed discussion of each module is provided below.

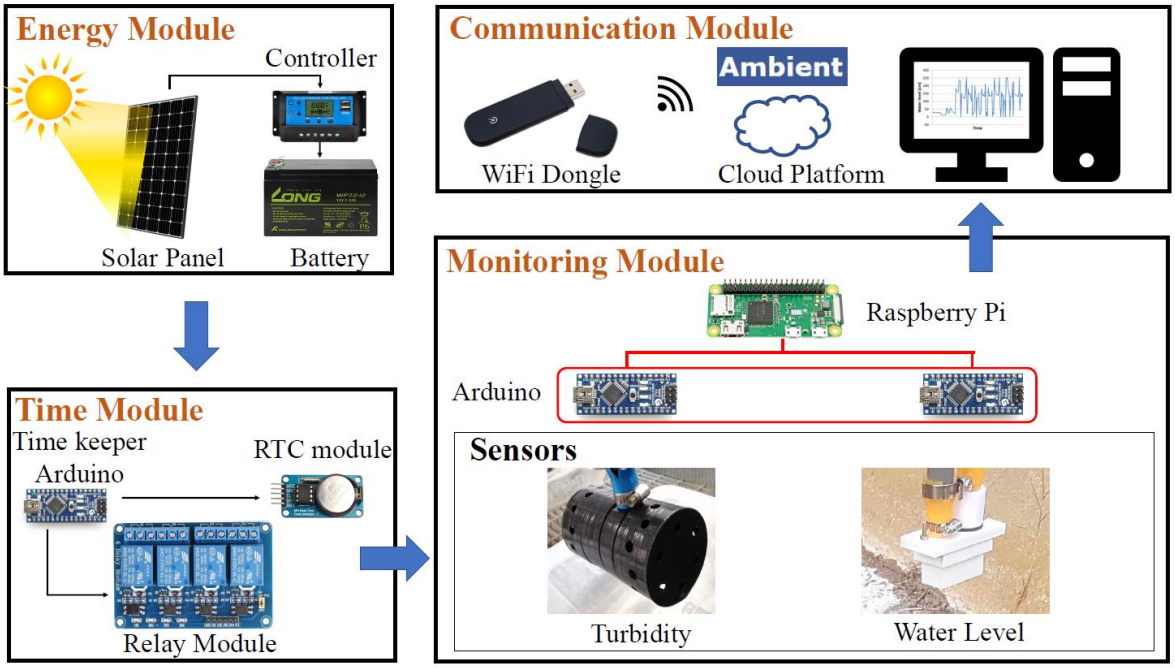

Fig. 7.2: Overview of 3D-printed IoT-based water quality monitoring system

7.2.2.1 Energy Module

In this research, to utilize the abundant sunshine (4–8 h/day) with a high intensity of average daily solar irradiation (4,000–5,000 Wh/m^2) in Malaysia (Mohammad *et al.*, 2020), a photovoltaic system is designed. It comprises a 20-W polycrystalline solar panel, pulse width modulation (PWM) solar charge controller, and 12-V lead–acid rechargeable battery (Li *et al.*, 2020). The PWM-type solar charge controller is chosen because of its affordable price and suitability for use in small systems (Uno & Kukita, 2018). It regulates the battery voltage and current generated by the solar panel, preventing overcharging and gassing of the battery while ensuring an optimum charging speed (Mhetre *et al.*, 2019). To ensure that the WQMS functions continuously, while depending only on the photovoltaic system, the

residual capacity of the battery is calculated using the following equations; the procedure for determining the sampling time per day is discussed in the Results and Analysis section in the chapter

$$R_C = \left(1 + \frac{V(\int I_C dt - \int I_D dt)}{C_b}\right) \times 100\% \quad (7.1)$$

In Eq. (7.1), R_C represents the residual capacity of the battery (%), C_b represents the rated capacity of the battery (kW·h), V represents the voltage of the battery (V), and I_C and I_D represent the charging and discharging currents (A), respectively.

The terms $V \int I_C dt$ and $V \int I_D dt$ can be calculated using Eqs. (7.2) and (7.3).

$$V \int I_C dt = \sum_0^t C_p \times \frac{Irr}{G_s} \times K \quad (7.2)$$

In Eq. (2), C_P represents the rated capacity of the solar panel (kW), Irr represents the hourly average solar radiation (kW·h/m^2·h), t represents the ending time of measurement, G_s is the solar irradiance under standard test conditions (kW/m^2), and K represents the overall efficiency factor.

$$V \int I_D dt = \sum_0^t E_{Standby} + E_{Operating} + E_{Communication} \quad (7.3)$$

In Eq. (7.3), $E_{Standby}$, $E_{Operating}$, and $E_{Communication}$ represent the energy consumption (kW/h) of the WQMS in the standby (only the time module is functioning), operating (acquiring measurements for samples), and communication (transmitting data to the cloud system via a USB Wi-Fi dongle) modes, respectively.

7.2.2.2 Time Module

To routinely boot up the WQMS for sampling, a time module is implemented, comprising three major components: real-time clock (RTC) module, relay module, and Arduino (Fig. 7.3). Because there are multiple Arduinos used in this research, the Arduino in the time module is designated the timekeeper Arduino (TKA) to help differentiate between the applications. The RTC module, which provides timing and date information is connected to the TKA, and acts as the system switch. During operation, the WQMS is booted up for 5

min for sampling measurement, and subsequently, the RTC connected to the TKA sends a signal to the relay module to switch off, causing the connection to be cut off. During the standby mode, electricity is supplied only to the RTC and TKA, such that the energy can be effectively and efficiently utilized. The voltage supplied by the battery is 12 V; however, the recommended voltage for Arduino is between 7 and 12 V, whereas for Raspberry Pi, it is 5 V. Therefore, the supply voltage values are set to 8 V and 5 V for the Arduino and Raspberry Pi via pins, respectively.

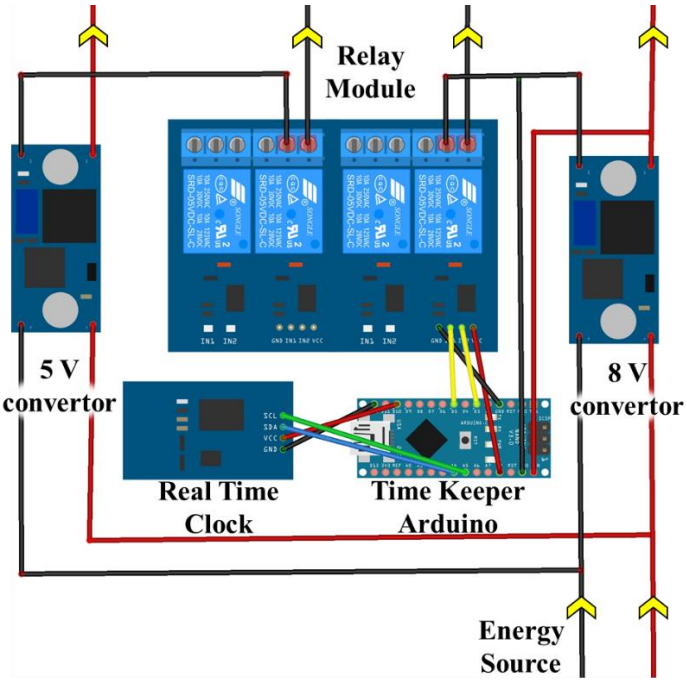

Fig. 7.3: Detailed connection diagram of proposed time module. Yellow arrows indicate current flow direction. Red and black lines represent positive and negative terminals, respectively. Green line connected to serial clock and blue line to serial data of RTC module are used to synchronize data transfer and operate timing of transfer between TKA and RTC modules, respectively. Yellow lines connected between relay module and TKA are used as switches.

7.2.2.3 Monitoring Module

To enable the proposed WQMS to monitor turbidity and water level, a turbidity sensor and water level sensor are designed and developed using electronic components and low-cost sensors (Fig. 7.4). The system utilizes a single board credit card-sized computer known as Raspberry Pi (Model: Zero WH) assisted by Arduinos. The details of the turbidity and water level sensors are described below.

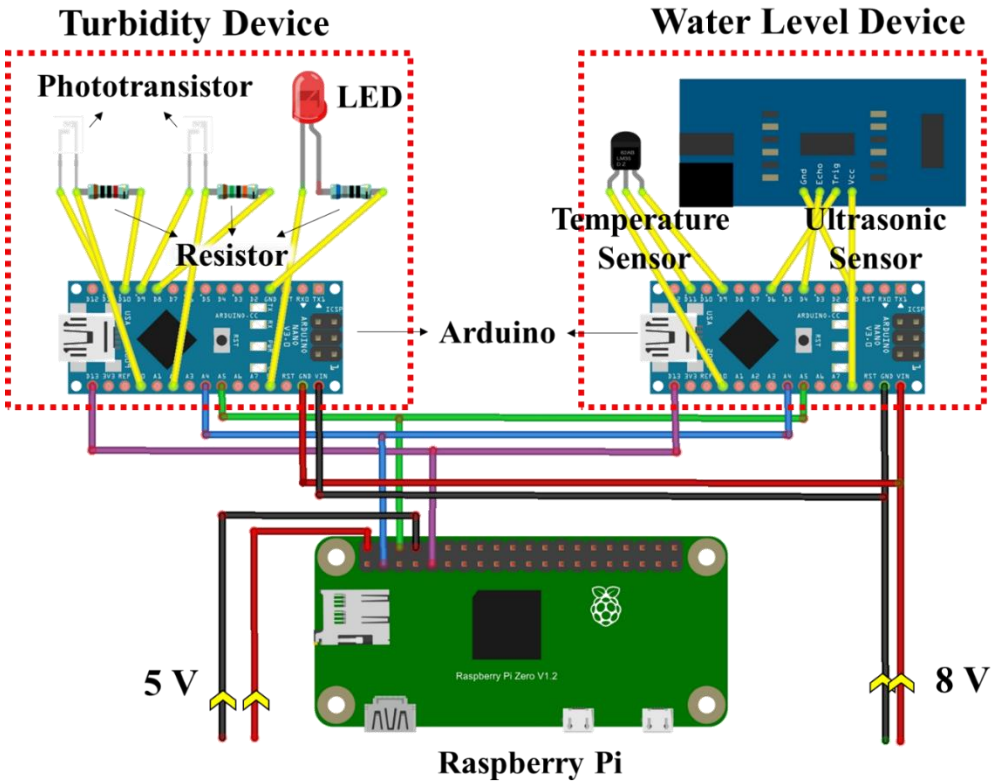

Fig. 7.4: Detailed connection diagram of proposed monitoring module. Yellow arrows indicate current flow direction. Red and black lines represent positive and negative terminals of battery, respectively. Green line connected to serial clock and blue line to serial data of Raspberry Pi are used to synchronize data transfer and operate timing of transfer between Arduinos and Raspberry Pi. Purple line represents ground terminal for Raspberry Pi. Yellow lines are used for receiving and transmitting information between electronic components and Arduinos

7.2.2.3.1 Turbidity Sensor

At present, there are many techniques available for measuring turbidity, among which the most commonly used are visual turbidity, turbidimetry, nephelometry, and ratiometric methods. Visual turbidity methods are subjective because the readings are based on personal perception and determination; therefore, these are only suitable for approximate estimation. The latter methods commonly utilize an incident light source (*e.g.*, a light-emitting diode (LED) laser and/or tungsten) and a phototransistor(s) for turbidity measurement. Turbidimetry and nephelometry methods differ mainly in the detection angle between the incident light source and the phototransistor. Trevathan *et al*. (2020) summarized the detection angles for both of these methods based on the most widely adopted standards: ISO 7027 and EPA Method 180.1. However, these methods have a significant drawback: nephelometry methods are considerably insensitive for detecting high turbidities because of multiple scattering caused by high particle concentrations, whereas turbidimetry methods are considerably insensitive for detecting low turbidities (Gillett & Marchiori, 2019; Kitchener *et al*., 2019). Ratiometric methods integrate both turbidimetry and nephelometry methods using two phototransistors positioned at 90° and 180° for the synchronous measurement of scattered light and attenuated light, respectively. Turbidity measurement using ratiometric methods not only provides high accuracies over a broad range of turbidities (Metzger *et al*., 2018) (*e.g.*, 0–1,000 formazin nephelometric units (FNUs)), but also minimizes the effects of the light source and water color (Zhu *et al*., 2020). Therefore, in this research, a ratiometric method was adopted for the development of the turbidity sensor.

In this research, sensor casings were designed using Autodesk Fusion 360 software and manufactured from polylactic acid (PLA) filament *via* 3D printing. The turbidity sensor will be continuously exposed to the environment, and therefore, to minimize adverse effects to the environment (*e.g.*, plastic pollution), PLA was chosen for its biodegradability, durability, and affordability (Lamberti *et al*., 2018; Lyu *et al*., 2020). Fig. 7.5(a) shows the actual setup and schematic of the designed turbidity sensor, which consists of a LED light source with a wavelength of 940 nm (chosen, for its low cost and good sensitivity in high turbidity water (Matos *et al*., 2019)) and two phototransistors L-51ROPT1D1 (Para Light

Electronics Co., Ltd.) at 90° and 180°. The diameter and length of the turbidity sensor are 7.0 cm and 11.4 cm, respectively, where the central part of the sensor is hollowed for continuous water flow.

To obtain the relationship between the signal measured by the developed turbidity sensor and its corresponding FNU values, calibration was performed using formazin at 25 °C as the standard solution, in compliance with the ISO 7027 method. Standard formazin solutions with 0, 1, 2, 4, 10, 20, 40, 100, 200, 400, and 1,000 FNU were prepared via serial dilution of a 4,000 FNU stock solution (Hach) using ultrapure water. The range of turbidity, 0–1,000 FNU, was selected based on the present turbidity concentrations of Malaysian rivers as reported in the Environmental Quality Report 2018 (Strategic Communication Division, 2019). Before the measurement, each standard solution was mixed well through gentle agitation and inversion to avoid entrainment of air bubbles within the sample (Liu *et al.*, 2015). To reduce random measurement noises, each standard solution was subjected to the measurement process for five times. The average measurements from the scattered light and attenuated light phototransistors were used together with ratiometric method to develop a calibration curve, as shown in Algorithm 7.S1 (Zhou *et al.*, 2021).

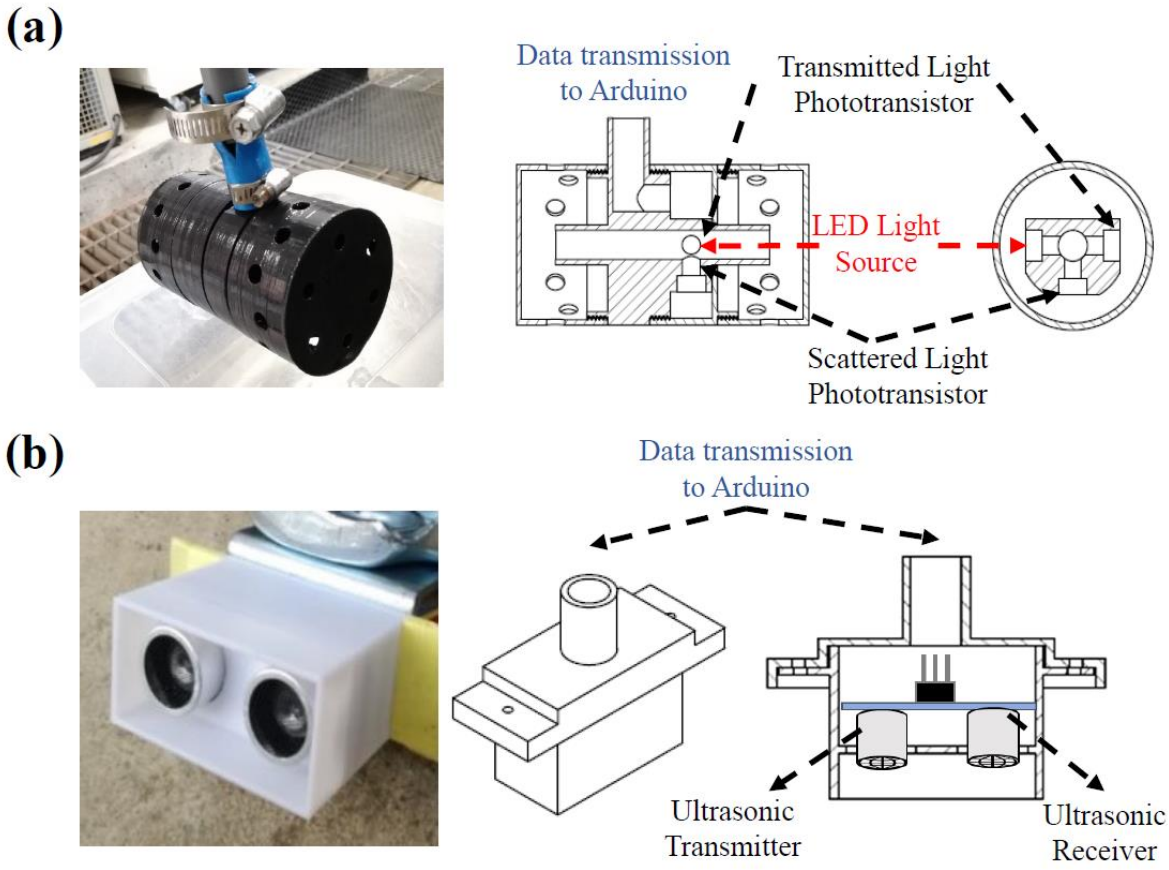

Fig. 7.5: Real setup and schematic of developed (a) turbidity sensor and (b) ultrasonic water level sensor.

7.2.2.3.2 Water Level Sensor

During the monsoon and inter-monsoon seasons, Malaysia experiences unpredictable downpour (extreme rainfall intensity exceeding 400 mm/h), higher frequencies of which are observed in Selangor (Syafrina *et al*., 2015). Therefore, in that region, on-site automated water level monitoring is a critical hydrological aspect of river management. Different physical sensors have recently been proposed and developed for water level measurement, the most commonly used of which are based on float-type, radar, and ultrasonic methods (Lucklum & Jakoby, 2009). However, float-type water level sensors have low accuracies because of large cumulative measurement errors and, thus, must be calibrated regularly (Chetpattananondh *et al.*, 2014). Meanwhile, both radar and ultrasonic-type water level

sensors can provide high-accuracy water level measurements and are resistant to pollution; however, in this research, an ultrasonic-based water level sensor was selected because its cost is lower than that of a radar-based water level sensor. Moreover, its measurement capability is less likely to be affected by raindrops (Zhang *et al*., 2019).

The designed ultrasonic water level sensor consists of an ultrasonic sensor (HC-SR04) with a 3D-printed housing and a temperature sensor, as shown in Fig. 7.5(b). The distance is measured based on the echolocation principle via calculation of the time taken for the receiver to detect the echo signal emitted by the transmitter, as expressed in Eq. (7.4) (Mvemba *et al.*, 2018).

$$d = \frac{v \times t_{tof}}{2} \tag{7.4}$$

In Eq. (4), d is the distance between the sensor and the water surface, v is the speed of sound in air, and t_{tof} represents the time taken for the echo signal to be detected by the receiver. The sound velocity is highly dependent on the working environment, particularly on the atmospheric temperature and humidity, and can be obtained using Eq. (5).

$$v = 331.5 + 0.606\theta + 0.0124H \tag{7.5}$$

In Eq. (5), θ represents the real-time atmospheric temperature in °C, whereas H represents the relative humidity. However, because the effect of humidity deviation on velocity is almost negligible (<0.2% on the accuracy of the measurement), the humidity parameter is not considered in this research (Shin *et al*., 2019).

The ultrasonic water level sensor was calibrated *via* adjustment in the distance between the sensor and a water tub that was placed 4 m below in an open area. This was performed to avoid the detection of surrounding objects, because the HC-SR04 sensor is sensitive and provides a high detection accuracy within a range of 2 to 400 cm (Asadullah & Ullah, 2017). The actual distance between the sensor and the water surface was measured, and the signal was recorded five times to reduce random measurement noise, as expressed in Algorithm 7.S2 (Liao *et al.*, 2020). To calibrate the temperature sensor, it was placed in an incubator with a pre-set temperature along with a digital thermometer.

7.2.2.4 Communication Module

For near-real-time monitoring of turbidity and water level, a data communication module was designed, consisting of a USB Wi-Fi dongle (model: Soracom Air) with a local subscriber identity module card plugged into the USB port of Raspberry Pi. Internet connection is established to enable communication *via* hypertext transfer protocol, one of the most commonly adopted text-based protocols for data transfer in IoT systems because it offers continuous and reliable connections and chunked transfer encoding (Viswanath *et al*., 2016). The measured parameters were uploaded and stored in an open cloud platform, *Ambient*, for centralized near-real-time monitoring and anomaly detection. Although the data can be stored in the platform for only one year, a user can download the dataset (in CSV format) for future use and/or distribution. The *Ambient* platform allows a user to illustrate a maximum of eight different graphs (dataset and GPS position of monitoring point) simultaneously. An example of the user interface of the cloud platform used in this study is shown in Fig. 7.S1.

7.3 Results and Analysis

7.3.1 Cost Analysis

The major components of the WQMS and their approximate costs expressed in US dollars are shown in Table 7.2. These products were purchased in Japan; the costs varied based on the dynamics of the global market exchange rate. The energy module constitutes a major portion of the total cost; however, the utility costs could be omitted because of the utilization of a photovoltaic system, which can function for years (lifespan of solar panel is 20–25 years (Lim *et al*., 2014) whereas for lead–acid batteries, it is 4–6 years (Dufo-López *et al.*, 2014)). Although the initial WQMS development cost (approximately US $261) in this study is slightly higher than those in previous studies (Table 7.1), the cost of the monitoring module is relatively low, particularly owing to the low-cost sensors, indicating that the replacements or add-on costs for these sensors are much lower than those for commercially available sensors (Fisher, 2014; Fletcher & Fisher, 2018).

Table 7.2 Summary and approximate costs of major hardware components of water quality monitoring system

Module	Component	Manufacturer	Cost per Unit (US$)	Quantity	Total Price (US$)
Energy	2. 20W Solar Panel with PWM controller	Saya	45.00	1	45.00
	3. 12V 7.2Ah Battery	Long	25.00	1	25.00
	4. DC-DC adjustable Converter	HiLetGo	2.00	2	4.00
Time	1. Arduino (Nano)	Elegoo	5.00	1	5.00
	2. Relay Module	Elegoo	18.00	1	18.00
	3. Real-Time Clock Module	HiLetGo	4.00	1	4.00
Monitoring	1. Raspberry Pi (Zero WH)	Raspberry Pi Foundation	26.00	1	26.00
	2. 32GB Micro SD	Toshiba	6.00	1	6.00
	3. Arduino (Nano)	Elegoo	5.00	2	10.00
	4. 940nm LED	OptoSupply	0.20	1	0.20
	5. 940nm Phototransistor	Para Light Electronics	0.20	2	0.40
	6. Ultrasonic sensor	HiLetGo	2.00	1	2.00
	7. Temperature sensor	Texas Instruments	0.60	1	0.60
	8. 3D printer Filament	Creality 3D	25.00	1	25.00
Data	1. USB Wi-Fi Dongle	Soracom	60.00	1	60.00
Miscellaneous	Electronics and piping components		30.00	1	30.00
Total					**261.20**

7.3.2 Optimum Sampling Frequency

To determine the optimum sampling frequency of the WQMS, which relies on only the photovoltaic system as its power source, calculations were performed to ensure sufficient energy storage during the worst-case scenario, in which there is negligible or no solar irradiation (Decker, 2014). Incident solar irradiation is the most important parameter affecting the power generated by a photovoltaic system. In this study, the average hourly irradiation data for the period 1999–2018 with a 1-km resolution were obtained from the Global Solar Atlas, which is under the World Bank Group (The World Bank Group, 2020).

The energy consumption of the WQMS was measured and averaged over at least five iterations using a multimeter in three different modes: standby, operating, and communication, as shown in Table 7.3. The highest energy consumption was observed during the communication stage; similar results were reported by Gray *et al*. (2019). With Eq. (7.1), the minimum residual capacity and the number of days that the battery will be capable of supplying energy to the system without charging were calculated at different sampling time intervals (10. 20, 30, 60, 120, 180, and 240 min) based on the hourly average solar irradiation, as illustrated in Fig. 7.6. It can be observed that, although sunshine is abundant in Malaysia, at a high sampling frequency (at least one sampling per hour), the minimum residual capacity computed ranged from 40 to 80%, and the battery could sustain the system for only 1–4 days without charging. As reported by Mayowa *et al*. (2015) and Tan *et al*. (2019), an increase in the number of consecutive wet days (a key indicator of extreme precipitation) in Malaysia may increase the frequency of cloud days during the monsoon season. To prevent energy shortage due to these climate conditions, the battery should be capable of sustaining more than 85% of its residual capacity for more than five days without receiving solar irradiation at its maximum current consumption level (Martínez *et al.,* 2020). Therefore, the optimum sampling frequency is set to two hours.

Table 7.3 Power consumption measurement of WQMS in different modes

Mode	Current (A)	Voltage (V)	Power (W)
Standby	0.045	12	0.540
Operating	0.370	12	4.440
Communication	0.428	12	5.136

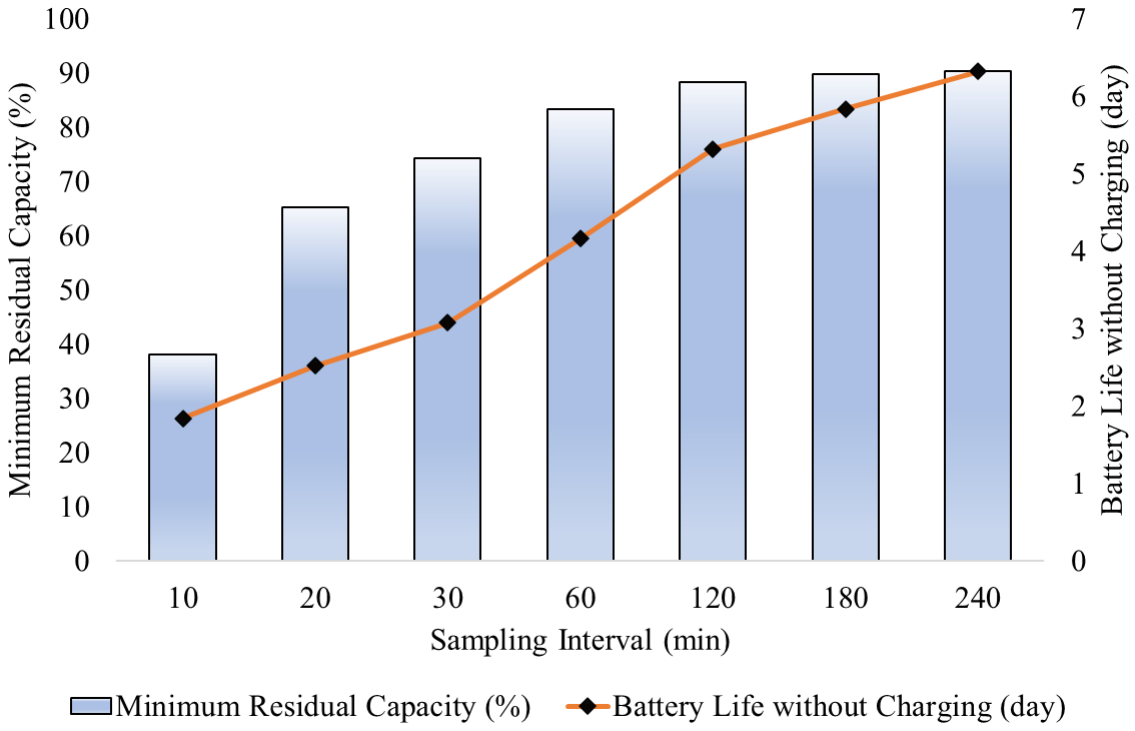

Fig. 7.6: Minimum residual capacity under worst scenario and battery life without charging for different sampling intervals

7.3.3 Sensor Calibration and Validation

After the WQMS was assembled and tested, the developed sensors were calibrated. For the turbidity sensor, as shown in Fig. 7.7(a), the signal received by the attenuated light phototransistor decreased as the turbidity increased, because the suspended particles blocked the transmission of the received light. On the other hand, for the scattered light phototransistor, the signal received increased as the turbidity increased owning to more light was scattered by the higher-concentration suspension in the solution. Both the scattered and attenuated light phototransistors exhibited appropriate corresponding relationships between signal value and turbidity, with a coefficient of determination R^2>0.97. However, at low turbidities (FNU<4), both phototransistors provided constant signals, which may be due to sensitivity limitations. Consequently, the reliable measurement range of the developed turbidity sensor was 10–1,000 NTU. To minimize the effect of light refraction and aging of the LED light source, the ratiometric method was adopted, as illustrated in Fig. 7.7(b). The fitted formula derived from the calibration dataset was used to process the on-site monitoring data.

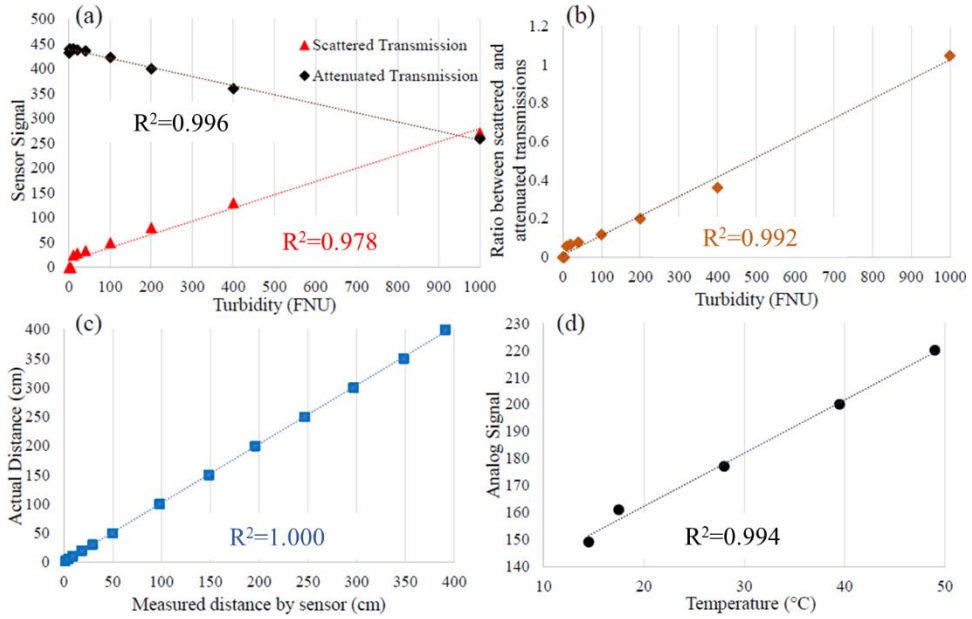

Fig. 7.7: Calibration curves for turbidity using (a) attenuated and scattered light methods and (b) ratio method, and calibration curves for (c) ultrasonic water level sensor and (d) atmospheric temperature sensor

For the water level sensor, the calibration distance was set from 2 to 400 cm, as illustrated in Fig. 7.7(c). The analog signal transmitted by the temperature sensor and the observed temperature were recorded, as illustrated in Fig. 7.7(d). Both the water level and temperature sensors presented a high linearity, with R^2>0.99, and can be deployed for on-site monitoring. However, the HC-SR04 sensor is not water-resistant and may be damaged when exposed to rain. Therefore, to validate if the designed casing would be protective against rainfall, the sensor was tested on a rainy day, and the time-series data were captured, as shown in Fig. 7.8.

For this validation, the maximum rain intensity was obtained from the Weather News, and the device was operated continuously from 14:30 to 17:00 on July 27, 2019, in Lake Biwa, Japan. Owing to the nonlinear wave dynamics at Lake Biwa, the time-series water level measured by the sensor fluctuated significantly, ranging from 128 to 150 cm from the sensor to the water surface. Nevertheless, the water level sensor operated normally with the protection of the designed casing, preventing rainfall from damaging the system and ensuring an appropriate linearity between the actual water level and the water level measured by the sensor, as all the recorded data were within the measurement range.

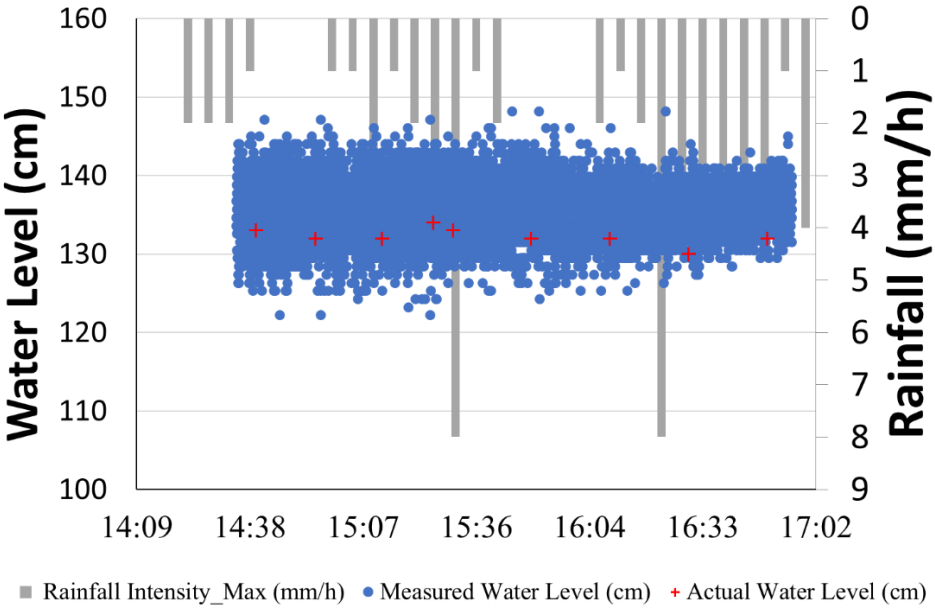

Fig. 7.8: Validation of water level sensor operating under rainfall

7.3.4 Field Study

In this study, the WQMS was set up at one of the main drainages next to the tidal gate of the West Estate Sime Darby Plantation, for continuous monitoring of turbidity and water level every two hours for eight weeks, from November 28, 2019 to January 21, 2020. The installation of the system and the dimensions of the drainage are shown in Fig. 7.9.

The turbidity values recorded at the monitoring station ranged from 0 to 926 FNU, with an average of 525 FNU, as illustrated in Fig. 7.10(a). The system was installed during the monsoon season, wherein the frequency of heavy rainfall was high (Wong *et al.*, 2016), which may have resuspended settled sediments and eroded soil particles from the plantation into the water bodies. Therefore, the turbidity values observed were relatively dynamic and higher than those in the dry season (ranging from 4 to 207 NTU) (Al-Badaii *et al.*, 2013). It is worth noting that this is the first study to reveal the time-series turbidity values for a palm oil plantation during the monsoon season. Based on the results obtained, the trend and average turbidity values (approximately 500 FNU) can be identified for the detection of anomalous phenomena in the plantation field. Several anomalous occurrences were observed during deployment, wherein the turbidity values sharply increased up to 900 FNU. This type of information is important to the relevant authorities for identifying pollution sources and appropriately adopting immediate measures.

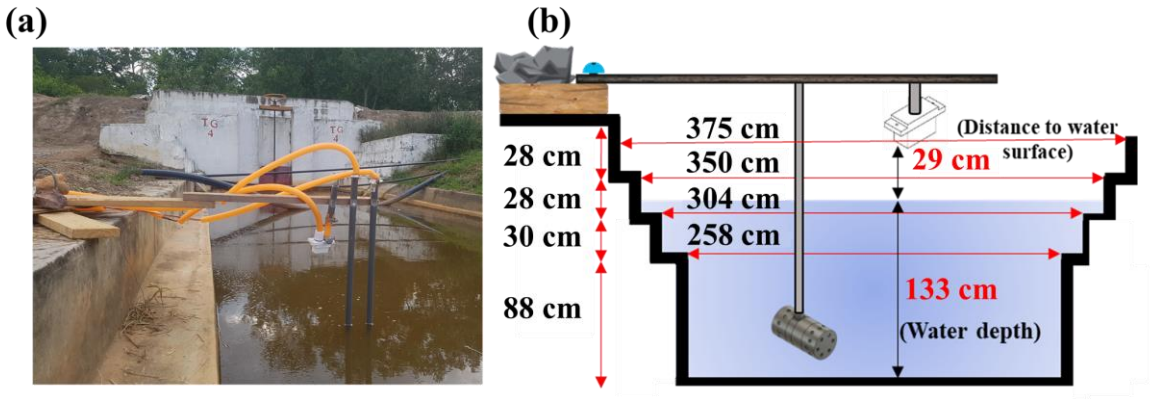

Fig. 7.9: Installation of water quality monitoring system and dimensions of drainage

Because the West Estate Sime Darby Plantation is located in a rural and remote area with highly limited network coverage, some of the data were not transmitted to the cloud system, leading to a discontinuity in the graph. This may also be caused by a failed connection between the Raspberry Pi and Arduino during data transmission. In addition, turbidity data became unavailable after December 26, 2019 because no measurements were obtained by the turbidity sensor. As reported by Matos *et al*. (2019), this may be a result of biofouling on the phototransistor and LED light source due to the high turbidity of water and presence of biological organisms, preventing the device from functioning. Therefore, maintenance work should be performed at least once a month to ensure that the device is running smoothly and correctly.

An important factor that affects the water level measurement accuracy is the measuring angle. Therefore, to ensure an accurate measurement, the support system was reinforced using heavy rocks as anchors to prevent sensor displacement by strong winds, as shown in Fig. 7.9. During the deployment, the average water level recorded was 129.9 cm, and it could be observed that the water level was higher in the middle of the December–January period, as a result of the monsoon season, as shown in Fig. 7.10(b). The maximum and minimum water levels recorded were 160 and 9 cm, respectively. Concurrently, the average atmospheric temperature recorded was 30°C, and the maximum and minimum atmospheric temperatures were 29°C and 41°C, respectively, as illustrated in Fig. 7.10(c). The results obtained reflect the typical climate in Malaysia; however, the maximum temperature observed was slightly higher than those reported by Amirabadizadeh *et al*. (2015) and Yatim *et al*. (2019). A possible reason for this trend could be that the temperature sensor was stored in a sealed container in an open area without a shelter, resulting in a higher observed temperature than the typical climate in Malaysia.

7.4 Discussion of Findings

At present, the most commonly adopted technologies for real- or near-real-time water quality monitoring are high-end or certified reference sensors. This concept has been adopted by many developed countries (such as Canada, Japan, and the United States) and has been promoted for use in developing countries. Thailand was among its pioneers in Southeast Asia, having installed 126 real-time monitoring stations across the nation to monitor pH, turbidity, dissolved oxygen, conductivity, and water temperature (Pollution Control Department, 2016). However, although this solution can easily address challenges in continuous monitoring, the initial investment cost required for installation is enormous, at approximately US $8.4 million, along with the annual maintenance cost for each monitoring station, which is approximately US $3,155 (Pollution Control Department, 2014), making it infeasible for application in other developing countries. Therefore, the framework of the low-cost 3D-printed IoT-based WQMS developed in this study, including its system architecture, sensor development and validation, optimal sampling frequency, and deployment could be a possible solution for the sixth UNSDG and promote environmental sustainability through the utilization of renewable energy.

Based on the results of the field study, the contact-type sensor (for turbidity) requires monthly maintenance to prevent the deposition of mud/silt and biofouling problems, whereas the non-contact sensor (for water level) consistently provides accurate measurements. This study has demonstrated the feasibility of addressing global issues through an economical and practical approach. Through the use of IR 4.0 technologies and low-cost sensors, which have widespread positive implications for the environment, a sustainable and standalone WQMS that measures turbidity and water level every two hours has been developed.

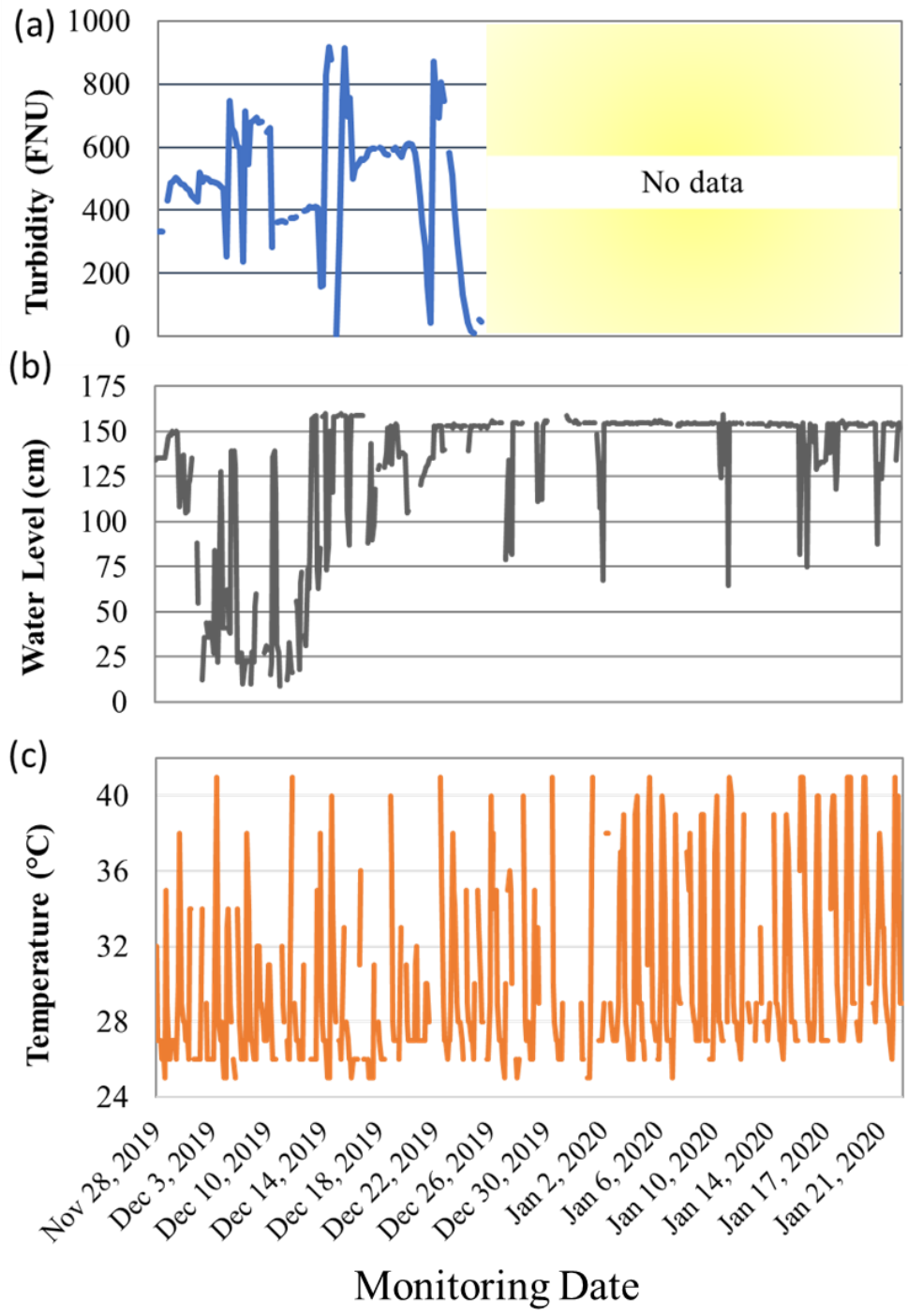

Fig. 7.10: Time-series data of turbidity, water level, and temperature recorded by water quality monitoring system during deployment period

7.4.1 Theoretical Contributions

The implementation of IR 4.0, replacing traditional water quality monitoring, is imperative, and thus, extensive research has been conducted; however, the linkage between theoretical developments and real-world applications is still at a nascent stage (Yadav *et al.*, 2020). Primarily, the present study addressed the implementation challenges of IoT-based WQMSs, utilizing low-cost sensors based on existing methodologies (photovoltaic system, 3D printing) for the development of the monitoring system. Because most studies thus far have presented only an overview of their respective developed systems (Table 7.1), a compact and solar-powered WQMS architecture has not yet been clearly established. Therefore, this study provides a detailed explanation of the function of each module constituting the architecture to facilitate the future development/improvement of WQMSs.

Several studies have attempted to utilize commercially available low-cost turbidity sensors for measurement (Gillett & Marchiori, 2019; Kitchener *et al*., 2019; Pasika & Gandla, 2020); however, details on the designs of these sensors have not been provided (*e.g.*, type of light source and wavelength of LED), which prevents comparison among the different turbidity sensors for validation. Therefore, in this study, to ensure that the sensor measurements are comparable, the sensors have been developed and validated according to international standards, such as ISO or USEPA.

7.4.2 Practical Implications

This study highlighted and demonstrated how the integration of 3D printing, IoT systems, and low-cost sensors could be a key driver in addressing inadequacies in WQMSs for sustainable water resource management, particularly in developing countries, as highlighted in the UNSDGs. The affordable cost (in installation and maintenance) and acceptable measurement accuracy range of IoT-based monitoring systems could be the main drivers for their emergence as a next-generation solution (Miller, 2018) for sustainable water resource management.

The conventional water quality monitoring through laboratory-based techniques is difficult, time-consuming, and expensive Under the umbrella of IR 4.0, emerging innovations

that are highly decentralized, automated, and interdependently controllable (*via* open or closed platforms) may be possible solutions to the aforementioned problem and have therefore gained significant attention. Relevant authorities are moving toward smart monitoring as they significantly reduce the laborious work required for monitoring and are empowered to provide real- or near-real-time monitoring of specific water quality parameters, which could be an effective tool for addressing water quality related problems (Ahmed *et al*., 2019; Pasika & Gandla, 2020).

As small/desktop-scale 3D printers become more affordable and commercially widespread, 3D printing could become a promising and pragmatic alternative to conventional fabrication/prototyping processing (where sophisticated machines are required) for developing complicated geometries and structural details. The 3D-printing also allows developers to share computer-aided design files of their sensors over specific platforms (for instance, Thingiverse, GrabCAD, and Pinshape) to facilitate information flow among practitioners, and enable download, modification, and/or improvisation based on their requirements. Furthermore, the integration of 3D printing with IoT systems and low-cost sensors may present a new path for the relevant authorities to adopt this framework for the construction of devices for measuring other parameters, based on their local geographical and metrological conditions.

The application of the developed WQMS is not only useful for studying trends in water bodies in terms of certain parameters, but also aids relevant authorities in making immediate decisions when an abnormal measurement is observed. For conventional water quality measurement methods, monitoring frequencies are relatively low (weekly, monthly, or seasonal basis) that may hinder immediate and specific operation responses required to address water pollution arising from point or non-point sources (for example, illicit discharge and surface runoff) (Park *et al*., 2020). As reported by Wang *et al.* (2021), the traceability service provided by IoT systems is critical for establishing the accountability of these systems. Through the use of real- or near-real-time monitoring *via* an IoT system, the risk of pollution of an exposed water body can be tracked and immediate actions can be performed.

7.5 Conclusions

Water and air quality monitoring has typically been challenging in developing countries, particularly because of the high equipment cost, intensive labor, and extensive time required. Although there has been a remarkable increase in the use of low-cost sensors in the development of IoT-based WQMSs, they have not yet been widely implemented in field operations. To address this issue, a low-cost and novel 3D-printed IoT-based near-real-time WQMS powered by only a photovoltaic system was developed, calibrated, and deployed in a palm oil plantation on Carey Island, Malaysia, for two months. The designed WQMS comprises four major modules: energy, time, monitoring, and communication. The modules are composed of different sensors, Raspberry Pi, Arduinos, and a cloud platform. The proposed WQMS has proven the practicality of the integration of IoT with 3D printing, microcomputers, and low-cost sensors and has paved a new path for developing cost-effective and reliable systems for near-real-time water quality monitoring.

The study revealed the high potential of utilizing solar energy as the primary energy source for operating low-power WQMSs in tropical countries. For example, the abundant sunlight in Malaysia will allow the system to operate sustainably using energy harvested by the photovoltaic system when the sampling is limited to a maximum of once every two hours. Turbidity, a major water quality problem encountered in Southeast Asia, was used as a monitoring parameter together with the water level. Calibration and validation of the turbidity, temperature, and ultrasonic water level sensors were performed, and high linearities were obtained between the signals received and the actual measurements. The developed turbidity sensor provides an accurate measurement of turbidity within a range of 10 to 1,000 FNU, whereas the optimum measurement ranges for the ultrasonic and temperature sensors are 2–400 cm and 10–50°C, respectively. During the deployment period, the contact-type sensor (turbidity sensor) stopped functioning after a month, whereas the non-contact-type sensors (water level sensor) consistently continued to provide measurements. Therefore, to improve the turbidity sensor, self-cleaning mechanisms, such as installation of a wiper/brush to remove the deposition of mud/silt and microorganisms, will be necessary.

7.5 Way Beyond

To further improve its durability and reliability, the developed 3D-printed IoT-based WQMS could be integrated with a cyber-physical system, which would exhibit an improved self-resilience/optimization and prediction performance (Fatima *et al.,* 2020) that is more robust to random disturbances caused by environmental influences and will be useful for long-term trend analysis. A warning notification system could be incorporated into the system to inform relevant authorities for anomalous detections, such that immediate action/checking can be performed. Associating with artificial intelligence algorithms/models that can learn and capture non-linear characteristics in datasets and implement consistent calibration with past and current data (Wong *et al.,* 2020a), the sensor sensitivity can be improved, the impact of measurement errors can be minimized or almost eliminated, and warning notifications for future events (*e.g.,* flooding caused by overflows in plantation areas) can be provided (Jenny *et al*., 2020). An optimum maintenance time is required to ensure performance and cost-effectiveness of the system; therefore, further studies are necessary to evaluate effects of the environment on the accuracies and lifespans of the sensors.

The proposed WQMS implemented demonstrates the effective integration of IoT with 3D printing, microcomputers, and low-cost sensors. Based on the developed prototype, it could be further modified to address the monitoring frequency across wider area for air quality monitoring, paving a new path for the development of cost-effective and reliable systems for both water and air quality monitoring.

Supplementary Materials

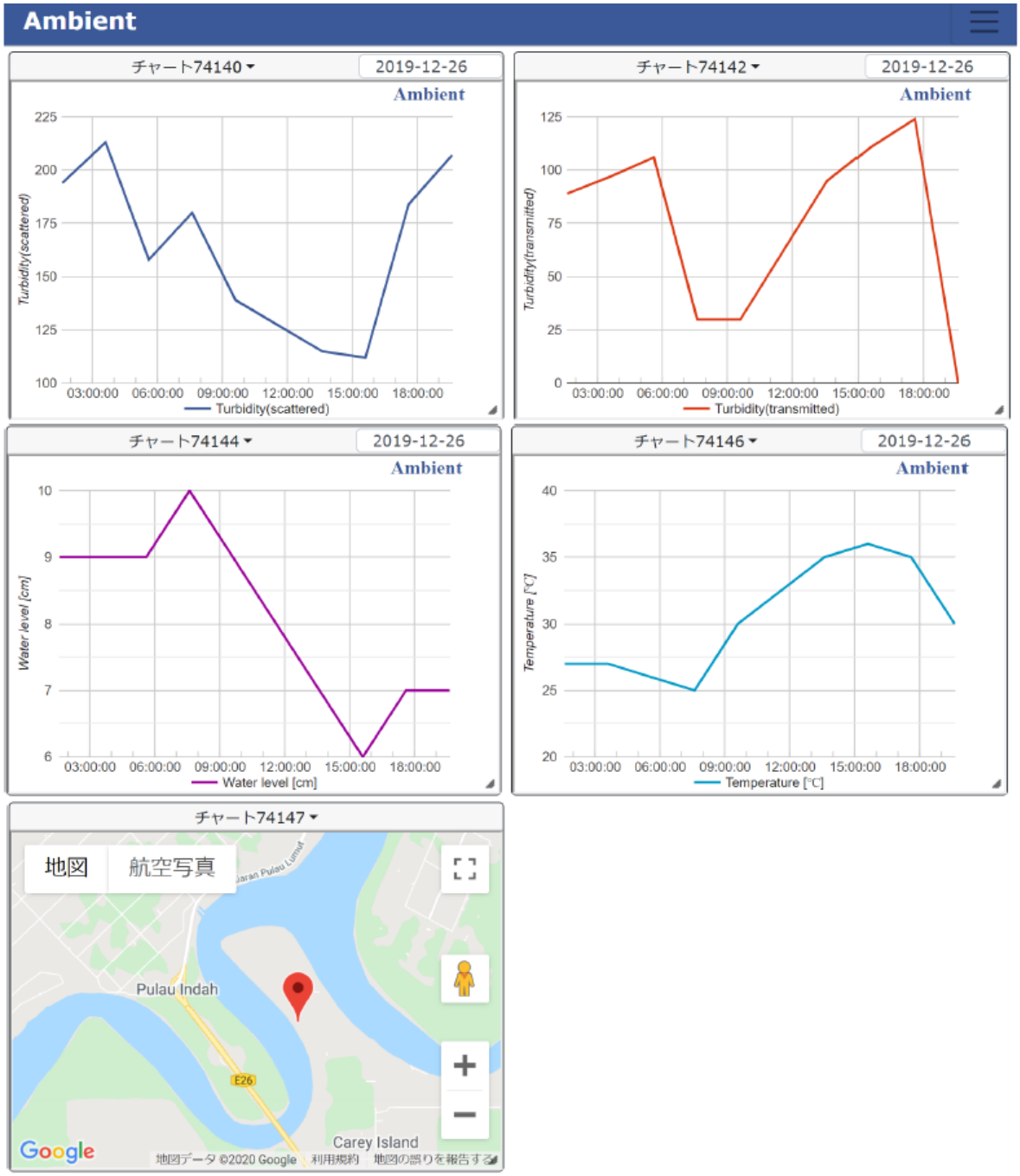

Fig. 7.S1: Interface of *Ambient* cloud platform with measured parameters and installation location.

Algorithm 7.S1: Turbidity sensor measurement

Measurement of Turbidity

Input: count: frequency of sampling; Signal $_{scattered/attenuated/ratio}$: voltage value received by phototransistors based on turbidimetry method, nephelometry method, and ratio method, respectively; FNU $_{scattered/attenuated}$: Turbidity measurement based on turbidimetry method, and nephelometry method, respectively; and FNU $_{Ratio}$: Turbidity measurement based on ratiometric method

Output: Turbidity: Averaged turbidity measurement based on ratiometric method

for *count* = 1 to 5 **do**
    Obtain $\boldsymbol{Signal_{Scattered}}$
    if ($\boldsymbol{Signal_{Scattered}}$ was not obtained**) then**
        Remove $\boldsymbol{Signal_{Scattered}}$ as an outlier
    end if
    Obtain $\boldsymbol{Signal_{Attenuated}}$
    if ($\boldsymbol{Signal_{Attenuated}}$ was not obtained**) then**
        Remove $\boldsymbol{Signal_{Attenuated}}$ as an outlier
    end if
    if (Both $\boldsymbol{Signal_{Scattered}}$ and $\boldsymbol{Signal_{Attenuated}}$ are not outliers**) then**
        $\boldsymbol{Signal_{Ratio}}$ = $\boldsymbol{Signal_{Scattered}}$ / $\boldsymbol{Signal_{Attenuated}}$
        $\boldsymbol{FNU_{Ratio}}[\boldsymbol{count}]$ = 0.001 * $\boldsymbol{Signal_{Ratio}}$ + 0.0116
        if ($\boldsymbol{FNU_{Ratio}}[\boldsymbol{count}]$ < 10 or $\boldsymbol{FNU_{Ratio}}[\boldsymbol{count}]$ > 1000) **then**
            Remove $\boldsymbol{FNU_{Ratio}}[\boldsymbol{count}]$ as an outlier
        end if
    else
        Set $\boldsymbol{FNU_{Ratio}}[\boldsymbol{count}]$ as an outlier
    end if
    Wait 10 seconds
end for
$\boldsymbol{Turbidity}$ = Average of $\sum_{\mathbf{count=1}}^{\mathbf{5}} \mathbf{FNU_{Ratio}}$
return $\boldsymbol{Turbidity}$

The algorithm for turbidity detection utilizes an Arduino microcontroller associated with a light-emitting diode (LED) light source with a wavelength of 940 nm and two phototransistors L-51ROPT1D1 for synchronous measurement of scattered and attenuated lights, as described in Algorithm 7.S1. The algorithm provides turbidity measurements based on the turbidimetry, nephelometry, and ratiometric methods (refer to Section 7.2.2.3 for a

detailed explanation). The sampling frequency is set at 5 to reduce the random measurement error, whereas the time interval for each sampling is set at 10 s. When the system boots up, the signals for both the scattered and attenuated phototransistors are recorded, unless no signals are transmitted from the sensor to the Arduino, owing to electronic issues (malfunctioned sensor, interrupted signal communication, electricity shortage or poor internet connection). To obtain the ratiometric turbidity, the ratio between the scattered and attenuated signals is obtained and converted using the equation in Line 12. The ratiometric turbidity value is sent to Raspberry Pi, providing a ratio value between 10 and 1000. Otherwise, the measurement is recorded as an outlier. The range between 10 and 1000 is chosen in accordance with the optimal measurement range obtained from the calibration curve (Fig. 7.7). The process is repeated five times, and an average value of the turbidity values is sent to the *Ambient* cloud platform.

Algorithm 7.S2: Water level sensor measurement

Measurement of Water Level

Input: count: frequency of sampling; Signal $_{Temp}$: voltage value received by temperature sensor; WL: water level measured by sensor; Signal $_{Time}$: Echo reflection time.
Output: Temperature: temperature measured by sensor; WaterLevel: Averaged atmospheric condition corrected water level;

1. **for** *count* = 1 to 5 **do**
2. Obtain $\boldsymbol{Signal}_{\boldsymbol{Temp}}$
3. **if (**$\boldsymbol{Signal}_{\boldsymbol{Temp}}$ was not obtained**) then**
4. Remove $\boldsymbol{Signal}_{\boldsymbol{Temp}}$ as an outlier
5. **else**
6. $\boldsymbol{Temp}[\boldsymbol{count}]$ = 1.9689 * $\boldsymbol{Signal}_{\boldsymbol{Temp}}$ + 122.92
7. **end if**
8. Obtain $\boldsymbol{Signal}_{\boldsymbol{Time}}$
9. **if (**$\boldsymbol{Signal}_{\boldsymbol{Temp}}$ or $\boldsymbol{Signal}_{\boldsymbol{Time}}$was not obtained**) then**
10. Remove $\boldsymbol{Signal}_{\boldsymbol{Time}}$ as an outlier
11. **else**
12. $\boldsymbol{WL}[\boldsymbol{count}]$ = (331.5 + 0.606 * $\boldsymbol{Temp}[\boldsymbol{count}]$) * $\boldsymbol{Signal}_{\boldsymbol{Time}}[\boldsymbol{count}]$ / 2
13. **if (**$\boldsymbol{WL}[\boldsymbol{count}]$ < 2 or $\boldsymbol{WL}[\boldsymbol{count}]$ > 400**) then**
14. Remove $\boldsymbol{WL}[\boldsymbol{count}]$ as an outlier
15. **end if**
16. **Wait 10 seconds**
16. **end for**
17. $\boldsymbol{WaterLevel}$ = Average of $\sum_{\boldsymbol{count=1}}^{\boldsymbol{5}} \boldsymbol{WL}$
18. **return** $\boldsymbol{Temperature}$, $\boldsymbol{WaterLevel}$

The algorithm for water level detection utilizes an Arduino microcontroller associated with an ultrasonic sensor (HC-SR04) and temperature sensor (LM61CIZ/NOPB), as mentioned in *Algorithm 7.S2.* The sampling frequency is set at 5 to reduce the random measurement error, whereas the time interval for each sampling is set at 10 s. When the system boots up, the signal of the temperature sensor is recorded, unless no signals are transmitted from the sensor to the Arduino, owing to electronical issues (malfunctioned sensor, interrupted signal communication, electricity shortage or poor internet connection). If the signal is received by the Arduino, the signal is converted to the actual temperature value using the equation in Line 6. Otherwise, the value is recorded as an outlier and sent to

the Raspberry Pi. The water level is computed using the equation in Line 12 after the echo reflection time is received by the ultrasonic sensor. The water level value is sent to Raspberry Pi, providing the computed water level value as < 400 or > 2. Otherwise, the measurement is recorded as an outlier. The process is repeated five times and an average value of the water level is sent to the *Ambient* cloud platform.

List of References

A. Decker (2014). Solar energy harvesting for autonomous field devices. *IET Wireless Sensor Systems, 4*(1), 1-8, doi:10.1049/iet-wss.2013.0011.

A. Jerom B, Manimegalai, R., & Manimegalai, R. An IoT Based Smart Water Quality Monitoring System using Cloud. In *2020 International Conference on Emerging Trends in Information Technology and Engineering (ic-ETITE), 24-25 Feb. 2020 2020* (pp. 1-7). doi:10.1109/ic-ETITE47903.2020.450.

Ahmed, U., Mumtaz, R., Anwar, H., Mumtaz, S., & Qamar, A. M. (2019). Water quality monitoring: from conventional to emerging technologies. *Water Supply*, *20*(1), 28-45, doi:10.2166/ws.2019.144

Al-Badaii, F., Shuhaimi-Othman, M., & Gasim, M. (2013). Water Quality Assessment of the Semenyih River, Selangor, Malaysia. *Journal of Chemistry*, *2013*, doi:10.1155/2013/871056.

Almasi, M., Milow, P., & Zakaria, R. B. M. (2018). Participatory mangrove forest management in the Carey Island, Malaysia. *Ukrainian Journal of Ecology, 8*, 328-339.

Amirabadizadeh, M., Huang, Y. F., & Lee, T. S. (2015). Recent Trends in Temperature and Precipitation in the Langat River Basin, Malaysia. *Advances in Meteorology, 2015*, 579437, doi:10.1155/2015/579437.

Arfanuzzaman, M., & Dahiya, B. (2019). Sustainable urbanization in Southeast Asia and beyond: Challenges of population growth, land use change, and environmental health. *50*(2), 725-744, doi:10.1111/grow.12297.

Asadullah, M., & Ullah, K. Smart home automation system using Bluetooth technology. In *2017 International Conference on Innovations in Electrical Engineering and Computational Technologies (ICIEECT), 5-7 April 2017 2017* (pp. 1-6). doi:10.1109/ICIEECT.2017.7916544.

Awan, U., Kraslawski, A., & Huiskonen, J. (2019). Progress from Blue to the Green World: Multilevel Governance for Pollution Prevention Planning and Sustainability. In C. M. Hussain (Ed.), *Handbook of Environmental Materials Management* (pp. 1-22). Cham: Springer International Publishing. doi:10.1007/978-3-319-58538-3_177-1

Awan, U., Sroufe, R., & Shahbaz, M. (2021). Industry 4.0 and the circular economy: A literature review and recommendations for future research. *Business Strategy and the Environment*, *30*(4), 2038-2060, doi:10.1002/bse.2731.

Bakrin Sofawi, A., Rozainah, M. Z., Normaniza, O., & Roslan, H. (2017). Mangrove rehabilitation on Carey Island, Malaysia: an evaluation of replanting techniques and sediment properties. *Journal of Marine Biology Research, 13*(4), 390-401. doi:10.1080/17451000.2016.1267365

Castell, N., Dauge, F. R., Schneider, P., Vogt, M., Lerner, U., Fishbain, B., et al. (2017). Can commercial low-cost sensor platforms contribute to air quality monitoring and exposure estimates? *Environment International, 99*, 293-302, doi:10.1016/j.envint.2016.12.007.

Cheng, Y., Awan, U., Ahmad, S., & Tan, Z. (2021). How do technological innovation and fiscal decentralization affect the environment? A story of the fourth industrial revolution and sustainable growth. *Technological Forecasting and Social Change, 162*, 120398, doi:10.1016/j.techfore.2020.120398.

Chetpattananondh, K., Tapoanoi, T., Phukpattaranont, P., & Jindapetch, N. (2014). A self-calibration water level measurement using an interdigital capacitive sensor. *Sensors and Actuators A: Physical, 209*, 175-182, doi:10.1016/j.sna.2014.01.040.

Chowdury, M. S. U., Emran, T. B., Ghosh, S., Pathak, A., Alam, M. M., Absar, N., et al. (2019). IoT Based Real-time River Water Quality Monitoring System. *Procedia Computer Science, 155*, 161-168, doi:10.1016/j.procs.2019.08.025.

Daigavane, V. V., & Gaikwad, D. M. (2017). Water Quality Monitoring System Based on IOT. *Advances in Wireless and Mobile Communications, 10*(5), 10.

Darmalim, U., Darmalim, F., Darmalim, S., Hidayat, A. A., Budiarto, A., Mahesworo, B., et al. (2020). IoT Solution for Intelligent Pond Monitoring. *IOP Conference Series: Earth and Environmental Science, 426*, 012145, doi:10.1088/1755-1315/426/1/012145.

Dufo-López, R., Lujano-Rojas, J. M., & Bernal-Agustín, J. L. (2014). Comparison of different lead–acid battery lifetime prediction models for use in simulation of stand-alone photovoltaic systems. *Applied Energy, 115*, 242-253, doi:10.1016/j.apenergy.2013.11.021.

Encinas, C., Ruiz, E., Cortez, J., & Espinoza, A. Design and implementation of a distributed IoT system for the monitoring of water quality in aquaculture. In *2017 Wireless Telecommunications Symposium (WTS), 26-28 April 2017 2017* (pp. 1-7). doi:10.1109/WTS.2017.7943540.

EPA, U. S. (2020). EPA's Water Quality Framework- Next Steps Toward Improved Accountability

Farooq, M. S., Riaz, S., Abid, A., Umer, T., & Zikria, Y. B. (2020). Role of IoT Technology in Agriculture: A Systematic Literature Review. *Electronics, 9*(2), 319. doi:10.3390/electronics9020319

Fatima, I., Malik, S. U. R., Anjum, A., & Ahmad, N. (2020). Cyber Physical Systems and IoT: Architectural Practices, Interoperability, and Transformation. *IT Professional, 22*(3), 46-54, doi:10.1109/MITP.2019.2912604.

Fisher, D. K. (2014). Rapid deployment of internet-connected environmental monitoring devices. *Journal of Advances in Internet of Things, 4*(04), 46. doi:10.4236/ait.2014.44007.

Fletcher, R. S., & Fisher, D. K. A. S. (2018). A Miniature Sensor for Measuring Reflectance, Relative Humidity, and Temperature: A Greenhouse Example. *Journal of Agricultural Sciences, 9*(11), 1516-1527. doi:10.4236/as.2018.911106.

Gillett, D., & Marchiori, A. (2019). A Low-Cost Continuous Turbidity Monitor. *Sensors, 19*(14), 18, doi:10.3390/s19143039.

Gray, C., Ayre, R., Hinton, K., & Campbell, L. (2019). 'Smart'is not free: Energy consumption of consumer home automation systems. *IEEE Transactions on Consumer Electronics, 66*(1), 87-95. doi:10.1109/TCE.2019.2962605

Jenny, H., Alonso, E. G., Wang, Y., & Minguez, R. (2020). Using Artificial Intelligence for Smart Water Management Systems. doi:10.22617/BRF200191-2

Khosravani, M. R., & Reinicke, T. (2020). 3D-printed sensors: Current progress and future challenges. *Sensors and Actuators A: Physical, 305*, 111916, doi:10.1016/j.sna.2020.111916.

Kitchener, B. G. B., Dixon, S. D., Howarth, K. O., Parsons, A. J., Wainwright, J., Bateman, M. D., et al. (2019). A low-cost bench-top research device for turbidity measurement by radially distributed illumination intensity sensing at multiple wavelengths. *HardwareX, 5*, e00052, doi:10.1016/j.ohx.2019.e00052.

Koditala, N. K., & Pandey, P. S. Water Quality Monitoring System Using IoT and Machine Learning. In *2018 International Conference on Research in Intelligent and Computing in Engineering (RICE), 22-24 Aug. 2018 2018* (pp. 1-5). doi:10.1109/RICE.2018.8509050.

Kshirsagar, R., Mudhalwadkar, R. P., & Kalaskar, S. Design and Development of IoT Based Water Quality Measurement System. In *2019 3rd International Conference on Trends in Electronics and Informatics (ICOEI), 23-25 April 2019 2019* (pp. 1199-1202). doi:10.1109/ICOEI.2019.8862663.

Kumar, A., Wasan, P., Luthra, S., & Dixit, G. (2020). Development of a framework for selecting a sustainable location of waste electrical and electronic equipment recycling plant in emerging economies. *Journal of Cleaner Production, 277*, 122645, doi:10.1016/j.jclepro.2020.122645.

Lamberti, P., Spinelli, G., Kuzhir, P., Guadagno, L., Naddeo, C., Romano, V., et al. (2018). *Evaluation of thermal and electrical conductivity of carbon-based PLA nanocomposites for 3D printing* (Vol. 1981). doi:10.1063/1.5046020

Li, W.-T., Tushar, W., Yuen, C., Ng, B. K. K., Tai, S., & Chew, K. T. (2020). Energy efficiency improvement of solar water heating systems – An IoT based

commissioning methodology. *Energy and Buildings, 224*, 110231, doi:10.1016/j.enbuild.2020.110231.

Liao, H., Zhou, Z., Zhao, X., Zhang, L., Mumtaz, S., Jolfaei, A., et al. (2020). Learning-Based Context-Aware Resource Allocation for Edge-Computing-Empowered Industrial IoT. *IEEE Internet of Things Journal, 7*(5), 4260-4277, doi:10.1109/JIOT.2019.2963371.

Lim, Y. S., Lo, C. K., Kee, S. Y., Ewe, H. T., & Faidz, A. R. (2014). Design and evaluation of passive concentrator and reflector systems for bifacial solar panel on a highly cloudy region – A case study in Malaysia. *Renewable Energy, 63*, 415-425, doi:10.1016/j.renene.2013.10.008.

Liu, H., Yang, P., Song, H., Guo, Y., Zhan, S., Huang, H., et al. (2015). Generalized weighted ratio method for accurate turbidity measurement over a wide range. *Optics Express, 23*, 32703, doi:10.1364/OE.23.032703.

Lucklum, F., & Jakoby, B. (2009). Non-contact liquid level measurement with electromagnetic–acoustic resonator sensors. *Measurement Science and Technology, 20*(12), 124002, doi:10.1088/0957-0233/20/12/124002.

Lyu, Y., Chen, Y., Lin, Z., Zhang, J., & Shi, X. (2020). Manipulating phase structure of biodegradable PLA/PBAT system: Effects on dynamic rheological responses and 3D printing. *Composites Science and Technology, 200*, 108399, doi:10.1016/j.compscitech.2020.108399.

Martínez, R., Vela, N., el Aatik, A., Murray, E., Roche, P., & Navarro, J. M. (2020). On the Use of an IoT Integrated System for Water Quality Monitoring and Management in Wastewater Treatment Plants. *12*(4), 1096. doi:10.3390/w12041096

Matos, T., Faria, C. L., Martins, M. S., Henriques, R., Gomes, P., & Goncalves, L. M. (2019). Development of a cost-effective optical sensor for continuous monitoring of turbidity and suspended particulate matter in marine environment. *Sensors, 19*(20), 4439. doi:10.3390/s19204439

Mayowa, O. O., Pour, S. H., Shahid, S., Mohsenipour, M., Harun, S. B., Heryansyah, A., et al. (2015). Trends in rainfall and rainfall-related extremes in the east coast of peninsular Malaysia. *Journal of Earth System Science, 124*(8), 1609-1622, doi:10.1007/s12040-015-0639-9.

Medema, W., Adamowski, J., Orr, C., Furber, A., Wals, A., & Milot, N. (2017). Building a Foundation for Knowledge Co-Creation in Collaborative Water Governance: Dimensions of Stakeholder Networks Facilitated through Bridging Organizations. *9*(1), 60. doi:10.3390/w9010060

Metzger, M., Konrad, A., Blendinger, F., Modler, A., Meixner, A. J., Bucher, V., et al. (2018). Low-Cost GRIN-Lens-Based Nephelometric Turbidity Sensing in the Range of 0.1–1000 NTU. *18*(4), 1115. doi:10.3390/s18041115

Mhetre, C., Narkhede, P., Pashte, Y., Patankar, N., & N, P. Solar Powered Wireless Sensor Network Using Zigbee Module. In *2019 International Conference on Intelligent Computing and Control Systems (ICCS), 15-17 May 2019 2019* (pp. 468-473). doi:10.1109/ICCS45141.2019.9065494.

Miller, D. (2018). Blockchain and the Internet of Things in the Industrial Sector. *IT Professional, 20*(3), 15-18, doi:10.1109/MITP.2018.032501742.

Mohammad, S. T., Al-Kayiem, H. H., Aurybi, M. A., & Khlief, A. K. (2020). Measurement of global and direct normal solar energy radiation in Seri Iskandar and comparison with other cities of Malaysia. *Case Studies in Thermal Engineering, 18*, 100591, doi:10.1016/j.csite.2020.100591.

Mulyana, Y., & Hakim, D. L. (2018). Prototype of Water Turbidity Monitoring System. *IOP Conference Series: Materials Science and Engineering, 384*, 012052, doi:10.1088/1757-899x/384/1/012052.

Mvemba, P. K., Band, S. K. G. G., Lay-Ekuakille, A., & Giannoccaro, N. I. (2018). Advanced acoustic sensing system on a mobile robot: design, construction and measurements. *IEEE Instrumentation & Measurement Magazine, 21*(2), 4-9, doi:10.1109/MIM.2018.8327971.

Nandakumar, L., Sangeeth, M., Thomson, M. A. M., Tommy, A., Kiran, M. P., & Raji, P. Real Time Water Contamination Monitor using Cloud, IoT and Embedded Platforms. In *2020 International Conference on Smart Electronics and Communication (ICOSEC), 10-12 Sept. 2020 2020* (pp. 854-858). doi:10.1109/ICOSEC49089.2020.9215276.

Oelen, A., Aart, C. V., & Boer, V. D. Measuring Surface Water Quality Using a Low-Cost Sensor Kit within the Context of Rural Africa. In *P-ICT4D@WebSci, 2018*.

Ogata, Y., Ishigaki, T., Ebie, Y., Sutthasil, N., Witthayaphirom, C., Chiemchaisri, C., et al. (2018). Design considerations of constructed wetlands to reduce landfill leachate contamination in tropical regions. *Journal of Material Cycles and Waste Management, 20*(4), 1961-1968, doi:10.1007/s10163-018-0755-0.

Park, J., Kim, K. T., & Lee, W. H. (2020). Recent Advances in Information and Communications Technology (ICT) and Sensor Technology for Monitoring Water Quality. *12*(2), 510. doi:10.3390/w12020510

Pasika, S., & Gandla, S. T. (2020). Smart water quality monitoring system with cost-effective using IoT. *Heliyon, 6*(7), e04096, doi:10.1016/j.heliyon.2020.e04096.

Patang, F., & Soegianto, A. (2020). Oxidative responses of macro-invertebrates in relation to environmental variables in rivers of East Kalimantan, Indonesia. *Chemistry and Ecology, 36*(9), 855-867, doi:10.1080/02757540.2020.1791101.

Pollution Control Department (2014). Project of Water Quality Monitoring Development.

Pollution Control Department (2016). National Surface Water Quality Database System. http://iwis.pcd.go.th/index.php. Accessed 12th December 2020.

Prasad, P. (2015). Recent trend in wireless sensor network and its applications: a survey. *Sensor Review, 35*(2), 229-236, doi:10.1108/SR-08-2014-683.

Regan, F., Lawlor, O'Flynn, B., & Wallace (2010). Experiences and Recommendations in Deploying a Real-Time, Water Quality Monitoring System. *Measurement Science and Technology, 21*, doi:10.1088/0957-0233/21/12/124004.

Rohit, M. H., Hoque, Z. T., Karim, S. M. M., & Siddique, S. Cost Efficient Automated Pisciculture Assistance System Using Internet of Things (IoT). In *2019 IEEE/ACM 1st International Workshop on Software Engineering Research & Practices for the Internet of Things (SERP4IoT), 27-27 May 2019 2019* (pp. 49-52). doi:10.1109/SERP4IoT.2019.00015.

Rüßmann, M., Lorenz, M., Gerbert, P., Waldner, M., Justus, J., Engel, P., et al. (2015). Industry 4.0: The future of productivity and growth in manufacturing industries. (Vol. 9, pp. 54-89): Boston Consulting Group.

Shin, S., Kim, M., & Choi, S. B. (2019). Ultrasonic Distance Measurement Method With Crosstalk Rejection at High Measurement Rate. *IEEE Transactions on Instrumentation and Measurement, 68*(4), 972-979, doi:10.1109/TIM.2018.2863999.

Strategic Communication Division (2019). Malaysia Environmental Quality Report 2018. In Department of Environment (Ed.). Malaysia: Ministry of Environment.

Syafrina, A. H., Zalina, M. D., & Juneng, L. (2015). Historical trend of hourly extreme rainfall in Peninsular Malaysia. *Theoretical and Applied Climatology, 120*(1), 259-285, doi:10.1007/s00704-014-1145-8.

Talavera, J. M., Tobón, L. E., Gómez, J. A., Culman, M. A., Aranda, J. M., Parra, D. T., et al. (2017). Review of IoT applications in agro-industrial and environmental fields. *Computers and Electronics in Agriculture, 142*, 283-297, doi:10.1016/j.compag.2017.09.015.

Tan, M. L., Samat, N., Chan, N. W., Lee, A. J., & Li, C. (2019). Analysis of Precipitation and Temperature Extremes over the Muda River Basin, Malaysia. *11*(2), 283. doi:10.3390/w11020283

The World Bank Group Global Solar Atlas. https://globalsolaratlas.info. Accessed December 12th 2019.

Trevathan, J., Read, W., & Schmidtke, S. (2020). Towards the Development of an Affordable and Practical Light Attenuation Turbidity Sensor for Remote Near Real-Time Aquatic Monitoring. *20*(7), 1993. doi:10.3390/s20071993

Tushar, W., Wijerathne, N., Li, W., Yuen, C., Poor, H. V., Saha, T. K., et al. (2018). Internet of Things for Green Building Management: Disruptive Innovations Through Low-

Cost Sensor Technology and Artificial Intelligence. *IEEE Signal Processing Magazine, 35*(5), 100-110, doi:10.1109/MSP.2018.2842096.

Uno, M., & Kukita, A. (2018). Single-Switch Single-Magnetic PWM Converter Integrating Voltage Equalizer for Partially Shaded Photovoltaic Modules in Standalone Applications. *IEEE Transactions on Power Electronics, 33*(2), 1259-1270, doi:10.1109/TPEL.2017.2678526.

Viswanath, S. K., Yuen, C., Tushar, W., Li, W., Wen, C., Hu, K., et al. (2016). System design of the internet of things for residential smart grid. *IEEE Wireless Communications, 23*(5), 90-98, doi:10.1109/MWC.2016.7721747.

Wang, B., Farooque, M., Zhong, R. Y., Zhang, A., & Liu, Y. (2021). Internet of Things (IoT)-Enabled accountability in source separation of household waste for a circular economy in China. *Journal of Cleaner Production, 300*, 126773, doi:10.1016/j.jclepro.2021.126773.

Wang, Y., Ho, I. W. H., Chen, Y., Wang, Y., & Lin, Y. (2021). Real-time Water Quality Monitoring and Estimation in AIoT for Freshwater Biodiversity Conservation. *IEEE Internet of Things Journal*, 1-1, doi:10.1109/JIOT.2021.3078166.

Weather News. https://weathernews.jp/s/.

WHO (2019). Safer Water, Better Health. World Health Organization.

Wong, C.-L., Liew, J., Yusop, Z., Ismail, T., Venneker, R., & Uhlenbrook, S. (2016). Rainfall Characteristics and Regionalization in Peninsular Malaysia Based on a High Resolution Gridded Data Set. *Water, 8*, 500, doi:10.3390/w8110500.

Wong, Y. J., Arumugasamy, S. K., Chung, C. H., Selvarajoo, A., & Sethu, V. (2020a). Comparative study of artificial neural network (ANN), adaptive neuro-fuzzy inference system (ANFIS) and multiple linear regression (MLR) for modeling of Cu (II) adsorption from aqueous solution using biochar derived from rambutan (Nephelium lappaceum) peel. *Environmental Monitoring and Assessment, 192*(7), 439, doi:10.1007/s10661-020-08268-4.

Wong, Y. J., Shimizu, Y., He, K., & Nik Sulaiman, N. M. (2020b). Comparison among different ASEAN water quality indices for the assessment of the spatial variation of surface water quality in the Selangor river basin, Malaysia. *Environmental Monitoring and Assessment, 192*(10), 644, doi:10.1007/s10661-020-08543-4.

Wong, Y. J., Shimizu, Y., Kamiya, A., Maneechot, L., Bharambe, K. P., Fong, C. S., et al. (2021). Application of artificial intelligence methods for monsoonal river classification in Selangor river basin, Malaysia. *Environmental Monitoring and Assessment, 193*(7), 438, doi:10.1007/s10661-021-09202-y.

WWAP (2021). The United Nations World Water Development Report 2021: Valuing Water United Nations World Water Assessment Programme (WWAP), United Nations Educational, Scientific and Cultural Organization (UNESCO).

Yadav, S., Luthra, S., & Garg, D. (2020). Internet of things (IoT) based coordination system in Agri-food supply chain: development of an efficient framework using DEMATEL-ISM. *Operations Management Research*, doi:10.1007/s12063-020-00164-x.

Yatim, A. N. M., Latif, M. T., Ahamad, F., Khan, M. F., Nadzir, M. S. M., & Juneng, L. (2019). Observed Trends in Extreme Temperature over the Klang Valley, Malaysia. *Advances in Atmospheric Sciences, 36*(12), 1355-1370, doi:10.1007/s00376-019-9075-0.

Zakaria, R. M., Aslezaeim, N., & Sofawi, A. B. Effects of water properties and soil texture on the growth of a mangrove palm; Nypa fruticans on carey Island, Malaysia. In, *2017*

Zhang, Z., Zhou, Y., Liu, H., Zhang, L., & Wang, H. (2019). Visual Measurement of Water Level under Complex Illumination Conditions. *Sensors, 19*(19), 4141.

Zhou, Z., Wang, Z., Yu, H., Liao, H., Mumtaz, S., Oliveira, L., et al. (2021). Learning-Based URLLC-Aware Task Offloading for Internet of Health Things. *IEEE Journal on Selected Areas in Communications, 39*(2), 396-410, doi:10.1109/JSAC.2020.3020680.

Zhu, Y., Cao, P., Liu, S., Zheng, Y., & Huang, C. (2020). Development of a New Method for Turbidity Measurement Using Two NIR Digital Cameras. *ACS Omega, 5*(10), 5421-5428, doi:10.1021/acsomega.9b04488

Chapter 8

Conclusions and Recommendations

8.1 Summary and Conclusions

In this research, spatiotemporal effects of land use, climate and COVID-19 impacts on the environment in East (Taiwan) and Southeast Asia (Malaysia) were studied using four case studies (Chapter 3 to Chapter 6). The impacts of changing land use and occurrence of extreme climatic events have been alarming across the globe; however, the local scale conditions remain unknown. Therefore, to address this question, Chapters 3 and 4 which focus on the streamflow conditions under changing land use and changing climate, respectively, are studied. In addition, the occurrence of the COVID-19 pandemic has brought profound impacts on many aspects of life and the economy; notably, due to the new normal lifestyle, the nature has been reclaiming itself. However, the air quality conditions in the absence of lockdown were not reported. Therefore, to understand the impacts of COVID-19, Chapters 5 and 6 performed the comparison in pollutants concentration between business-as-usual and simulated concentrations, using linear regression models and artificial intelligence (AI) models, respectively.

In Chapter 3, it could be observed that network optimization played an important role in improving the prediction accuracy of the land use type classification from satellite images in Malaysia. Compared to artificial neural network (ANN), support vector machine (SVM) has lesser sensitivity on the hyperparameter adjustment, but higher variation is observed across different training algorithms/membership functions. This is mainly due to SVM is rule-based algorithm where the characteristics among parameters must be well understood before making the predictions. Therefore, in this research, ANN might be more suitable for predicting the land use type from the satellite images. For future land use simulation, the prediction accuracy for utilizing the present land use maps (1990 and 2000) to simulate 2016

land use maps could reach up to 97%, indicating the accuracy of the LCM. The forestry in the Selangor river basin experienced drastic loss up to 300% in 2050 as compared to 1990, and the urban area expanded up to 200% over 60 years. The simulated land use is used to simulate the future streamflow. Extreme streamflow such as no flow rate or very high flow rate up to 100 m^3/s is more commonly encountered in the future. Through the simulation, this is important to have proper management for water resources to prevent prolonged drought or extreme rainfall induced flood events.

For Chapter 4, the present, near-, mid- and far future of extreme flooding events across different cities in Taiwan were simulated using high resolution Meteorological Research Institute of the Japan Meteorological Agency version 3.2 (hereinafter referred to as MRI-AGCM3.2s) dataset under Rainfall-Runoff-Inundation (RRI) model. Bias-correction procedure is crucial when using MRI-AGCM 3.2s dataset as huge variation are observed between uncorrected and gauge datasets. The precipitation and temperature trends are observed to vary dynamically in the future, with increment of temperature more than 3°C and rainfall volume change spatiotemporally across different cities. For near-and-mid future simulation, the maximum river flood rate is expected to increase more than 20%. However, for the far-future, the East and South regions of Taiwan are expected to face severe flooding issues; whereas prolonged drought and water stress issues are expected in the Central and Northern regions, providing insightful findings to the responsible authorities to have better water storage and management.

In Chapter 5, long-term COVID-19 impacts on the atmospheric environment in Taiwan, incorporating public transportation use and meteorological impacts in the absence of lockdowns was studied. Substantial improvements were observed in the studied air pollutants, wherein both PM_{10} and $PM_{2.5}$ showed the highest annual mean concentration reduction in 2020 relative to 2018-2019, by 24 and 18%, respectively, followed by SO_2, NO_2, CO and O_3, with reductions of 15, 9.6 and 7.4 and 1.3%, respectively, even in the absence of lockdown. The occurrence frequency of air pollutants that may cause adverse health effects decreased by more than 30% in 2020 compared to 2018-2019, particularly in O_3 and $PM_{2.5}$.

This research makes an important contribution to the literature as it is the first to investigate the impact and patterns of different modes of public transportation (*i.e.,* including roadway, railway, air, and waterway) on air quality improvements in 2020. The change trends of CO and NO_2, the major pollutants emitted from the public transportation sector, were found to be in parallel with the shift in traffic volume patterns in 2020.

In Chapter 6, utilizing four different AI methods, namely generalized additive model (GAM), gradient boosting machine (GBM), generalized linear model (GLM) and random forest (RF) to quantify the spatiotemporal impacts of COVID-19 on NO_2 and O_3 concentrations across 62 cities in Taiwan under meteorological-normalized BAU conditions. The selection of modelling method and the optimization of hyperparameter is crucial for each studied monitoring station for simulating the BAU concentrations of air pollutants. For GLM, the optimal data distribution for both NO_2 and O_3 modelling is Gaussian data distribution, whereas for GAM, the optimal data distribution for NO_2 and O_3 simulation is Quasi and Poisson, respectively. Meanwhile, for RF and GBM, the optimized number of trees is highly site dependent. Due to the complicated and non-linear characteristics between the air pollutants with temporal and meteorological parameters, regression-based models (GAM and GLM) have the poorest performance. For Taiwan, it could be observed that tree-based models (RF and GBM) are more suitable for simulating the NO_2 and O_3 BAU concentrations. Throughout 2020, even in the absence of a lockdown, the daily mean meteorological-normalized NO_2 and O_3 across Taiwan were observed to reduce by 14.9% and 5.8%, respectively with significant spatiotemporal variation. Due to the frequent occurrence of downpour in recent decades, further studies on higher temporal resolution such as hourly are required to better understand the meteorological impacts to the air pollutants.

Based on the findings from Chapter 3 to Chapter 6, a common issue facing in the developing countries is the inadequate number of monitoring stations as the assessment of the surface water and ground air quality is often labor-intensive, costly and time consuming. Therefore, to address the possible issues, Chapter 7 presented the effective integration of IoT with 3D printing, microcomputers, and low-cost sensors on water quality monitoring and its

possibility to be widely used for environmental monitoring, paving a new path for the development of cost-effective and reliable systems for both water and air quality monitoring.

The application and integration of remote sensing techniques, geographical information system (GIS), AI, big data analysis/management and IoT system has been gaining popularity in addressing/evaluating environmental issues. The number of monitoring station for pollutant concentrations are limited in most developing countries, leading to the limited local scale pollution management. Concurrently, due to limited data availability, the hydrological or air quality modelling are facing huge simulation challenges due to low simulation accuracy. Therefore, this research has studied and proven the integration of these techniques to possibly evaluate/address the environmental issues in the region, overcoming the low simulation accuracy by optimizing the models and proposing new monitoring technique for enhancing the spatiotemporal monitoring frequency.

8.2 Recommendations

In this research, only flood simulations were performed in this research. However, as summarized in Chapters 1 and 2, the impacts of drought are also critical in these regions. The economical impacts of drought, particularly in agricultural areas were not accessed in this research. Therefore, in the future, utilizing the available dataset, the drought impacts should be accessed and possible mitigation solutions such as proper water management/storage during drought should be studied.

In addition, for the BAU air pollutants concentration simulation in both Chapters 5 and 6, due to the limitation of the dataset available, the cross-boundary pollution was omitted. The long-range transportation of air pollutants in the neighboring countries also poses significant impacts to Taiwan and should be considered in the future studies. Last but not least, as there are no detailed data available on the local emissions (industrial, domestic) and sudden/accidental pollution, which may have further limited the ability to identify the underlying reasons for the improvements in the research even though back trajectory tool was applied.